Thermal-Fluid Behavior of Mixed Refrigerants for Cryogenic Applications

by

Rodrigo Sebastian Barraza Vicencio

A dissertation submitted in partial fulfillment of

the requirements for the degree of

Doctor of Philosophy

(Mechanical Engineering)

at the

UNIVERSITY OF WISCONSIN-MADISON

2015

Date of final oral examination: 04/28/2015

The dissertation is approved by the following members of the Final Oral Committee:

Gregory f. Nellis, Professor, Mechanical Engineering
Sanford A. Klein, Professor, Mechanical Engineering
Douglas T. Reindl, Professor, Engineering Professional Development
Franklin Miller, Assistant Professor, Mechanical Engineering
Tim A. Shedd, Associate Professor, Mechanical Engineering

ABSTRACT

The use of mixed gas working fluids has become common in Joule–Thomson type cryocoolers for a variety of applications. However, there is a scarcity of data currently available with supporting theory capable of predicting the heat transfer coefficients associated with two-phase, multi-component mixtures at cryogenic temperatures. This document describes an experimental facility designed and constructed to measure the heat transfer coefficients and frictional pressure drop in small diameter, horizontal test sections with two-phase, multi-component zeotropic mixtures at cryogenic temperatures. The aim of this facility is to enable the collection of high accuracy data to overcome the scarcity of heat transfer and pressure drop data for zeotropic mixtures undergoing a phase change (boiling). Results are available for hydrocarbon mixtures (comprised of methane, ethane, and propane) and synthetic refrigerant mixtures (including R-14, R-23, R-32, and R-134a), which are commonly used in small Joule–Thomson cryocoolers. The measured heat transfer coefficients for hydrocarbon and synthetic mixtures included nitrogen and argon, respectively for dilution.

The heat transfer coefficient measurements have been shown to be repeatable and accurate with an uncertainty of less than 10%. The pressure drop measurements have been calibrated, validated and the facility is capable of measuring the frictional pressure drop under both adiabatic and diabatic conditions. The measured heat transfer coefficient data are presented over a temperature range from 100 K to room temperature along with their sensitivity to parameters such as heat flux, mass flux, pressure, tube diameter, and mixture composition.

These measured data are then used to evaluate models to characterize the pressure drop and heat transfer process in horizontal tubes. The heat transfer coefficient data is predicted well using correlations as described by Granryd [1] and Little [2]. Granryd is the recommended correlation to predict heat transfer coefficient of zeotropic mixtures. Granryd shows the best accuracy with an Absolute Average Deviation (AAD) of 15% and predicting 87% of the data with a relative error lower than 30%. Little seems to exhibits greater accuracy at high Reynolds number or high thermodynamic quality or both; however, its accuracy is substantially reduced for low qualities and low Reynolds number. The measured frictional pressure drop data are compared to several pressure drop correlations available in the literature and the Awad and Muzychka correlation [3] was able to predict the frictional pressure drop over the range of experimental data considered, with an AAD of 17%. The second best correlation is Sun and Mishima [4] with an AAD of 18%. In addition, the Cicchitti et al. [5], Müller-Steinhagen and Heck [6] and Mishima and Hibiki [7] correlations also show reasonable agreement with the experimental data. Based on our data, the Awad and Muzychka (definition 1) [3] homogeneous model is recommended for prediction of pressure drop because this correlation agrees with 86% of our data with a relative absolute error lower than 30%. Also, Awad and Muzychka (definition 1) [3] requires only liquid and vapor viscosity, quality, and mixture density.

ACKNOWLEDGMENTS

This work is dedicated to Anita for her endless support, patience and love. We have spent the last five years in Madison having many marvelous experiences. Also, we have met many fascinating people that we hope to keep in touch with after we return to Chile.

I am very grateful to have chosen the University of Wisconsin-Madison as my graduate school. I especially want to thank to Professor Sanford Klein for giving me the opportunity to be part of the Solar Energy Laboratory. I have been very fortunate to be advised by Greg Nellis, Sanford Klein, and Douglas Reindl because of their dedication, support, and leadership. I am definitely a better person and engineer after working with you. All the knowledge and experience that I have obtained at the Solar Energy Laboratory will help me to approach and lead quality engineering research in my future professional development.

Also, I want to thank to Fredrick Schwartz and Jacob Kilbane because the success of this project would not have been possible without your invaluable collaboration. Jake is sharp, a hard worker, and always willing to help. Jake participated actively in the building of the experimental test facility and always tries to proposed ideas to improve designs and make the construction process easier. Fritz is a trustworthy person, a hard worker, and always willing to collaborate in many tasks and even work overtime when it was necessary. Fritz performed many modifications to the original test facility as necessary to improve the performance and control of the test apparatus. Fritz was also responsible for collecting most of the experimental data shown in this report during never-ending work days.

This research has been sponsored by the American Society of Heating, Refrigerating, and Air-Conditioning Engineers (ASHRAE), Research Project 1602-TRP. Rodrigo Barraza was

supported between 2010 and 2014 by Fulbright and CONICYT, Gobierno de Chile, doctoral fellowships. Finally, the Universidad Técnica Federico Santa Maria provided financial support for seven months between September 2014 and February 2015.

TABLE OF CONTENT

LIST OF FIGURES

LIST OF TABLES

NOMENCLATURE

A : area

AAD : average absolute deviation

Bo : Boiling number

Bo : Bond number

C : Chisholm parameter

C : constant Mishra correlation

C : specific heat at constant pressure

C_{lv} : enhancement factor

CFD : computational fluid dynamics

Cp : specific heat at constant pressure

C_R : capacitance

Co : Convective number

D : diameter

D : diffusion coefficient

ID : inner diameter

f : fluid property

f : function

f : friction factor

Eo : Eotvos number

F : enhancement factor

F : function

F_D : diffusion factor

Fr : Froude number

g : gravitational acceleration

G : mass flux

h : enthalpy

htc : heat transfer coefficient

i : index of each sub-HX

i : axial node

I : current

j : radial node

JT : Joule-Thomson

K : coefficient

k : thermal conductivity

L : length

L_c : average conduction length

La : Laplace number

M : molar mass

MLI : multi-layer insulation

m : slope

$\dot{m}$: mass flow rate

N : number of turns

N : number of sub-heat exchangers

Nu : Nusselt number

NTU : number of transfer units

$\dot{Q}''$: heat flux

OD : outer diameter

P : pressure

P : pressure

Pe : Peclet number

Pr : Prandtl number

PRT : platinum resistance thermometer

$\dot{q}$: rate of heat

$\dot{Q}$: rate of heat

$\dot{Q}''$: heat flux

r : radius

$r[j]$: the radius in the medium point between the node [i,j] and [i,j+1]

R : electrical resistance

R : roughness

R_c : thermal contact resistance
relrough : relative roughness
Re : Reynolds Number
RMS : root mean square
S : suppression factor
t : time
T : temperature
$T_s\,[i]$: temperature of the block surface
th : wall thickness
U : velocity
u : uncertainty
UA : conductance
V : voltage
V_1 : volatility parameter
x : quality
x : liquid mass fraction
$x_{(fd,h)}$: hydrodynamic entry length
$x_{(fd,t)}$: thermal entry length
$x[j]$: the radius for the node [j]
X : Lockhart-Martinelli coefficient
$\Delta x[i]$: length of each sub-HX
We : Weber number
y : vapor mass fraction
z : composition
z : length

Subscripts

A : test section approach
a : average
avg : average

B : actual inlet to the active portion of the test section
B : boiling
b : fluid as a whole
C : actual outlet of the active portion of the test section
C : corrected
c : combined
c : contact
c : convective boiling
c : corrected
c : cryocooler
c-HX : cryocooler HX
cc : cooling capacity
cold : cold side
cal : calibration
D : test section departure
d : discharge
DAQ : Data AcQuisition System
D : diameter
H : hydraulic
hot : hot side
i : inner
i : instrument
in : inlet
int : interphase
JT : Joule-Thomson
L : axial
l : liquid
lo : liquid only
lv : latent or vaporization
LMTD : Logarithmic mean temperature difference
m : mean

m : metal
max : maximum
min : minimum
mixt : mixture
MLI : multi-layer insulation
n : nucleate boiling
nb : nucleate boiling
p : constant pressure
p : precision
r : radial
r : reduced
r-HX : recuperative HX
RMS : root mean square
out : outlet
s : suction
ss : stainless steel
tv : turbulent liquid/laminar vapor
tt : turbulent liquid/turbulent vapor
test section: test section
turb : turbulent
v : vapor
v : vapor only
vt : laminar liquid/turbulent vapor
vv : laminar liquid/laminar vapor
w : wall
0 : reference
1 : more volatile component
1 : first inlet temperature measurement
2 : second inlet temperature measurement
3 : first outlet temperature measurement
4 : second outlet temperature measurement

5 : first block temperature measurement

6 : second block temperature measurement

$2ph$: two-phase

Superscripts

m : constant Mishra correlation

n : constant Mishra correlation

Greek Symbols

α : void fraction

Δ : difference

Δ : delta

δ : uncertainty

∂ : differential

δ : gap between tubes in the recuperative heat exchanger

ε : effectiveness

ε : emissivity

ρ : density

μ : viscosity (kg/m-s)

π : pi number

σ : surface tension

ϕ : diameter

ϕ : two-phase multiplier

Γ : physical property coefficient

1. INTRODUCTION

1.1. Motivation

Two types of mixtures are currently used in the refrigeration industry: azeotropes and zeotropes (sometimes referred to as "non-azeotropes"). An azeotropic mixture is formed by two or more constituents that, together, behave like a single component refrigerant. This behavior is attributable to the strong thermodynamic interactions between unlike molecules that comprise the mixture. When an azeotropic mixture experiences evaporation or condensation at constant pressure, the temperature remains constant, just as it does for pure fluids. Zeotropic (or non-azeotropic) mixtures behave differently than pure fluids during constant pressure phase change (condensation and boiling) by exhibiting a temperature change or "glide" between the dew and bubble points rather than a constant temperature as is the case for pure fluids. Boiling is initiated at the bubble point temperature and the mixture temperature increases to the dew point temperature as the phase change proceeds to a vapor state. Zeotropic mixtures are the focus of this study.

The use of chlorofluorocarbons (CFCs) and hydrochlorofluorocarbons (HCFCs) in the refrigeration industry is quickly ceasing due to environmental impacts such as ozone depletion and greenhouse gas effects. CFC and HCFC refrigerants can be replaced with a single component refrigerant or azeotropic mixture that have similar properties, and also with a zeotropic mixture that is able to provide refrigeration at nearly constant temperature. A zeotropic mixture is formed by two or more fluids. Some examples are R-404a (R-125 (44%)/R-143a (52%)/R-134a (4%), by weight) and R-407c (R-32 (23%)/R-125 (25%)/R-134a (52%), by weight) which are zeotropic mixtures that have replaced R-502 and R-22, respectively. These mixtures have a temperature glide between 0.5 and 7 K.

Studies have also shown an improvement in the performance of Rankine cycles using zeotropic mixtures with low grade heat sources. Li et al. [8] observed an increase in thermal efficiency of solar organic Rankine cycle with a zeotropic mixtures when a recuperator heat exchanger is included in the system. Also, the use of mixtures allows a wide range of selection of fluids to be used in these systems. Chen et al. [9] has shown improvements of thermal efficiencies between 10 and 30%. Wang and Zhao [10] analyze a low temperature solar Rankine cycle operating with different composition of mixtures R-245fa/R-152a. This study did not find any improvement of thermal efficiency using any of the analyzed mixtures in comparison with pure R-245fa, but Wang showed that a smaller expander is required when zeotropic mixtures are used. Consequently, a reduction of capital cost of the system may be expected.

Zeotropes are also widely used in applications such as air conditioning, heat pumps and refrigeration systems. Zeotropic mixtures may provide a thermodynamic performance advantage resulting from reduced entropy generation when the temperature glide is approximately the same as the temperature change of the heat transfer fluid (e.g., air or water) circulating in the condenser or evaporator; consequently, the refrigeration cycle efficiency could be improved using appropriate heat exchangers [11]. Studies have shown improvements in the thermal efficiency of 9% [12] and 30% [13] for air conditioning and heat pump systems, respectively, using zeotropic mixtures. In addition, mixed gas refrigeration systems have been found to be an option for providing cooling capacity in the temperature range between 120 and 240 K (and sometimes lower) for a variety of applications. The optimum mixture for such systems generally leads to a zeotrope with a very large temperature glide. Ideally, the mixture should exhibit a dew point temperature at the compressor discharge pressure that is close to ambient temperature and a bubble point temperature at the compressor suction pressure that is near to the required refrigeration temperature [14].

A typical Joule–Thomson refrigeration cycle (JT) using a pure substance such as nitrogen as the working fluid provides a relatively low efficiency and requires a high working pressure (250 bar). However, the JT cycle has the advantages of low cost, high reliability, and is a low cost option for small loads associated with industrial and medical applications. Many researchers, including Little [15], Luo et al. [16] and Boiarski et al. [17], have demonstrated that the JT cycle efficiency increases substantially (e.g., by an order of magnitude) when the system uses zeotropic mixtures (such as nitrogen-hydrocarbon mixtures) as the working fluid. In addition, the required working pressure is significantly reduced compared to pure fluids. Consequently, the Joule–Thomson cycle has recently become more attractive and is now competitive with other refrigeration systems for low or cryogenic temperature applications. Typical evaporating temperatures for these systems range between 70 K and 230 K, with cooling capacities ranging from less than 1 W to several MW. The JT cycle is currently used in many specialty cryogenic applications, such as cryosurgical probes, cooling infrared sensors, cryopreservation, liquefaction, biomedical samples, and current leads.

Many applications utilize heat exchangers with small tubes or mini-channels using two-phase flow because they are able to transfer higher heat flux in a smaller space than traditional heat exchangers. As the channel size is reduced, the surface area to volume ratio increases which reduces both material and fluid requirements. The advantage of using small tubes in heat exchangers is even more significant if two-phase-flow occurs throughout the heat exchanger because of its higher heat transfer coefficient; however, the reduction in channel size increases the frictional pressure drop; thereby, creating parasitic effects to the refrigeration system. Designers often seek to optimize their systems by balancing the advantages and drawbacks of using two-phase flow in small channels; consequently, accurately predicting both the pressure drop and heat transfer coefficient is essential.

The thermal performance of JT systems strongly depends on the proper optimization of the gas mixtures. Several authors including Keppler et al. [18], Little [19], Gong et al. [20], Alexeev et al. [21] and Skye et al. [22] have proposed systematic techniques to optimize the composition of gas mixtures as a function of the operating conditions. Many of the optimization techniques used for these systems are largely focused only on the thermodynamic performance of the mixture and ignore the details of the heat transfer process; however, the performance of the recuperative heat exchanger is critical for plants with fixed heat exchangers.

The thermodynamic properties for mixtures are generally well understood, but the thermal behavior of gas mixtures within heat exchangers is not yet well characterized; consequently, current optimization techniques do not consistently yield the best performance when used to charge actual JT machines. When a JT system is charged with a mixture, it is often the case that the mixture composition to optimize the actual system is only obtained after many additional trial-and-error experimental iterations are performed. This trial-and-error optimization process greatly increases the development time and cost.

Effects of the heat transfer processes on cycle performance cannot be effectively accounted during the optimization because there are very few data or theories available that can reliably predict heat transfer coefficients of boiling zeotropic multi-component mixtures in small diameter horizontal tubes. The studied zeotropic mixtures experience two-phase (condensation or boiling) with very large temperature glides while operating at cryogenic temperatures. Although frictional pressure drop correlations for multi-phase and multi-component fluid operating at the conditions described here are an important tool for designers, there is little information in the open literature that discusses this topic and validates the models with experimental data.

1.2. Objectives

The goals of this project are:

- Build and validate an experimental test facility to make accurate measurements of the heat transfer coefficient due to convection (to within 10%) and frictional pressure drop for boiling gas mixtures. Generally, the phase change is experienced from 150 K to room temperature. The measurements will be performed in heated horizontal tube test sections with inner diameters of 0.5, 1.5 and 3.0 mm.
- Provide measurements of heat transfer coefficients for at least two sets of gas mixtures: hydrocarbon mixtures (methane, ethane, propane, and nitrogen (for dilution)) and refrigerant mixtures (R-14, R-23, R-32, R-134a, and argon which is used for dilution).
- Provide measurements of pressure drop across the test section.
- Assess the usefulness of currently available correlations for heat transfer and pressure drop in terms of their ability to predict the data.

The collected data is intended to enable understanding the mechanisms that drive the two-phase, multi-component heat transfer and frictional pressure drop. The collected data can be used to validate existing correlations or, if necessary, support the development of new correlations which will allow optimization models to include heat transfer and frictional pressure drop constraints in the design of heat exchangers.

2. EXPERIMENTAL FACILITY

2.1. Design conditions

The experimental facility is built to measure forced convection heat transfer coefficient of zeotropic mixtures in a horizontal test section while the mixture is boiling. Also, the pressure drop across the test section can be measured under diabatic and adiabatic conditions. Three different tube sizes are tested including inner diameters of 0.5, 1.5, and 3.0 mm. The test facility provides the ability to measure heat transfer coefficients and frictional pressure drops for mixtures over a range of diameters, mass flux, heat flux, pressure, temperature, gas mixtures, and compositions as indicated in Table 1.

Table 1. Range of operation of the test facility

Parameter	Value		Unit
	minimum	maximum	
Inner diameter (*ID*)	0.5	3.0	mm
Mass flux (*G*)	150	250	kg/s m^2
Heat flux ($\dot{Q}''$)	0	120	kW/m^2
Pressure (*P*)	200	1135.3	kPa
Temperature (*T*)	150	300	K

At least two mixtures will be tested. One consists of traditional synthetic refrigerants (R-14, R-23, R-32, and R-134a), and the other a mixture of hydrocarbons (methane, ethane, and propane). The mixture of synthetic refrigerants is diluted using argon (0, 20, and 40%) and the hydrocarbons mixture using nitrogen (0, 20, and 40%). The mixtures composition are listed in Table 2:

Table 2. Zeotropic mixtures tested on the test facility

Mixtures	**Composition (vol/vol)**		
Hydrocarbon mixtures			
Methane	45%	36%	27%
Ethane	35%	28%	21%
Propane	20%	16%	12%
Nitrogen	0%	20%	40%
Synthetic refrigerant mixtures			
R-14	35%	28%	21%
R-23	15%	12%	9%
R-32	15%	12%	9%
R-134a	35%	28%	21%
Argon	0%	20%	40%

2.2. Description

The schematic of the experimental facility is shown in Figure 1. The experimental facility can be divided in two sections: the compressor and control station and the heat transfer section. Figure 2 shows a photo of the actual equipment that comprises the compressor and control station. The compressors take the gas mixture at a low pressure and compress it to the required high pressure with the necessary mass flow rate to provide the desired gas mixture flow rate to the system. After leaving the compressors, the discharge gas is cleaned, dried and cooled to room temperature by oil separators, a filter-dryer and an after-cooler, respectively. An arrangement of throttle valves, a pressure regulator, and a bypass loop are used to control the pressure and flow rate through the test section.

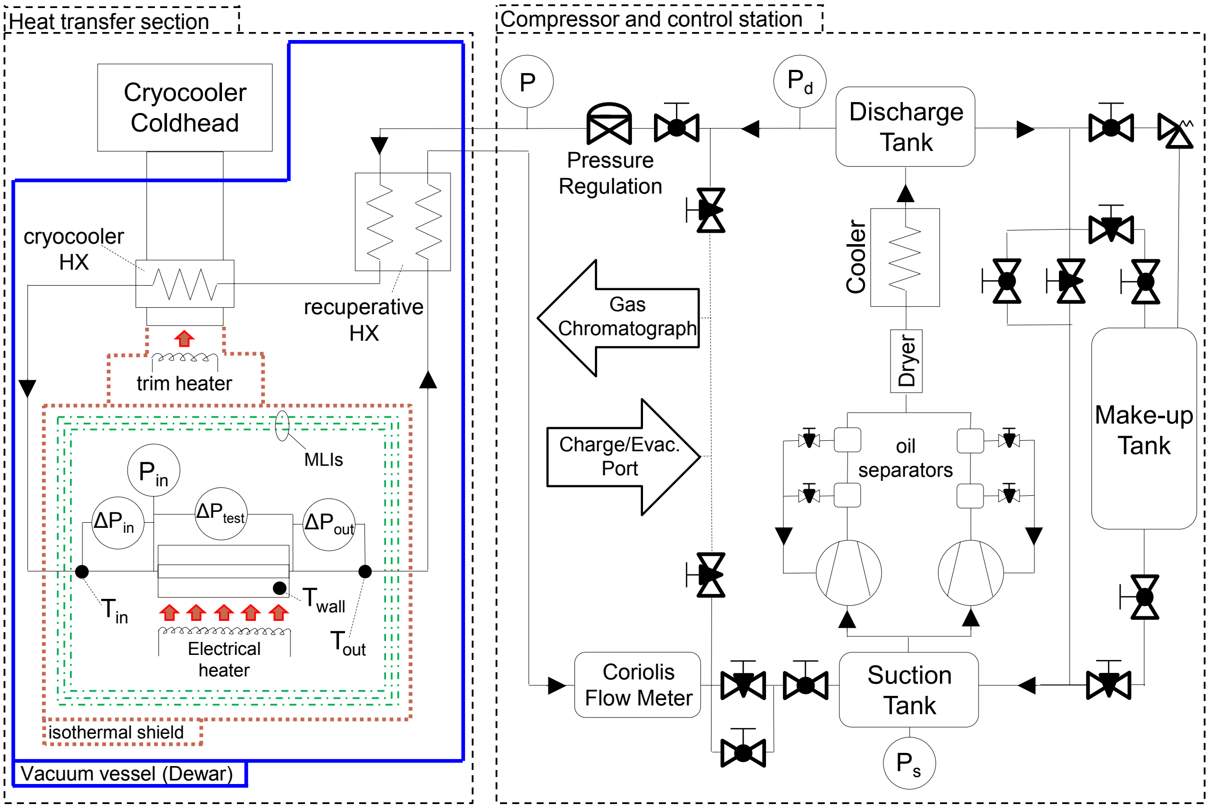

Figure 1. Schematic of experimental test facility

In addition, a make-up tank allows the system pressure to be maintained at a constant value for every condition. A Coriolis flow meter (Endress Hauser, model 83A02) measures the mass flow rate. The precise make-up of the circulating mixture composition is continuously monitored using a TCD gas chromatograph (HP 5890 II) by sampling the gas mixture at room temperature from either the low or the high pressure sides of the system.

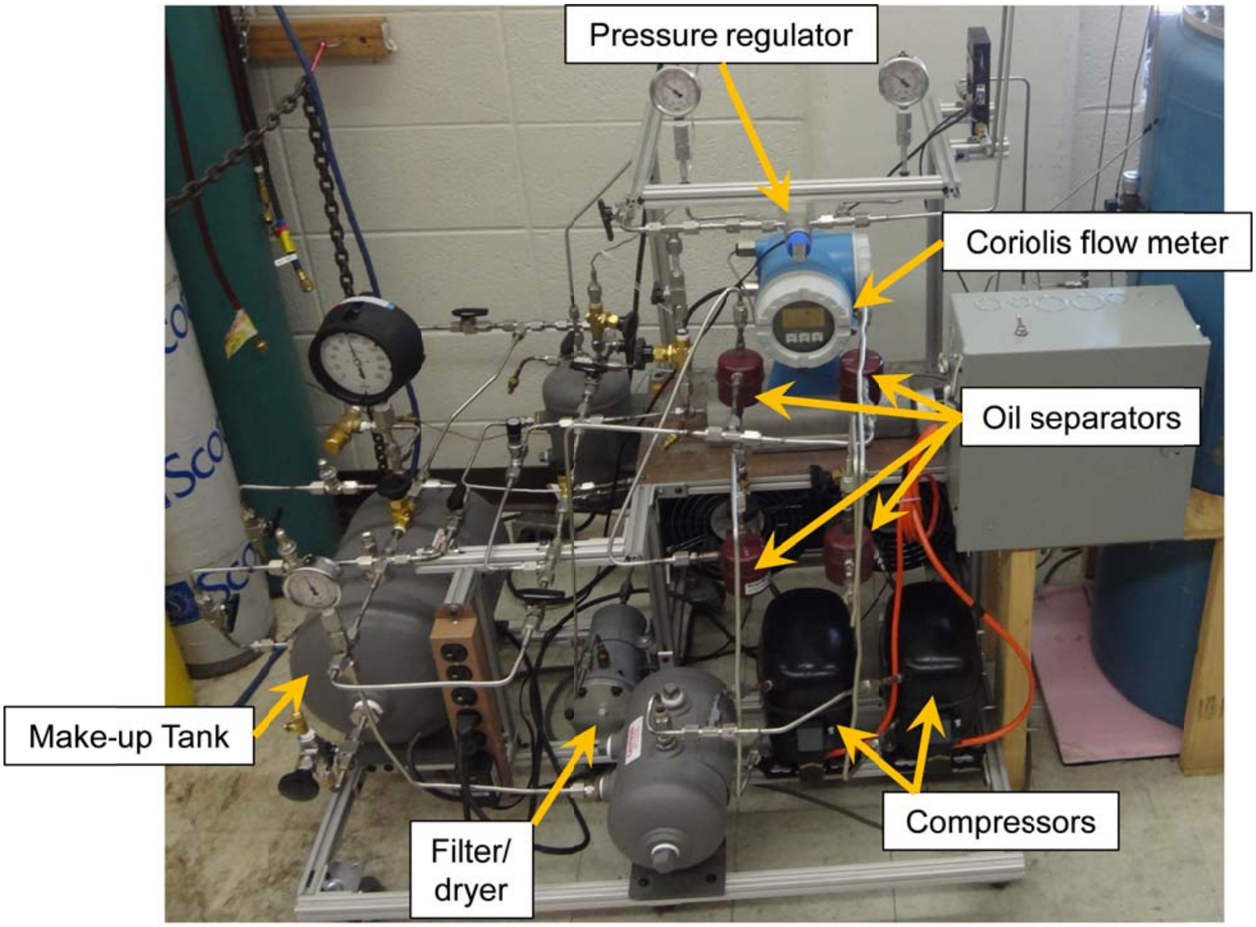

Figure 2. View of the compression station equipment outside of the Dewar

The heat transfer section is composed of a recuperative heat exchanger, cryocooler heat exchanger, and the test section. The entire heat transfer section is placed inside of a Dewar which maintains a high vacuum environment to minimize convection losses. In addition, an isothermal copper shield connected to the cryocooler encloses the test section to minimize radiative heat exchange. Multi-layer radiation shields (MLIs) are located between the test section and the isothermal shield. The heat transfer section is thermally isolated from the bulk of the test using low conductivity thin wall stainless steel tube. The circulating mixture is cooled from room temperature to the required test temperature (which could vary from 150 K to room temperature) in two stages. First, the gas mixture is precooled using a recuperative heat exchanger (labeled recuperative HX in the Figure 1). Finally, the fluid achieves the desired target temperature in the cryocooler heat exchanger (cryocooler HX), where the cryocooler itself removes the necessary thermal energy to cool the fluid to its terminal temperature before entering the test section. The cold head of the cryocooler is equipped with cartridge heaters (i.e., trim heaters) to precisely control the gas mixture supply temperature to the test section. Figure 3 shows a view of the actual heat transfer section and the Dewar.

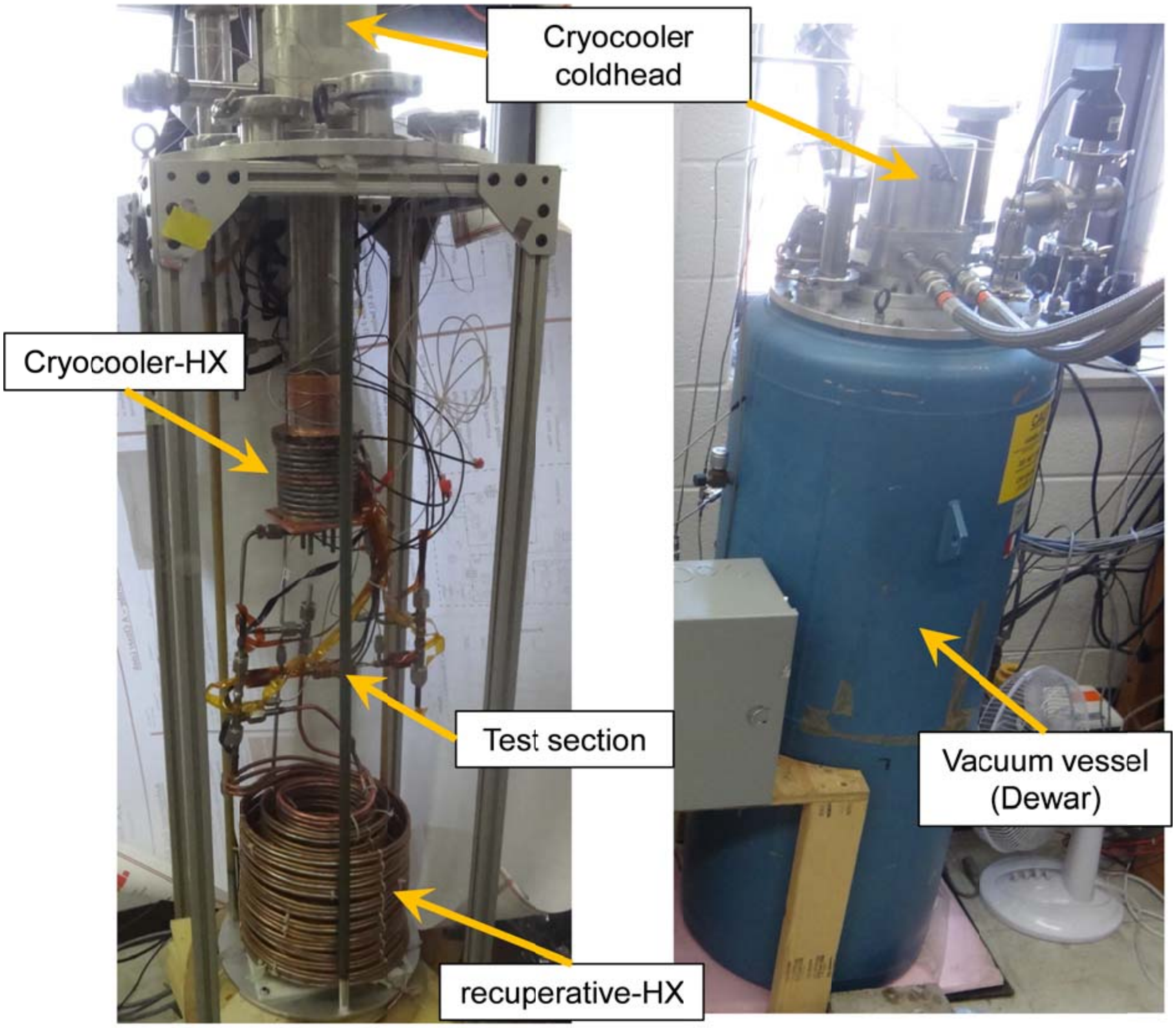

Figure 3. View of the actual test facility inside of the Dewar and the Dewar

2.3. Compressor and control station

2.3.1. Compressors

Two compressors Danfoss SC18CLX (Figure 4) installed in parallel provide the mass flow rate required ($\dot{m}_r$) in the test facility. Each compressor has a swept volume of 117 cm^3.

Figure 4. Compressor Danfoss SC18CLX

250 kg/m^2-s is the maximum mass flux presented in Table 1. This mass flux is equivalent to mass flow rates of 0.05, 0.44, and 1.77 g/s in the 0.5, 1.5, 3.0 mm test sections, respectively. These mass flow rates may be supplied on the range of pressure between 200 kPa and 1100 kPa in the test section. The installed compressors are able to provide the maximum mass flow rates ($\dot{m}_c$) reported on Table 3 for each planned refrigerant mixture and tested pressure. The maximum mass flow rates ($\dot{m}_c$) is calculated based on the compressors displacement without taking into account their volumetric efficiency.

Table 3. Test matrix

Base mixture	**Dilution**	***P* = 200 kPa**			**1100 kPa**		
		0.5 mm	1.5 mm	3.0 mm	0.5 mm	1.5 mm	3.0 mm
	$\dot{m}_r$ [g/s]	0.05	0.44	1.77	0.05	0.44	1.77
methane/ethane/propane (0.45/0.35/0.20)	0% N_2 $\dot{m}_c$ [g/s]	2.08	2.08	**2.08**	21.8	21.8	21.8
	20% N_2 $\dot{m}_c$ [g/s]	2.35	2.35	2.35	24.2	24.2	24.2
	40% N_2 $\dot{m}_c$ [g/s]	2.61	2.61	2.61	2.61	2.61	2.61
R-14/R-23/R-32/R-134a (0.35/0.15/0.15/0.35)	0% Ar $\dot{m}_c$ [g/s]	7.29	7.29	7.29	79.3	79.3	79.3
	20% Ar $\dot{m}_c$ [g/s]	6.48	6.48	6.48	70.5	70.5	70.5
	40% Ar $\dot{m}_c$ [g/s]	5.72	5.72	5.72	59.4	59.4	59.4

The most challenging condition occurs for the 45% methane, 35% ethane, and 20% propane gas mixture operating with the 3.0 mm inner diameter test section at a test section pressure of 200 kPa. For this condition, the required mass flow ($\dot{m}_r$) rate is 1.77 g/s and the compressors are capable of providing a maximum of 2.08 g/s.

2.3.2. Oil separator configuration

The oil is removed from the compressed gas installing two oil separators (temprite 320) in series for each compressor as shown in Figure 5.

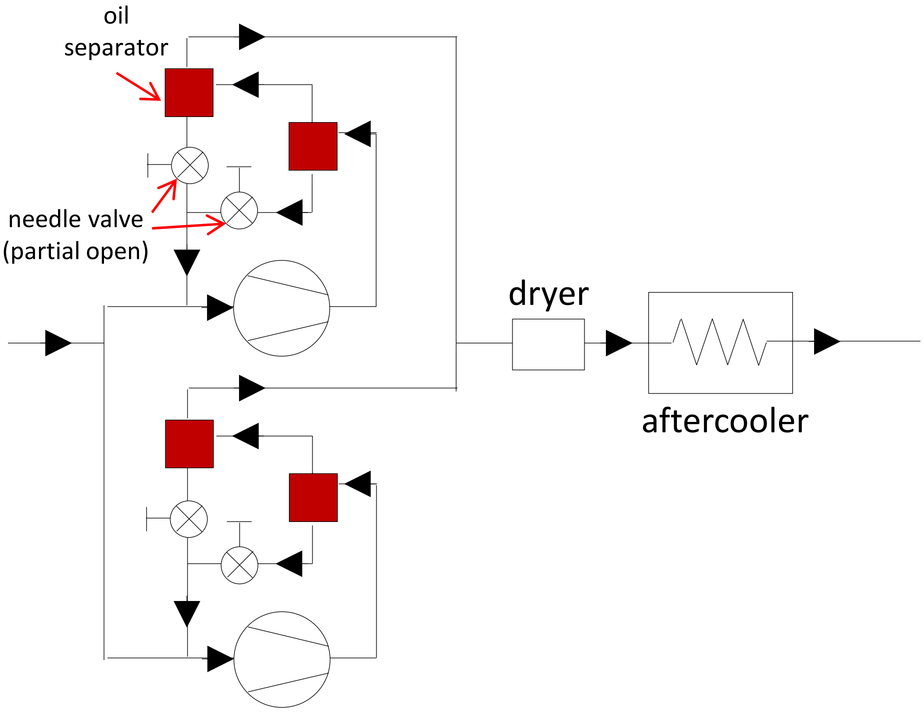

Figure 5. Schematic of the oil separator system

The oil lines coming from the bottom of each oil separator are connected to the service port of the compressors. Needle valves are installed in the oil lines leaving each oil separator. The needle valves are partially open to allow oil to flow with minimal gas flow. The pressure difference between the high pressure side and the service port drives a continuous oil re-circulation. Figure 6 shows a photo of the actual oil separator system.

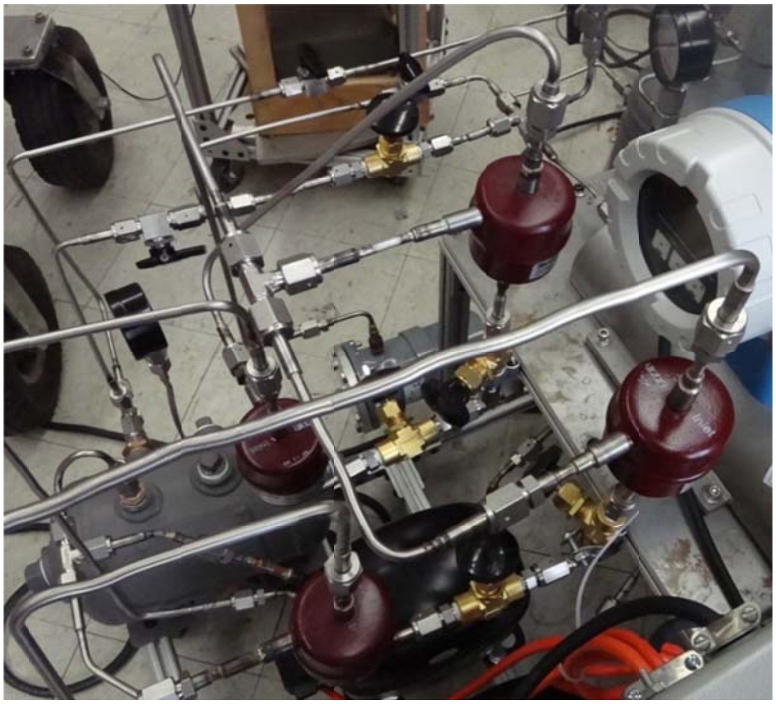

Figure 6. Oil separator system

An additional apparatus is installed to remove the excess of oil not captured by the oil separators and the moisture of the gas mixture. A core catch all filter-dryer RCW42 is installed as shown in Figure 7. The "clean gas" leaving the oil separators is forced to pass through a replaceable ceramic element of the filter-dryer.

Figure 7. Filter-dryer RCW42

2.3.3. Aftercooler

The clean compressed hot gas mixture is cooled to near ambient temperature in the aftercooler located after the filter-dryer. The aftercooler is a standard tube-fin heat exchanger Lytron 6320G3 BD with two fans, as is shown in Figure 8. A hydrostatic test was performed in situ. The aftercooler was pressurized up to 1450 kPa (200 psig) using methanol.

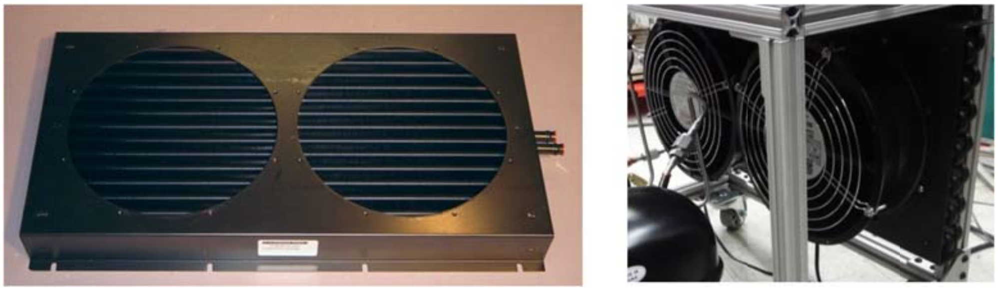

Figure 8. Aftercooler, standard tube-fin heat exchanger Lytron 6320G3 BD

2.4. Heat transfer section

The cryocooler does not have sufficient cooling capacity to reduce the temperature of the mixture from room temperature to the target 150 K temperature by itself; consequently, a recuperative heat exchanger is designed to pre-cooled the tested mixture. The cryocooler provides cooling to the fluid by the means of the cryocooler heat exchanger, which is installed immediately after the recuperative heat exchanger. The heat transfer section is schematically shown in Figure 9.

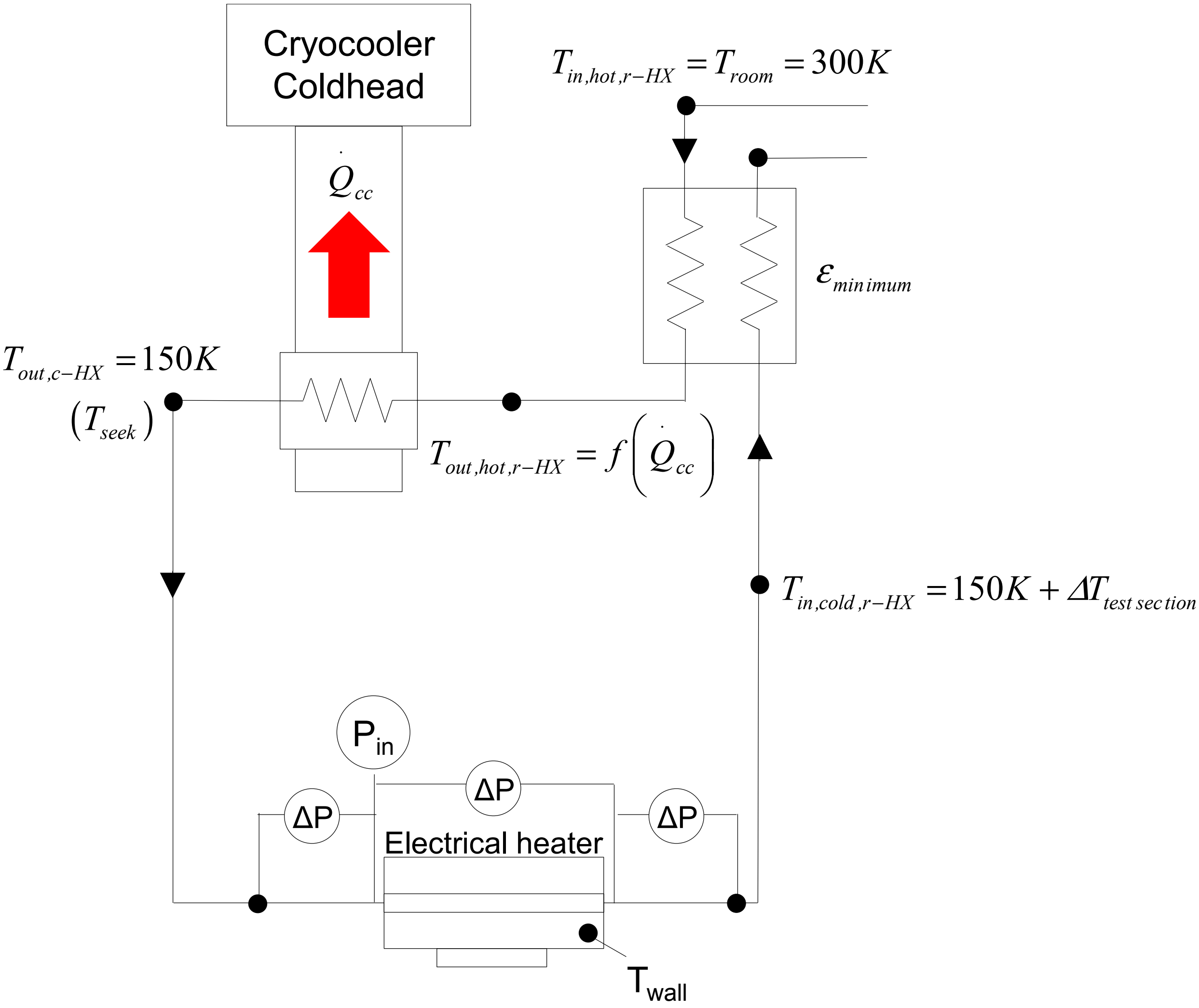

Figure 9. Heat transfer section

The design of the recuperative heat exchanger is a function of cooling capacity ($\dot{Q}_{cc}$) provided by the cryocooler. The design of the cryocooler heat exchanger is a function of cooling capacity and the equilibrium temperature or cryocooler base temperature at which that cooling capacity is provided. $T_{out,c\text{-}HX}$ is the temperature required in the inlet of the test section, which varies from 150 K to room temperature. As mentioned before, $\dot{Q}_{cc}$ increases as the temperature required increases, consequently, the challenging condition is faced when $T_{out,c\text{-}HX}$ is 150 K. The provided $\dot{Q}_{cc}$ defines what is the temperature required ($T_{out,hot,r\text{-}HX}$) in the outlet of the hot side of the recuperative heat exchanger according to:

$$\dot{Q}_{cc} = \dot{m}\left[h_{in.c-HX}\left(T_{out,hot,r-HX},P\right) - h_{out.c-HX}\left(T_{out,c-HX},P\right)\right] \tag{1}$$

The effectiveness required by the recuperative heat exchanger is given by the ratio between the required heat transfer rate ($\dot{Q}_{r-HX}$) and the maximum possible heat transfer rate ($\dot{Q}_{max,r-HX}$) in the recuperative heat exchanger as shown in Eq. (2).

$$\varepsilon_{min} = \varepsilon_{r-HX} = \frac{\dot{Q}_{r-HX}}{\dot{Q}_{max,r-HX}} \tag{2}$$

$\dot{Q}_{max,r-HX}$ is a function of the inlet ($T_{in,hot,r\text{-}HX}$) and outlet ($T_{out,hot,r\text{-}HX}$) temperature in the hot side of the recuperative heat exchanger.

$$\dot{Q}_{r-HX} = \dot{m}\left[h_{in,hot,r-HX}\left(T_{in,hot,r-HX},P\right) - h_{out,hot,r-HX}\left(T_{out,hot,r-HX},P\right)\right] \tag{3}$$

The inlet temperature in the hot side ($T_{in,hot,r\text{-}HX}$) is the room temperature, which is assumed to be 300 K. Eq. (4) shows the dependency of $\dot{Q}_{max,r-HX}$ on the inlet temperatures in the cold and hot side of the recuperative heat exchanger

$$\dot{Q}_{max,r-HX} = \dot{m}\left[h_{in,hot,r-HX}\left(T_{in,hot,r-HX},P\right) - h_{in,cold,r-HX}\left(T_{in,cold,r-HX},P\right)\right] \tag{4}$$

The inlet temperature in the cold side of the recuperative heat exchanger is defined by the increment of temperature in the test section ($\Delta T_{test\ section}$)

$$T_{in,cold,r-HX} = T_{out,c-HX} + \Delta T_{test\ section} \qquad (5)$$

$\Delta T_{test\ section}$ is limited between 5 and 10 K for the hydrocarbons mixture and 10 to 20 K for the refrigerant mixture. The maximum cooling power is required when mixtures flow in the 3.0 mm test section because of the constant mass flux condition for the three test section. The maximum mass flux is 250 kg/m^2-s. Figure 10 shows the effectiveness required in the recuperative heat exchanger as a function of the cryocooler cooling capacity ($\dot{Q}_{cc}$) to cool the mixtures up to the seek temperature in the 3.0 mm test section. The low (200 kPa) and high (1100 kPa) limits of pressure are analyzed.

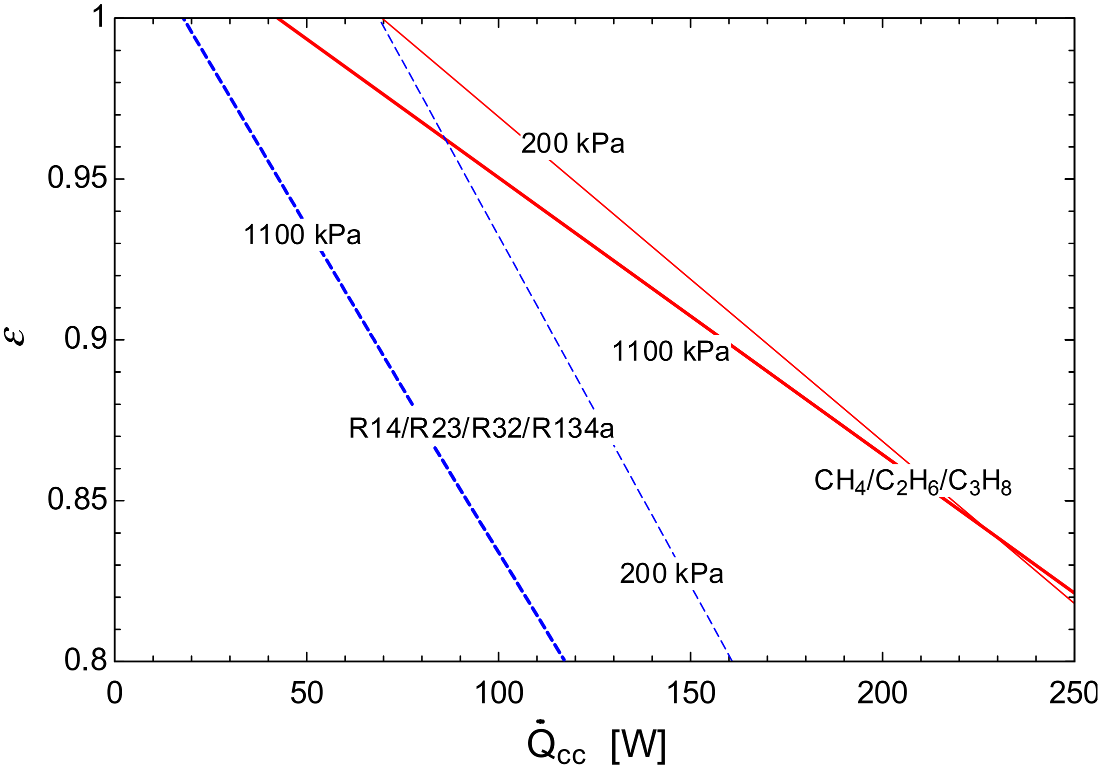

Figure 10. Required effectiveness (ε) in the recuperative heat exchanger as a function of the cryocooler cooling capacity

It is observed that the most challenging condition is faced when the mixture composed of methane, ethane and propane (45%/35%/20% in volume) is tested at low pressure (200 kPa). This mixture requires either larger cryocooler cooling capacity ($\dot{Q}_{cc}$) or a higher recuperative heat exchanger effectiveness due to its lower specific heat at constant pressure (Cp).

2.4.1. Cryocooler heat exchanger

Figure 11 shows the cryocooler heat exchanger where the pre-cooled fluid is cooled to the desired temperature (from 150 K to room temperature). The cryocooler heat exchanger is a refrigerated copper tube with a nominal diameter of 6.35 mm (0.25 in), which is helically wound to a copper cylinder, tube with an outer diameter ($OD_{cylinder}$) of 79.4 mm (3.125 in) and an inner diameter ($ID_{cylinder}$) of 74.8 mm (2.945 in). The tested mixture enters in the bottom of the heat exchanger and leaves in the top of the heat exchanger closer to the cryocooler. The cryocooler heat exchanger is bolted to the cryocooler through counter-bored holes that are drilled in a copper plate where the copper cylinder is soldered. It is expected to have a high thermal contact resistance between the cryocooler base and the cryocooler heat exchanger with this kind of attachment; in order to reduce the thermal contact resistance indium gasket is placed between the cryocooler heat exchanger and the cryocooler.

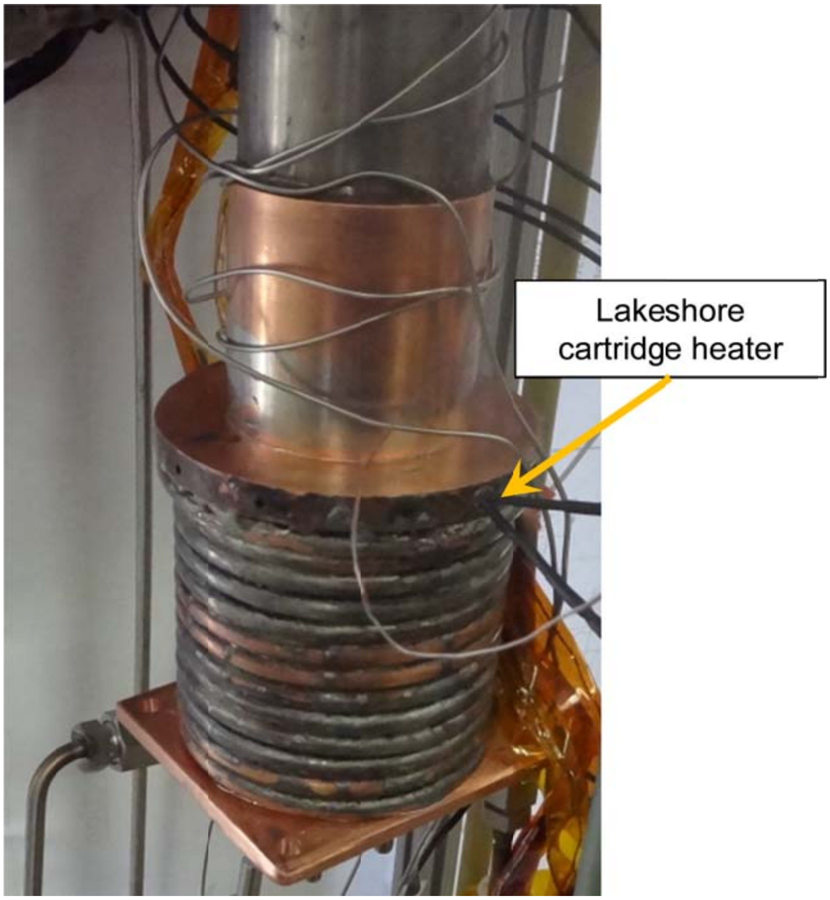

Figure 11. Cryocooler heat exchanger

In addition, two 100 W electrical Lakeshore cartridge heaters (indicated by the arrow in Figure 11) are installed to control the cryocooler temperature.

Design considerations

The length of the heat exchanger tubing or number of turns (*N*) of the tubing around the copper cylinder is determined from a thermal analysis that balances the increased heat exchanger effectiveness associated with a longer cylinder with the increment of conduction resistance. The thermal analysis is framed as a 1-D conduction heat transfer problem, which is represented as shown in Figure 12.

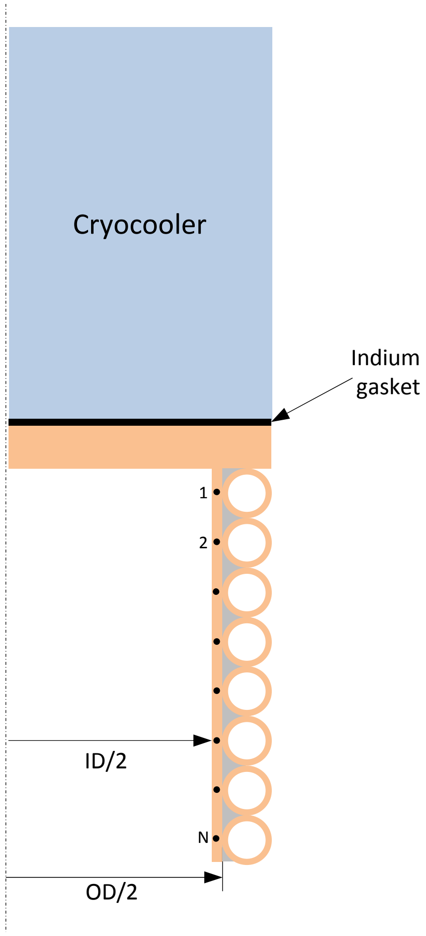

Figure 12. Schematic of the cryocooler heat exchanger and the grid of the one-dimensional heat transfer analysis.

The parameter N is the number of nodes in the axial direction, and it is equal to the number of turns. The energy balance for an internal node in the cooper cylinder is illustrated in Figure 13. The energy balance suggested by Figure 13 is:

$$\dot{Q}[i+1]+\dot{Q}_{fluid}[i]-\dot{Q}[i]=0 \tag{6}$$

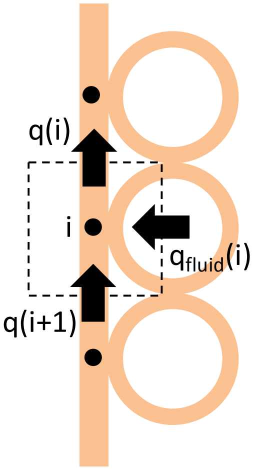

Figure 13. Energy balance in for an internal node in the copper block.

The axial heat transfer rate due to conduction ($\dot{Q}[i]$) through the cylinder is given by:

$$\dot{Q}[i]=\frac{\pi}{4}\left[\left(OD_{cylinder}+4th_{tube}\right)^2-ID_{cylinder}^{\;\;2}\right]k\frac{\left(T[i]-T[i-1]\right)}{OD_{tube}} \tag{7}$$

Each node is exposed to convection with the mixture. The energy balance shows that heat transfer rate is a function of the energy released by the mixture in each turn, which is expressed as:

$$\dot{Q}_{fluid}[i]=\dot{m}\left[h\left(T_{in}[i],P\right)-h\left(T_{out}[i],P\right)\right] \tag{8}$$

The maximum heat transfer rate is expressed as the difference between the enthalpy at the inlet temperature and the enthalpy if the mixture achieves the temperature of the copper cylinder ($T[i]$). The temperature drop across the wall of the tubing is neglected

$$\dot{Q}_{fluid,max}[i]=\dot{m}\left[h\left(T_{in}[i],P\right)-h\left(T[i],P\right)\right] \tag{9}$$

The effectiveness ($\varepsilon[i]$) for each turn is calculated as follow

$$\dot{Q}_{fluid}[i] = \dot{Q}_{fluid,max}[i]\varepsilon[i] \tag{10}$$

Also, the heat exchanger effectiveness is determined based on the number of transfer units ($NTU[i]$) of the heat exchanger. According to Nellis and Klein [23], when the capacitance ratio is equal to zero, $\varepsilon[i]$ is expressed as.

$$\varepsilon[i] = 1 - e^{(-NTU[i])} \tag{11}$$

$NTU[i]$ is defined as the ratio between the $UA[i]$ and the capacitance

$$NTU[i] = \frac{UA[i]}{\dot{m}\overline{Cp}[i]} \tag{12}$$

where $\overline{Cp}[i]$ is the average specific heat capacity of the mixture for each turn.

$$\overline{Cp}[i] = \frac{\left(h_{out}[i] - h_{in}[i]\right)}{\left(T_{out}[i] - T_{in}[i]\right)} \tag{13}$$

The $UA[i]$ is only given by the thermal resistance due to convection between the mixture and the inner surface of the pipe.

$$\frac{1}{UA[i]} = \frac{1}{htc[i]\left(\pi ID_{tube}\right)\left(\pi\left(ID_{cylinder} + OD_{tube}\right)\right)} \tag{14}$$

htc is the heat transfer coefficient of the mixture, which is conservatively estimated assuming that the mixture behaves as singe phase vapor. It is expected that *htc* will be larger because there is two-phase flow inside of the cryocooler heat exchanger.

There are two boundary conditions associated to this problem: the top boundary that depends of the temperature of the surface of the cryocooler (T_c) and the adiabatic bottom boundary. In the top boundary, the heat transfer rate extracted by the cryocooler ($\dot{Q}[1]$) is given by Eq. (15), which is described by the ratio of the temperature difference between the cryocooler surface and the node in the first row of the helically wound copper tube, and the sum of the thermal resistances between these nodes.

$$\dot{Q}[1]=\frac{\left(T[1]-T_c\right)}{\dfrac{OD_{tube}/2}{\dfrac{\pi}{4}\left(\left(OD_{cylinder}+4th_{tube}\right)^2-ID_{cylinder}{}^2\right)k\left(T[1]\right)}+\dfrac{th_{plate}}{\dfrac{\pi}{4}OD_{cylinder}{}^2\,k\left(\dfrac{T_c+T[1]}{2}\right)}+R_c} \tag{15}$$

The thermal resistance is composed by the axial conduction in the copper cylinder and copper plate, and the contact resistance (R_c) across the indium gasket that is located between copper plate and the cryocooler base. For an Indium gasket R_c is 0.0001421 K/W at a contact pressure of 100 kN/m^2 [24]. k is the thermal conductivity of copper.

The adiabatic bottom boundary is expressed as:

$$\dot{Q}[N+1]=0 \tag{16}$$

The effectiveness of the cryocooler heat exchanger is determined as follow:

$$\dot{Q}=\dot{Q}_{max}\,\varepsilon \tag{17}$$

here $\dot{Q}$ is defined as the enthalpy difference between the inlet and the outlet of the cryocooler heat exchanger.

$$\dot{Q} = \dot{m}\left(h\left(T_{in}[1],P\right) - h\left(T_{out}[M],P\right)\right) \tag{18}$$

and $\dot{Q}_{max}$ is supposed as the enthalpy difference between the inlet and the outlet assuming that the mixture achieves the temperature of the cryocooler surface when it leaves the heat exchanger.

$$\dot{Q}_{max} = \dot{m}\left(h\left(T_{in}[1],P\right) - h\left(T_{c},P\right)\right) \tag{19}$$

Figure 14 shows the effectiveness of the cryocooler heat exchanger as a function of the number of turns for the mixture methane, ethane and propane (45%/35%/20% in volume) flowing with a pressure of 200 kPa. Also, it is shown on the right axis the required temperature on the base of the cryocooler to cool the mixture up to the seek temperature (150 K).

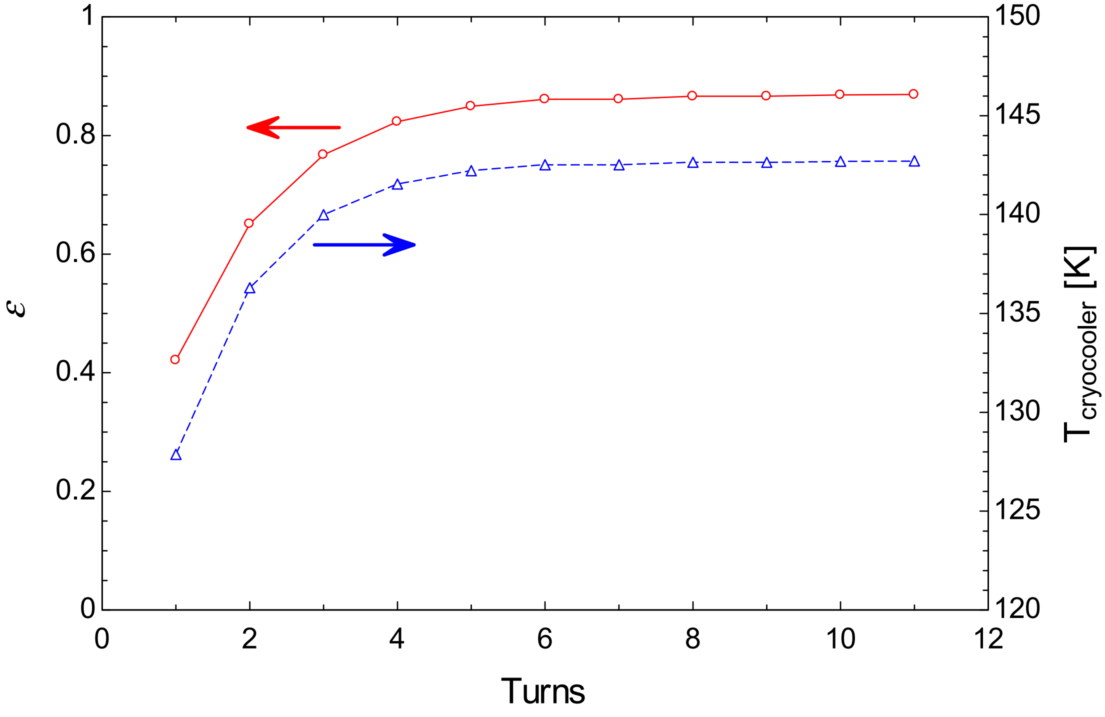

Figure 14. The effectiveness of the cryocooler heat exchanger as a function of number of turns.

The effectiveness starts to keep constant around 87% after 6 turns. If the cryocooler has 6 turns or more, the cryocooler temperature required to achieve the seek temperature of the mixture is 142 K.

2.4.2. Cryocooler

The cryocooler or cold head provides the cooling power to the system. The selected cryocooler is a Gifford McMahon cold head AL-125 manufactured by Cryomech. According to the manufacturer, the cryocooler provides a cooling capacity ($\dot{Q}_{cc}$) of 125 W at 80 K. It is expected that the cryocooler cooling capacity increases as temperature increases. Cryomech AL-125 is shown in Figure 15.

Figure 15. Cryocooler, cryomech AL-125

The cryocooler cooling capacity as a function of temperature was experimentally determined. The cooling power test was performed installing the cold head in a Dewar while the cold head is exposed to high vacuum (lower than 1x10^{-4} torr) minimizing convection losses. Two (2) 100 W electrical cartridge heaters were installed in the base of the cryocooler. Seven (7) MLI layers were installed over the cryocooler to minimize radiation losses. Without any applied load the cryocooler reaches an equilibrium temperature of 28 K. A heating load ranging from 0 to 160 W was then supplied in the base of the cryocooler. For each level of power supplied, the steady state temperature in the base of the cryocooler was measured after thermal equilibrium is achieved. The cryocooler cooling capacity as a function of temperature is shown in Figure 16.

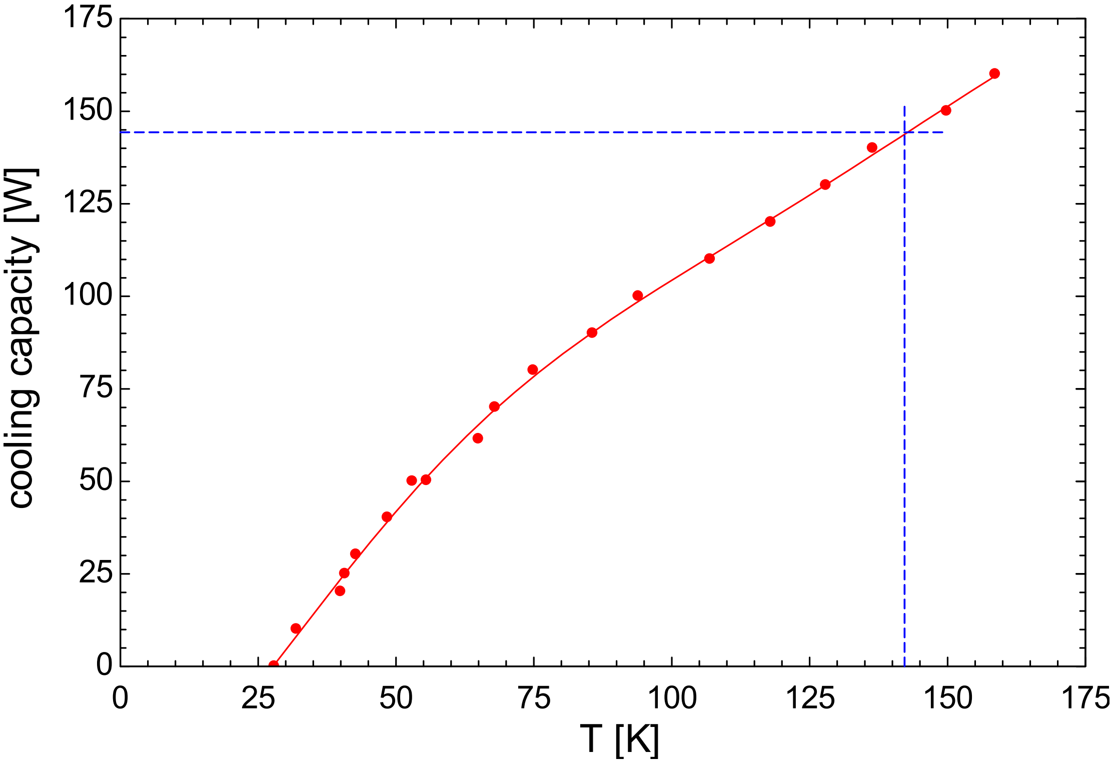

Figure 16. Cryocooler cooling capacity as a function of temperature

The cold head does not perform as good as the manufacturer reported. It only supplies a cooling power of 90 W when the base temperature is 80 K, instead of the 125 W reported by the manufacturer. The cold head has been used for more than 10 years; therefore, it is expected that its function may deviate from its original performance. A cryocooler temperature of 142 K is required to cool the mixture methane, ethane and propane (45%/35%/20% in volume) up to the seek temperature when the testing pressure is 200 kPa, according to Figure 14. The tested cryocooler is able to provide a cooling capacity of 145 W at the required cryocooler temperature (142 K). Figure 10 shows that the recuperative heat exchanger requires an effectiveness (ε) of 92.5% as the cryocooler provides a cooling load of 145 W.

2.4.3. Recuperative heat exchanger

The recuperative heat exchanger is a paired tube heat exchanger as shown in Figure 17. It consists of two parallel tubes with nominal diameter of 6.35 mm (0.25 in), one with the outgoing cold gas mixture, and the other with the hot incoming gas mixture. The length of the heat exchanger is 25 m.

Figure 17. Recuperative heat exchanger

The main goal of the recuperative heat exchanger is to minimize the cooling requirement on the cryocooler in order to pre-cool the incoming gas mixture.

Design considerations

A counter-flow heat exchanger is proposed as recuperative heat exchanger. The recuperative heat exchanger is modeled using the sub-heat exchanger methodology [23] because the mixture is expected to experience a large change in properties as it flows through the heat exchanger. The hot stream enters as superheated vapor and exits as a two-phase mixture. The cold stream enters as a two-phase mixture and exits as superheated vapor. The sub-heat exchanger methodology is shown schematically in Figure 18.

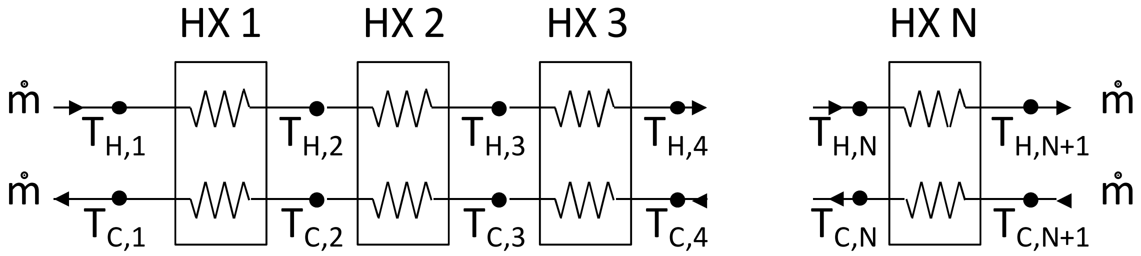

Figure 18. Schematic sub-heat exchanger methodology.

Each sub-heat exchanger is solved using the effectiveness-NTU method [23]. The total heat transfer rate ($\dot{Q}_{r-HX}$) is computed as the difference in the enthalpies of the inlet and outlet states on the hot side fluid:

$$\dot{Q}_{r-HX} = \dot{m}\left(h_{hot}[1] - h_{hot}[N+1]\right) \tag{20}$$

The heat exchanger is divided into N sub-heat exchangers, and the heat transfer rate in each sub-heat exchanger is defined as being equal, Eq. (21):

$$\dot{Q}_{r-HX}[i] = \dot{Q}_{r-HX} / N \tag{21}$$

The energy balance on the hot stream gives the enthalpy leaving the hot side of each of the sub-heat exchanger, and it is expressed as:

$$\dot{Q}_{r-HX}[i] = \dot{m}\left(h_{hot}[i] - h_{hot}[i+1]\right) \tag{22}$$

In the hot-side fluid, the leaving temperature ($T_{hot}[i+1]$) in each sub-heat exchanger is obtained from the enthalpy and pressure using REFPROP [25]. The enthalpy of the fluid leaving the cold side is calculated from the energy balance on the cold stream, which is expressed as:

$$\dot{Q}_{r-HX}[i] = \dot{m}\left(h_{cold}[i] - h_{cold}[i+1]\right) \tag{23}$$

The leaving temperature ($T_{cold}[i]$) in the cold stream of each sub-heat exchanger is obtained in a similar way as the hot side. The average specific heat capacity of the hot ($\overline{Cp}_{hot}[i]$) and cold ($\overline{Cp}_{cold}[i]$) streams are estimated as the ratio of the specific enthalpy difference and the temperature difference across each sub-heat exchanger section according to Eqs. (24) and (25):

$$\overline{Cp}_{hot}[i] = \frac{\left(h_{hot}[i] - h_{hot}[i+1]\right)}{\left(T_{hot}[i] - T_{hot}[i+1]\right)} \tag{24}$$

$$\overline{Cp}_{cold}[i] = \frac{\left(h_{cold}[i] - h_{cold}[i+1]\right)}{\left(T_{cold}[i] - T_{cold}[i+1]\right)} \tag{25}$$

The minimum and maximum capacitances are determined by Eqs (26) and (27), respectively:

$$\dot{C}_{min}[i] = min\left(\dot{m}\overline{Cp}_{hot}[i], \dot{m}\overline{Cp}_{cold}[i]\right) \tag{26}$$

$$\dot{C}_{max}\left[i\right]=max\left(\dot{m}\overline{Cp}_{hot}\left[i\right],\dot{m}\overline{Cp}_{cold}\left[i\right]\right) \tag{27}$$

The capacitance rate is defined as:

$$C_R\left[i\right]=\frac{\dot{C}_{min}\left[i\right]}{\dot{C}_{max}\left[i\right]} \tag{28}$$

The maximum possible heat transfer rate ($\dot{Q}_{r-HX,max}\left[i\right]$) of each sub-heat exchanger is defined as:

$$\dot{Q}_{r-HX,max}\left[i\right]=\dot{C}_{min}\left[i\right]\left(T_{hot}\left[i\right]-T_{cold}\left[i+1\right]\right) \tag{29}$$

The effectiveness of each sub HX is obtained from Eq. (30):

$$\dot{Q}_{r-HX}\left[i\right]=\dot{Q}_{r-HX,max}\left[i\right]\varepsilon_{r-HX}\left[i\right] \tag{30}$$

The number of transfer units required in each sub-heat exchanger, *NTU*[*i*], is obtained using the effectiveness-NTU relation for counter-flow heat exchangers [23].

$$\varepsilon_{r-HX}\left[i\right]=\frac{1-exp\left(-NTU\left[i\right]\left(1-C_R\left[i\right]\right)\right)}{1-C_R\left[i\right]\,exp\left(-NTU\left[i\right]\left(1-C_R\left[i\right]\right)\right)} \tag{31}$$

The conductance (*UA*[*i*]) required by each sub heat exchanger can be computed as a function of *NTU*[*i*]

$$UA\left[i\right]=\dot{C}_{min}\left[i\right]NTU\left[i\right] \tag{32}$$

Two configurations are considered for the design of the recuperative heat exchanger: a paired tube heat exchanger and a tube in tube heat exchanger (concentric tubes). The paired tube heat exchanger consists of two parallel tubes with nominal diameter of 6.35 mm (0.25 in), where the separate tubes are soldered together to achieve good thermal contact as schematically shown in Figure 19.

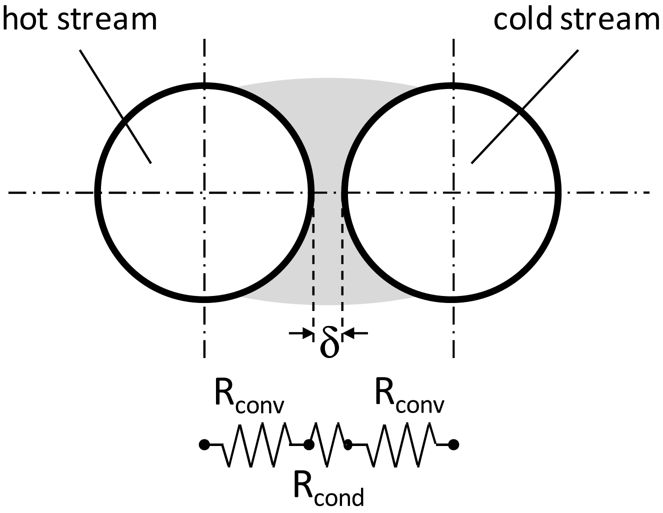

Figure 19. Cross-sectional view of the recuperative heat exchanger, paired tube configuration.

For the paired tube configuration, the calculated conductance of each sub-heat exchanger is defined as:

$$\frac{1}{UA[i]}=\frac{1}{htc_{cold}[i]\pi\, ID\, \Delta x[i]}+\frac{L_c}{k_m[i]\, OD\, \Delta x[i]}+\frac{1}{htc_{hot}[i]\pi\, ID\, \Delta x[i]} \tag{33}$$

The first term expresses the thermal resistance between the cold mixture and the inside surface of the tube. The variable $htc_{cold}[i]$ is the local cold heat transfer coefficient due to convection, $\Delta x[i]$ is the length of each sub-heat exchanger, and ID is the inner diameter. The second term is the resistance due to conduction where $k_m[i]$ is the metal thermal conductivity, OD is the outer diameter, and L_c is the average conduction length. L_c is expressed as:

$$L_c = \delta + 2\frac{OD}{\pi}\int_0^{\pi/2}\left(1 - \cos\theta\right)d\theta = \delta + OD\left(1 - \frac{2}{\pi}\right) \approx \delta + 0.36\,OD \tag{34}$$

The third term shows the thermal resistance between the hot mixture and the inside surface of the tube where $htc_{hot}[i]$ is the local heat transfer coefficient due to convection on the hot heat exchanger. The local hot ($htc_{hot}[i]$) and cold ($htc_{cold}[i]$) heat transfer coefficient are estimated assuming that the mixture behaves as single phase vapor, which is conservatively estimated because it is expected that htc will be larger because of two-phase condition in the most part of the recuperative heat exchanger. $\Delta x[i]$ is calculated by solving Eq. (33).

The second alternative configuration, tube-in–tube, is formed by two concentric tubes. The inner tube has a nominal diameter of ¼” and the outer tube has a nominal diameter of ½”. The schematic of this configuration is presented in Figure 20.

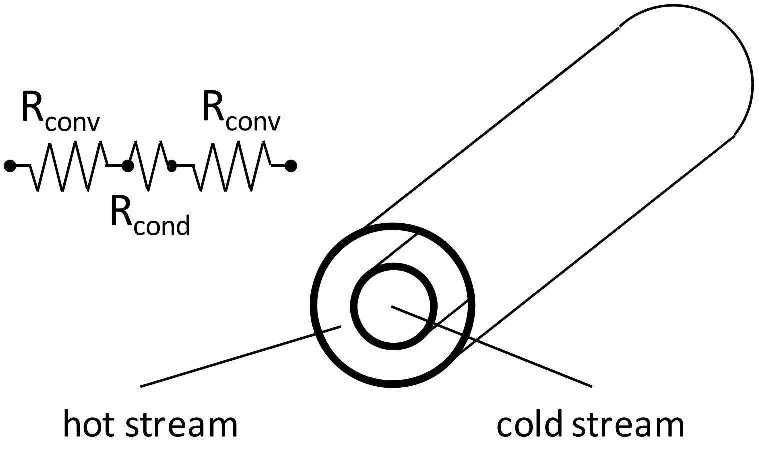

Figure 20. Schematic tube in tube heat exchanger configuration.

For the tube in tube configuration, the calculated conductance of each sub-heat exchanger is defined as:

$$\frac{1}{UA[i]}=\frac{1}{htc_{cold}[i]\pi\, ID\,\Delta x[i]}+\frac{ln\left(\frac{OD}{ID}\right)}{2\pi k_m[i]\Delta x[i]}+\frac{1}{htc_{hot}[i]\pi\, OD\,\Delta x[i]} \tag{35}$$

The first term expresses the thermal resistance between the cold mixture and the inside surface of the tube. *ID* is the inner diameter of the inner tube. The second term is the resistance due to conduction. *OD* is the outer diameter of the inner tube. The third term shows the thermal resistance between the hot mixture and the inside surface of the tube.

The length of both heat exchanger configurations is calculated as the sum of the length of each sub-heat exchanger, and it is expressed as:

$$L_{r-HX}=\sum_{I=1}^{N}\Delta x[i] \tag{36}$$

The number of sub-heat exchangers is set as 40 (N = 40). The mixture methane, ethane and propane (45%/35%/20% in volume) with a pressure of 200 kPa is selected to be analyzed. The results for both configurations are presented in Figure 21 and Figure 22 that show the length of both alternatives for the recuperative heat exchanger as a function of the effectiveness.

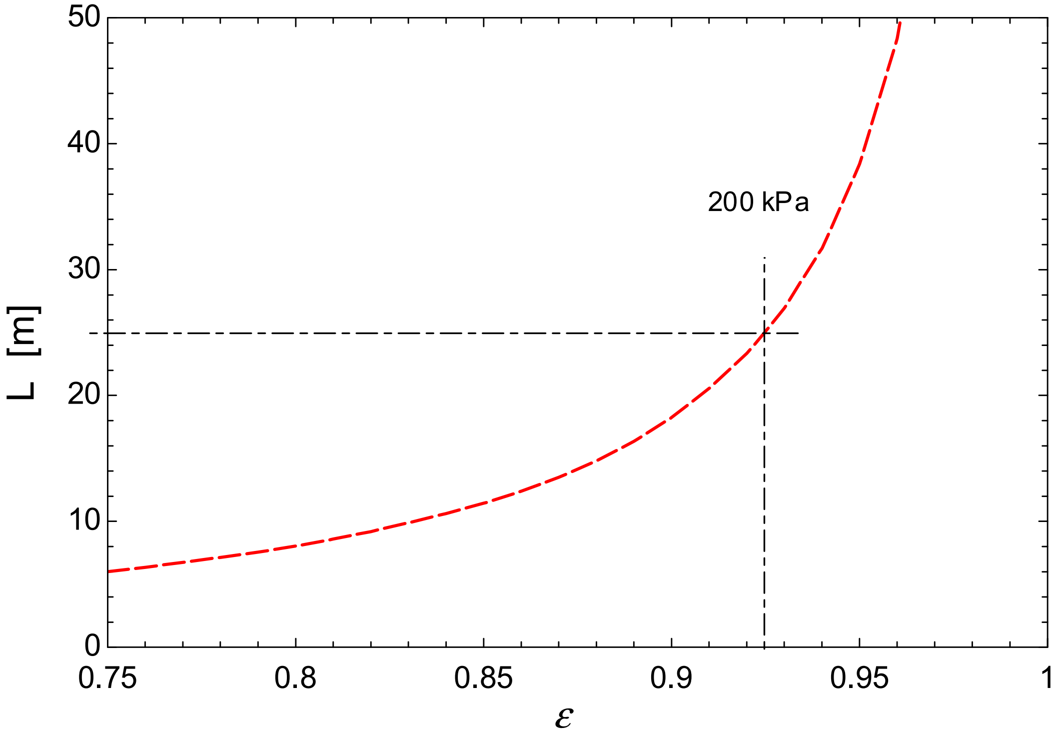

Figure 21. . Heat exchanger length in the paired tube configuration as a function of effectiveness.

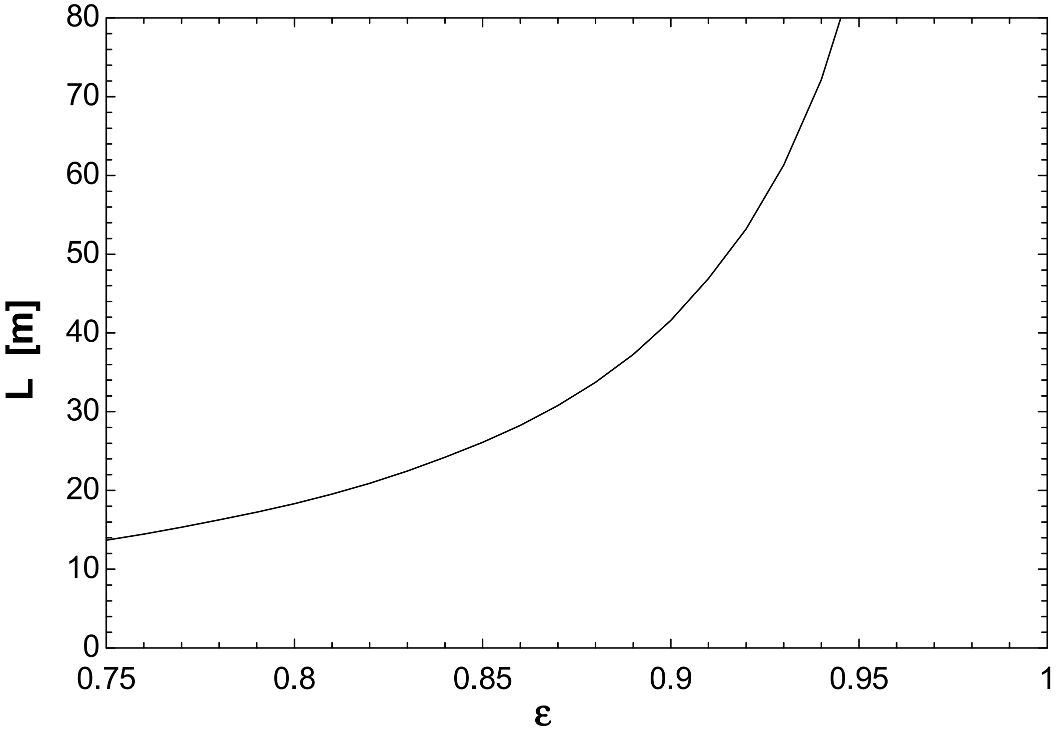

Figure 22. Heat exchanger length in the tube in tube configuration as a function of effectiveness.

The best configuration for the recuperative heat exchanger is the paired tube configuration because it requires a shorter heat exchanger to provide the same effectiveness. In the paired tube configuration, a length of 25 m corresponds with the 92.5% effectiveness required.

2.4.4. Test section

Three separate test sections are necessary to perform the experiments; each test section has a different inner diameter corresponding to *ID* = 0.5, 1.5, and 3.0 mm. The test section itself is comprised of a thin wall stainless tube enveloped by a solid copper "block" which provides the test section with thermal mass and uniform wall temperature. The dimensions of the test sections are shown in Table 4.

Table 4. Dimensions of test sections

Parameter	**Value**			**unit**	**instrument**
Inner diameter SS304 tube (*ID*)	**0.506±0.003**	**1.527±0.003**	**2.871***	mm	microscope
Outer diameter SS304 tube (*OD*)	0.721±0.003	1.821±0.003	3.396±0.003	mm	micrometer
Wall thickness SS304 tube (*th*)	0.108*	0.147*	0.262±0.007	mm	microscope
R_{rms} (roughness)	1.290±0.010	0.860±0.010	0.400±0.010	µm	Zygo
R_{rms}/ID	0.0026*	0.0006*	0.0001*		
Length copper block (*L*)	17.50±0.01	52.50±0.01	105.00±0.01	mm	caliper
Outer diameter copper block	12.70±0.01	19.05±0.01	25.40±0.01	mm	caliper
PRTs location	6.30±0.01	9.03±0.01	12.70±0.01	mm	caliper
$L_{\Delta P}$	68.24±0.01	125.80±0.01	153.80±0.01	mm	caliper
Pressure tap diameter	0.63±0.01	0.63±0.01	0.63±0.01	mm	caliper
Length tap – inlet (L_{in})	25.37±0.01	33.00±0.01	30.80±0.01	mm	caliper
Length outlet – tap (L_{out})	25.37±0.01	40.30±0.01	18.00±0.01	mm	caliper

*calculated value

A schematic of the test apparatus is shown in Figure 23, four distinct locations are identified as follows: "A" is the test section approach, where the refrigerant inlet temperature is measured using two platinum resistance thermometers (PRT) submerged in the flow. "B" is the actual inlet to the active portion of the test section, where pressure only is measured. "C" is the actual outlet of the test section. "D" is the test section departure, where the outlet temperature is measured using two PRTs submerged in the flow. Pressure is measured near to the inlet. The pressure tap is located a distance L_{in} from B to minimize flow perturbation on the test section. In addition, the differential pressure between the segments of the test apparatus are measured (i.e. between A and B, B and C, and C and D). The temperature sensors at locations "A" and "D" are large and disrupt the flow substantially; therefore, they cannot be located directly at the inlet and exit to the test section (i.e., at locations "B" and "C", respectively).

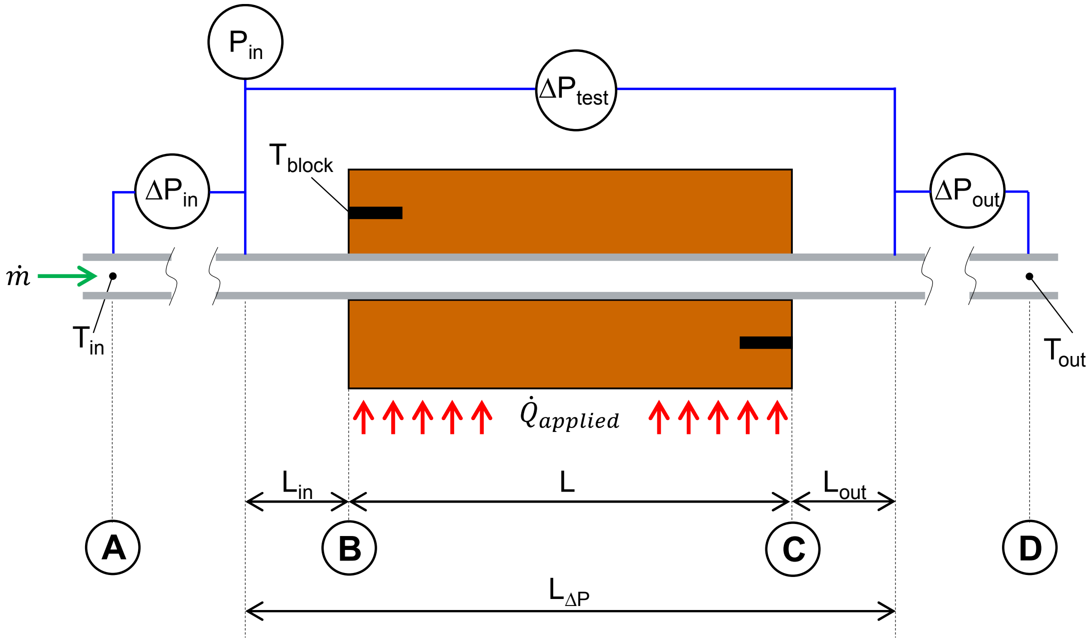

Figure 23. Schematic of test section

Figure 24 shows a picture of the medium test section installed on the test facility.

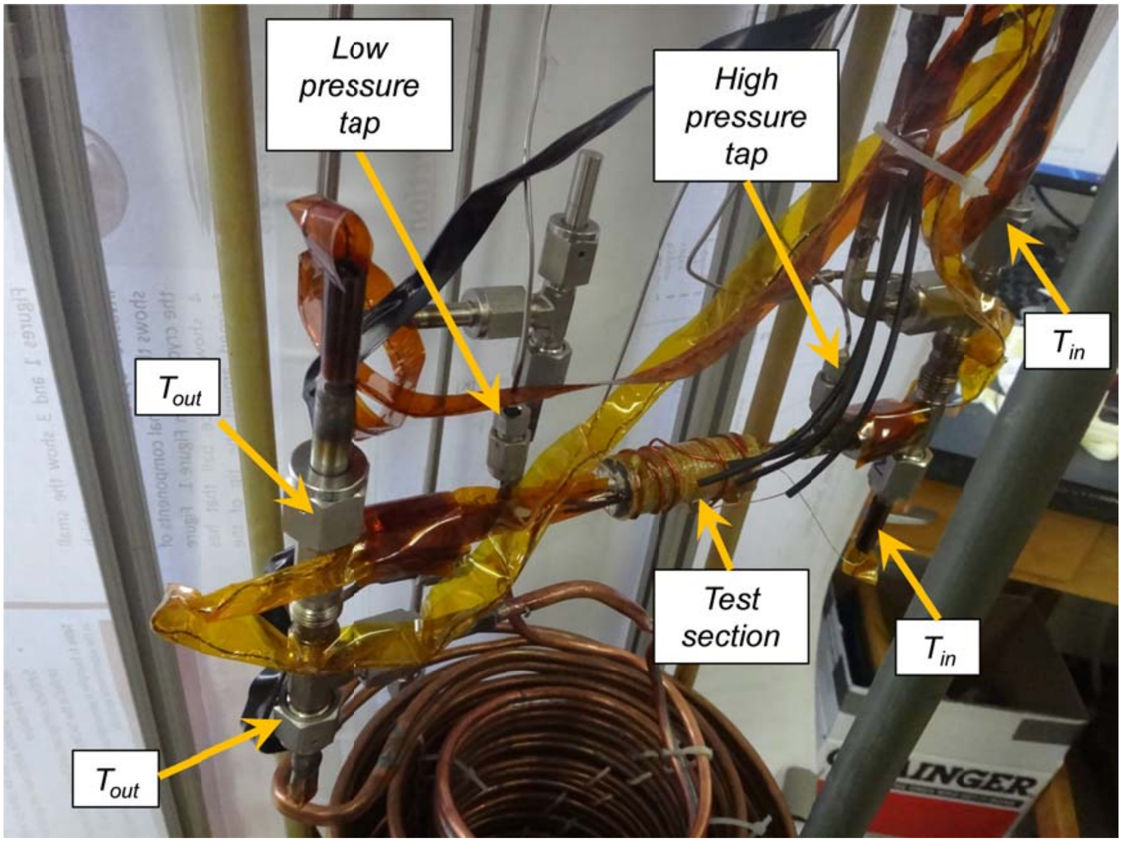

Figure 24. Actual test section

All of the test sections were designed taking into account the length and the heat load apply to the test section. The length of the test section depends on the length required to have hydro dynamically and thermally fully developed flow. The heat load applied to the test section is determined by balancing the uncertainty in the heat transfer coefficient with the desire to keep constant fluid properties between the inlet and the outlet of the test section. It is important to note that we are trying to measure the local heat transfer coefficient.

Length of test sections

The flow is already hydro dynamically fully developed when it enters the test section, but it may be disrupted because of fittings and sudden expansions and contractions. The actual design of the test section has a pressure tap before the test section. The proposed design is shown in Figure 25.

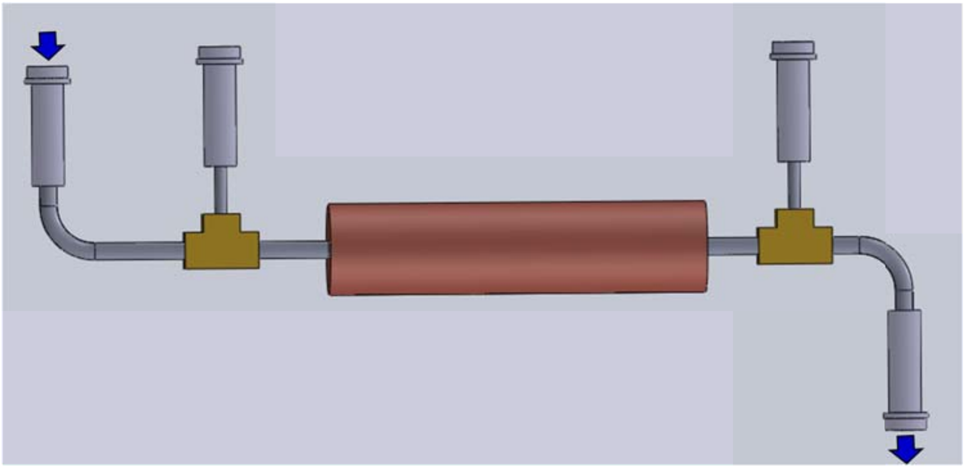

Figure 25. Test section design as originally proposed

The high-pressure tap itself disturbs the flow somewhat. The piping system before the test section is composed by tubing size (6.35 mm (0.25 in) nominal diameter) greater than the three test section tested. The effect of a sudden contraction was tested using a Computational Fluid Dynamics (CFD) model developed in the ANSYS Fluent package. The parameters used in the CFD model are shown in Table 5.

Table 5. Parameters used in the CFD model

Temperature	200	K
Density	55.5	kg/m^3
Specific heat	1200	J/kg-K
Thermal conductivity	0.0207	W/m-K
Viscosity	2.156×10^{-5}	Pa-s
Reynolds number	35000	

The geometry used in the CFD model is show in Figure 26

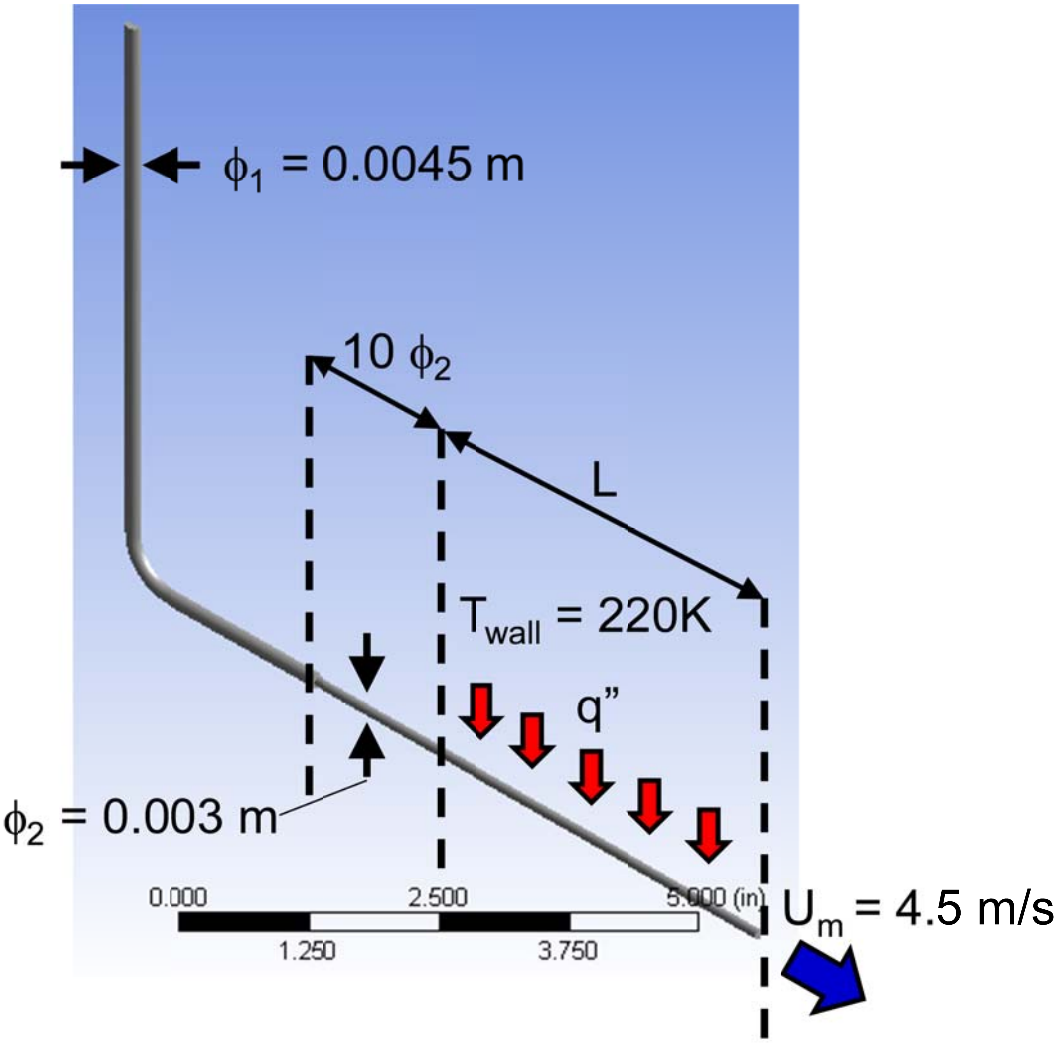

Figure 26. Setup CFD model in Ansys

Hydrodynamic flow is considered fully developed when the wall shear stress is constant. One of the results of the CFD model is shown in Figure 27. This figure shows clearly a constant shear stress, fully developed condition, before a length of ten (10) inner diameters.

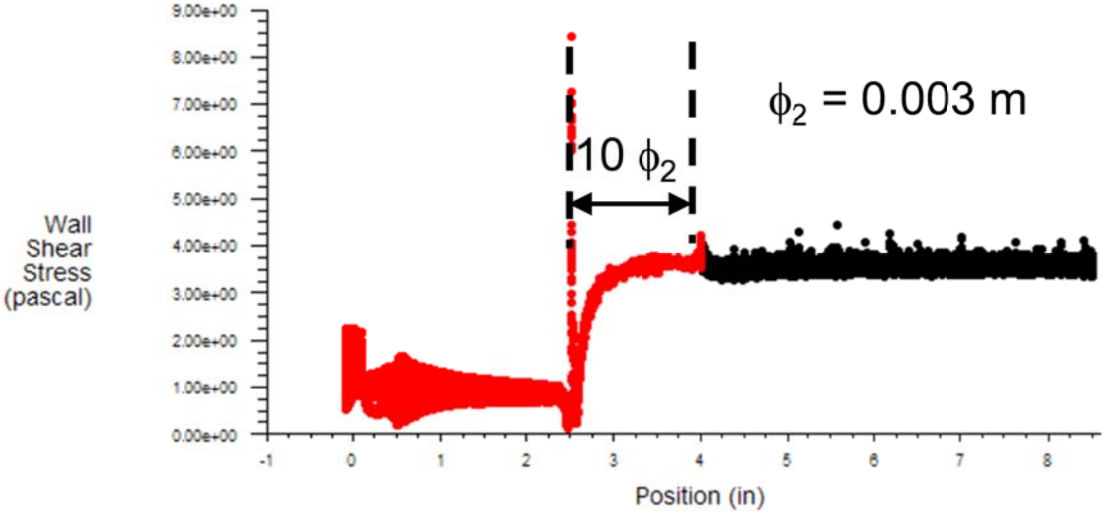

Figure 27. Results of Ansys model, wall shear stress as a function of length

When the flow enters the portion of the test section enveloped by the copper block, it is exposed to a heat load that is applied by a nichrome wire installed on the outer surface of the copper block. The wall temperature is held uniform due to the high conductivity and large cross-sectional area of the copper. Consequently, a thermal boundary layer appears and grows. When the boundary layer begins to grow, the local Nusselt number is large, and it, subsequently, decreases as the thermal boundary layer grows. When the local Nusselt number approaching a constant value, it indicates that, the flow has achieved a fully developed thermal condition. This phenomenon is studied using the same CFD model described in Figure 26 and Table 5. The local Nusselt number is shown in Figure 28 as a function of the length of the copper block. The thermal fully developed condition is achieved within 15 inner diameters.

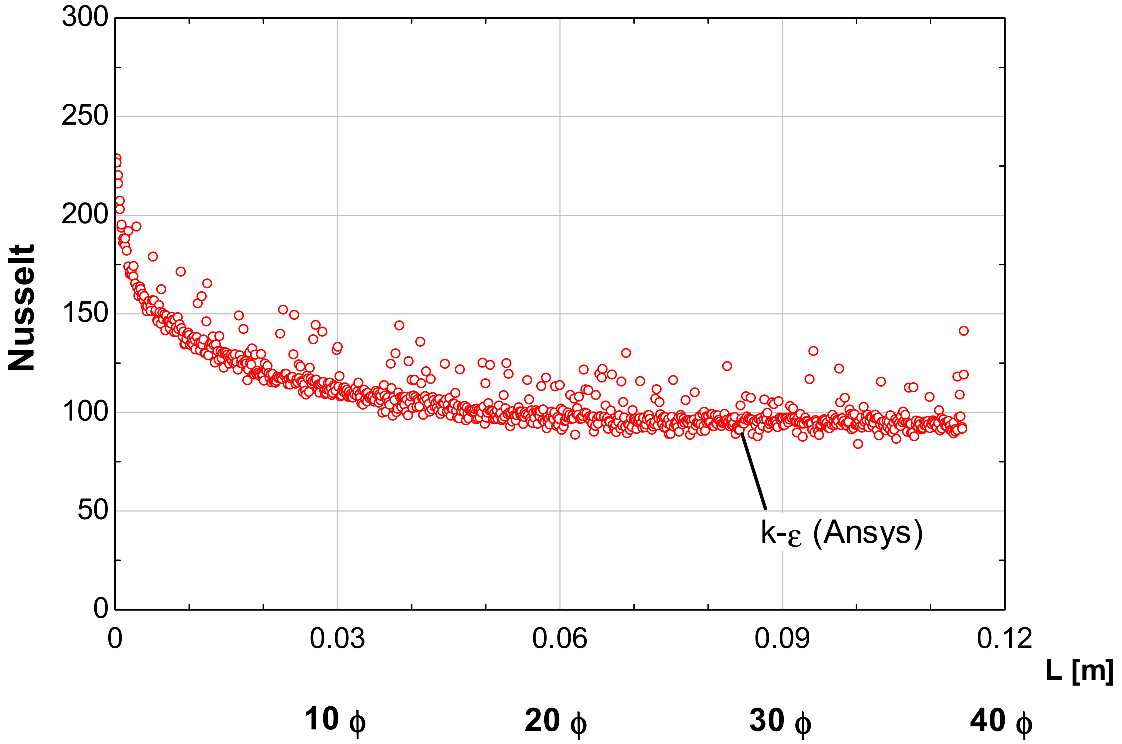

Figure 28. Results of Ansys model, Nusselt as a function of length

The CFD model is validated against a mixing length model and also the Dittus-Boelter correlation. Both the CFD model and the mixing length model describe a hydro dynamically fully developed flow exposed to heating in a constant temperature wall pipe. The mixing length model is a 2D eddy diffusivity of momentum model that uses the Spalding velocity profile as described by Nellis and Klein [23]. The Dittus-Boelter [26] correlation is shown in Eq. (37), and it gives the local Nusselt number for a turbulent thermal and hydro dynamically flow.

$$Nusselt = 0.023\,Re^{0.8}\,Pr^{0.4} \tag{37}$$

Figure 29 shows the comparison of the results between these three approaches. The mixing length model shows good agreement with the CFD model. It has the same trend, but the Nusselt numbers predicted by the mixing length model are greater than CFD model. The Dittus-Boelter correlation matches with the CFD model when the flow is thermal fully developed.

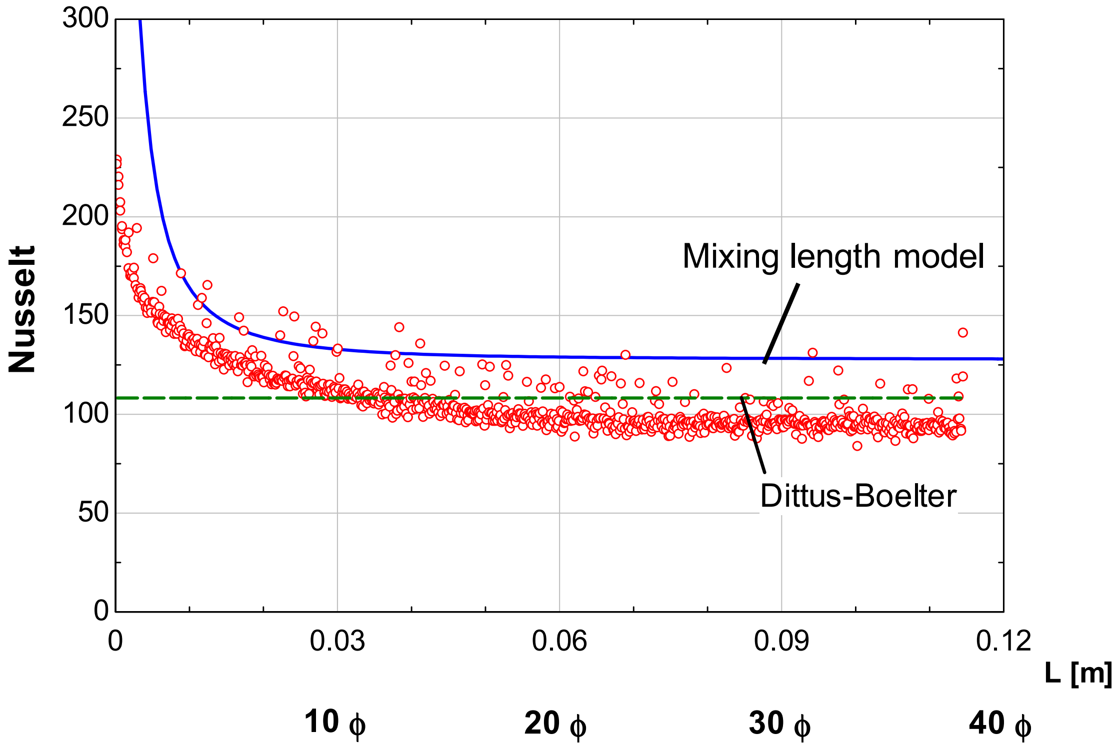

Figure 29. Comparison between CFD model, mixing length model, and Dittus-Boelter

The average heat transfer coefficient is measured in the test facility. However, we are trying to determine the local heat transfer coefficient. The local heat transfer coefficient is large at the beginning of the heating zone, and decreases up to the point where it achieves a thermal fully developed condition. Consequently, there is a difference between the actual average and the local heat transfer coefficient that we are attempted to measure because of the influence of the developing zone. The difference is called an error in this report and is quantified using Eq. (38).

$$Error = \frac{Nusselt_{avg} - Nusselt_{local}}{Nusselt_{local}} \qquad (38)$$

The local and average Nusselt number and the difference (error) between them as a function of the length of the test section surrounded by the copper block is shown in Figure 30. A difference (error) of 10% is observed when the length is 35 inner diameters.

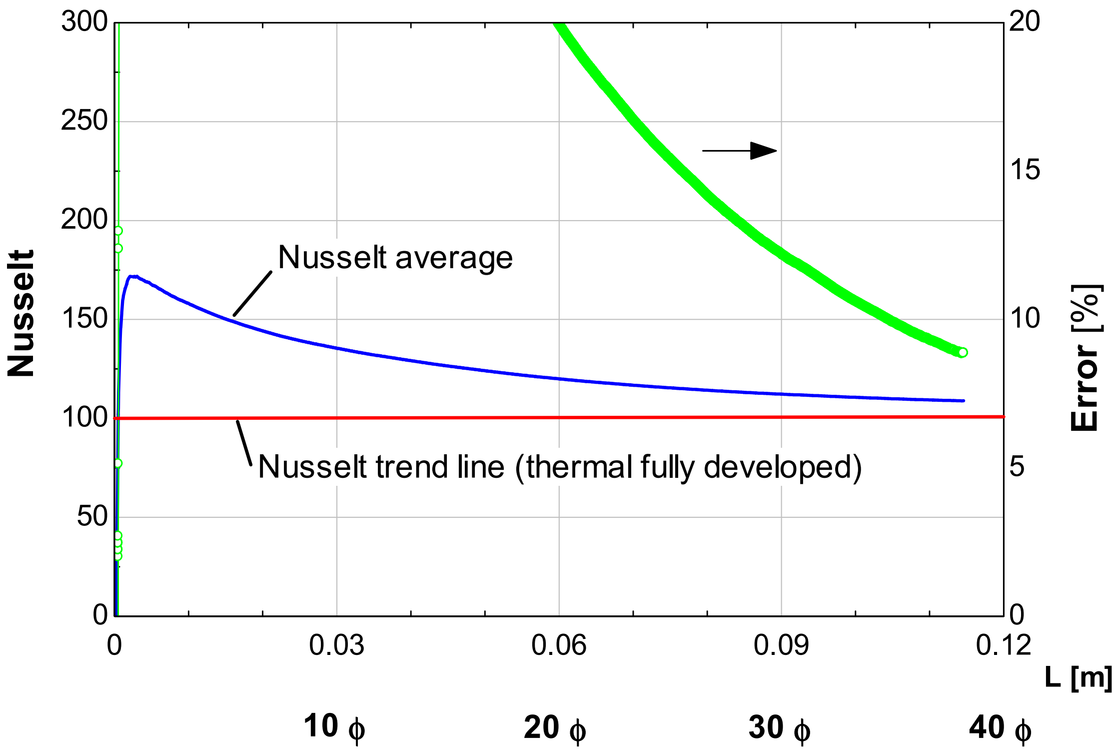

Figure 30. Local and average Nusselt number and error as a function of the length of the heating section

The final design of the test section is shown in Figure 31. This final design takes into account the dimensions that allows both a hydro-dynamic and thermal conditions to be fully developed, and a difference lower than 10% between the local heat transfer coefficient (that we wish to measure) and the average Nusselt number (that we actually measure). The length of the test section is defined as 35 inner diameters.

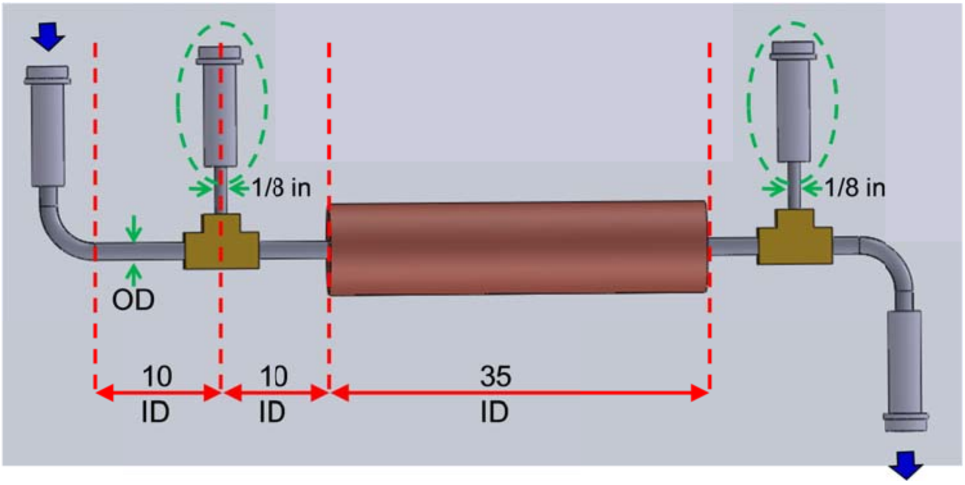

Figure 31. Actual design of test section

Heat load applied

The rate of heat supplied is dictated by the target limit to uncertainty in the measurements. In this case, the uncertainty target is 10% or less. The *htc* is found by solving Eq. (39):

$$htc = \frac{\dot{Q}}{Area\,\Delta T_{LMTD}} = f\left(\dot{Q}, \Delta T_{LMTD}\right) \tag{39}$$

Consequently, the uncertainty in the measurement of *htc* is given by:

$$\delta htc = \sqrt{\left(\frac{\partial htc}{\partial \dot{Q}}\delta \dot{Q}\right)^2 + \left(\frac{\partial htc}{\partial \Delta T_{LMTD}}\delta \Delta T_{LMTD}\right)^2} = \sqrt{\left(\frac{1}{Area\,\Delta T_{LMTD}}\delta \dot{Q}\right)^2 + \left(-\frac{\dot{Q}}{Area\left(\Delta T_{LMTD}\right)^2}\delta \Delta T_{LMTD}\right)^2} \tag{40}$$

where the uncertainties associated to the rate of heat supplied ($\delta \dot{Q}$) and the logarithmic temperature difference, LMTD, $\delta \Delta T_{LMTD}$ are:

$$\delta\dot{Q}=\sqrt{\left(\frac{\partial\dot{Q}}{\partial V}\delta V\right)^2+\left(\frac{\partial\dot{Q}}{\partial I}\delta I\right)^2}=\sqrt{\left(I\,\delta V\right)^2+\left(V\,\delta I\right)^2} \tag{41}$$

$$\delta\Delta T_{LMTD}=\sqrt{\left(\frac{\partial\Delta T_{LMTD}}{\partial T_{in}}\delta T_{in}\right)^2+\left(\frac{\partial\Delta T_{LMTD}}{\partial T_{out}}\delta T_{out}\right)^2+\left(\frac{\partial\Delta T_{LMTD}}{\partial T_{wall}}\delta T_{wall}\right)^2} \tag{42}$$

Where $\frac{\partial\Delta T_{LMTD}}{\partial T_{in}}$, $\frac{\partial\Delta T_{LMTD}}{\partial T_{out}}$ and $\frac{\partial\Delta T_{LMTD}}{\partial T_{wall}}$ are defined by Eqs. (43), (44), and (45), respectively.

$$\frac{\partial\Delta T_{LMTD}}{\partial T_{in}}=\frac{\left(\frac{T_{out}-T_{in}}{T_{wall}-T_{in}}\right)-ln\left(\frac{T_{wall}-T_{in}}{T_{wall}-T_{out}}\right)}{ln\left(\frac{T_{wall}-T_{in}}{T_{wall}-T_{out}}\right)^2} \tag{43}$$

$$\frac{\partial\Delta T_{LMTD}}{\partial T_{out}}=\frac{\left(\frac{T_{in}-T_{out}}{T_{wall}-T_{out}}\right)-ln\left(\frac{T_{wall}-T_{in}}{T_{wall}-T_{out}}\right)}{ln\left(\frac{T_{wall}-T_{in}}{T_{wall}-T_{out}}\right)^2} \tag{44}$$

$$\frac{\partial\Delta T_{LMTD}}{\partial T_{wall}}=\frac{\left(T_{in}-T_{out}\right)^2}{\left(T_{wall}-T_{in}\right)\left(T_{wall}-T_{out}\right)ln\left(\frac{T_{wall}-T_{in}}{T_{wall}-T_{out}}\right)^2} \tag{45}$$

All of the temperatures are measured using Platinum Resistive Thermometers (PRT's) connected in a 4-wire configuration and excited by a precise current source. Calibration of each PRT will be made using nitrogen liquid and ice bath to provide a calibration uncertainty of ±0.25 K [27]. Redundant PRT's reduces uncertainty. If two (2) measurements of temperature are performed at each point then the uncertainty is reduced to ±0.18 K according to:

$$\delta T = \sqrt{\left(\frac{1}{2}\delta T_1\right)^2 + \left(\frac{1}{2}\delta T_2\right)^2} \tag{46}$$

The analysis to predict the uncertainty of the experiments and define the length of the tube section and the range of the heat addition includes the calculation of temperatures (T_{out} and T_{wall}) by using an energy balance and solving the heat transfer rate equations using as input data the inside tube diameter (*ID*), the inlet fluid temperature (T_{in}), the length of the section (*L*), and the rate of heat supplied ($\dot{Q}$). The energy balance is a function of the inlet and the outlet enthalpies of the gas mixture. The gas mixture properties will be obtained using REFPROP [25]. The heat transfer rate equation is a function of *htc*. An accurate correlation to predict the local *htc* for zeotropic mixtures in the two-phase region does not exist. The Chen correlation [28] is used to predict *htc* and it is shown in Eq. (47):

$$htc = \frac{k_l\, Nu_l\, f\left(X_{tt}\right)}{ID} \tag{47}$$

Nu_l is the Nusselt number of the liquid phase, and k_l is the thermal conductivity of the liquid phase. $f(X_{tt})$ is a parameter defines as a function of the Lockhart and Martinelli coefficient (X_{tt}) liquid and vapor phases turbulent according to Eq. (48), The Lockhart and Martinelli coefficient (X_{tt}) both phases turbulent is defined in Eq. (49).

$$f\left(X_{tt}\right) = \begin{cases} 1 & \dfrac{1}{X_{tt}} < 0.1 \\ 2.35\left(\dfrac{1}{X_{tt}} + 0.213\right)^{0.736} & \dfrac{1}{X_{tt}} \geq 0.1 \end{cases} \tag{48}$$

$$X_{tt} = \left(\frac{\rho_v}{\rho_l}\right)^{0.5} \left(\frac{\mu_l}{\mu_v}\right)^{0.1} \left(\frac{1-x}{x}\right)^{0.9} \tag{49}$$

where ρ, μ, and x are the local density, viscosity and quality. The subscripts l and v denote liquid and vapor fraction. Moreover, Nu_l is calculated using Dittus-Boelter [26].

$$Nu_l = 0.023 Re^{0.8} Pr^{0.4} \tag{50}$$

Little [2] stated that, for some zeotropic mixtures, the Chen correlation over-estimates heat transfer coefficients. The overestimation of *htc* is useful information for the uncertainty analysis because with higher *htc* the temperature difference between the wall and the bulk gas mixture is reduced increasing the relative uncertainty of the experiment; therefore, an overprediction of htc is a more exacting scenario than an accurate prediction. Figure 32 and Figure 33 show the prediction of *htc* for the two gas mixtures shown in Table 2 (without dilution) as a function of the local thermodynamic quality (x) using a mass flux of 250 kg/m^2-s.

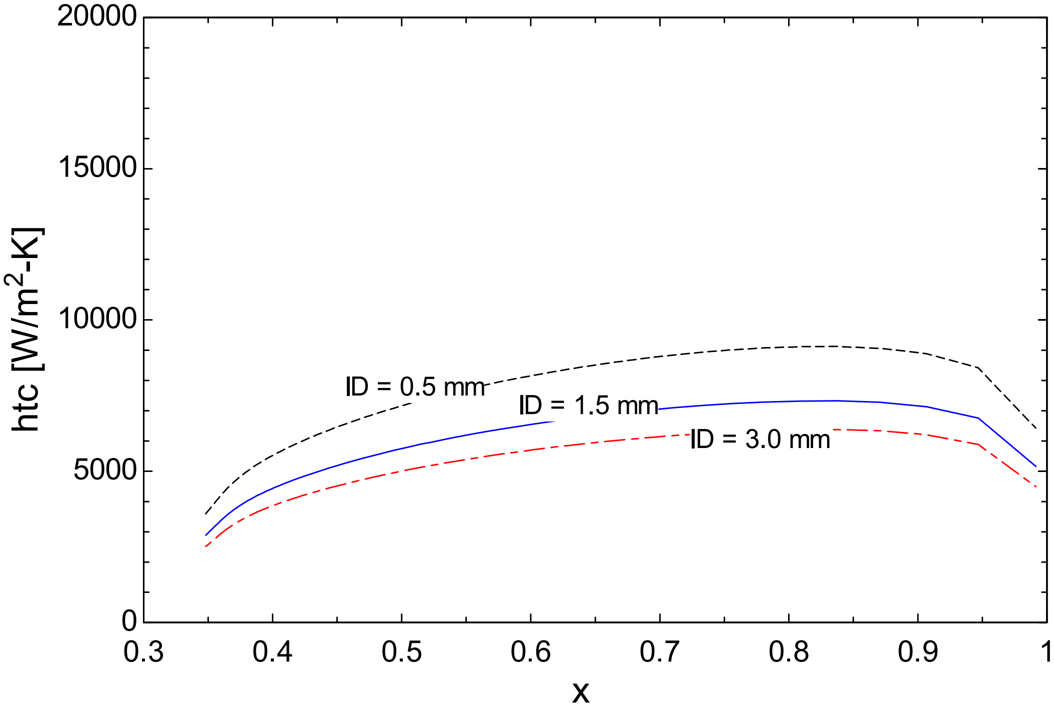

Figure 32. Prediction of *htc* as a function of quality (x) for different inner diameters (*ID*) for a gas mixture (35% R-14, 15% R-23, 15% R-32, and 35% R-134a) and G = 250 kg/m^2-s.

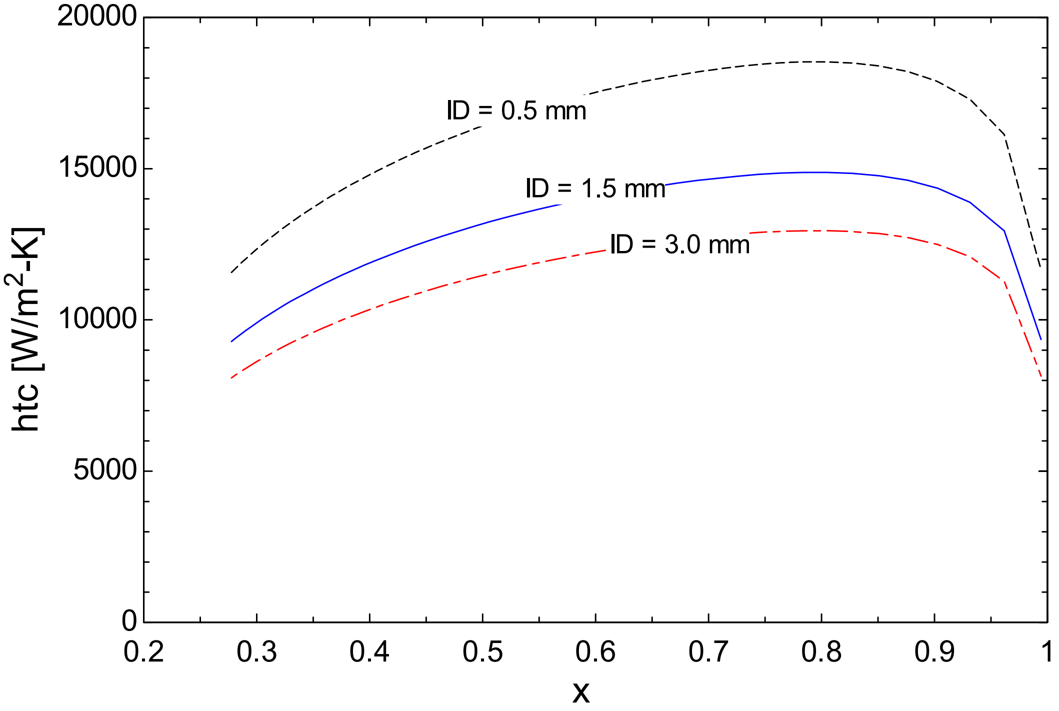

Figure 33. Prediction of *htc* as a function of quality (*x*) for different inner diameters (*ID*) for a gas mixture (45% methane, 35% ethane, and 20% propane) and G = 250 kg/m^2-s

Figure 32 and Figure 33 show that the higher *htc* is observed in when the mixture of hydrocarbons is used in the test section with an inner diameter of 0.5 mm. When a constant heat is supplied to the test section, the temperature difference between the wall and the bulk gas mixture decreases as the *htc* increases. The higher *htc* is the toughest condition because the relative uncertainty of the temperatures measurement increases when in the test section is measured a low temperature difference between the wall and the bulk gas mixture. Using the *htc* predicted using Chen correlation and REFPROP property data, the temperatures are calculated for different lengths of the tube section. Once the temperatures are calculated, the uncertainty analysis is carried out, and the result for the most challenging condition is presented in the following figure.

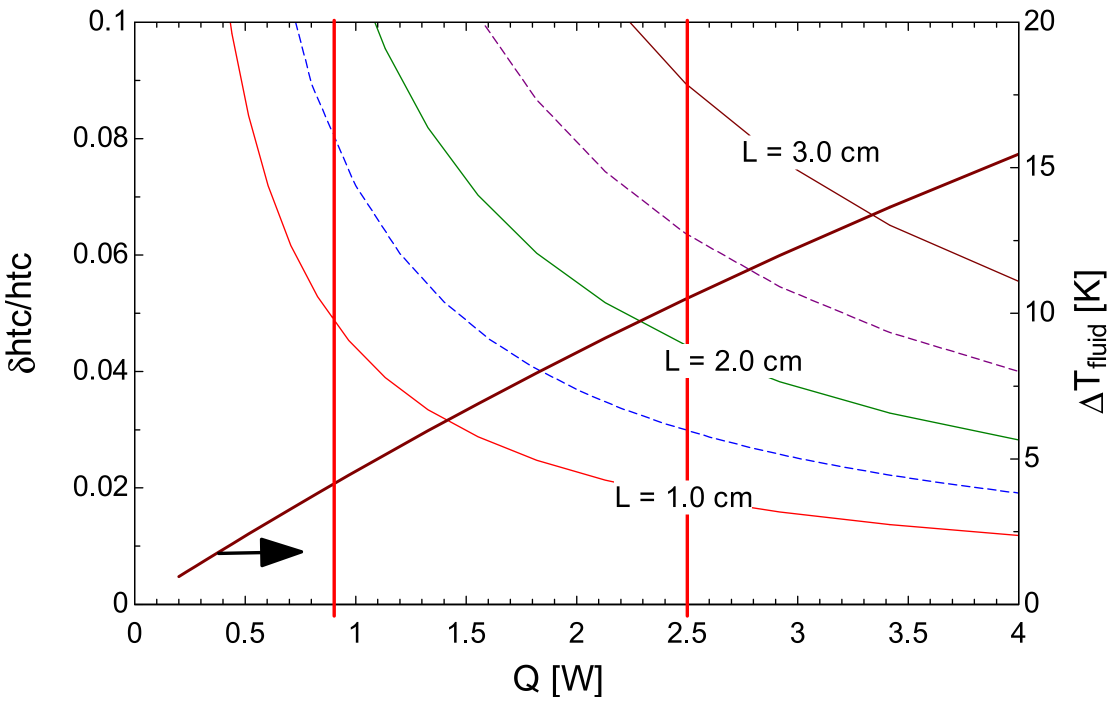

Figure 34. Uncertainty analysis for a gas mixture (45% methane, 35% ethane, and 20% propane) with inner diameters (*ID*) = 0.5 mm and G = 250 kg/m^2-s

The uncertainty decreases when the rate of heat supplied increases. The increment in the heat supplied increases the difference between the bulk fluid temperature and the wall temperature reducing the impact of the uncertainty in the temperature measurements. However, as the heat rate is increased, the properties of the mixture may experience larger changes between the change between the inlet and outlet conditions. The variation in fluid properties is undesirable because Eq. (39) is based in constant properties. The variation in fluid properties is obtained using Eq. (51), where *f* is the selected property:

$$\delta f = \frac{f\left(T_{out}, P_{in}\right) - f\left(T_{in}, P_{in}\right)}{f\left(T_{in}, P_{in}\right)} \tag{51}$$

Reynolds, Prandtl and Peclet numbers are selected to evaluate the change of fluid properties because of the change between the inlet and the outlet conditions. Figure 35 shows the variation of the dimensionless numbers as a function of the heat applied.

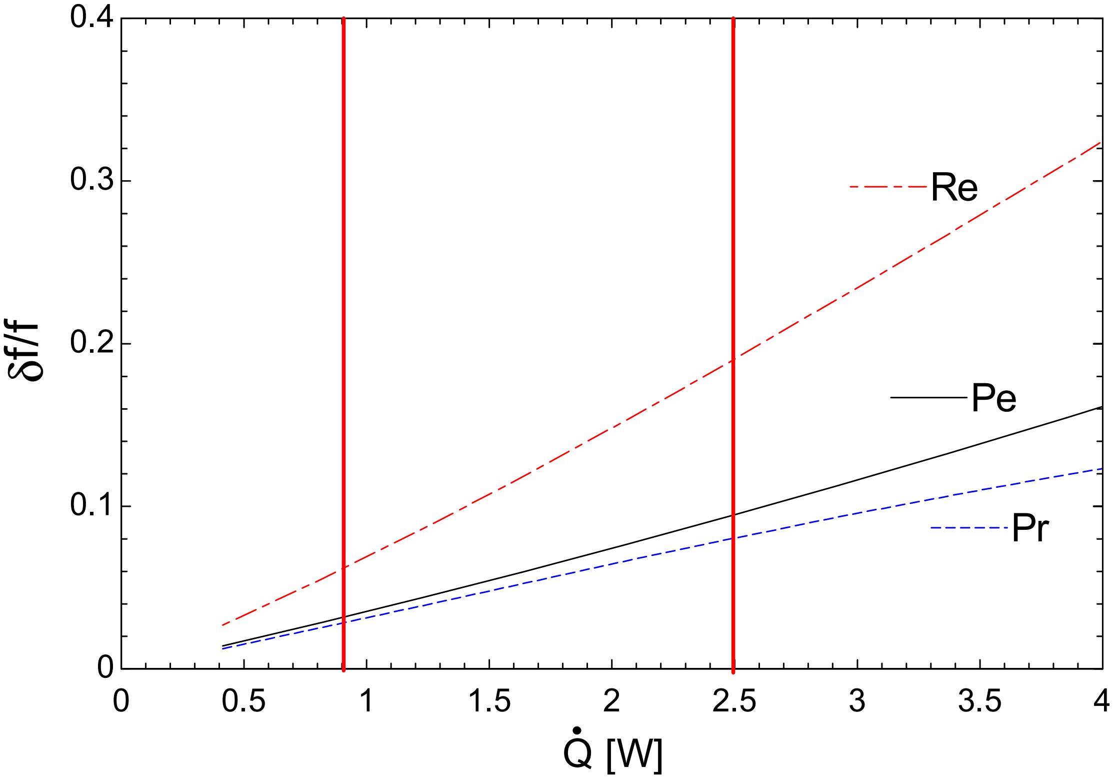

Figure 35. Variation of Reynolds, Prandtl and Peclet numbers of the gas mixture (45% methane, 35% ethane, and 20% propane) as a function of the heat applied.

The length of the 0.5 mm test section is 17.5 mm. The minimum heat load to be applied in the test section has been determined by the means of the uncertainty analysis. 0.9 W is the minimum heat that may be applied to hydrocarbon mixture in the 0.5 mm test section to keep the measured uncertainty below 10% when the test section length is 17.5 mm. The maximum heat load is limited by the desire to keep nearly constant fluid properties between the inlet and the outlet of the test section in order to measure the local heat transfer coefficient. The Reynolds number variation only is influenced by the viscosity change. Around 20% variation is observed when the heat applied is 2.5 W. The Prandtl and Peclet numbers change less than 10 % below 2.5 W. Therefore 2.5 W is chosen as the upper limit for the heat applied. The selected range heat loads for each test section and for each mixture are shown in Table 6.

Table 6. Range heat loads for each test section and for each mixture

Base Mixture	***ID* (mm)**		
	0.5	**1.5**	**3.0**
45% Methane 35% Ethane 20% Propane	0.9 – 2.5 W	6 – 22 W	20 – 80 W
35% R-14 15% R-23 15% R-32 35% R-134a	0.4 – 1.2 W	2 – 11 W	10 – 40 W

Construction considerations

As noted earlier in this report, the heating zone of the test section is formed by copper block, which is installed (brazed) over the stainless steel pipe. On the surface of the copper block a nichrome wire is installed to apply the heat load. The copper block adds thermal mass in order to enable an isothermal pipe wall condition to be maintained. The copper block brazing process includes: (1) applying brazing flux to both the inner surface of the copper block and the external surface of the stainless steel pipe, (2) position the copper block over the stainless steel pipe, (3) apply silver brazing alloy in one side while the copper block is heated to allow the alloy flow to the other side, and (4) the copper block is rotated over the stainless steel pipe in order to allow a proper attachment and contact. Figure 36 shows the copper block features.

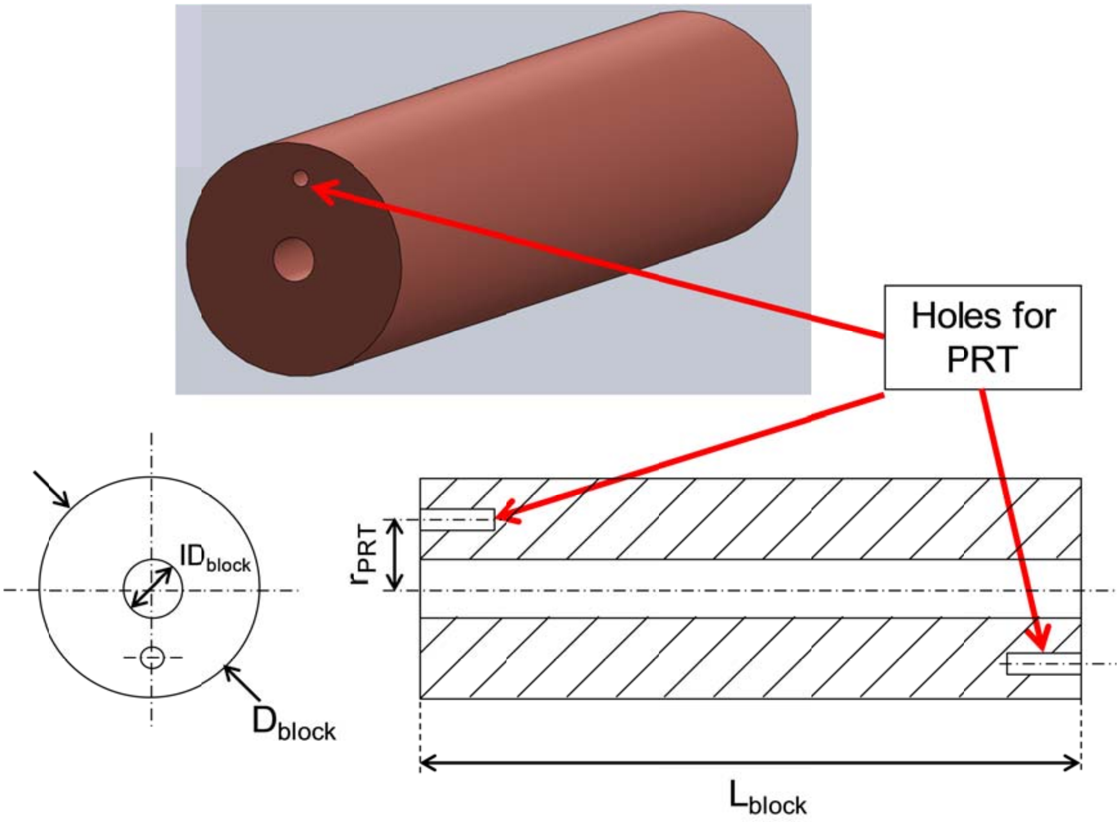

Figure 36. Copper block design

The dimensions of the copper block for each test section are shown in Table 4.

The heat is applied over the copper block by a nichrome wire. Nichrome wire is a high resistivity wire (34 Ω/m @ 305 K). A layer of wipe paper is installed over the copper block to provide electrical isolation. The wipe paper is attached to the copper block using varnish. The nichrome is rolled over the paper surface and is always in contact with the surface. Each end of the nichrome wire is connected to two copper wires in order to provide a four-wire connection. Varnish is applied over the nichrome wire and its ends to provide good thermal contact. Figure 37 shows the nichrome heater over one of the test sections.

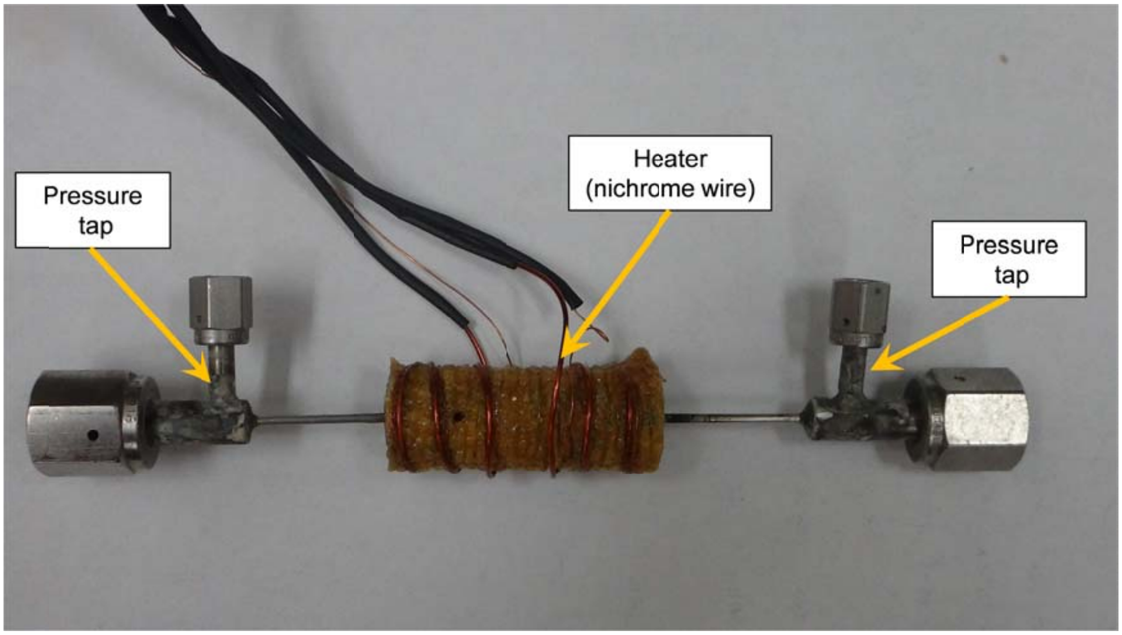

Figure 37. Actual 1.5 mm test section with nichrome heater

Table 7 shows the characteristics of the nichrome heaters for each test section.

Table 7. Features for the nichrome heaters for each test section

	Test section (*ID*)		
	0.5 mm	1.5 mm	3.0 mm
Length [m]	0.25	1.20	3.50
Maximum power [W]	8	42	120
Maximum current [A]	1.0	1.0	1.0

Inner diameter and surface roughness measurement

The inner diameter participates in the calculation of the heat transfer coefficient; consequently, the measurement of the diameter affects the uncertainty of the heat transfer coefficient. The inner diameters of the tubes of the three test sections were measured using a digital image obtained with an optical microscope. The measured inner diameter for the medium test section is 1.527 mm. The digital image is shown in Figure 38.

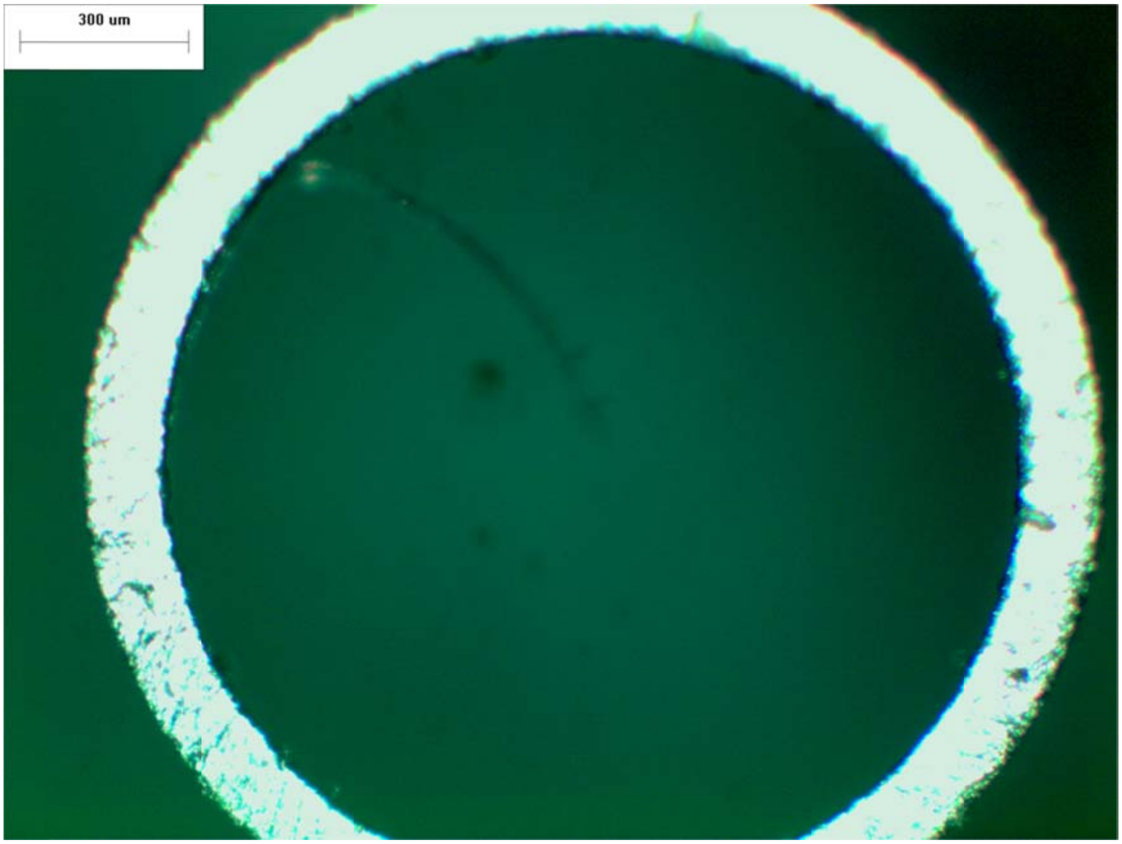

Figure 38. Digital image to measure the inner diameter of the stainless steel pipe of the 1.5 mm test section

Another important parameter is the surface roughness of the stainless steel tube because it affects the calculation of the single phase heat transfer coefficient and the frictional pressure drop. The surface roughness of the pipe was measured using a 3D optical surface profilers, Zygo interferometer. The RMS surface roughness for the medium test section is 0.86 μm, and the relative roughness 0.0006. An example of the result of the inner surface profile of the stainless steel tube is shown in Figure 39.

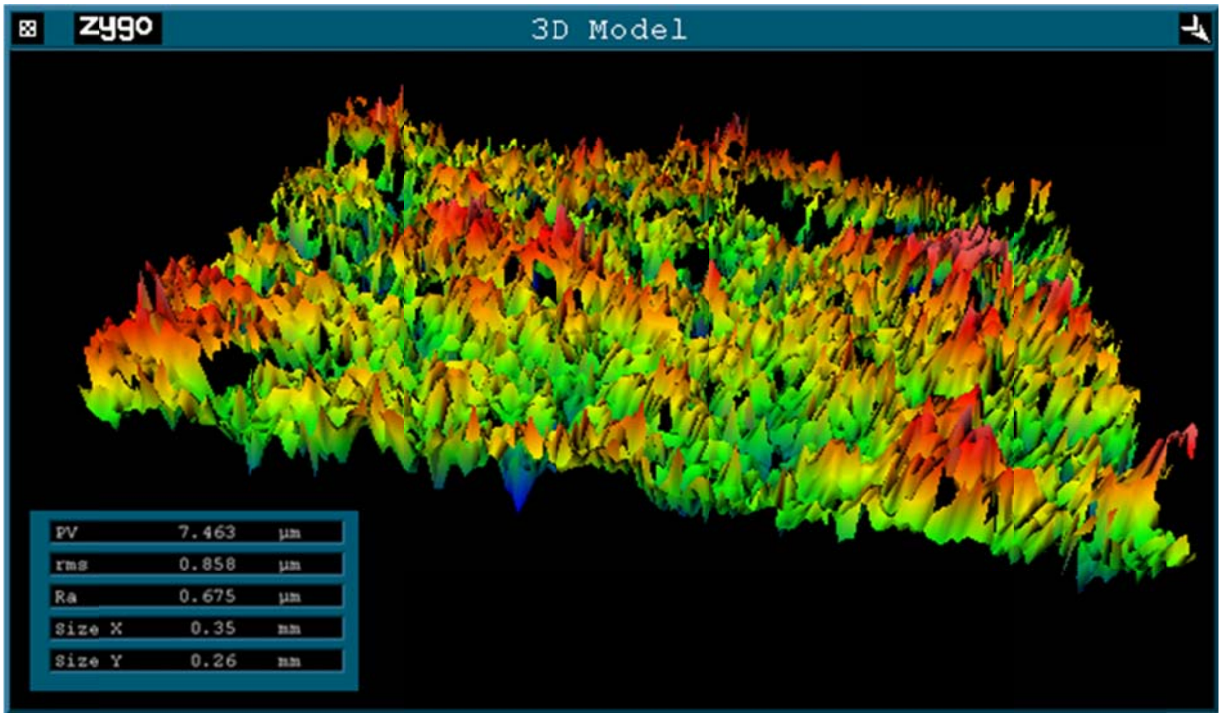

PV	7.463	µm
rms	0.858	µm
Ra	0.675	µm
Size X	0.35	mm
Size Y	0.26	mm

Figure 39. Inner surface profile of the stainless steel tube (1.5 mm test section)

2.5. Instrumentation and Calibration

2.5.1. Data Acquisition System

A CR23X micrologger (Campbell Scientific Inc) as shown in Figure 40 is used as the Data AcQuisition system (DAQ) in this test facility. This DAQ is capable of measuring voltage with an accuracy of 0.025% (full-scale range) when it operates in ambient conditions between 0 to 40 °C. The full scale may be set in the ranges of 5000 mV, 1000 mV, 200 mV, 50 mV, or 10 mV. The DAQ measures every second the voltage across the temperature sensors, pressure and differential pressure transducers, Coriolis mass flow meter, and the additional measurements required to determine the power applied to the test section.

Figure 40. DAQ CR23X micrologger of Campbell Scientific Inc.

2.5.2. Temperature sensors

The temperature measurements are carried out using PT-103 Lakeshore Platinum Resistance Thermometers (PRTs), The PRTs use a four wire connection configuration with a continuous excitation of 1 [mA] supplied by a precise current source (Lakeshore 120). The inlet (T_A), outlet (T_D), and block (T_{block}) temperatures are measured using two PRT sensors in each location and their responses are time averaged every two minutes (120 data points).

The PRTs are installed in two arrays. The PRTs, which measure TA and TD, are immersed in the flow to provide a direct measurement of the mixture temperature. Figure 41 shows one of the temperature sensors immersed in the flow.

Figure 41. Temperature sensor designed to be immersed in the flow

Also, PRTs measure the copper block temperature. In this array, the copper block has two holes that are slightly larger than the PRT diameter, and are filled with Apiezon N grease to minimize the thermal contact resistance. The PRT installed in the copper block is shown in Figure 42.

Figure 42. PRT installed in the copper block

PRTs exhibit a known relationship between the resistance across the PRT and their temperature. This relationship is given by the standard curve proposed by Callendar – Van Dusen's [29]. When temperatures are above 273.15 [K], the standard curve is given by Eq. (52):

$$\frac{R_{St}(T)}{R_0} = 1 + 3.9083x10^{-3}\ T - 5.775x10^{-7}\,T^2 \tag{52}$$

If temperatures are below 273.15 [K], the standard curve is indicated by Eq. (53).

$$\frac{R_{St}(T)}{R_0} = 1 + 3.9083x10^{-3}\,T - 5.775x10^{-7}\,T^2 - 4.18301x10^{-12}\ T^3\left(T - 100[C]\right) \tag{53}$$

where the reference resistance (R_0) is 100 [ohm], and the temperature (T) is in degrees Celsius.

The PRTs are field-calibrated using a two point calibration that includes the saturation temperature of the liquid nitrogen (77.1 K @ 98 kPa) and the freezing point of water (273.15 K). Figure 43 (left) shows the PRT calibration in liquid nitrogen. The freezing point is obtained with an ice water bath using distilled water for the water and the ice as shown in Figure 43 (right). Lakeshore, the provider of the PRTs, reports an accuracy of 0.25 K using the same calibration technique [27].

Figure 43. Calibration PRTs in liquid nitrogen (left side) and calibration PRTs in ice water bath (right side)

The two point calibration takes advantage of the fact that the difference between the voltages measured at two temperatures by an uncalibrated PRT exhibits a linear relationship with the voltage that is provided by the standard curve (Eqs. (52) or (53)) at the same these two temperatures. Consequently, if we measure the voltage for two known temperatures (reference temperatures), we are able to measure with accuracy of 0.25 K a third temperature. See Figure 44.

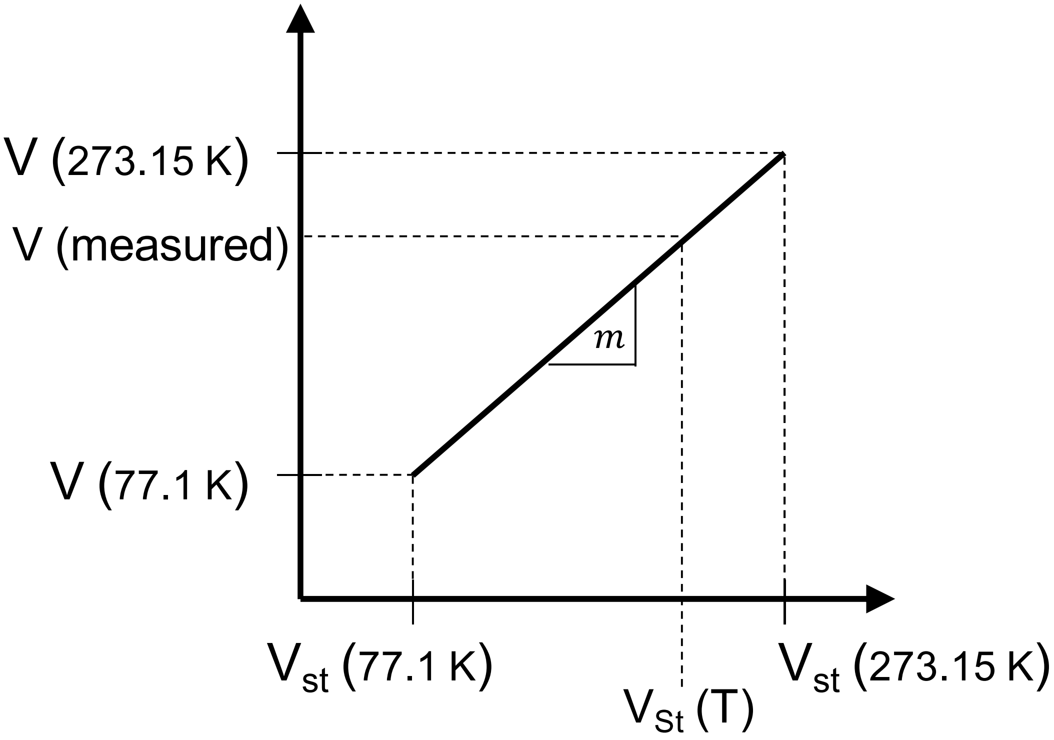

Figure 44. Linearity of voltage difference in PRTs

So, the temperature is obtained from the following expression:

$$V_{St}(T) = \frac{V(T) - \left[V(T_1) - mV_{St}(T_1)\right]}{m} \qquad (54)$$

where the slope (m) is defined by Eq. (55).

$$m = \frac{V(T_2) - V(T_1)}{V_{St}(T_2) - V_{St}(T_1)} \tag{55}$$

where T_1 is the saturation temperature of nitrogen (77,10 K at an atmospheric pressure of 98.26 kPa (737 mmHg)), T_2 is the freezing point of water (273.15 K), V_{St} is the voltage obtained from the standard curve for PRT, and V is the actual measured voltage. V_{St} is obtained by calculating the standard resistance from the standard curve (Eqs. (52) or (53)), and using Eq. (56).

$$V_{St}(T) = I\,R_{St}(T) \tag{56}$$

where the current (I) through PRTs is equal to 0.3 mA.

2.5.3. Heat load measurement

Electrical energy is applied to the test section using a high resistivity (nichrome) wire wrapped over the surface of the copper block. The rate of heat applied by ohmic dissipation is calculated by the precise measurement of the current and voltage applied using a four-wire measurement. The circuit used to measure the heat load ($\dot{Q}_{applied}$) is shown in Figure 45. $\dot{Q}_{applied}$ to the test section is calculated as the product of the DC current (I) and the voltage (V) applied to the nichrome heater.

$$\dot{Q}_{applied} = V\,I \tag{57}$$

The current is determined by measuring the voltage across a calibrated shunt resistance (R_{shunt} = 0.025 [ohm]).

$$I = \frac{V_{shunt}}{R_{shunt}} \tag{58}$$

The voltage is measured across the small resistance of a voltage divider, which is formed by two known resistances (100 kohm and 1000 kohm) installed in series. The voltage across the nichome heater is calculated using Eq. (59).

$$V = V_{100k}\left(1+\frac{1000k}{100k}\right)=11V_{100k} \tag{59}$$

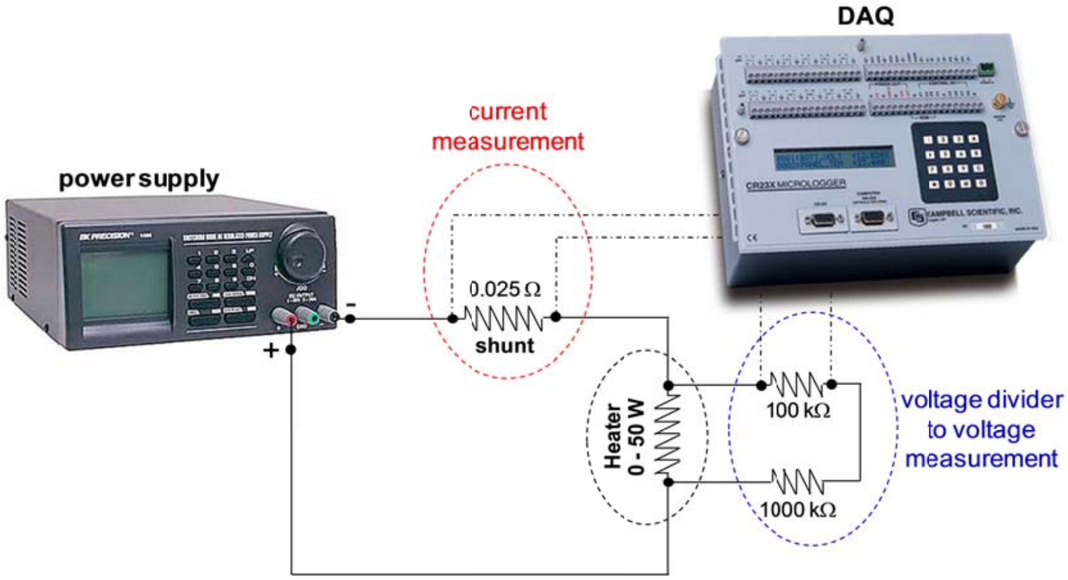

Figure 45. Heat load measurement configuration

The voltage divider and the shunt resistance were calibrated in situ using an HP 34401A multimeter.

2.5.4. Pressure measurement

A pressure transducer (Setra Model 204) is used to measure the absolute pressure at the actual inlet of the test section (location B in Figure 23). The pressure drop between A and B and B and C are measured using two differential pressure transducers (Omega MM-30psid). The pressure drop between C and D is also measured using a differential pressure transducer (Setra 204D).

2.5.5. Mass flow rate measurement

The mass flow rate that circulates through the test facility is measured by a Coriolis mass flow meter Proline Promass 83A02, which is shown in Figure 46.

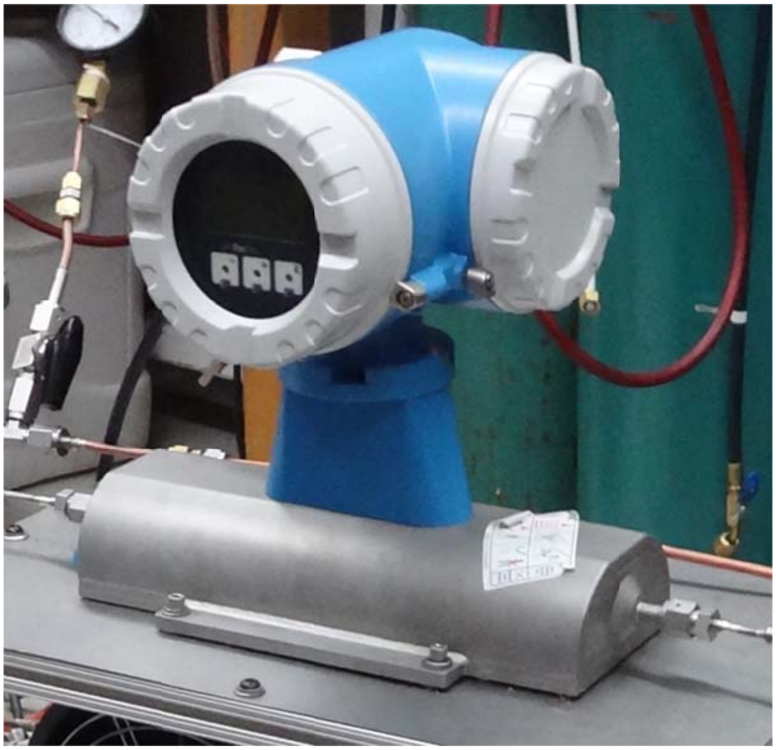

Figure 46. Coriolis mass flow meter Proline Promass 83A02

The maximum mass flow rate ($\dot{m}_{max}$) that can be measured by the mass flow meter is expressed by Eq. (60).

$$\dot{m}_{max} = 0.868\,\rho_{gas} \tag{60}$$

where ρ_{gas} is the gas density. The maximum mass flux is 250 kg/s-m^2. This mass flux results in the 0.5 mm, 1.5 mm, and 3.0 mm inner diameter test sections having a mass flow rate of 0.05 g/s, 0.44 g/s, and 1.77 g/s, respectively. Figure 47 shows the relative uncertainty as a function of the measured mass flow rate.

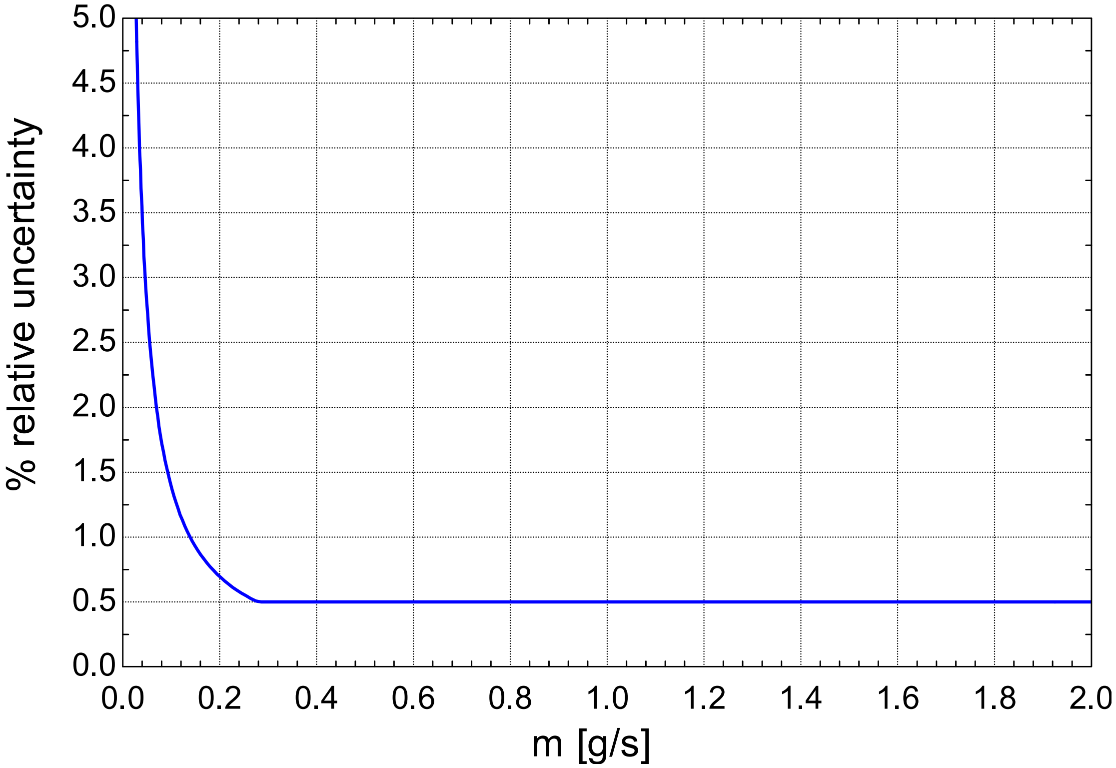

Figure 47. Relative uncertainty as a function of mass flow rate

The largest relative error (2.5% relative error) is observed when the 0.05 g/s mass flow rate is tested (0.5 mm inner diameter test section). A 0.5% relative error is expected when the mass flow rate are 0.44 g/s and 1.77 g/s (1.5 mm, and 3.0 mm inner diameter test sections, respectively).

2.6. Data Reduction

2.6.1. Heat Transfer Coefficient

2.6.1.1. Measured Heat Transfer Coefficient

The resistive heat applied ($\dot{Q}_{applied}$) to the copper block is measured electrically and the majority of the applied heat is transferred to the mixture; however, some fraction of the applied heat is lost due to radiation and conduction. An energy balance on the test section is shown in Figure 48. Losses due to convection are minimized by the high vacuum environment within the Dewar where the test section is located. The energy absorbed by the fluid ($\dot{Q}_{fluid}$) is expressed by the energy balance that removes the heat losses from the heat applied according to:

$$\dot{Q}_{fluid} = \dot{Q}_{applied} - \dot{Q}_{leak,radiation} - \dot{Q}_{leak,conduction} \tag{61}$$

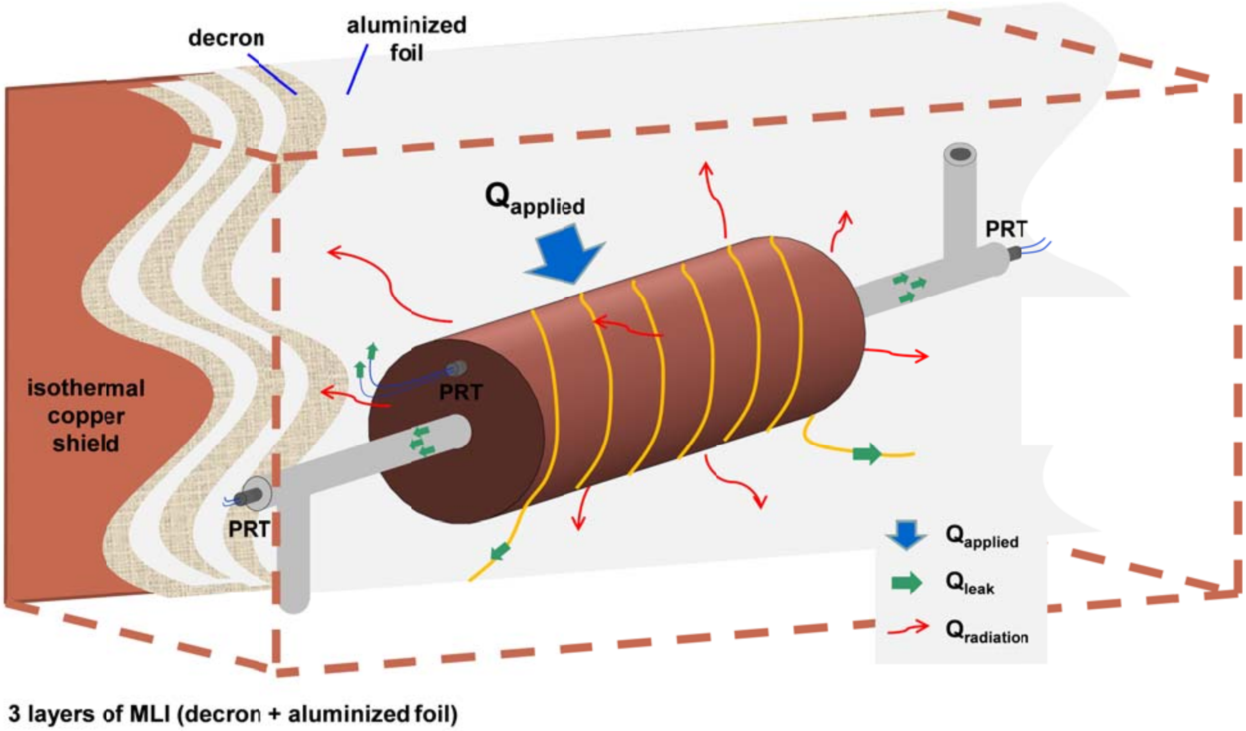

Figure 48. Schematic of the energy balance in the test section

The heat loss from the test section due to conduction ($\dot{Q}_{leak,conduction}$) is related to the temperature difference between the test section (the hottest point) and the coldest point in the system (the cryocooler cold head) through the thin stainless steel tube, sensors wires, and heater wires. All of the wires are in thermal contact with the cryocooler before they leave the Dewar in order to minimize heat losses. The thermal resistance of the system to conduction ($R_{leak,system}$) is measured by applying a small amount of heat in the test section while the inside and outside of the tube are exposed to high vacuum and is calculated according to:

$$R_{leak,system} = \frac{T_{block} - T_{cryocooler}}{\dot{Q}_{applied} - \dot{Q}_{leak,radiation}} \tag{62}$$

The thermal resistance ($R_{leak,system}$) for the test section due to the heat leak by conduction was determined to be 247 K/W, 97 K/W and 38 K/W for the 0.5, 1.5 and 3.0 mm test sections, respectively. During the test, the heat loss from the test section due to conduction ($\dot{Q}_{leak,conduction}$) is calculated according to:

$$\dot{Q}_{leak,conduction} = \frac{T_{block} - T_A}{R_{leak,system}} \tag{63}$$

Assuming the cryocooler temperature is similar to the inlet temperature. (T_A) because the high effectiveness of the cryocooler heat exchanger.

The heat leak due to radiation ($\dot{Q}_{leak,radiation}$) is enabled due the temperature difference between the test section and the isothermal shield that is connected to the cryocooler as shown by Eq (64).

$$\dot{Q}_{leak,radiation} = \frac{\sigma\left(T_{block}^{\ 4} - T_A^{\ 4}\right)}{R_{radiation}} \tag{64}$$

$R_{radiation}$ is the thermal resistance due to radiation. The radiation losses are minimized because the test section is enclosed in an isothermal shield that is thermally connected to the cryocooler as shown in Figure 49. The isothermal shield is assumed to achieve the cryocooler temperature,

$T_{shield} = T_{cryocooler} = T_A$. The isothermal shield is coated with a MLI layer at its inner and outer surface in order to minimize its emissivity. In addition, three MLI layers are wrapped around the test section between the test section and the isothermal shield. The heat loss due to radiation is estimated using a thermal network that involves the test section, the MLI layers and the isothermal shield. The emissivity of the test section (ε_{test}) and the MLI layer (ε_{MLI}) are estimated to be 0.8 and 0.05, respectively. $R_{radiation}$ is calculated according to:

$$R_{radiation} = \frac{1-\varepsilon_{test}}{\varepsilon_{test}\,A_{test}} + \frac{1}{A_{test}} + \frac{1-\varepsilon_{MLI}}{\varepsilon_{MLI}\,A_{MLI}} + 2\left(2\frac{1-\varepsilon_{MLI}}{\varepsilon_{MLI}\,A_{MLI}} + \frac{1}{A_{MLI}}\right) + \frac{1-\varepsilon_{MLI}}{\varepsilon_{MLI}\,A_{MLI}} + \frac{1}{A_{MLI}} + \frac{1-\varepsilon_{MLI}}{\varepsilon_{MLI}\,A_{shield}} \quad (65)$$

A_{test}, A_{MLI}, and A_{shield} are the surface area of the test section, MLI, and isothermal shield, respectively.

Figure 49. Isothermal shield

The cryocooler surface and the cryocooler heat exchanger lose some of the cooling power because of radiation between them and the Dewar. The installation of the isothermal shield increases these losses due to the increment of surface area with the same temperature than the cryocooler. These losses do not affect the heat transfer coefficient measurement; however, they reduce the cooling capacity available to be transferred to the gas mixture. As discussed before, in the 3.0 mm inner diameter test section, when the composition is 45% methane, 35% ethane, and 20% propane, the mass flux 250 kg/m^2-s and the tested pressure is 200 kPa, the cooling required for the gas mixture is close to the cooling capacity supplied by the cryocooler; consequently, minimizing the radiation losses is necessary. The radiation losses related with the cryocooler, cryocooler heat exchanger and the isothermal shield without any insulation is 14.2 W assuming a cryocooler temperature of 150 K and an ambient temperature of 300 K. These losses may be substantially reduced if some layers of multi-layer insulation (MLI) are added enclosing these sections as is shown in Figure 50.

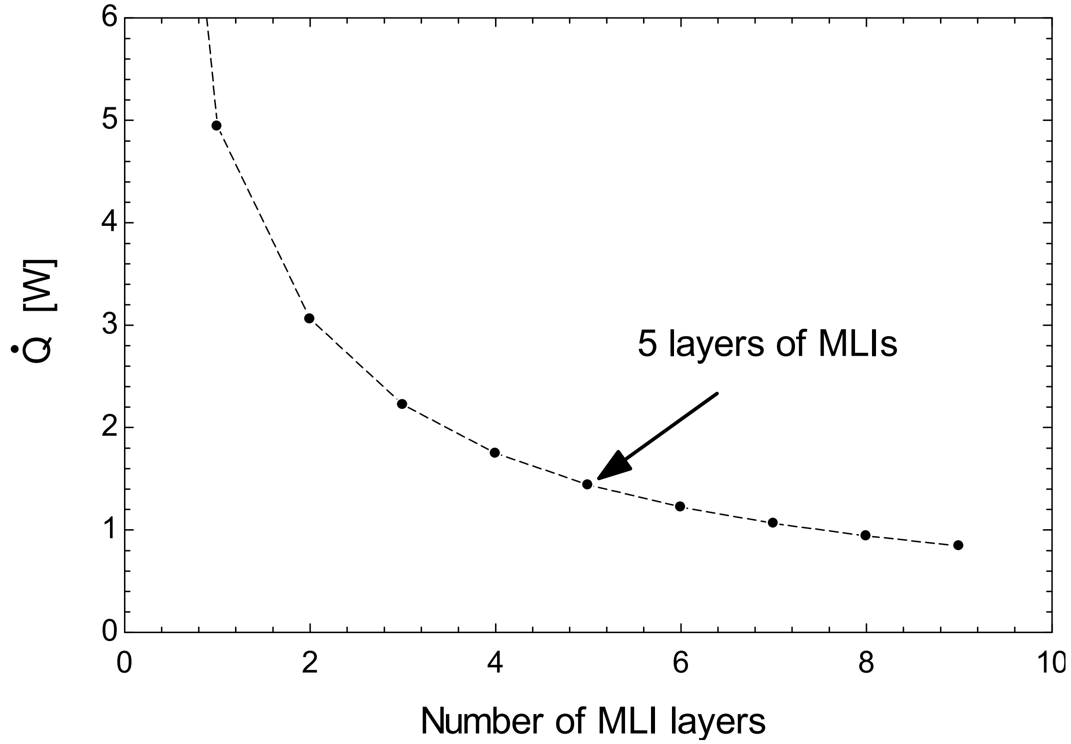

Figure 50. Heat leak by radiation as a function of number of MLI layers

The MLI provides a high radiation resistance due to its low emissivity ($\varepsilon \approx 0.05$). Heat transfer by conduction through the contact between MLI layers is avoided placing dacron netting between them. The installation of five MLI layers reduces the radiation losses by about 90%.

The effect of the heat losses (conduction & radiation) with fluid flowing is shown in Figure 51.

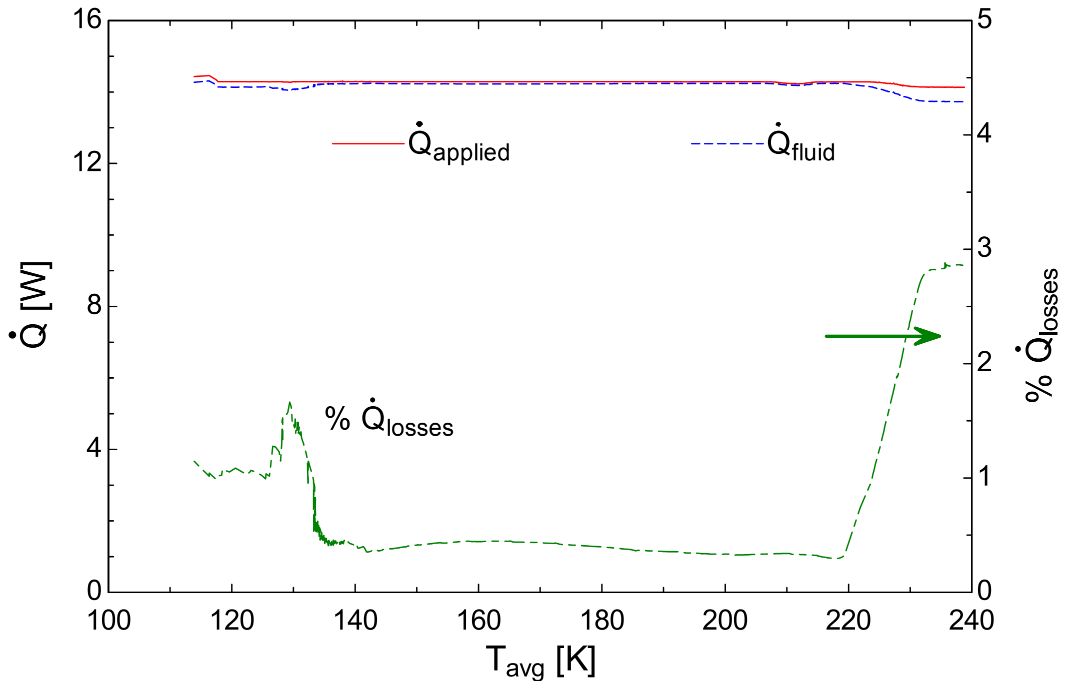

Figure 51. Heat applied, heat absorbed by the fluid and losses

The heat applied, $\dot{Q}_{applied}$, is almost completely transferred to the fluid ($\dot{Q}_{fluid}$). The heat losses increase slightly when the fluid passing through the test section is liquid-only or vapor-only because the lower single phase heat transfer coefficient that allows the copper block to get hotter; thereby, increasing the heat losses. The right axis of Figure 51 shows the ratio between the losses and the heat applied ($\dot{Q}_{applied}$), which is calculated using

$$\% \dot{Q}_{losses} = 100\% \frac{\dot{Q}_{leak,conduction} + \dot{Q}_{leak,radiation}}{\dot{Q}_{applied}} \tag{66}$$

In the two-phase region, the heat losses represent less than 0.5% of $\dot{Q}_{applied}$ while the heat losses reach approximately 3% when the flow is vapor-only. Fortunately, the two-phase region where the losses are smallest coincides with the main region of interest for this project.

It is assumed that the copper block and the stainless steel tube have no axial temperature gradient; consequently, the tube wall is isothermal. The wall temperature (T_{wall}) may be calculated using a thermal resistance network between the location of PRTs sensors in the copper block and the inner wall tube. The wall temperature is obtained by solving the thermal network using Eq. (67).

$$\dot{Q}_{fluid} = \frac{T_{block} - T_{wall}}{\dfrac{ln\left(\dfrac{D_{PRT}}{OD}\right)}{2\pi k_{copper} L} + \dfrac{ln\left(\dfrac{OD}{ID}\right)}{2\pi k_{ss} L}} \tag{67}$$

where D_{PRT} is the diameter at the location of the PRTs sensors in the copper block. ID and OD are the inner and outer diameter of the stainless steel tube. k_{copper} and k_{ss} are the thermal conductivity of the copper and stainless steel, respectively. L is the length of copper block.

The test section may be understood as a heat exchanger that has a wall with constant temperature on the hot side, and a fluid that change temperature in the cold side. In this situation, the hot side is the isothermal tube wall and the cold side is the zeotropic mixture that changes temperature as heat is added during boiling. The heat transfer coefficient (*htc*) is determined using Eq. (68), which is similar to the approach used by Nellis et al. [30].

$$htc = \frac{\dot{Q}_{fluid}}{Area\ \Delta T_{LMTD}} \tag{68}$$

The surface area used as the basis for the heat transfer coefficients is the inside area of the tube ($Area = \pi\ L\ ID$). Thin-walled stainless tubing is used for the test section to minimize measurement uncertainty caused by axial conduction. ΔT_{LMTD} is the logarithmic temperature difference, which is expressed as

$$\Delta T_{LMTD} = \frac{(T_{wall} - T_A) - (T_{wall} - T_D)}{ln\left(\frac{T_{wall} - T_A}{T_{wall} - T_D}\right)} \tag{69}$$

Eq. (68) provides the calculation for the uncorrected measured heat transfer coefficient. The subsequent section discusses how the measured heat transfer coefficients are corrected in order to account for the Joule Thomson effect and fin effect. As an example, Figure 52 shows the heat transfer coefficient measured for hydrocarbon mixture 45% CH_4, 35% C_2H_6, 20% C_3H_8 at P=270 kPa, $\dot{Q}''$ =56 kW/m^2, G = 144 kg/m2-s, and ID = 1.5 mm.

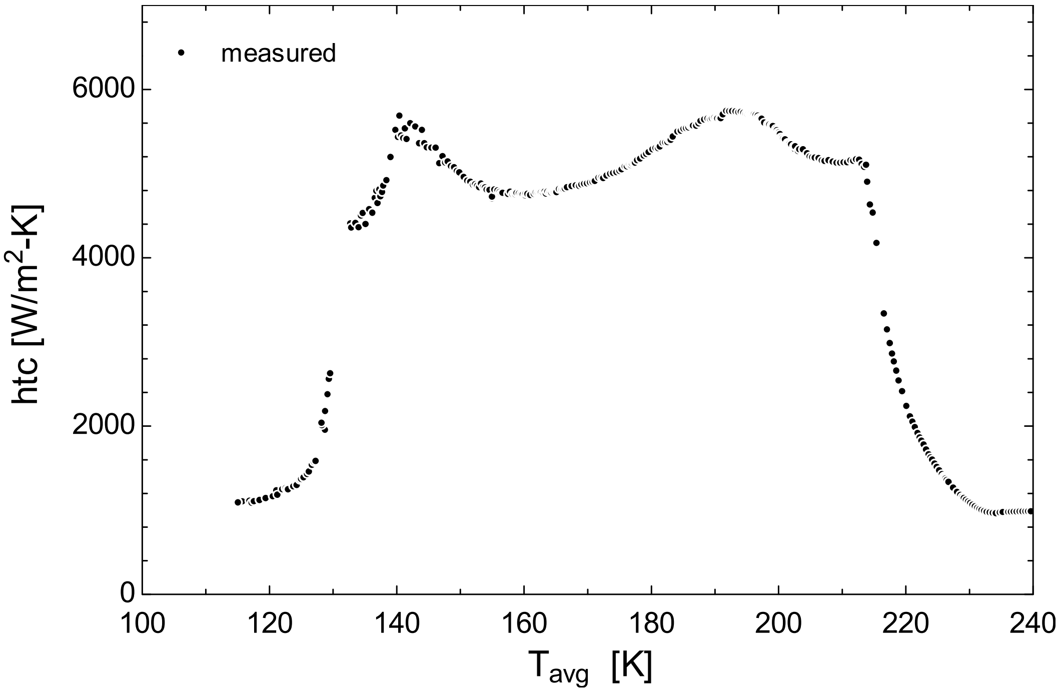

Figure 52. Uncorrected measured heat transfer coefficient hydrocarbon mixture 45% CH_4, 35% C_2H_6, 20% C_3H_8 at P=270 kPa, $\dot{Q}''$ =56 kW/m^2, G = 144 kg/m^2-s, and ID = 1.5 mm

2.6.1.2. Corrected Heat Transfer Coefficient

Correction by Joule-Thomson effect

The temperature sensors that measure the test section approach (A) and departure (D) temperatures are submerged in the circulating mixture. These temperature sensors are located some distance (greater than 10 inner diameters) from the actual inlet and outlet of the test section in order to avoid perturbations in the flow entering the test section. In some test conditions, the flow experiences a Joule-Thomson effect $\left(\frac{\partial T}{\partial P}\right)_h$ so that the actual inlet temperature (B) may differ from the measured inlet temperature (A). A similar phenomenon is expected to occur in the outlet between C and D. The calculated heat transfer coefficient could be affected by this temperature change as it will impact the log-mean temperature difference. As shown in Figure 53, there is a quasi-adiabatic section between points A and B, and C and D.

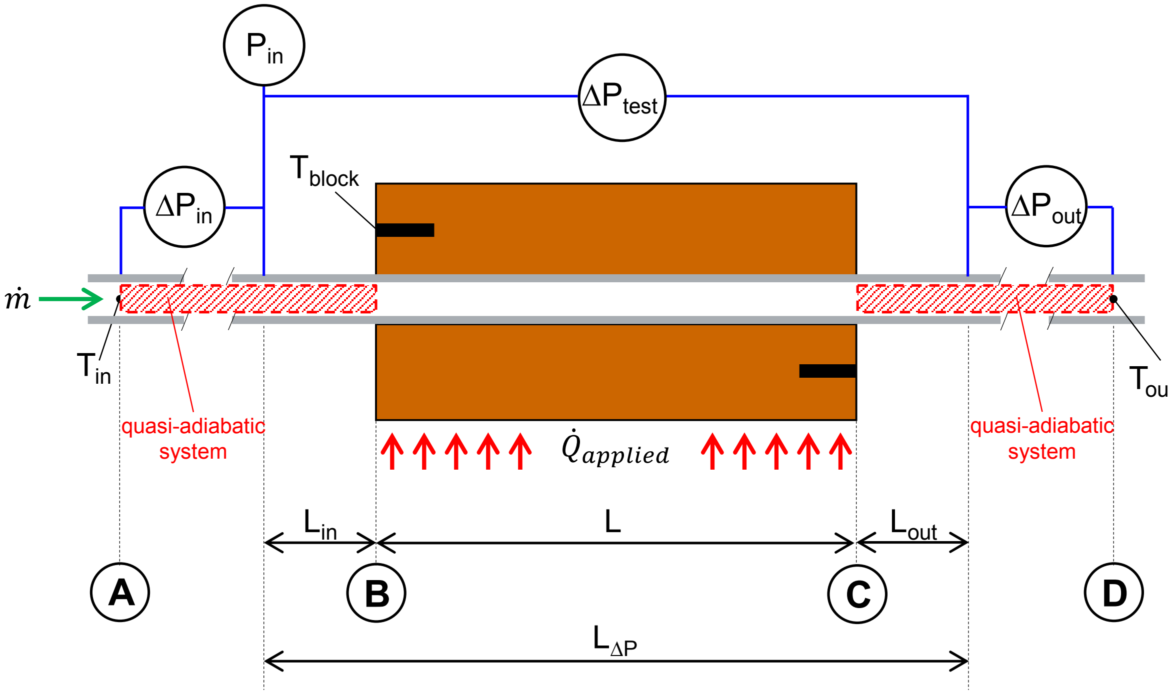

Figure 53. Schematic of instrumentation location on test section

Consequently, the temperatures in the actual inlet and outlet of the test section can be estimated with Eqs. (70) and (71), respectively.

$$T_B = T_A - \left(\frac{\partial T}{\partial P}\right)_h \left(\Delta P_{in} + \Delta P_{test}\frac{L_{in}}{L_{\Delta P}}\right) \tag{70}$$

$$T_C = T_D + \left(\frac{\partial T}{\partial P}\right)_h \left(\Delta P_{out} + \Delta P_{test}\frac{L_{out}}{L_{\Delta P}}\right) \tag{71}$$

The new logarithmic temperature difference ($\Delta T_{LMTD,JT}$), which is obtained using the actual inlet and outlet temperature of the test section (T_B and T_C) is expressed in Eq. (72).

$$\Delta T_{LMTD,JT} = \frac{\left(T_{wall} - T_B\right) - \left(T_{wall} - T_C\right)}{ln\left(\frac{T_{wall} - T_B}{T_{wall} - T_C}\right)} \tag{72}$$

and the heat transfer coefficient (htc_{JT}) corrected for the Joule-Thomson effect but still assuming an isothermal wall tube, is given by Eq. (73).

$$htc_{JT} = \frac{\dot{Q}_{fluid}}{Area\,\Delta T_{LMTD,JT}} \tag{73}$$

As an example, Figure 54 shows the heat transfer coefficient measured and corrected by Joule-Thomson effect for hydrocarbon mixture 45% CH_4, 35% C_2H_6, 20% C_3H_8 at P=270 kPa, $\dot{Q}''$ =56 kW/m^2, G = 144 kg/m2-s, and ID = 1.5 mm.

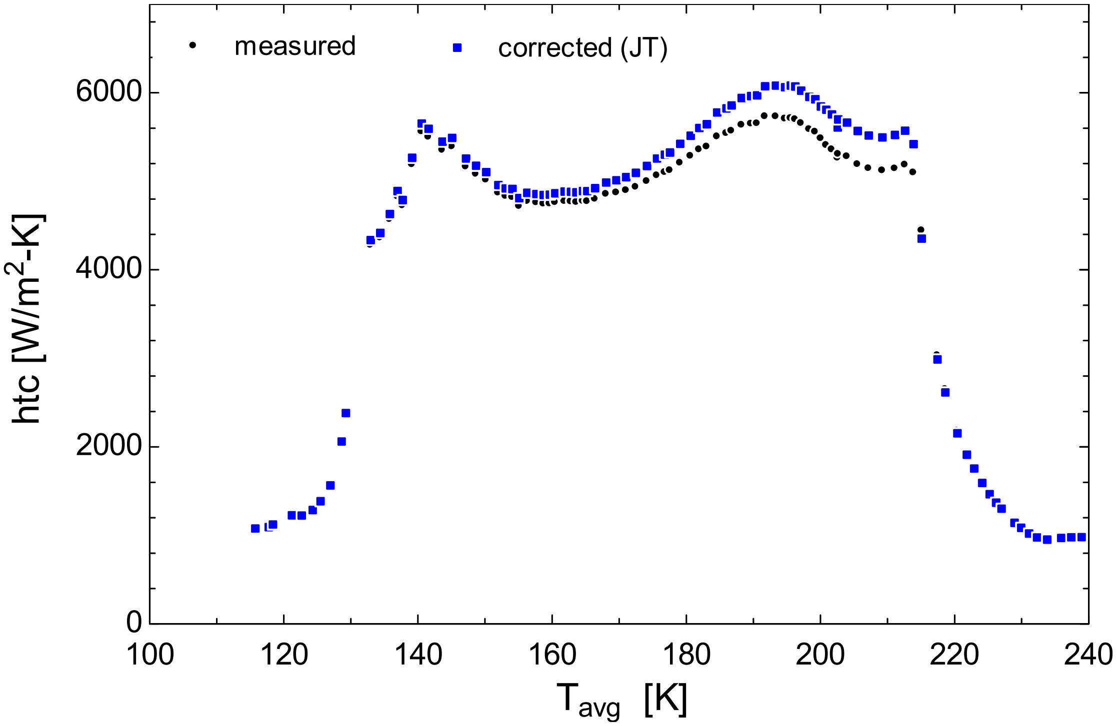

Figure 54. Heat transfer coefficient measured and corrected by Joule Thomson effect hydrocarbon mixture 45% CH_4, 35% C_2H_6, 20% C_3H_8 at P=270 kPa, $\dot{Q}''$ =56 kW/m^2, G = 144 kg/m^2-s, and ID = 1.5 mm

Correction by fin effect

During the validation of the test facility, which was performed with pure nitrogen, very good agreement of the trend of the experimental data with the trend predicted by well-known single-phase correlations was observed. However, the heat transfer coefficient that was measured was substantially higher than the value predicted by the correlations. The explanation for this difference is a phenomenon that is referred to as the "fin effect". The fin effect means that the assumption that the heat transfer between the test section and the fluid only occurs where the copper block is located is no longer applicable. A fraction of the heat applied is conducted axially through the stainless steel tube and transferred from there to the fluid. This effect is schematically shown in Figure 55.

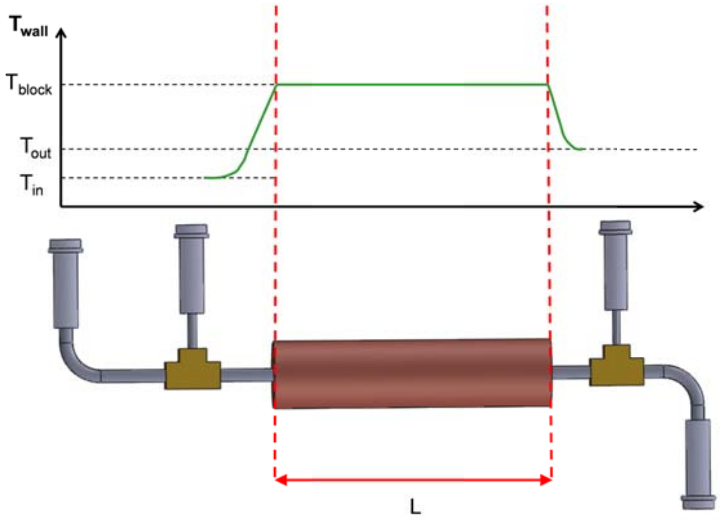

Figure 55. Schematic of fin effect phenomenon, wall temperature profile

The heat conducted axially by the stainless steel tube due to the fin effect will be completely transferred to the fluid if radiation losses from the outer surface of the tube are neglected. The fin effect, essentially, increases the active heat transfer area in the test section. The measured heat transfer coefficient can be corrected by taking into account the fin effect. The heat conducted axially by the tube that extends from both sides of the test section is calculated using the solution for a constant cross-section extended surface that is infinitely long [23]. This solution is a function of the cross sectional area of the tube, heat transfer coefficient, fluid temperature, and block temperature. The geometry and boundary conditions of the problem are shown in Figure 56. The heat flowing axially ($\dot{Q}_{fin}$) through the stainless steel tube is obtained using Eqs. (74) and (75).

$$\dot{Q}_{fin,in} = \left(T_{block} - T_B\right)\sqrt{htc_{JT+fin}\left(\pi\, ID\right)k_{ss}\left(\frac{\pi}{4}\left(OD^2 - ID^2\right)\right)} \tag{74}$$

$$\dot{Q}_{fin,out} = \left(T_{block} - T_C\right)\sqrt{htc_{JT+fin}\left(\pi\, ID\right)k_{ss}\left(\frac{\pi}{4}\left(OD^2 - ID^2\right)\right)} \tag{75}$$

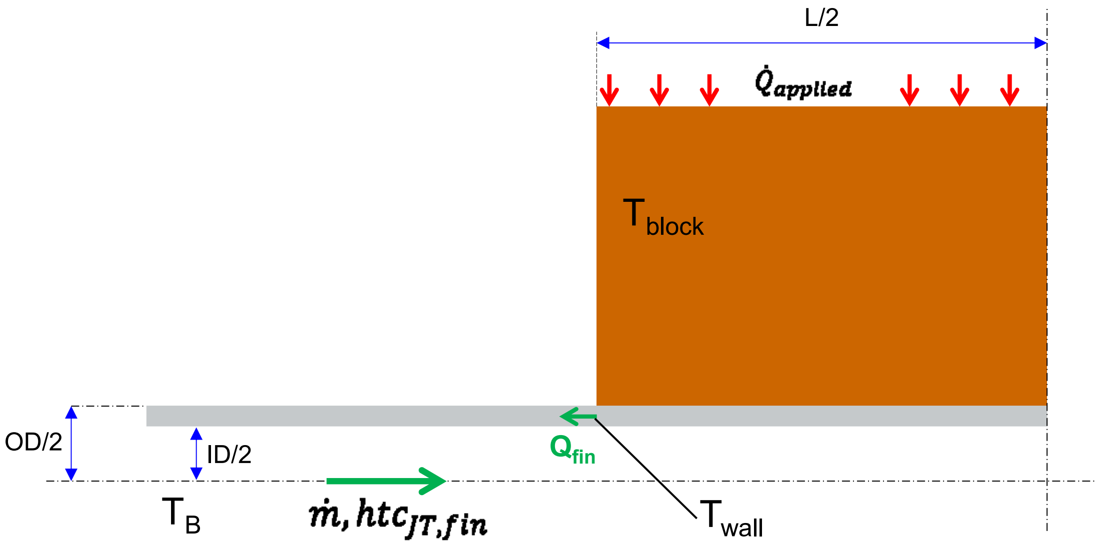

Figure 56. Schematic of geometry and boundary condition for the fin problem

The heat transferred ($\dot{Q}_{fluid,c}$) to the fluid only in the test section can be estimated by recognizing that

$$\dot{Q}_{fluid} = \dot{Q}_{fluid,c} + \dot{Q}_{fin,in} + \dot{Q}_{fin,out} \tag{76}$$

and the corrected heat transfer coefficient (htc_c) is given by Eq. (77)

$$htc_c = htc_{JT+fin} = \frac{\dot{Q}_{fluid,c}}{Area\ \Delta T_{LMTD,JT}} \tag{77}$$

The corrected heat transfer coefficient (htc_c) is determined by simultaneously solving Eqs. (74)-(77). As an example, Figure 57 shows the heat transfer coefficient measured and corrected by Joule-Thomson effect and fin effect for hydrocarbon mixture 45% CH_4, 35% C_2H_6, 20% C_3H_8 at P=270 kPa, $\dot{Q}''$ =56 kW/m^2, G = 144 kg/m2-s, and ID = 1.5 mm.

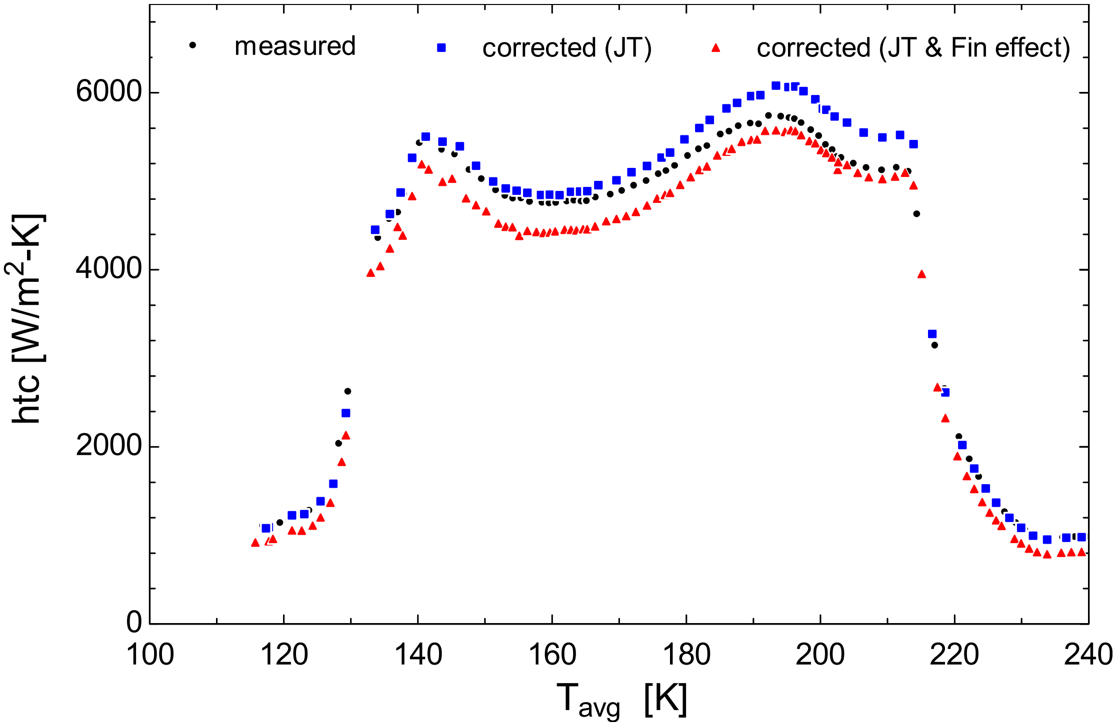

Figure 57. Heat transfer coefficient measured and corrected by Joule Thomson effect and by fin effect, hydrocarbon mixture 45% CH_4, 35% C_2H_6, 20% C_3H_8 at P=270 kPa, $\dot{Q}''$ =56 kW/m^2, G = 144 kg/m^2-s, and ID = 1.5 mm

An effective method to reduce the fin effect is to reduce the cross sectional area of the stainless steel tube. In our case, the test section was replaced by installing a thin stainless steel tube. The dimensions of the actual 1.5 mm test section and the old one are shown in Table 8.

Table 8. Dimensions of actual 1.5 mm test section and the old one

Parameter	**Actual**	**Old**	**unit**	**instrument**
Inner diameter SS304 tube (*ID*)	**1.527±0.003**	**1.515±0.003**	mm	microscope
Outer diameter SS304 tube (*OD*)	1.821±0.003	3.180±0.003	mm	micrometer
Wall thickness SS304 tube (*th*)	0.147*	0.833*	mm	microscope
R_{rms} (roughness)	0.860±0.010	2.560±0.010	µm	Zygo
R_{rms}/ID	0.0006*	0.0017*		
Length copper block (*L*)	52.50±0.01	50.00±0.01	mm	caliper
Outer diameter copper block	19.05±0.01	19.05±0.01	mm	caliper
PRTs location	9.03±0.01	9.03±0.01	mm	caliper
$L_{\Delta P}$	125.80±0.01	91.30±0.01	mm	caliper
Pressure tap diameter	0.63±0.01	0.63±0.01	mm	caliper
Length tap – inlet (L_{in})	33.00±0.01	20.10±0.01	mm	caliper
Length outlet – tap (L_{out})	40.30±0.01	21.20±0.01	mm	caliper

*calculated

As an example, Figure 58 shows the heat transfer coefficient measured and corrected by Joule Thomson effect and fin effect using the new test section for hydrocarbon mixture 45% CH_4, 35% C_2H_6, 20% C_3H_8 at P=270 kPa, $\dot{Q}''$ =56 kW/m^2, G = 240 kg/m^2-s, and ID = 1.5 mm.

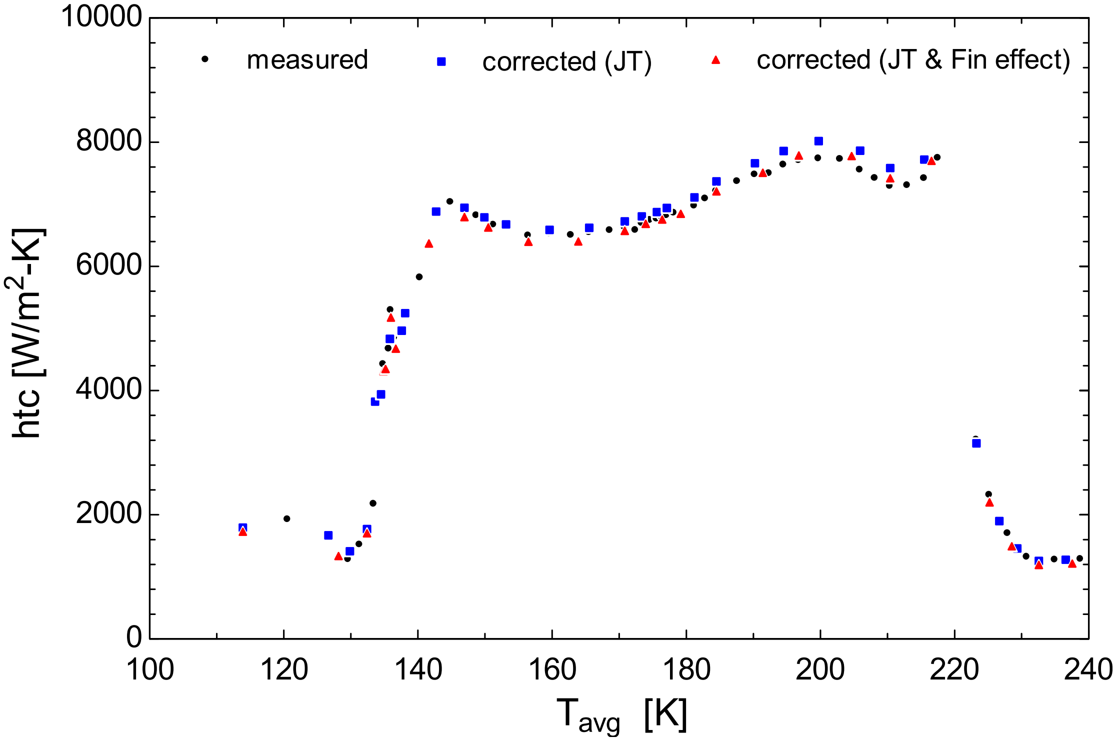

Figure 58. Heat transfer coefficient measured and corrected by Joule Thomson effect and by fin effect hydrocarbon mixture 45% CH_4, 35% C_2H_6, 20% C_3H_8 at P=270 kPa, $\dot{Q}''$ =56 kW/m^2, G = 240 kg/m^2-s, and ID = 1.5 mm

It is clear that the fin effect is substantially reduced. Also, the Joule-Thomson effect is minimized because the design of the test section was improved to reduce pressure drop.

2.6.2. Pressure Drop

The measured two-phase pressure drop (ΔP_{test}) is formed by the addition of four components: friction ($\Delta P_{friction}$), static (ΔP_{static}), momentum ($\Delta P_{momentum}$), and form (ΔP_{form}) contributions. Eq. (78) shows the measured two-phase pressure drop definition.

$$\Delta P_{test} = \Delta P_{friction} + \Delta P_{static} + \Delta P_{momentum} + \Delta P_{form} \tag{78}$$

In the actual configuration, ΔP_{test} is measured in a horizontal test section where there is no change in static pressure (ΔP_{static} = 0). The form term (ΔP_{form}) is related to the pressure losses due to flow perturbations created by the presence of the inlet and outlet pressure taps. The two-phase pressure drop may be measured under adiabatic and diabatic conditions. When pressure drop and heat transfer coefficients are measured simultaneously, heat is applied at the test section which changes the kinetic energy of the fluid between the inlet and the outlet pressure taps. The kinetic energy effect in the pressure drop is quantified by the momentum pressure drop term ($\Delta P_{momentum}$). The experimental pressure drop for this diabatic measurement is given by Eq. (79).

$$\Delta P_{test} = \Delta P_{friction} + \Delta P_{momentum} + \Delta P_{form} \tag{79}$$

In the present study, $\Delta P_{momentum}$ is calculated using Eq. (80).

$$\Delta P_{momentum} = G^2 \left[\left(\frac{(1-x)^2}{\rho_l (1-\alpha)} + \frac{x^2}{\rho_v \alpha} \right)_{out} - \left(\frac{(1-x)^2}{\rho_l (1-\alpha)} + \frac{x^2}{\rho_v \alpha} \right)_{in} \right] \tag{80}$$

where G is mass flux, x is quality, ρ_l and ρ_v are the liquid and vapor density, respectively, and α is void fraction. The void fraction is estimated using the drift flux model for horizontal tubes of Rouhani and Axelsson [31] in Eq. (81):

$$\alpha = \frac{x}{\rho_v} \left[\left(1 + 0.12(1-x)\right) \left(\frac{x}{\rho_v} + \frac{1-x}{\rho_l} \right) + \frac{1.18(1-x)\left(g\sigma(\rho_l - \rho_v)\right)^{0.25}}{G \rho_l^{0.5}} \right]^{-1} \tag{81}$$

When ΔP_{test} is measured under adiabatic conditions, the measured term is composed only of a friction term and form term (Eq. (82)) because $\Delta P_{momentum} = 0$.

$$\Delta P_{test} = \Delta P_{friction} + \Delta P_{form} \tag{82}$$

2.7. Uncertainty Analysis

The uncertainty of a measurement (u_c) is calculated as the combination of systematic and random errors [32].

$$u_c = \sqrt{{u_p}^2 + {u_i}^2 + {u_{DAQ}}^2 + {u_{bias}}^2} \tag{83}$$

The systematic errors determine the accuracy of the measurement and are obtained by the analysis of calibration methodology, manufacturer's specified accuracy, and the resolution of each instrument (u_i) as well as the DAQ system (u_{DAQ}). The random errors (u_p) quantify the precision of the measurement and are determined by the standard deviation of 120 data points (1 record per second) under steady state conditions. The summary of the instrument uncertainties installed in the test facility are shown in Table 9.

Table 9. The summary of the instruments uncertainties installed on the test facility

Instrument	**Manufacturer**	**Model**	$\mathbf{u_i}$		$\mathbf{u_{DAQ}}$[6]	
Coriolis mass flowmeter	Endress Hauser	83A02	0.56% o.r. 0.0015 g/s	[1,a] [1,b]	0.0018 g/s	
Test section heat load						
heater voltage			0.0025 V 0.0073 V	[2,c] [2,d]	0.0275 V 0.0794 V	[c] [d]
heater current			0.0011 A	[2]	0.0010 A	
PRTs	Lakeshore		0.25 K	[2]	0.26 K	
Pressure	Setra	204	0.28 psi	[3]	0.25 psi	
Differential pressure	Setra	204D	0.06 psi	[3]	0.03 psi	
	Omega	MMDDU030V5P3D0T3A5CE	0.02 psi	[4]	0.02 psi	
Gas chromatograph TCD	HP 5890 II		4% o.r.	[5]	N/A	

o.r.:	of reading	1	[33]	a	Mass flowrate >= 0.278 g/s
N/A	No applied	2	Calibrated in situ	b	Mass flowrate < 0.278 g/s
		3	[34], [35]	c	ID = 0.5 & 1.5 mm
		4	[36]	d	ID = 3.0 mm
		5	[37]		
		6	[38]		

The uncertainty related to a bias error (u_{bias}) is neglected in this arrangement. In the actual configuration, there are two phenomena that can produce a bias error: self-heating of PRTs and heat leak due to axial conduction through the PRTs wires. The self-heating is the generation of heat due to the excitation. The self-heating in the PRTs was tested by providing 0.3, 1.0, and 3.0 Amp as excitation during the calibration. A measurably different reading was not observed for any of these conditions. The heat leak due to conduction is controlled by wrapping the PRT wires in the support wire that is submerged in the flow. In addition, the PRTs leads are wrapped on the cryocooler to minimize the heat leak.

Once the combined uncertainty (u_c) for each measurement is known, the uncertainty propagation feature provided by EES [39] is used to determine the uncertainty of the heat transfer coefficient, average temperature, pressure drop, and heat absorbed by the fluid. As an example, Eq. (84) shows that the heat transfer coefficient is a function of the heat applied to the test section ($\dot{Q}_{applied}$), inlet (T_1 and T_2), outlet (T_3 and T_4) and block temperature (T_5 and T_6), mixture composition (z), inlet pressure (P_{in}) and the pressure drop between A and B (ΔP_{in}), B and C (ΔP_{test}), C and D (ΔP_{out}), and test section dimensions.

$$htc_c = \frac{\dot{Q}_{fluid,c}}{Area\, \Delta T_{LMTD,JT}} = f\left(\dot{Q}_{applied}, T_1, T_2, T_3, T_4, T_5, T_6, z[1,n], P_{in}, \Delta P_{in}, \Delta P_{test}, \Delta P_{out}, ID, L\right) \qquad (84)$$

Consequently, the uncertainty in the measurement of heat transfer coefficient (δhtc_c) is given by:

$$\delta htc_c = \sqrt{\left(\frac{\partial htc_c}{\partial \dot{Q}_{applied}}\delta \dot{Q}_{applied}\right)^2 + \left(\frac{\partial htc_c}{\partial T_1}\delta T_1\right)^2 + \left(\frac{\partial htc_c}{\partial T_2}\delta T_2\right)^2 + ...+\left(\frac{\partial htc_c}{\partial ID}\delta ID\right)^2} \quad (85)$$

Table 10 shows the results of the uncertainty analysis for one data point of heat transfer coefficient measured for the hydrocarbon mixture (45% CH_4, 35% C_2H_6 and 20% C_3H_8 by volume) in a horizontal test section with an inner diameter of 1.5 mm at the conditions of 56 W/m^2 heat flux, 240 kg/m^2-s mass flux, and an inlet pressure of 270 kPa. The measurements of block temperature (T_5 and T_6) have the greatest uncertainty contribution to the measured heat transfer coefficient. Also, the outlet (T_3 and T_4) and inlet (T_1 and T_2) temperatures are also very important as evidenced by their respective % contributions to the uncertainty.

Table 10. Results of the uncertainty analysis for one data point

***htc* = 6924 ± 285 W/m^2-K**

Measurement*	**Value**	u_c	**Contribution %**
T_1	179.1 K	0.4 K	5.7 %
T_2	179.1 K	0.4 K	5.7 %
T_3	182.1 K	0.4 K	11.0 %
T_4	182.1 K	0.4 K	11.0 %
T_5	189.3 K	0.4 K	32.3 %
T_6	189.9 K	0.4 K	32.6 %
ΔP_{in}	1.12 psi	0.07 psi	0.1 %
ΔP_{out}	1.44 psi	0.16 psi	1.2 %
$Q_{applied}$	14.29 W	0.03 W	0.4 %

*measurements shown with contribution greater than 0.1%

2.8. Validation

2.8.1. Heat Losses

The heat loss estimation is verified by applying a known heat input to the flow of a known mass flow rate of pure nitrogen while pressure and temperature are measured. Figure 59 compares the energy absorbed by the fluid using two methods.

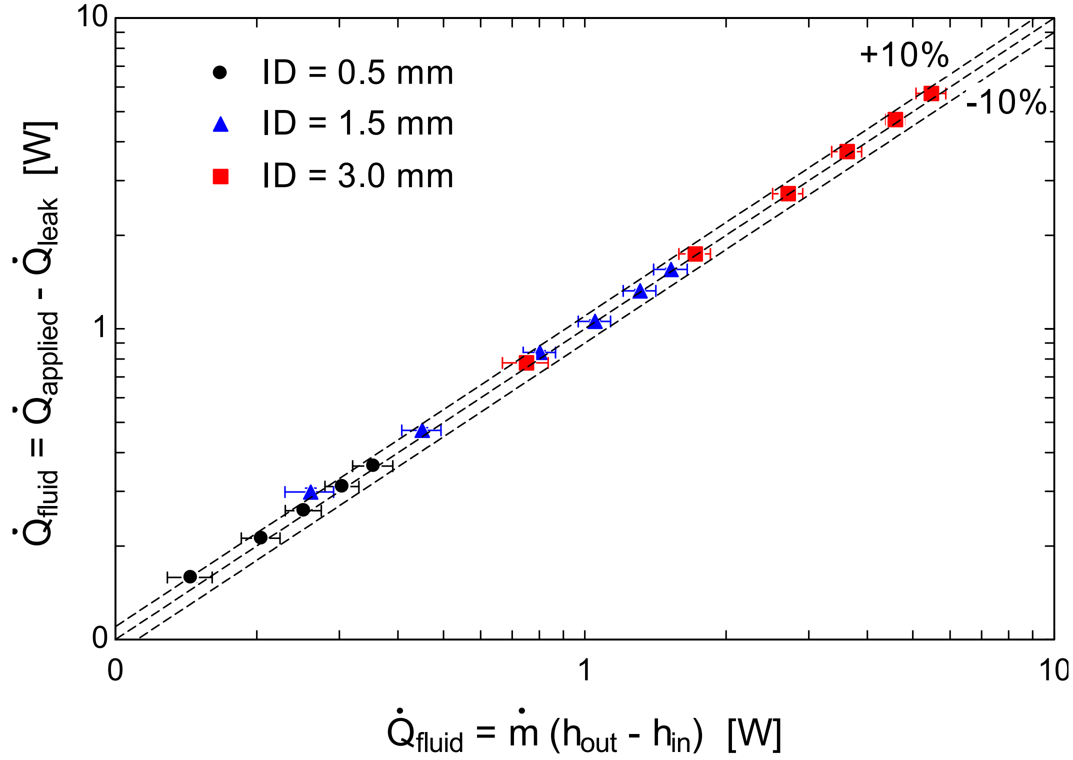

Figure 59. Heat absorbed by single-phase pure nitrogen calculated by heat applied less losses vs enthalpy difference

First, the heat absorbed by the fluid is estimated after removing the heat losses due to radiation and conduction from the heat applied to the test section as shown in Eqs. (61) and (76) (axis y in Figure 59). The second method calculates the heat absorbed by the fluid as the enthalpy difference between the inlet and the outlet of the nitrogen in the test section using measured fluid temperature and pressure (axis x in Figure 59). Eq. (86) shows the heat absorbed by the fluid calculated according to the enthalpy difference:

$$\dot{Q}_{fluid} = \dot{m}\left(h_{out} - h_{in}\right) \tag{86}$$

Agreement within 10% is observed between both methods.

2.8.2. Heat Transfer Coefficient

2.8.2.1. Single Pure Fluid

Figure 60 shows the result of a validation of the test facility that is performed by measuring the heat transfer coefficient of single-phase pure nitrogen and comparing the results with the corresponding local heat transfer coefficient predicted by a well-known single-phase correlation as Gnielinski [40]. Agreement within 10% is observed between the measured and the predicted data for pure nitrogen.

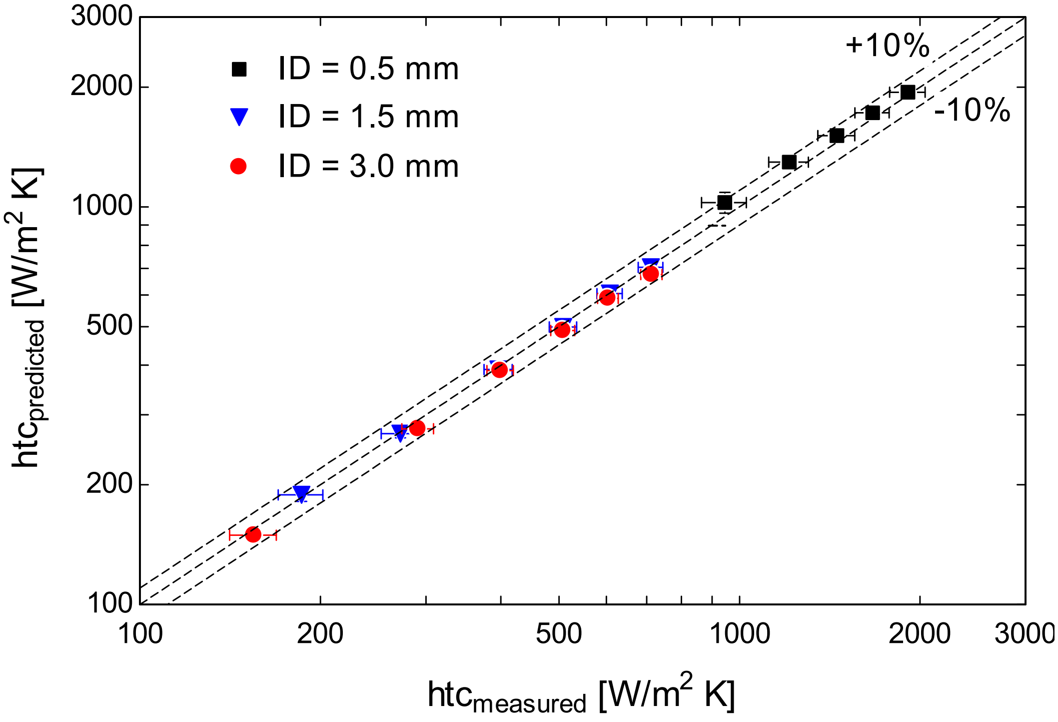

Figure 60. Measured and predicted heat transfer coefficient single-phase pure nitrogen

2.8.2.2. Repeatability

A test condition could be achieved by either warming up or cooling down the system. It is expected that similar results should be obtained independent of the direction used to carry out the test. Figure 61 shows two set of heat transfer coefficient data measured at the same test condition (composition, G, P, $\dot{Q}''$ and diameter). One of the data set (circles) is measured during cooling of the system, and the other data set (squares) is obtained while warming the system. No significant difference is observed between the two sets of heat transfer coefficient data, to within the estimated uncertainty of the measurements. Consequently, heat transfer coefficient measurements show good repeatability.

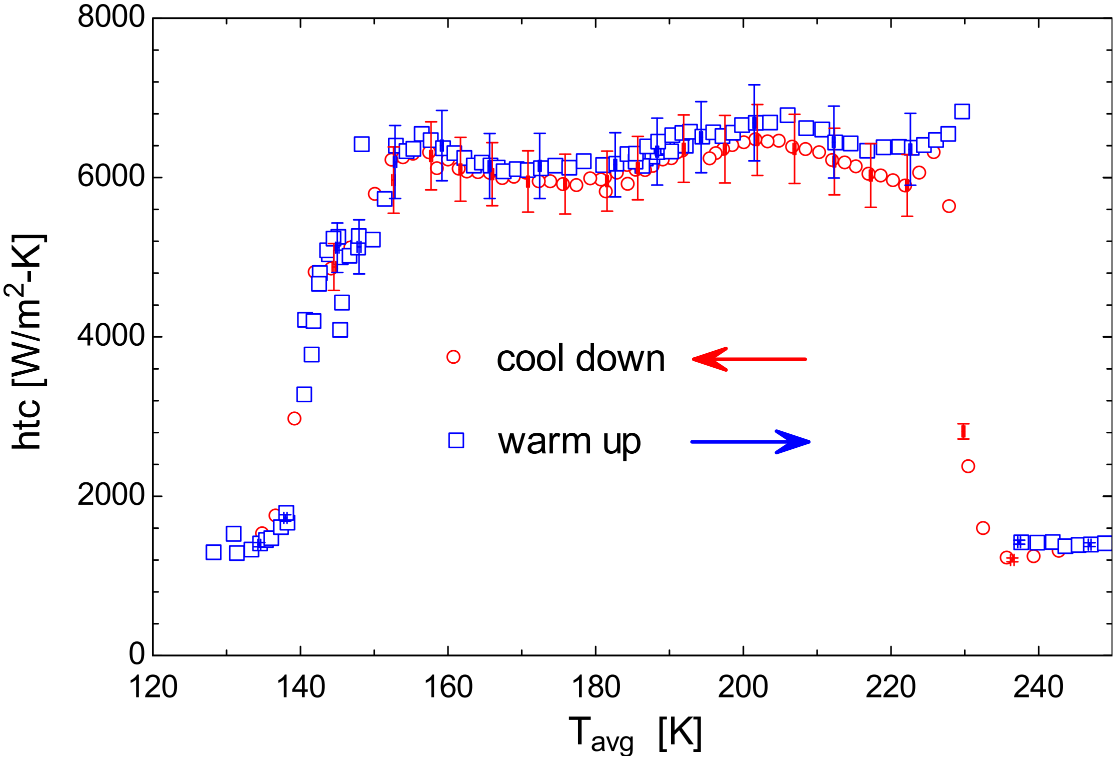

Figure 61. Measured heat transfer coefficient for $CH_4/C_2H_6/C_3H_8$ mixture (45%/35%/20% by volume) with P = 420 kPa, Q'' = 32 kW/m^2, ID = 1.5 mm and G = 240 kg/m^2-s during cooling and warming of the system

2.8.2.3. Isothermal wall assumption

A numerical model of the thermal behavior of the test section is formulated to evaluate the effect of assuming an isothermal wall tube in the calculation of the heat transfer coefficient. A finite element method in cylindrical coordinates is used to develop the numerical model, which is shown in Appendix A. A good agreement is obtained when the heat transfer coefficient assuming constant wall tube is compared with the results of the numerical model; consequently, the assumption of a constant wall temperature allows a determination of the heat transfer coefficient for gas mixtures in a precise manner. The isothermal wall tube and numerical heat transfer coefficient as a function of the average temperature are shown in Figure 62.

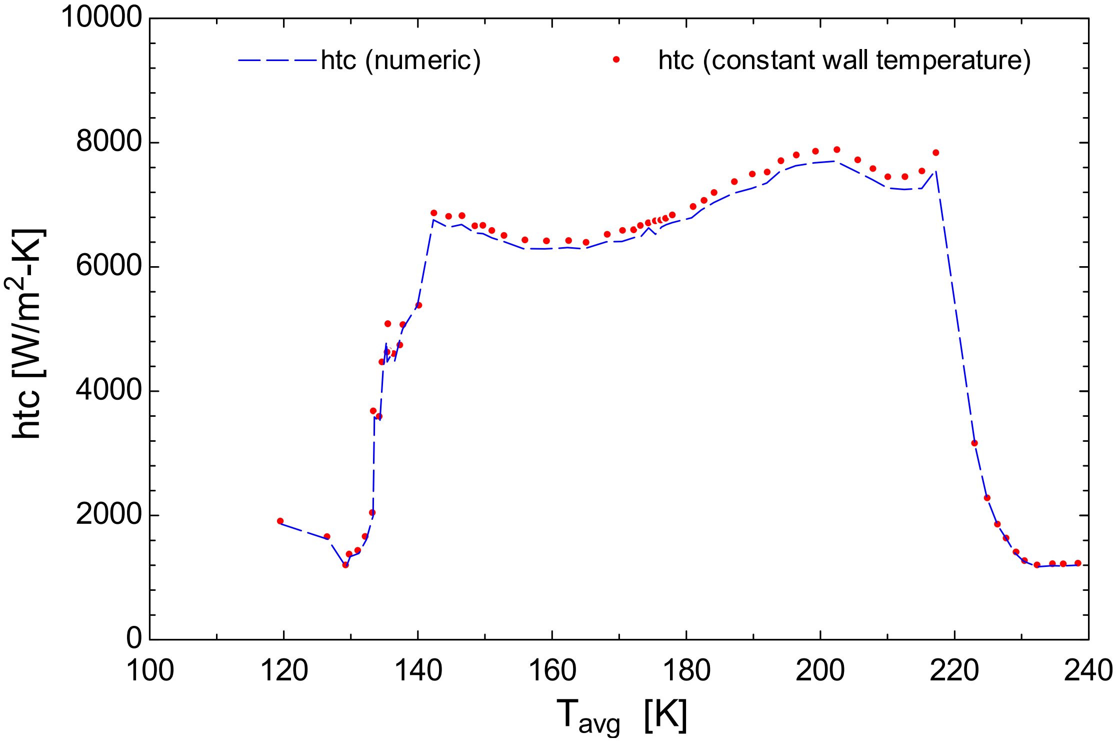

Figure 62. Heat transfer coefficient (numerical) as a function of the average temperature (Run 4).

2.8.3. Pressure drop

2.8.3.1. Form Term

The pressure drop of single-phase pure nitrogen is measured in the test section under adiabatic conditions. The measured pressure drop is given by Eq. (87), which sums the contribution of the friction and form components:

$$\Delta P_{test} = \Delta P_{friction} + \Delta P_{form} = f \frac{L_{\Delta P}}{ID} \frac{G^2}{2\rho} + K_{cal} \frac{G^2}{2\rho} \tag{87}$$

The friction pressure drop is a function of the friction factor (*f*), which can be calculated using the Zigrang and Sylvester [41] correlation:

$$f = \left(-2\,log\left(\frac{relrough}{3.7} - \frac{5.02}{Re} log\left(\frac{relrough}{3.7} + \frac{13}{Re} \right) \right) \right)^{-2} \tag{88}$$

$L_{\Delta P}$ is the distance between the pressure taps, R_{RMS} is the RMS roughness of the stainless steel tube. These parameters are shown in Table 4. *Re* is the Reynolds number.

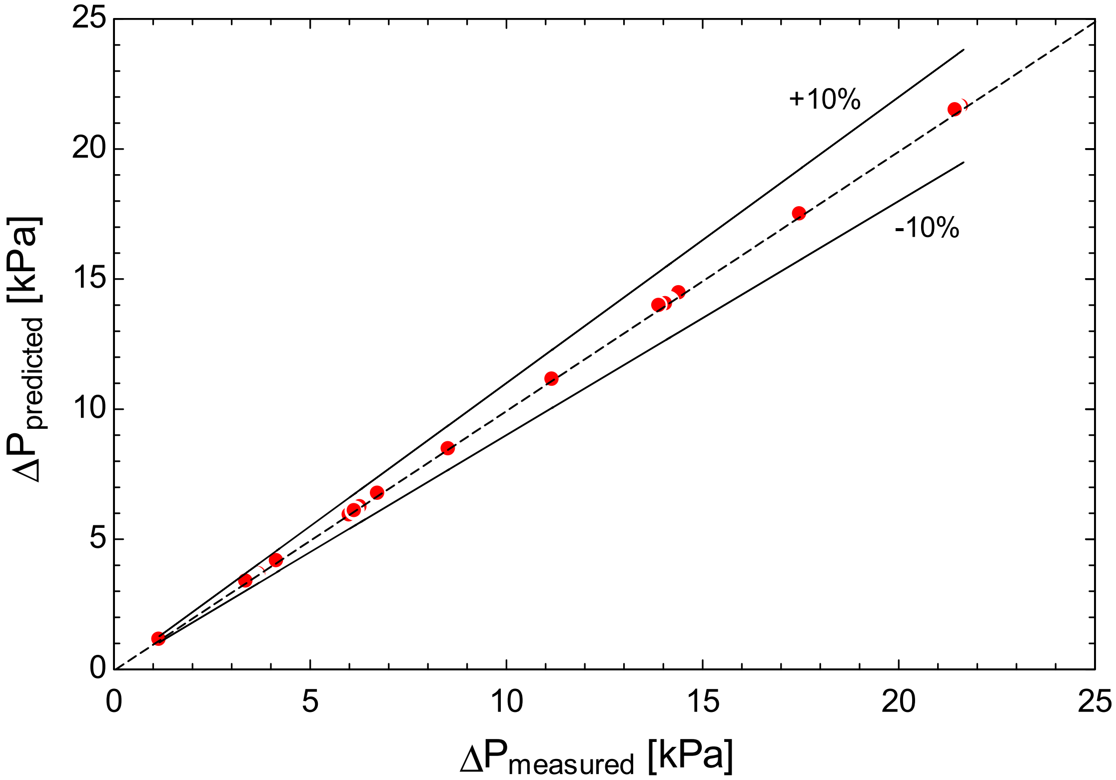

Figure 63. Pressure drop measured and predicted for single-phase pure nitrogen (1.5 mm)

The form coefficient (K_{cal}) is obtained adjusting the measured and calculated pressure drop for single-phase pure nitrogen. The measurements show that K_{cal} = 1.25 for the 0.5 mm test section and K_{cal} = 1.15 for the 1,5 mm test section. Figure 63 shows the predicted pressure drop as a function of the measured pressure drop using the adjusted parameter (K_{cal}) for the 1.5 mm test section.

2.8.3.2. Acceleration Term

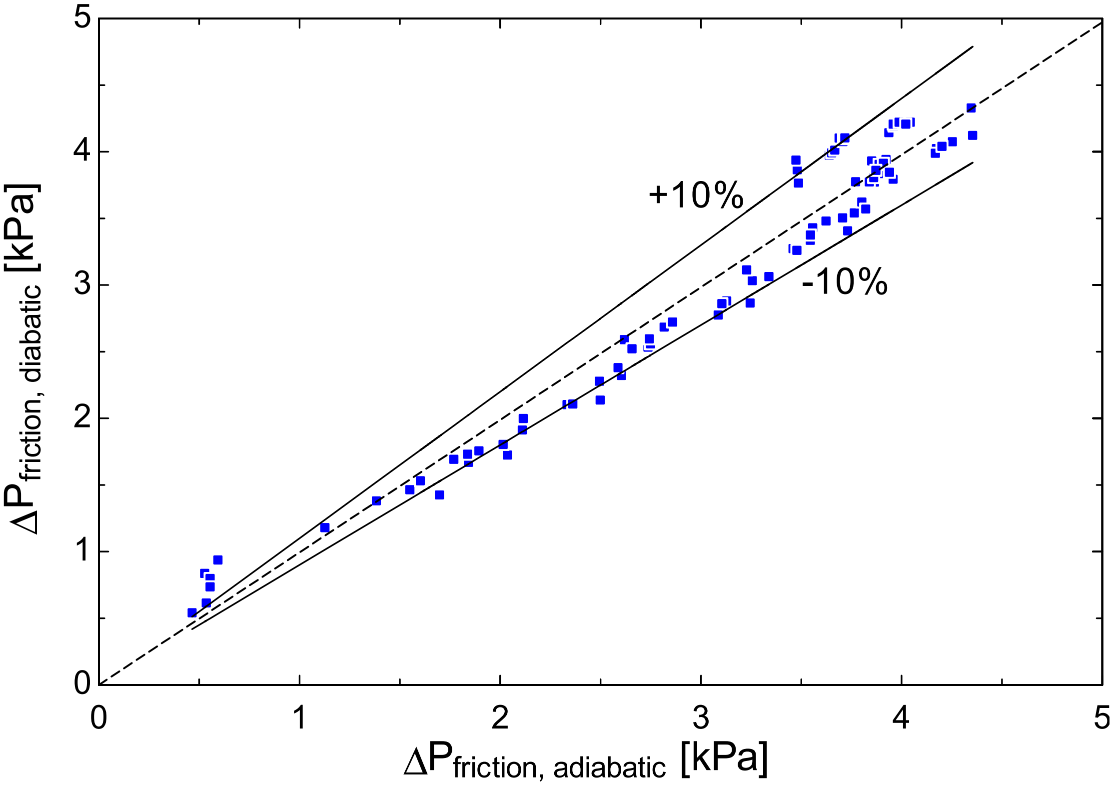

Figure 64. Pressure drop measured under diabatic (HC-4) and adiabatic (HC-3) conditions

The pressure drop is measured for a gas mixture without the application of any heat to the test section (adiabatic), mixture HC-3 according to Table 23. The test is repeated, but now heat is applied and the other test conditions (composition, *G, P* and diameter) are maintained, referred as mixture HC-4 in Table 23. The pressure drop by friction predicted using Eqs. (79) and (82) are compared in Figure 64. The momentum pressure drop seems to be estimated reasonably well using the Rouhani-Axelsson [31] void fraction model. Most of the measured points agree to within ±10%. Also, this test shows repeatability on the measurement of friction pressure drop.

Figure 65 shows the same data as a function of average. The most important difference is observed between 165 and 180 K, corresponding to the range of 10 and 30% of thermodynamic quality where the difference between the corrected diabatic experimental data exceeds 25% with respect the adiabatic data.

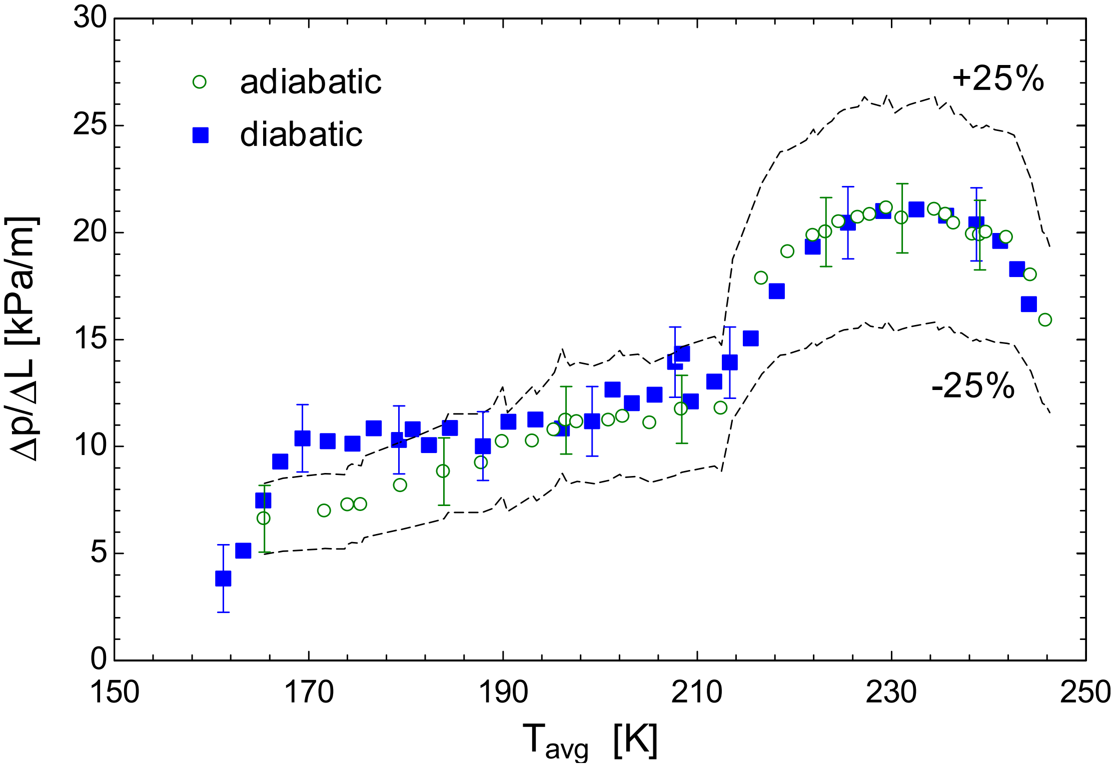

Figure 65. Diabatic (HC-4) vs adiabatic (HC-3) frictional pressure drop as a function of average temperature

2.8.3.3. Single phase

The frictional pressure drop measurement was validated by collecting pressure drop data in the superheated region (i.e., single phase vapor) for all of the mixtures and conditions tested. Figure 66 compares the experimental pressure drop with the pressure drop calculated using the Zigrang and Sylvester [41] friction factor relation (Eq. (88)) using the flow properties corresponding to the measurement conditions, diameter and measured roughness of the test sections. The experimental and predicted data agree to within 25%.

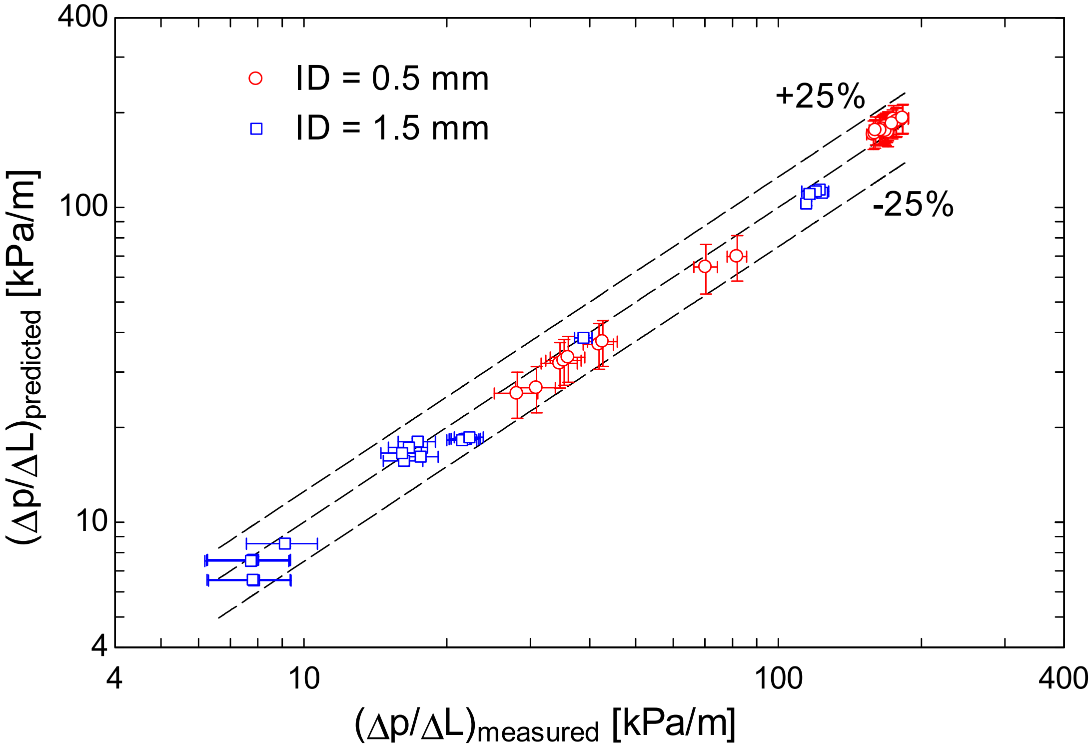

Figure 66. Measured vs predicted frictional pressure drop superheating vapor region (single phase)

3. MIXTURES CHARACTERIZATION AND PROPERTIES

3.1. Mixtures

The refrigerants of interest in this study are zeotropic mixtures that experience a temperature change in the two-phase region when the evaporating pressure is kept constant. The temperature difference between the bubble and the dew points is known as the *temperature glide*. Two-phase condition is maintained over a temperature range or glide of more than 80 K. The evaporating pressure considered corresponds to bubble and dew point temperatures located on the range from 100 K to room temperature.

All of the refrigerants analyzed are multicomponent mixtures, consisting of two, three, four, and five components. The components and composition of the mixtures tested in the present study have been chosen for their applicability to Joule-Thomson refrigeration systems used in cryoprobe applications where cooling power is required in the range of 150 to 200 K. Specifically, the components in the mixture were selected based on their saturation temperatures because of the temperature glide they exhibit in the desired region. To enable optimizing the overall cycle efficiency, the selected compositions must have a temperature glide between room temperature and the temperature at which cooling power is needed. The net result is that two-phase flow will exist on both sides of the regenerative heat exchanger in order to increase the regenerative heat exchanger effectiveness and the efficiency of the refrigeration cycle.

Five different zeotropic mixtures have been tested. Hydrocarbon mixtures have shown good performance when they are used in Joule-Thomson refrigeration systems. Three specific zeotropic mixtures formed by hydrocarbons have been tested. The first is a “binary” mixture with a molar composition of 40% methane and 60% ethane. No dilution is attempted for the binary mixture. The second is a ternary hydrocarbon mixture composed of methane, ethane, and propane with mole fractions of 45%, 35%, and 20%, respectively. Finally, a quaternary mixture is formed when the hydrocarbon mixture is diluted (in-situ) using nitrogen (20% and 40%).

Although there are some experience using hydrocarbon refrigerants as working fluids in refrigeration equipment in Europe, this class of refrigerants (in a pure component or as a mixture) have received limited approval in the U.S. through the Environmental Protection Agency, Significant New Alternatives Policy [42]. As a result, we also considered synthetic refrigerant mixtures to be relevant for Joule-Thomson refrigeration systems that intended for use in the U.S. The mixtures include R-14, R-23, R-32, and R-134a with molar composition of 35%, 15%, 15%, and 35%, respectively. In addition, a five component mixture is formed when dilutions with argon are performed. Diluted synthetic mixtures are formed, in situ, by adding 20% and 40% of argon to the synthetic refrigerant mixture.

3.2. Thermodynamic and Transport properties

During the measurement of the heat transfer coefficient and the frictional pressure drop of the tested zeotropic mixtures, the actual composition of the mixture is periodically quantitated using a gas chromatograph. Knowing the temperature, pressure, and composition fixes the state and makes it possible to determine all of the thermodynamic and transport properties for the mixture, including the vapor-liquid fraction (quality). Also, the equilibrium compositions of the vapor and liquid can be determined. REFPROP [25] is used as a tool to calculate these properties.

It is important to note that in the case of the synthetic refrigerant mixture, REFPROP does not provide mixing parameters for all of the binary pairs that participate in the mixture; consequently, the estimation of properties may be less accurate than it is for hydrocarbon mixtures. For the synthetic refrigerant mixture formed by R-14, R-23, R-32 and R-134a, there are mixing data for only three of the six binary pairs involved. When the synthetic refrigerant mixture is diluted with argon, the estimation of properties may be even less accurate because there are no mixing parameters available for any binary pair involving argon and any of the components of the synthetic refrigerant mixture. Also, the available thermodynamic data for the synthetic refrigerant mixture suggests that boiling is experienced at constant temperature at low thermodynamic qualities between *x*=0 and *x*=0.3; therefore, no data is reported in this range of quality for synthetic mixtures.

Table 11 shows the average properties of the liquid and vapor for the hydrocarbon and synthetic mixtures at the two evaporating pressure tested.

Table 11. Average values for thermodynamic and transport properties

	Mixtures				
	Hydrocarbons		**Synthetic**		
	P = 270 kPa	*790 kPa*	*270 kPa*	*790 kPa*	
Liquid fraction					
Cp (J/kg-K)	2279	2420	1287	1339	$\propto P^{0.05}$
μ (μPa-s)	228.6	156.7	414.3	274.5	$\propto P^{-0.37}$
k (W/m-K)	0.1613	0.1413	0.1180	0.1036	$\propto P^{-0.12}$
ρ (kg/m^3)	580.5	542.8	1390	1305	$\propto P^{-0.06}$
Vapor fraction					
Cp (J/kg-K)	1901	2045	657.3	743.2	$\propto P^{0.09}$
μ (μPa-s)	6.631	7.532	12.15	13.56	$\propto P^{0.11}$
k (W/m-K)	0.01641	0.01948	0.01051	0.01278	$\propto P^{0.17}$
ρ (kg/m^3)	3.725	10.20	12.39	34.40	$\propto P^{0.95}$

Liquid viscosity and vapor density seem to be the properties that are more affected because of evaporating pressure variations. The liquid viscosity is reduced as the evaporating pressure increases. Liquid viscosity varies inversely proportional to the 0.4 power of the evaporating pressure. The variation of the vapor density is more significant as a function of pressure. The vapor density is proportional to the evaporating pressure.

3.3. Joule-Thomson effect verification

A verification of the Joule-Thomson effect predicted by REFPROP is performed. The Joule-Thomson effect is the variation of temperature as a function of pressure drop in adiabatic condition, $\left(\frac{\partial T}{\partial P}\right)_h$, and it is verified for each base mixture. Figure 67 shows the schematic of the measurement.

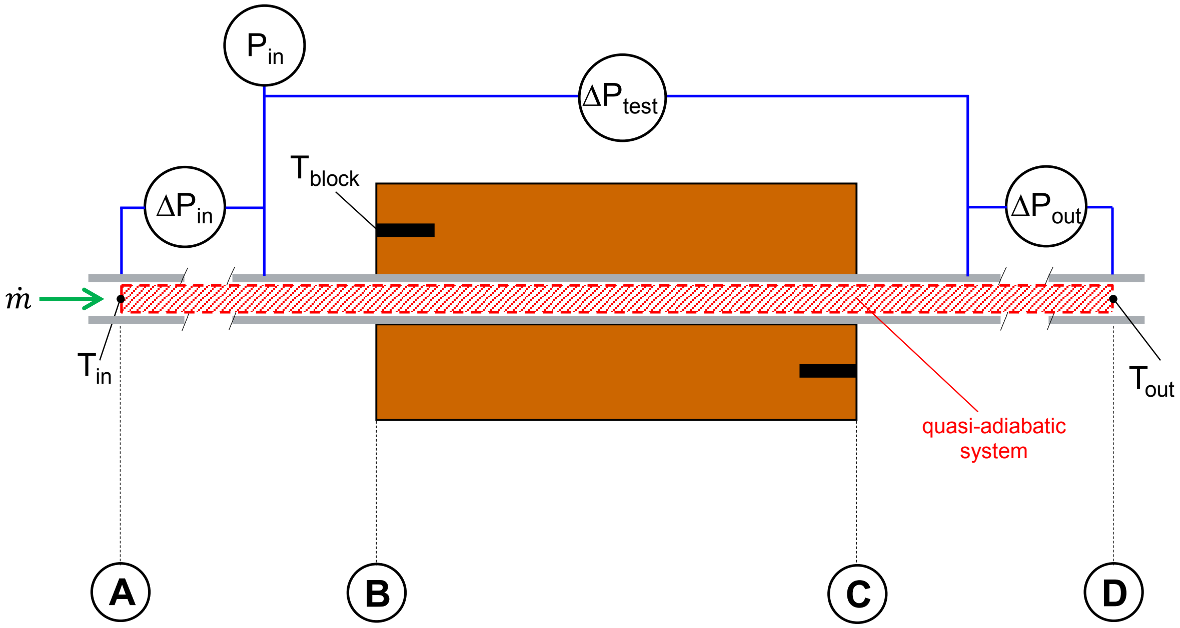

Figure 67. Schematic of measurement of Joule Thomson effect

At steady state conditions, the inlet (T_A) and outlet (T_D) temperatures and the pressure drop between these locations are measured. No heat is applied to the test section. $\left(\frac{\partial T}{\partial P}\right)_h$ is approximated using Eq. (89):

$$\left(\frac{\partial T}{\partial P}\right)_h \left(T_{avg}\right) = \frac{T_A - T_D}{\Delta P_{in} + \Delta P_{test} + \Delta P_{out}} \tag{89}$$

Figure 68 to Figure 71 show the comparison between the measured and predicted $\left(\frac{\partial T}{\partial P}\right)_h$. The prediction was made using REFPROP.

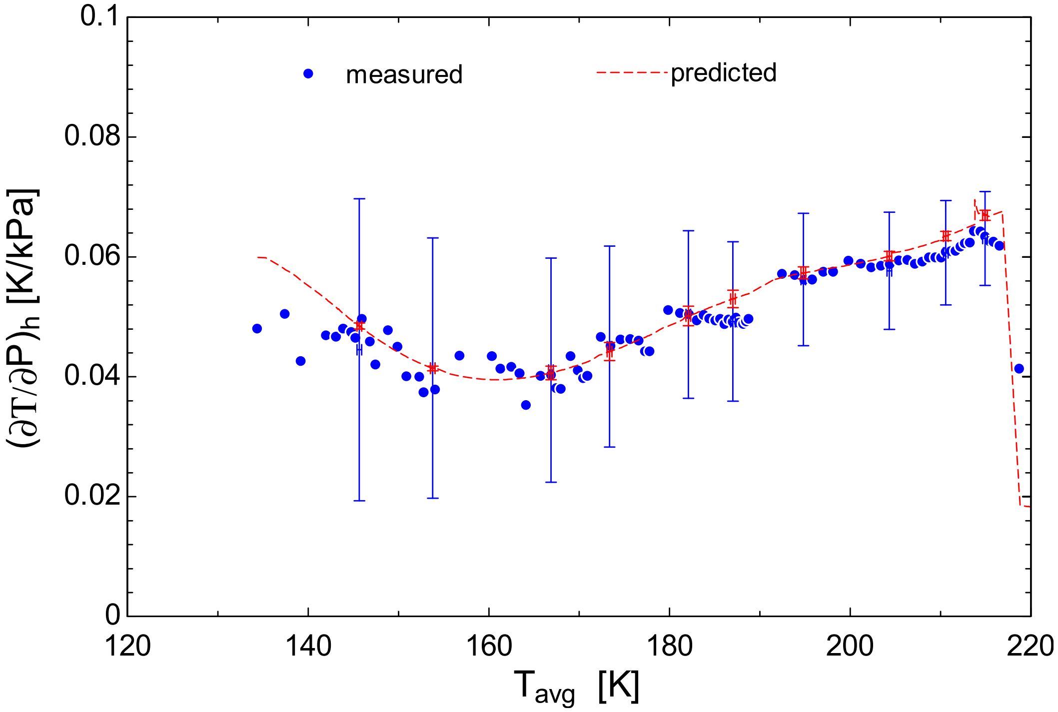

Figure 68. Measured and predicted Joule-Thomson effect as a function of average temperature, hydrocarbon mixture 45% CH4, 35% C2H6, 20% C3H8 at P=270 kPa

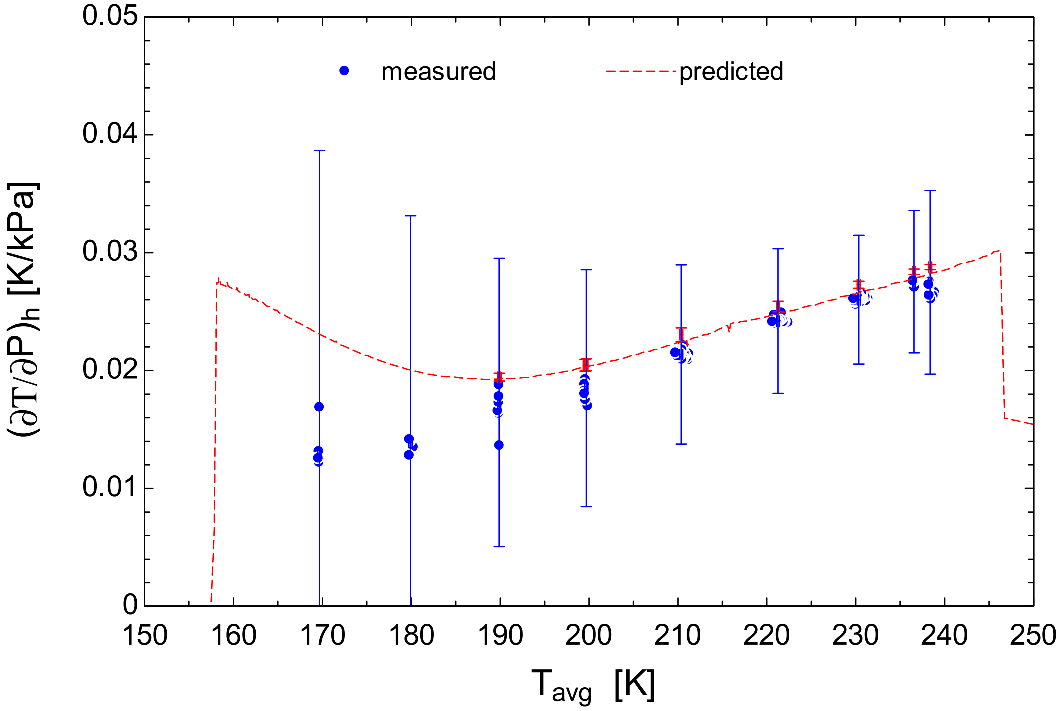

Figure 69. Measured and predicted Joule-Thomson effect as a function of average temperature, hydrocarbon mixture 45% CH_4, 35% C_2H_6, 20% C_3H_8 at *P*=790 kPa

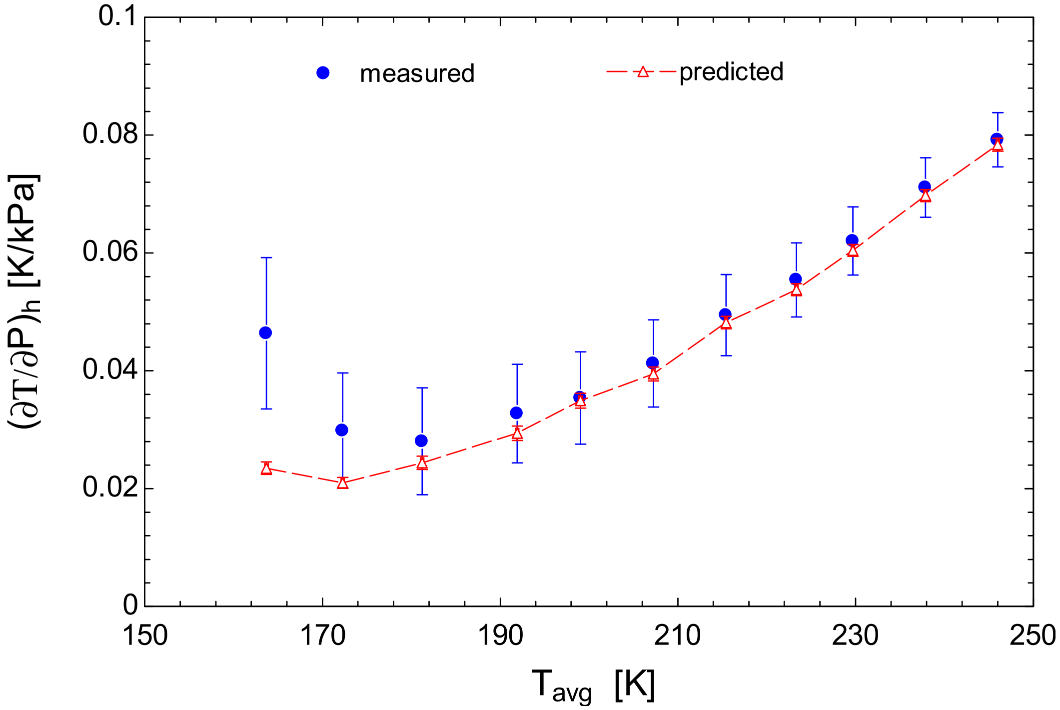

Figure 70. Measured and predicted Joule-Thomson effect as a function of average temperature, Synthetic refrigerant mixture 35% R-14, 15% R-23, 15% R-32 and 35% R-134a at *P*=270 kPa

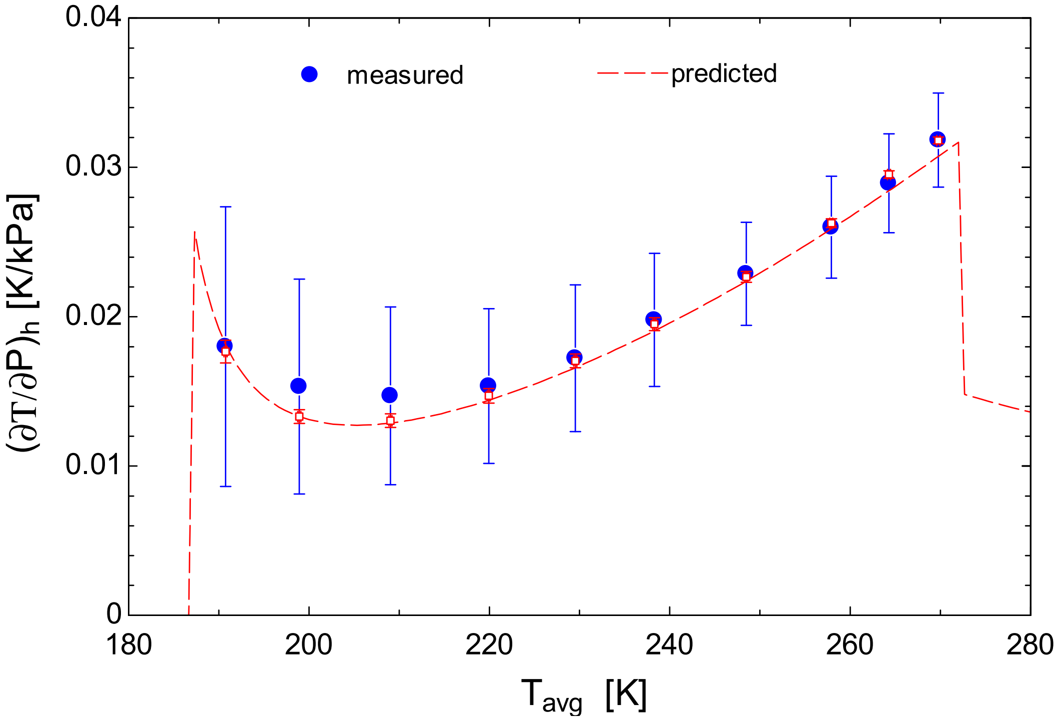

Figure 71. Measured and predicted Joule-Thomson effect as a function of average temperature, Synthetic refrigerant mixture 35% R-14, 15% R-23, 15% R-32 and 35% R-134a at P=790 kPa

The measured and predicted (using REFPROP) value for the Joule Thomson effects have a good agreement. It is observed that the error bar increases when temperature decreases because as the mixture quality is diminished the pressure drop decreases; consequently, the variation of temperature decreases up to approach a similar magnitude than the uncertainty of the temperature measurement.

3.4. Enthalpy verification

REFPROP predicted properties also may be verified by comparing the measurement of the heat absorbed by the fluid and the prediction using enthalpy difference according to the temperature and pressure measured at the inlet and outlet conditions. The temperature measurements in the inlet and outlet of the test section using the specific heat or the enthalpies lead to the heat absorbed by the fluid definition shown in Eq. (90).

$$\dot{Q}_{fluid} = \dot{m}\,Cp\left(T_{out} - T_{in}\right) = \dot{m}\left(h_{out} - h_{in}\right) \tag{90}$$

The heat absorbed by the fluid may be also obtained using the energy balance on the test section. The energy balance takes into account the heat load applied minus the heat losses because of radiation and conduction.

$$\dot{Q}_{fluid} = \dot{Q}_{applied} - \dot{Q}_{radiation} - \dot{Q}_{condution} \tag{91}$$

Figure 72 through to Figure 75 show the heat absorbed by the fluid calculated using an energy balance and the enthalpy difference obtained using REFPROP as a function of the average temperature.

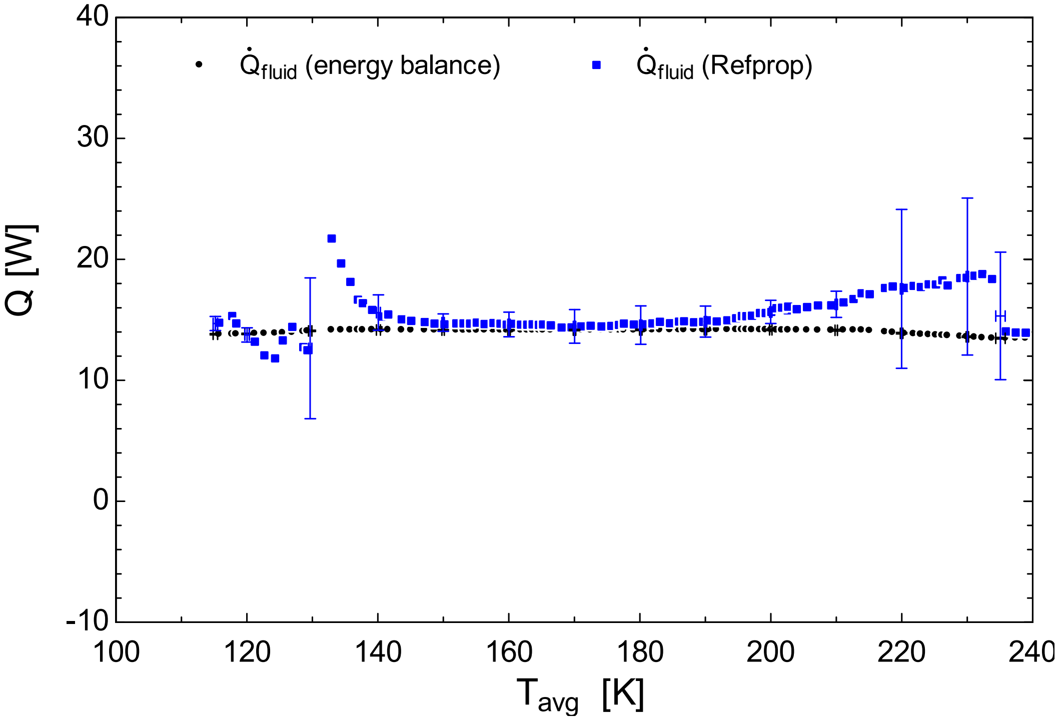

Figure 72. Heat absorbed by the fluid calculated using an energy balance and the enthalpy difference obtained using REFPROP as a function of the average temperature, hydrocarbon mixture 45% CH_4, 35% C_2H_6, 20% C_3H_8 at *P*=270 kPa, $\dot{Q}''$ =56 kW/m^2, *G* = 144 kg/m^2-s, and *ID* = 1.5 mm

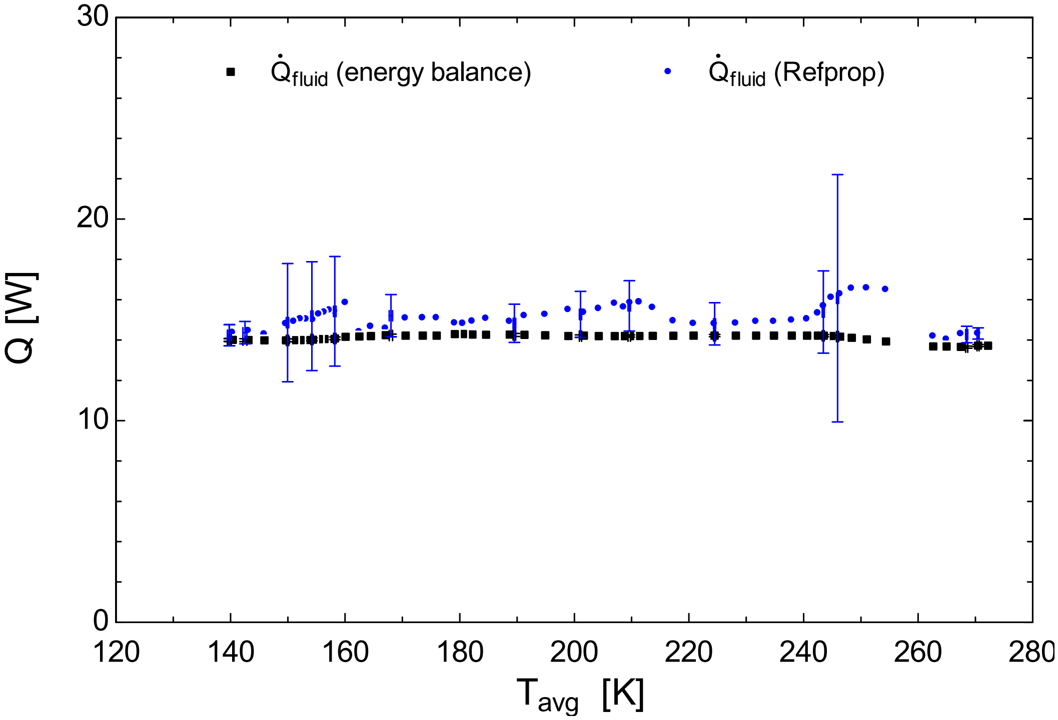

Figure 73. Heat absorbed by the fluid calculated using an energy balance and the enthalpy difference obtained using REFPROP as a function of the average temperature, hydrocarbon mixture 45% CH_4, 35% C_2H_6, 20% C_3H_8 at *P*=790 kPa, $\dot{Q}''$ =56 kW/m^2, *G* = 144 kg/m^2-s, and *ID* = 1.5 mm

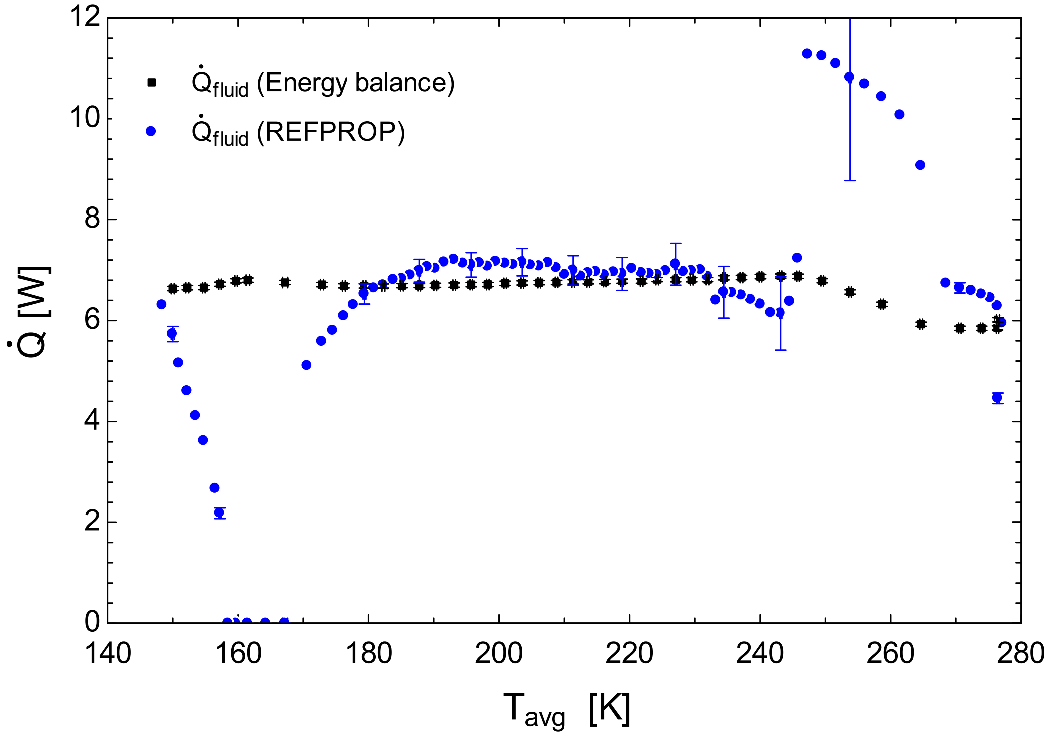

Figure 74. Heat absorbed by the fluid calculated using an energy balance and the enthalpy difference obtained using REFPROP as a function of the average temperature, synthetic mixture 35% R-14, 15% R-23, 15% R-32, 35% R-134a at *P*=270 kPa, $\dot{Q}''$ =56 kW/m^2, *G* = 144 kg/m^2-s, and *ID* = 1.5 mm

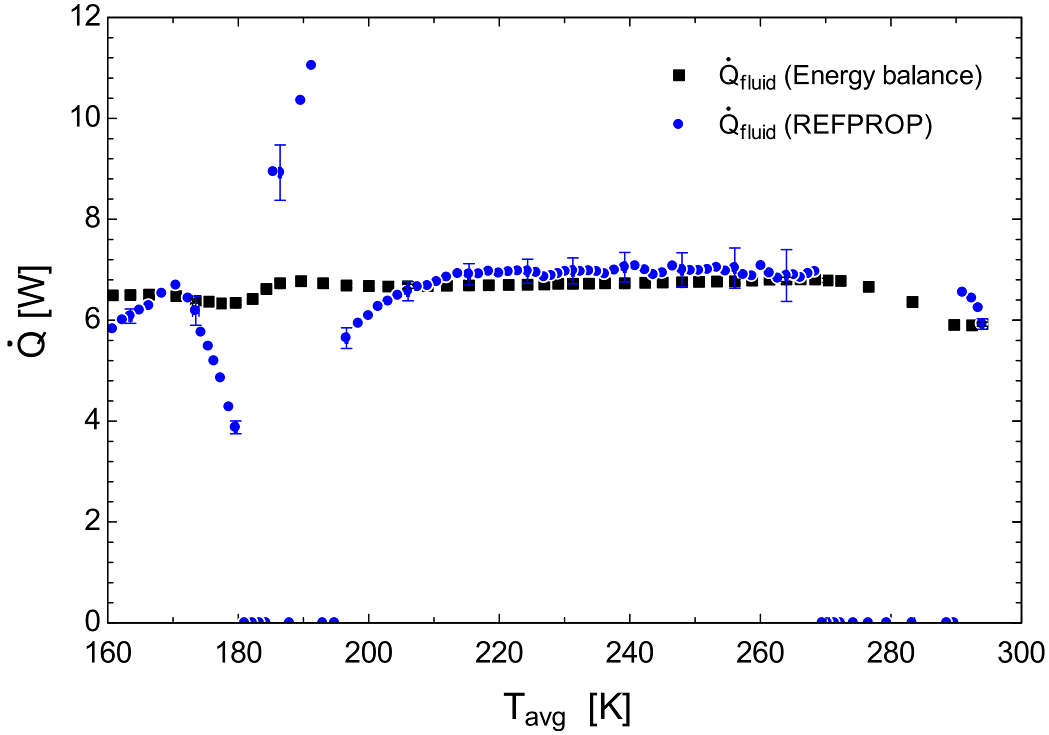

Figure 75. Heat absorbed by the fluid calculated using an energy balance and the enthalpy difference obtained using REFPROP as a function of the average temperature, synthetic mixture 35% R-14, 15% R-23, 15% R-32, 35% R-134a at *P*=790 kPa, $\dot{Q}''$ =56 kW/m^2, *G* = 144 kg/m^2-s, and *ID* = 1.5 mm

In general, both methods show a good agreement. There are some differences when the quality is low approaching to zero and also when it is high close to 1 for the hydrocarbon mixtures. The problem in the edges is more dramatically in the case of synthetic refrigerant mixtures. It is not clear if the observed difference occurs because of a problem with the thermodynamic properties or errors in the composition at these boundaries.

3.5. Tube or channel size

Experimental data were collected using three separate horizontal test sections having an inner diameter of 0.5, 1.5 and 3.0 mm. Some authors have claimed as the test section dimensions impacting the behavior of the flow. A fluid flowing in a mini-channel that experiences two-phase conditions may behave differently than if the same fluid flows in a large or conventional channel. As the diameter is reduced, surface tension can become a dominant effect because the diameter can approach the bubble size, obstructing the free bubble circulation and changing the flow profile. As Cheng and Mewes [11] described, there is not a consensus regarding the limit between conventional and mini-channel flow. Shah [43] and Mehendale et al. [44] propose a diameter of 6 mm as the boundary; on the other hand, Kandlikar [45] suggests the limit is 3 mm. Some authors relate the limit to dimensionless numbers such as the Laplace (*La*), Bond (*Bo*) and Eötvös (*Eo*) numbers. Triplett et al. [46] define the limit to be when the Laplace number equals unity. Brauner and Moalem-Maron [47] proposed the limit as a function of the Eötvös number ($Eo = (2\pi)^2$). Kew and Cornwell [48] also use Eötvös number, but set it equal to 4 ($Eo \le 4$). The Eötvös number is also known as the Bond (*Bo*) number and is defined in Eq. (92). The Eötvös number can be related to one over the Laplace number squared.

$$\ddot{E}o = \frac{D_H^{\ 2} g\left(\rho_l - \rho_v\right)}{\sigma} = 4\,Bo = La^{-2} \tag{92}$$

Figure 76 shows the hydraulic diameter (D_H) that defines the boundary between conventional channel and mini-channel for the mixtures studied here as a function of average quality according to the Triplett et al. [46] definition. This criterion produces the transition at the smaller diameter. All the other criteria indicate that the mixture tested should behave as a mini-channel flow in the tested sections. The Triplett et al. [46] definition suggests that synthetic mixtures may behave as a conventional channel in the 1.5 mm test sections and as a mini-channel in the 0.5 mm test section.

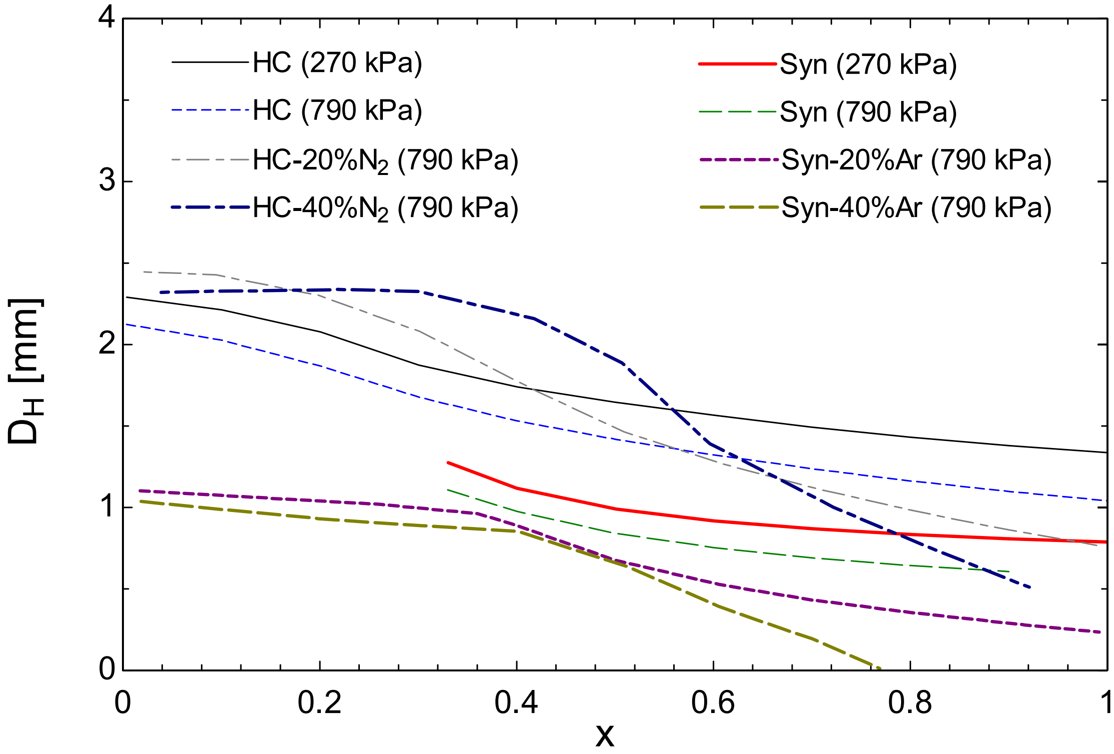

Figure 76. Hydraulic diameter (D_H) that limits between conventional channel and mini-channel according to Triplett et al.[46] as a function of average quality for the tested mixtures

The hydrocarbon mixture might experience the transition between the 3.0 and the 1.5 mm test sections. Also, it is observed that according to Triplett et al. [46] definition, the limit seems to be a function of the thermodynamic quality decaying as the quality increases.

4. TEST PROCEDURE AND SAMPLE RESULTS

4.1. Test procedure

A detail procedure about how the test facility is operated is presented by Schwartz [49]. The test facility shown in Figure 1 is charged with the desired gas mixture. The test pressure and flow are controlled by manipulating the arrangement of throttle valves, pressure regulator, and a bypass loop setting the required mass flux (G), evaporating pressure at the inlet of the test section. The measurements can be made during either cooling or warming the system. If the test is performed cooling the system, the cryocooler starts and high power is applied through the cartridge heaters (i.e., trim heaters) to slowly reduce the temperature of the gas mixture that is supplies to the test section. The set heat flux ($\dot{Q}''$) is applied to the test section. Measurements of the heat transfer coefficient and pressure drop are carried out with a constant mass flux (G), pressure, and heat flux ($\dot{Q}''$), and initial charged composition.

An individual test starts at a temperature that is 10 K above the dew temperature of the mixture. Figure 77 shows the inlet, outlet and wall temperature during the test where the system is slowly cooled. The mixture is in a superheated vapor state throughout the entire system. The power applied to the trim heaters is then gradually reduced causing the measured inlet temperature (T_A) of the test section to slowly decrease. The rate of temperature change is controlled in order to maintain a quasi-steady state condition in the test section for all measurements. Steady state is defined as a condition where the rate of change in the internal energy associated with the heat capacity of the test section is less than 2% of the heat applied to the test section (eq. (93)):

$$\frac{m_{copper}\, c_{copper} \dfrac{\partial T}{\partial t}}{\dot{Q}_{applied}} \le 2\% \tag{93}$$

As the test progresses, the system is cooled, and the fluid reaches the two-phase zone. As the thermodynamic quality of the mixture decreases and approaches to the liquid region, the pressure of system within the experimental test facility tends to decrease because of the lower specific volume. A make-up tank, which is initially filled with the same mixture used to charge the experimental facility, is used to maintain the system pressure constant throughout the test. The test is completed when subcooled liquid is present in both sides of the test section. In general, a test condition experiences temperatures between 150 K and room temperature.

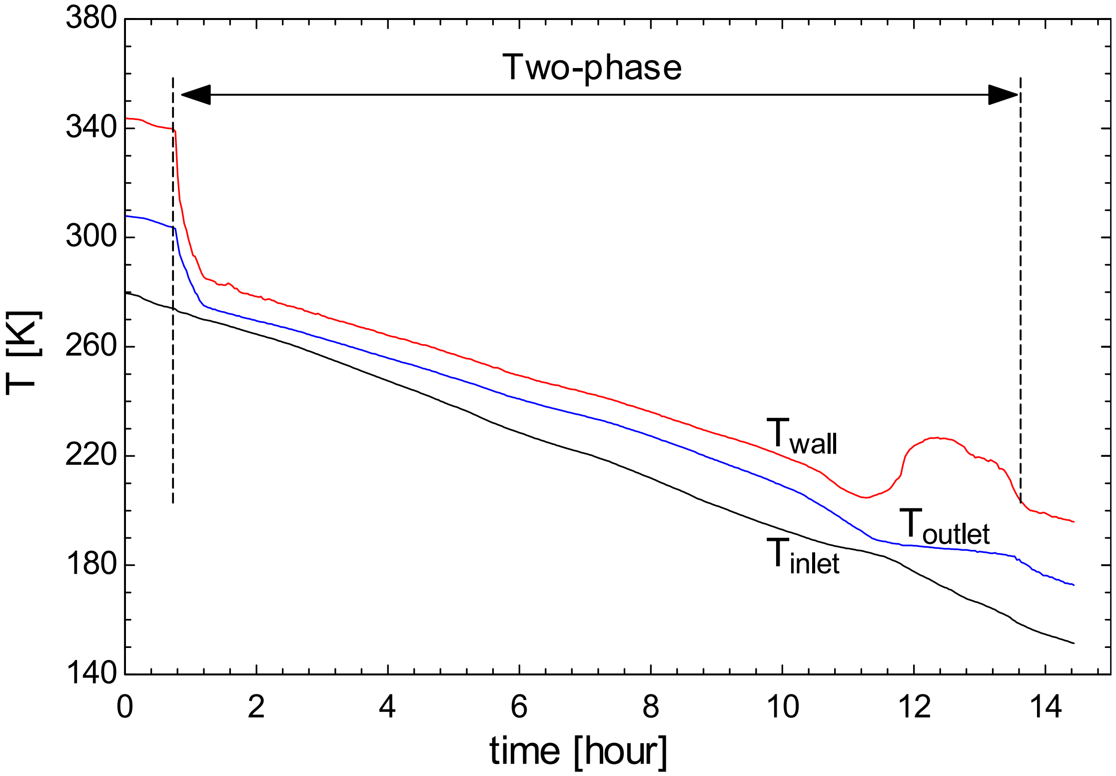

Figure 77. Typical temperatures profile as a function of time for a zeotropic gas mixture during test

The mixture composition is defined, initially, by the charge composition at room temperature. The circulating mixture composition is continuously monitored using a gas chromatograph equipped with a thermal conductivity detector by sampling the gas mixture at room temperature from either the low or the high pressure sides of the system. As the mixture reaches the two-phase region, some of the components of the mixture will preferentially condense, changing the circulating mixture composition, as shown in Figure 78. The composition of the mixture is measured at least every 20 K of variation the inlet temperature.

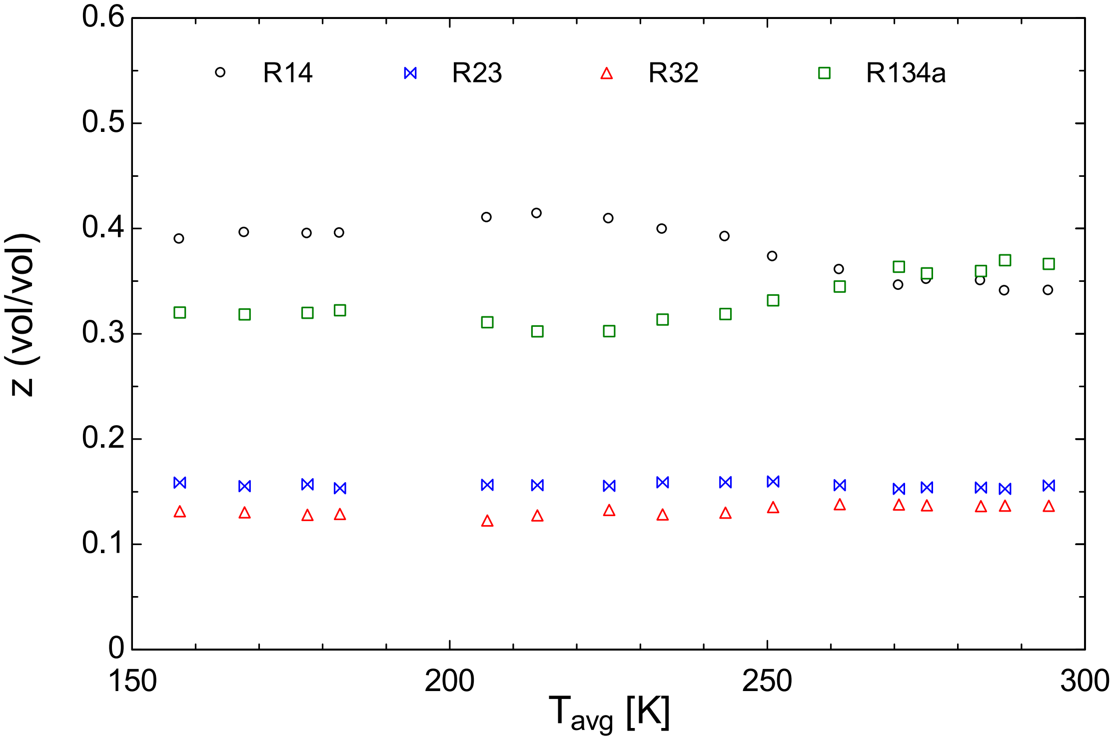

Figure 78. Mixture composition as a function of average temperature in the test section

4.2. Sample Results

Samples of the heat transfer coefficient and pressure drop results that can be obtained using the experimental facility described in this study are presented in Figure 79 and Figure 80, respectively. A mixture composed by methane, ethane and propane (45%, 35% and 20% by volume) was tested. In a horizontal test section with a diameter of 1.5 mm, pressure (270 kPa), heat flux (56 kW/m^2) and mass flux (240 kg/m^2-s) were kept constant. The temperature glide for the mixture that tested is between 135 and 222 K. The error bars show an uncertainty around 5% for the condition shown in Figure 79 for the heat transfer coefficient. The frictional pressure drop uncertainty decreases as the average temperature and quality increase. The uncertainty in the pressure drop is around 10% for most of the data.

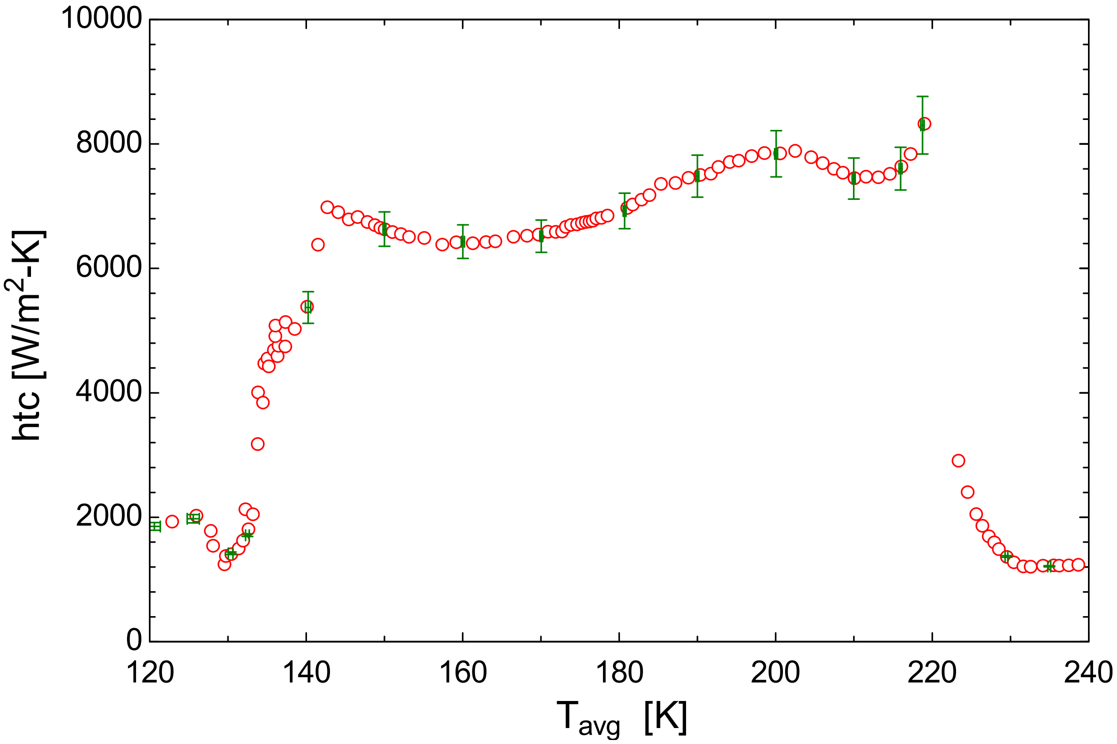

Figure 79. Heat transfer coefficient as a function of average temperature for $CH_4/C_2H_6/C_3H_8$ mixture (45%/35%/20% by volume) with P = 270 kPa, Q'' = 56 kW/m^2 and G = 240 kg/m^2-s.

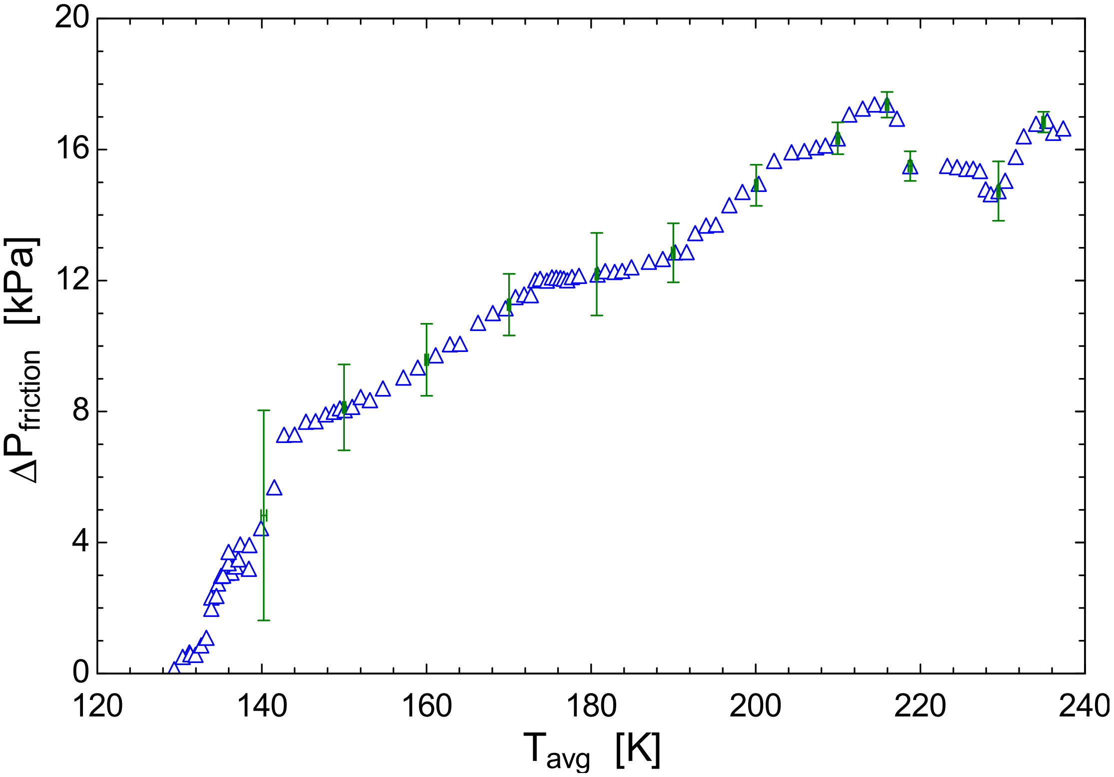

Figure 80. Friction pressure drop as a function of average temperature for $CH_4/C_2H_6/C_3H_8$ mixture (45%/35%/20% by volume) with *P* = 270 kPa, *Q"* = 56 kW/m^2 and *G* = 240 kg/m^2-s.

5. HEAT TRANSFER COEFFICIENTS

5.1. Literature review

One of the constraints that limits designers from evaluating the effects of the heat transfer processes on cycle performance as part of an optimization process is the lack of heat transfer data as well as models that can reliably predict heat transfer coefficients in small diameter horizontal tubes where multi-component, multi-phase, non-adiabatic zeotropic mixtures with very large temperature glides are operating at cryogenic temperatures. Nellis et al. [30] provides data for the local heat transfer coefficient during boiling of nitrogen-hydrocarbon gas mixtures over a range of composition, temperatures, mass fluxes, and pressures. According to their results, the heat transfer coefficient for mixtures under single-phase conditions is well predicted by standard correlations for single-phase flow as Dittus-Boelter. Also, they observe a minimal effect on the heat transfer coefficient due to composition and pressure, and a substantial effect related to the mass flux. Other authors such as Boiarski et al. [17], Gong et al [50], and Ardhapurkar et al. [51] have reported measurements of the overall heat transfer coefficient for a heat exchanger operating with mixtures at cryogenic temperatures. However, these data have limited utility because the overall heat transfer coefficient data cannot be extrapolated to other systems with system geometries differing from those which the data were obtained.

No other studies were found that provide experimental data for heat transfer coefficients with the number of components and the range of temperatures provided in this research. There are some studies that provide limited data for ternary mixtures, e.g., Zhang et al. [52], but the temperature glide of the studied mixtures are less than 10 K. In general, the existing empirical data are focused on measurements of the heat transfer coefficient for boiling of binary mixtures operating at near room temperature conditions with small temperature glides. Even though these data are not directly related to the present study, the heat transfer coefficient data obtained for binary mixtures are relevant because they provide an understanding of the heat transfer behavior of two-phase mixtures. Several studies in binary mixtures have shown that mixture behave differently than pure fluids while they undergo a phase change. Stephan [53] indicates that heat transfer coefficients for mixtures can be lower than those of pure fluids at the same flow conditions. The deterioration of the heat transfer coefficients is explained because the difference in composition of the liquid and vapor causes mass transfer that inhibits heat transfer [54]. The experimental work performed by Jung et al. [13] suggests a suppression of nucleate boiling for pure and mixed refrigerants; measured heat transfer coefficients for mixtures in this region are as much as 36% lower than the pure fluid values under the same flow condition. Sardesai et al. [55] explained that the mixture affects nucleate boiling because diffusion of constituents adds a thermal resistance; thereby, degrading the heat transfer coefficient. This degradation effect is substantially reduced in the convection-dominated region. Another reason for the variation in heat transfer coefficients of mixtures is due to the nonlinear and strong variation in thermodynamic and transport properties with composition and temperature. Shin et al. [56] concluded that heat transfer coefficients depend strongly on heat flux in the low quality region and become independent of heat flux as quality increases. The pool boiling heat transfer coefficient in the binary mixture of ammonia/water was studied by Inoue [57]. Inoue states that known heat transfer coefficient models are not capable of accurately predicting his experimental data. Also, Inoue shows that the heat transfer coefficients in ammonia/water mixtures become dramatically smaller than those expected for either of the pure component.

The boiling process that occurs as a fluid flows through a horizontal tube is complicated, even for a pure fluid. Steiner and Taborek [58] claims that different flow regimes drive different heat transfer coefficients during boiling. Collier and Thome [59] describe a typical flow boiling process in a horizontal tube, including the flow regimes that the fluid experiences during evaporation. As sub-cooled liquid flows through a tube while heat is applied at the tube wall, the liquid is heated and its temperature increases until it reaches its saturation temperature condition ($x=0$). As evaporation proceeds, the flow may experience different regimes or patterns including bubbly flow, plug flow, slug flow, stratified-wavy flow, annular flow and partial dry out before reaching a saturated vapor state ($x=1$). There are two phenomena that may drive boiling: nucleate and convective boiling. Nucleate boiling occurs at the wall-liquid interphase and, in general, it is the phenomenon that dominates at low qualities. The vapor bubbles produced by nucleation tend to accumulate in the center of the tube, occupying a significant proportion of the cross sectional area of the due to the large specific volume of the vapor even at low quality. This situation increases the liquid velocity and forces to the liquid to flow near the walls (annular flow) forming a thin layer which continues to evaporate due to nucleation. At the liquid vapor interface, the convective boiling process carries out the evaporation, and dominates the boiling process at higher qualities. When the quality is high, the liquid film may dry out at the top of the tube due to gravity force. Also, as the liquid film thins, it is eventually unable to wet the entire perimeter. When the tube diameter is reduced below 3 mm, some different behaviors are expected. First, the literature calls tubes with diameters between 0.2 and 3.0 mm minichannels [45]. In minichannels, the effect of surface tension is more relevant, affecting the flow regimes. According to Kandlikar [45], the dominant flow patterns in small channels are isolated bubbles, confined bubbles, and annular-slug. Consequently, the size of tubes is another relevant parameter to study.

The boiling heat transfer coefficient for a pure fluid depends on the mass flux, heat flux, thermodynamic quality, fluid properties, flow pattern, tube size, geometry and inclination. In the case of zeotropic mixtures, the heat transfer coefficients may also be influenced by the concentrations between the liquid and vapor fractions.

5.2. Test conditions

The first mixture is a hydrocarbon mixture composed of methane, ethane, and propane with a molar fraction of 45%, 35%, and 20%, respectively. The hydrocarbon mixture was premixed by a supplier. Table 12 shows the test conditions selected for the hydrocarbon mixtures. The test conditions are defined to study the effects of the change of mass flux (G), heat flux ($\dot{Q}''$), pressure (P), diameter (ID) and composition on the heat transfer coefficient. For example, the effect of mass flux is examined by measuring the heat transfer coefficients for two different mass fluxes with all of the other test conditions maintained constant. The effect of changing the composition is tested by diluting the hydrocarbon mixture with in-situ dilution using nitrogen (20% and 40%). The observed temperature glide of the hydrocarbon mixture is approximately 85 K and 130 K for the mixtures with dilutions.

Table 12. Hydrocarbon mixture, composition and test conditions

Run	Mixture	Composition (by volume)	*P* *kPa*	*G* $kg/s\text{-}m^2$	$\dot{Q}''$ kW/m^2	*ID* *mm*	T_{bubble} *K*	T_{dew} *K*
1	$CH_4/C_2H_6/C_3H_8$	0.45/0.35/0.20	787±3	143±12	56.5±1.4	0.5	160	246
2	$CH_4/C_2H_6/C_3H_8$	0.45/0.35/0.20	787±3	155±12	86.3±1.7	0.5	160	246
3	$CH_4/C_2H_6/C_3H_8/N_2$	0.36/0.28/0.16/0.20	788±3	145±12	56.6±1.4	0.5	105	240
4	$CH_4/C_2H_6/C_3H_8/N_2$	0.27/0.21/0.12/0.40	786±3	145±12	56.6±1.4	0.5	103	232
5	$CH_4/C_2H_6/C_3H_8$	0.45/0.35/0.20	270±3	139±1	59.8±0.2	1.5*	135	221
6	$CH_4/C_2H_6/C_3H_8$	0.45/0.35/0.20	269±3	138±1	89.5±0.3	1.5*	135	221
7	$CH_4/C_2H_6/C_3H_8$	0.45/0.35/0.20	269±3	144±1	57.0±0.2	1.5	135	221
8	$CH_4/C_2H_6/C_3H_8$	0.45/0.35/0.20	265±3	239±2	56.7±0.2	1.5	135	221
9	$CH_4/C_2H_6/C_3H_8$	0.45/0.35/0.20	785±3	143±1	56.9±0.2	1.5	160	246
10	$CH_4/C_2H_6/C_3H_8/N_2$	0.36/0.28/0.16/0.20	787±3	143±1	56.5±0.2	1.5	105	240
11	$CH_4/C_2H_6/C_3H_8/N_2$	0.27/0.21/0.12/0.40	786±3	143±1	56.8±0.2	1.5	103	232
12	$CH_4/C_2H_6/C_3H_8$	0.45/0.35/0.20	791±3	147±1	40.0±0.1	3.0	160	246
13	$CH_4/C_2H_6/C_3H_8$	0.45/0.35/0.20	790±3	146±1	55.7±0.1	3.0	160	246
14	$CH_4/C_2H_6/C_3H_8/N_2$	0.36/0.28/0.16/0.20	791±3	147±1	57.7±0.1	3.0	105	240
15	$CH_4/C_2H_6/C_3H_8/N_2$	0.27/0.21/0.12/0.40	790±3	147±1	57.5±0.1	3.0	103	232

*Old test section, dimensions are shown in Table **8**

The second mixture measured included components of R-14, R-23, R-32, and R-134a. This mixture is referred to as the "synthetic refrigerant mixture." The molar composition was 35%, 15%, 15%, and 35% for R-14, R-23, R-32, and R-134a, respectively. The synthetic refrigerant mixture is prepared in situ. The dilution for testing the change of composition is made in situ by adding 20% and 40% of argon on the synthetic refrigerant mixture. The temperature glides of the synthetic mixture range from 89 K for no dilution to 116 K for 20% dilution and 132 K for 40% dilution. Table 13 shows the test conditions selected for the synthetic refrigerant mixture.

Table 13. Synthetic refrigerant mixture, composition and test conditions.

Run	Mixture	Composition (by volume)	P kPa	G $kg/s\text{-}m^2$	$\dot{Q}''$ kW/m^2	ID mm	T_{bubble} K	T_{dew} K
16	R-14/R-23/R-32/R-134a	0.35/0.15/0.15/0.35	789±3	145±12	27.8±1.0	0.5	186	275
17	R-14/R-23/R-32/R-134a	0.35/0.15/0.15/0.35	788±3	145±12	41.7±1.2	0.5	186	275
18	R-14/R-23/R-32/R-134a/Ar	0.28/0.12/0.12/0.28/0.20	788±3	144±12	27.8±1.0	0.5	153	268
19	R-14/R-23/R-32/R-134a/Ar	0.21/0.09/0.09/0.21/0.40	788±3	143±12	27.8±1.0	0.5	129	261
20	R-14/R-23/R-32/R-134a	0.35/0.15/0.15/0.35	271±3	145±1	27.8±0.2	1.5	159	248
21	R-14/R-23/R-32/R-134a	0.35/0.15/0.15/0.35	790±3	143±1	27.8±0.2	1.5	186	275
22	R-14/R-23/R-32/R-134a	0.35/0.15/0.15/0.35	790±3	144±1	41.8±0.2	1.5	186	275
23	R-14/R-23/R-32/R-134a	0.35/0.15/0.15/0.35	788±3	242±2	27.8±0.2	1.5	186	275
24	R-14/R-23/R-32/R-134a/Ar	0.28/0.12/0.12/0.28/0.20	789±3	144±1	27.8±0.2	1.5	153	268
25	R-14/R-23/R-32/R-134a/Ar	0.21/0.09/0.09/0.21/0.40	789±3	143±1	27.9±0.2	1.5	129	261
26	R-14/R-23/R-32/R-134a	0.35/0.15/0.15/0.35	788±3	148±1	18.8±0.1	3.0	186	275
27	R-14/R-23/R-32/R-134a	0.35/0.15/0.15/0.35	791±3	148±1	28.1±0.1	3.0	186	275
28	R-14/R-23/R-32/R-134a/Ar	0.28/0.12/0.12/0.28/0.20	788±3	147±1	28.2±0.1	3.0	153	268
29	R-14/R-23/R-32/R-134a/Ar	0.21/0.09/0.09/0.21/0.40	788±3	148±1	28.2±0.1	3.0	129	261

The hydrocarbon binary mixture (referred to as "binary"), has a molar composition of 40% methane and 60% ethane. The binary mixture is prepared in situ. The effects of the change of mass flux (G), heat flux ($\dot{Q}''$), evaporating pressure (P), diameter (ID) are tested for binary mixture, but the composition effect is not tested. The observed temperature glide for the binary mixture is 53 K. Table 14 shows the test conditions selected for the binary mixture.

Table 14. Binary mixture, composition and test conditions.

Run	Mixture	Composition (by volume)	P kPa	G kg/s-m^2	$\dot{Q}''$ kW/m^2	ID mm	T_{bubble} K	T_{dew} K
30	CH_4/C_2H_6	0.60/0.40	784±3	145±12	55.9±1.4	0.5	155	208
31	CH_4/C_2H_6	0.60/0.40	789±3	142±12	86.3±1.7	0.5	155	208
32	CH_4/C_2H_6	0.60/0.40	785±3	242±2	85.4±0.3	1.5	155	208
33	CH_4/C_2H_6	0.60/0.40	786±3	242±2	56.9±0.2	1.5	155	208
34	CH_4/C_2H_6	0.60/0.40	266±3	241±2	56.7±0.2	1.5	132	185
35	CH_4/C_2H_6	0.60/0.40	788±3	145±1	56.8±0.2	1.5	155	208
36	CH_4/C_2H_6	0.60/0.40	785±3	147±1	40.0±0.1	3.0	155	208
37	CH_4/C_2H_6	0.60/0.40	788±3	147±1	57.5±0.1	3.0	155	208

5.3. Experimental heat transfer coefficient

A large set of heat transfer coefficient data for boiling zeotropic mixtures with large temperature glides flowing in horizontal tubes of 0.5 mm, 1.5 mm and 3.0 mm diameters have been collected. These data are shown in Appendices B, C and D as plots of heat transfer coefficients as a function of average temperature and quality. Also, the detail data will be posted on http://sel.me.wisc.edu/publications-theses.shtml so that they can be accessed by researchers in future studies.

The measured heat transfer coefficients depend on the average condition (temperature and quality) between the inlet and the outlet of the test section. The inlet and outlet conditions may be thermodynamically close to one another, but they are different. When the average quality is low, the inlet condition may be subcooled liquid. Also, the outlet condition could be superheated vapor when the average quality is high. Consequently, it is considered two-phase data, the data collected when two-phase condition is observed simultaneously in the inlet and outlet of the test section. Most of the data that fulfills this criterion have an average thermodynamic quality between 10 and 90%.

The experimental Nusselt number is obtained by normalizing the measured heat transfer coefficient (*htc*) with the inner diameter (*ID*) of the corresponding test section and the thermal conductivity of the mixture (k_{mixt}) as shown in Eq. (94):

$$Nusselt_{exp} = \frac{htc\,ID}{k_{mixt}} \tag{94}$$

The Reynolds number of the mixture is defined according to:

$$Re = \frac{G\,ID}{\mu_{mixt}} \tag{95}$$

where G is the mass flux and μ_{mixt} is the viscosity of the mixture. The mixtures properties are defined as the liquid and vapor properties weight using the mass quality (x) contribution. Eqs (96), (97) and (98) show the viscosity, thermal conductivity and specific heat for the mixture:

$$\mu_{mixt} = \mu_l\, x + \mu_v \left(1 - x\right) \tag{96}$$

$$k_{mixt} = k_l\, x + k_v \left(1 - x\right) \tag{97}$$

$$Cp_{mixt} = Cp_l\, x + Cp_v \left(1 - x\right) \tag{98}$$

Figure 81 presents the experimental Nusselt number as a function of the average quality. It seems that for each mixture analyzed, the Nusselt number tends to increase with quality. The rate of increase of the heat Nusselt number may vary for different mixtures, but the positive relationship between Nusselt number and quality is still observed. Partial dry-out of the wall is expected to occur at higher thermodynamic qualities, reducing the heat transfer coefficient of the mixture. For some test conditions, partial dry-out is observed for average thermodynamic quality over 70%. In most of the cases, the partial dry-out occurs when the average quality is greater than 85%.

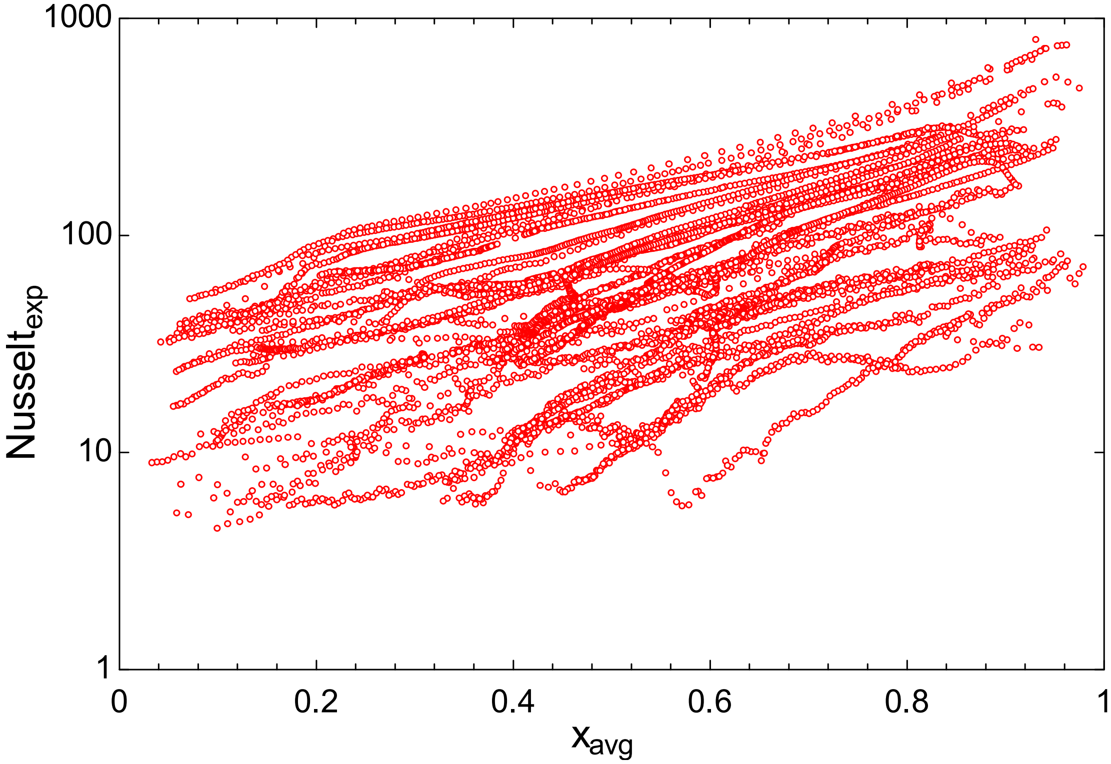

Figure 81. Experimental Nusselt number as a function of average quality.

Figure 82 presents the experimental Nusselt number as a function of the average Reynolds number of the mixture for all of the experimental data. As the Reynolds number increases, the experimental Nusselt number also rises. The experimental Nusselt number for zeotropic mixtures is clearly proportional to the average Reynolds number.

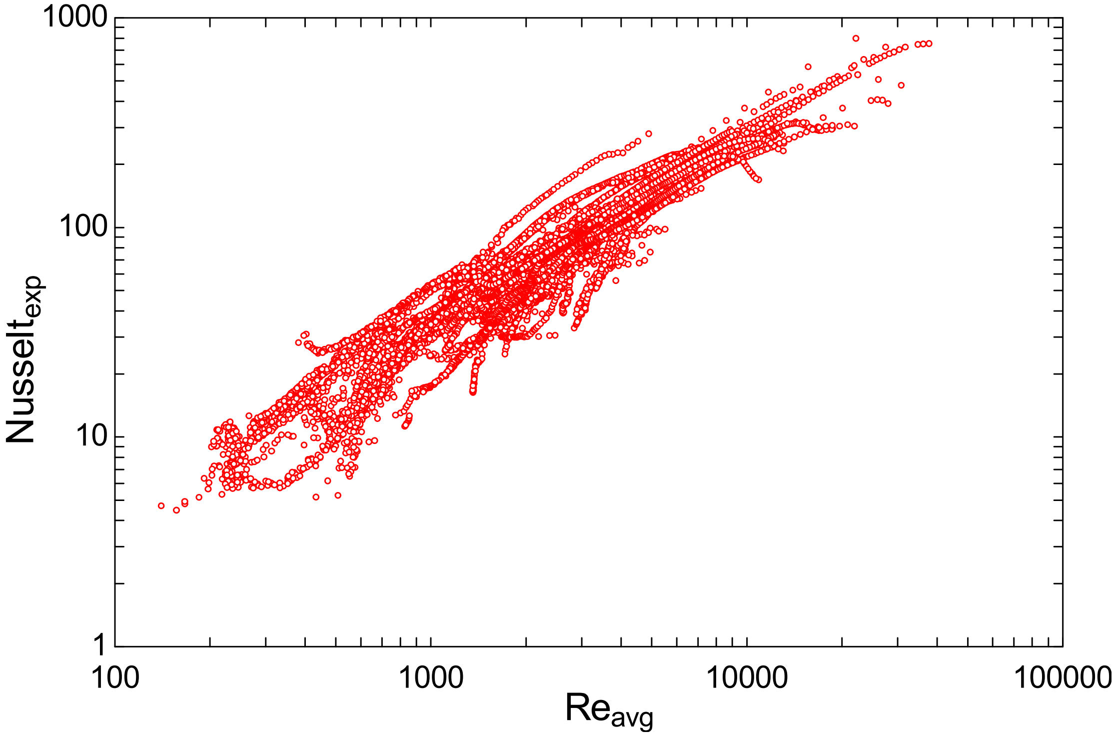

Figure 82. Experimental Nusselt number as a function of average Reynolds number.

5.3.1. Mass flux effects

Figure 83 to Figure 85 show the heat transfer coefficient data measured in the 1.5 mm test section for binary, hydrocarbon and synthetic refrigerant mixtures, respectively. The heat transfer coefficient is shown as a function of thermodynamic average quality where the quality is predicted using REFPROP. In order to illustrate the effect of mass flux (*G*), the data were collected for two different mass fluxes 144 and 240 kg/m^2-s, while the other conditions were kept constant.

The experimental data clearly show that increasing the mass flux tends to increase the heat transfer coefficients for the three mixtures analyzed. This result agrees with the observation made by Nellis et al. [30] for nitrogen-hydrocarbon mixtures at cryogenic conditions. The ratio between the measured heat transfer coefficient for the mass flux of 240 and 144 kg/s-m^2 is approximately 1.5, which is similar to the ratio predicted for turbulent flow using the Dittus and Boelter [26] correlation evaluated at these two flow conditions, as shown in eq. (99). Certainly, the flow velocity increases as the mass flux goes up enhancing the convective boiling.

$$\left(\frac{htc_{G=240}}{htc_{G=144}}\right)_{measured} = \left(\frac{Re_{G=240}}{Re_{G=144}}\right)^{0.8} \approx 1.5 \tag{99}$$

In regions with low thermodynamic quality, behavior that could be attributed to nucleate boiling is not observed even though it is understood that nucleate boiling could be the dominant mechanism, at least for conventional channels.

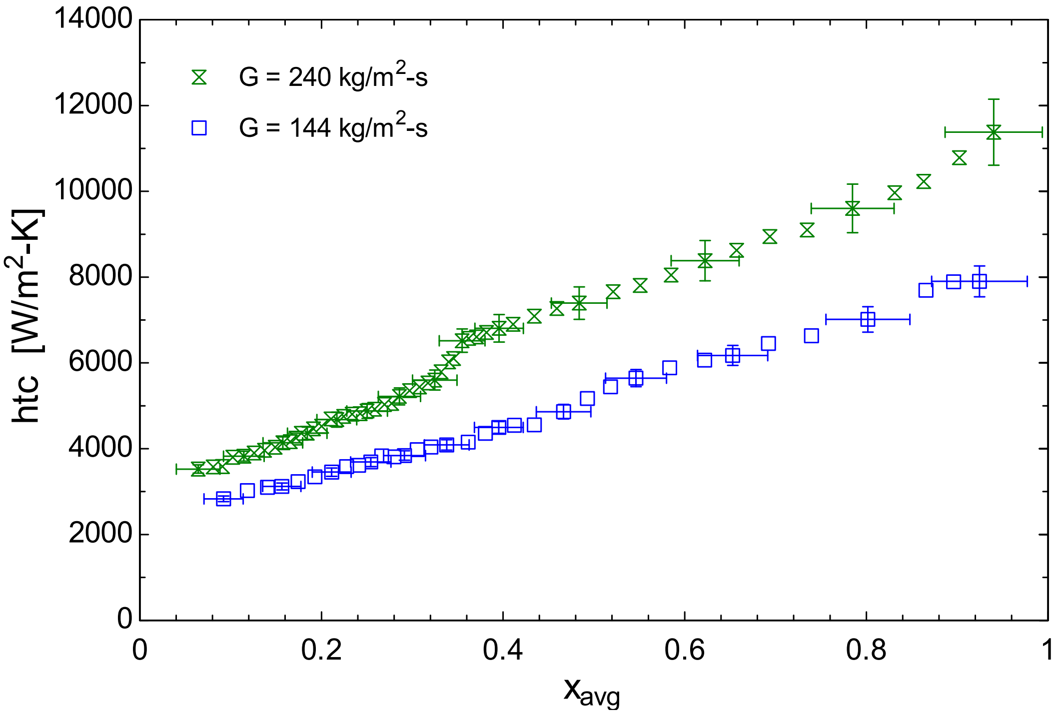

Figure 83. heat transfer coefficient as a function of average quality, mass flux effect, binary mixture, P = 790 kPa, Q'' = 56 kW/m^2, ID = 1.5 mm, Runs 33 and 35

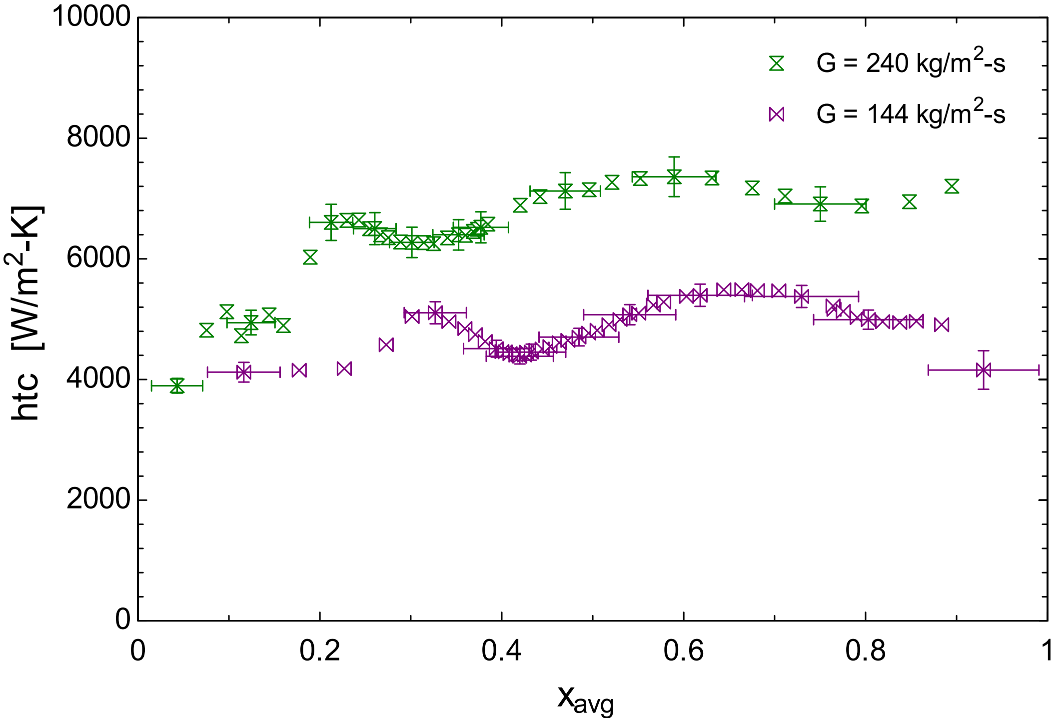

Figure 84. heat transfer coefficient as a function of average quality, mass flux effect, hydrocarbon mixture (no dilution), *P* = 270 kPa, *Q″* = 56 kW/m^2, *ID* = 1.5 mm, Runs 7 and 8

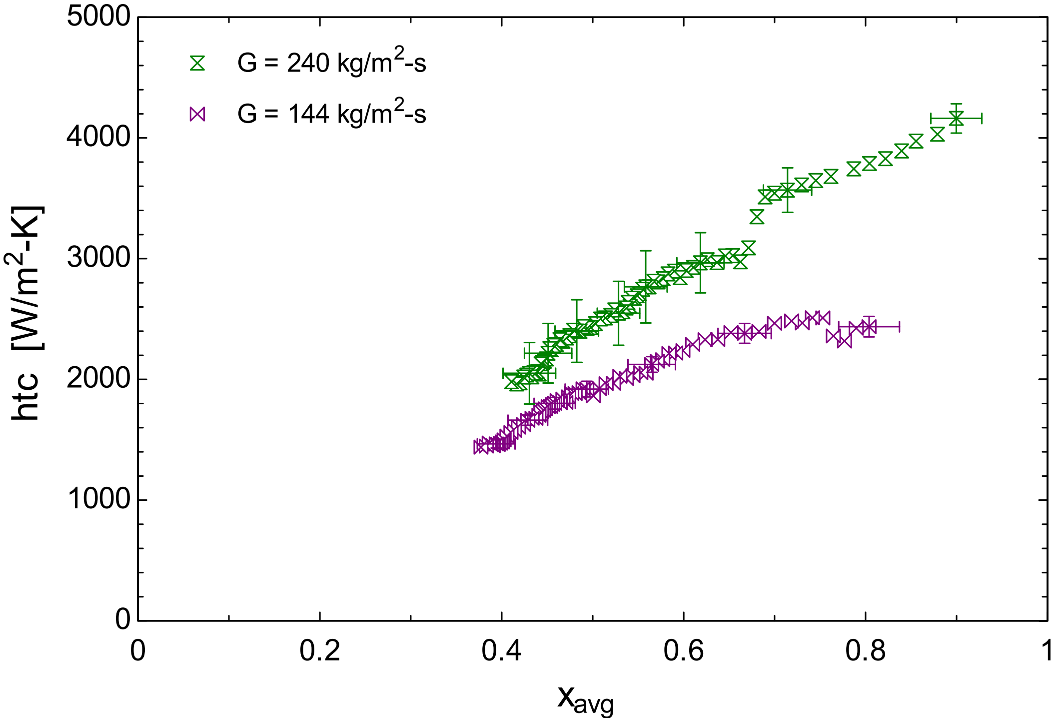

Figure 85. heat transfer coefficient as a function of average quality, mass flux effect, synthetic refrigerant mixture (no dilution), *P* = 790 kPa, *Q″* = 28 kW/m^2, *ID* = 1.5 mm, Runs 21 and 23

5.3.2. Heat flux effects

The effect of heat flux is investigated by collecting heat transfer coefficient data for two different heat fluxes ($\dot{Q}''$) while the other conditions are kept constant. In general, the boiling process could be driven by two phenomena: nucleate and convective boiling. Changing the heat flux may affect the nucleate boiling mechanism because bubble generation and departure are a function of the heat flux from the wall to the liquid. The convective component of the heat transfer coefficient is not expected to be significantly affected by changes on the heat flux.

Figure 86, Figure 87, and Figure 88 show the heat transfer coefficient data measured in the 1.5 mm test section for binary, hydrocarbons and synthetic refrigerant mixtures, respectively. Also, the heat flux effect is analyzed in the test section 0.5 and 3.0 mm, and these results may be seen in Appendices B, C, and D for the same mixtures. It is clear from the 9 comparison including the combination of the 3 mixtures and 3 diameters that the heat flux variations do not have any significant effect on the heat transfer coefficient for any diameter or mixture tested. A complete suppression of nucleate boiling is observed. This behavior could be attributable to the small diameter of the test section because bubble may be squeezed in the tube reducing dramatically the rate of bubble generation and departure. Also, as suggested by Sardesai et al. [55], the diffusion of constituents could add a thermal resistance that slows down the bubble generation mechanism. These results also suggest that convective boiling is the dominant boiling mechanism at the measured conditions.

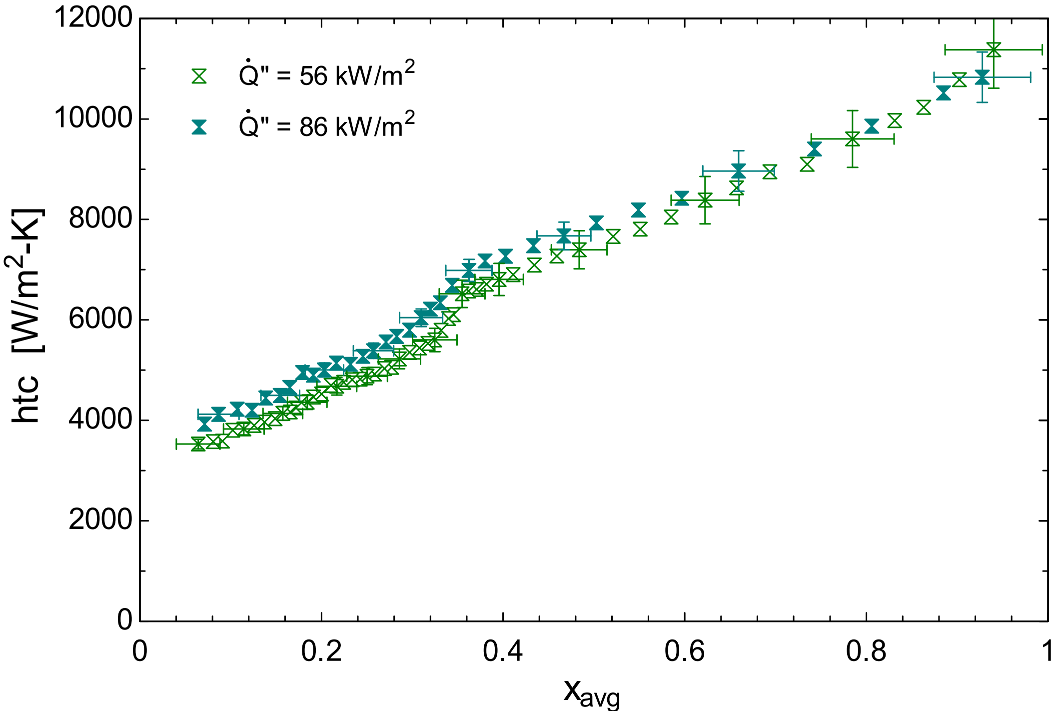

Figure 86. heat transfer coefficient as a function of average quality, heat flux effect, binary mixture, $G = 240$ kg/m^2-s, $P = 790$ kPa, $ID = 1.5$ mm, Runs 32 and 33

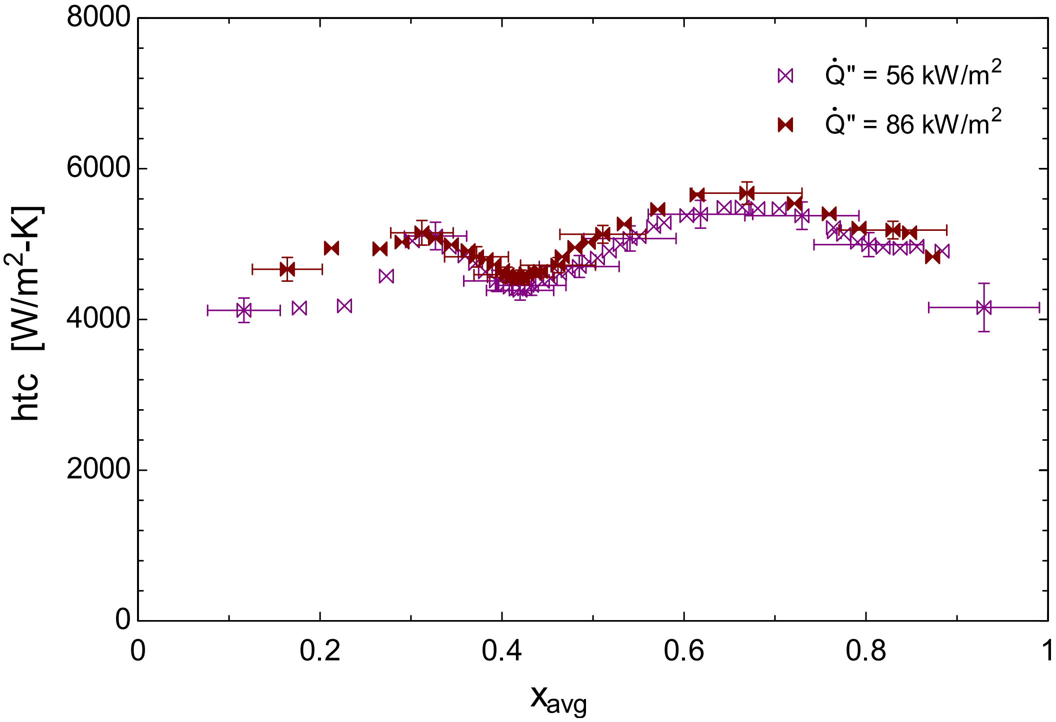

Figure 87. heat transfer coefficient as a function of average quality, heat flux effect, hydrocarbon mixture (No dilution), $G = 144$ kg/m^2-s, $P = 270$ kPa, $ID = 1.5$ mm, Runs 5 and 6

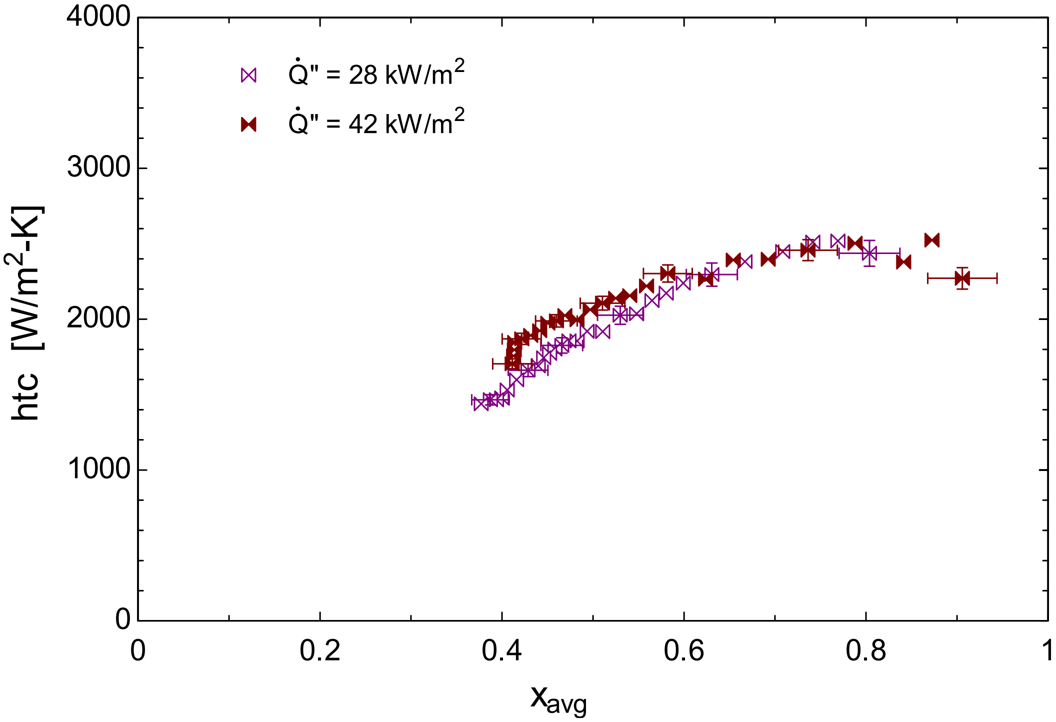

Figure 88. heat transfer coefficient as a function of average quality, heat flux effect, synthetic refrigerant mixture (No dilution), G = 144 kg/m^2-s, P = 270 kPa, ID = 1.5 mm, Runs 21 and 22

5.3.3. Pressure effects

As shown in Table 12 to Table 14 , the two-phase zone is displaced to a colder region when the pressure is reduced. The temperature glide remains almost constant as the evaporating pressure is changed. The influence of the evaporating pressure is studied by collecting heat transfer data at two different inlet pressures to the test section, 270 and 790 kPa, and keeping the other test conditions constant. Figure 89, Figure 90 and Figure 91 show the analysis for the binary, hydrocarbons and synthetic refrigerants mixtures data collected in the 1.5 mm test section.

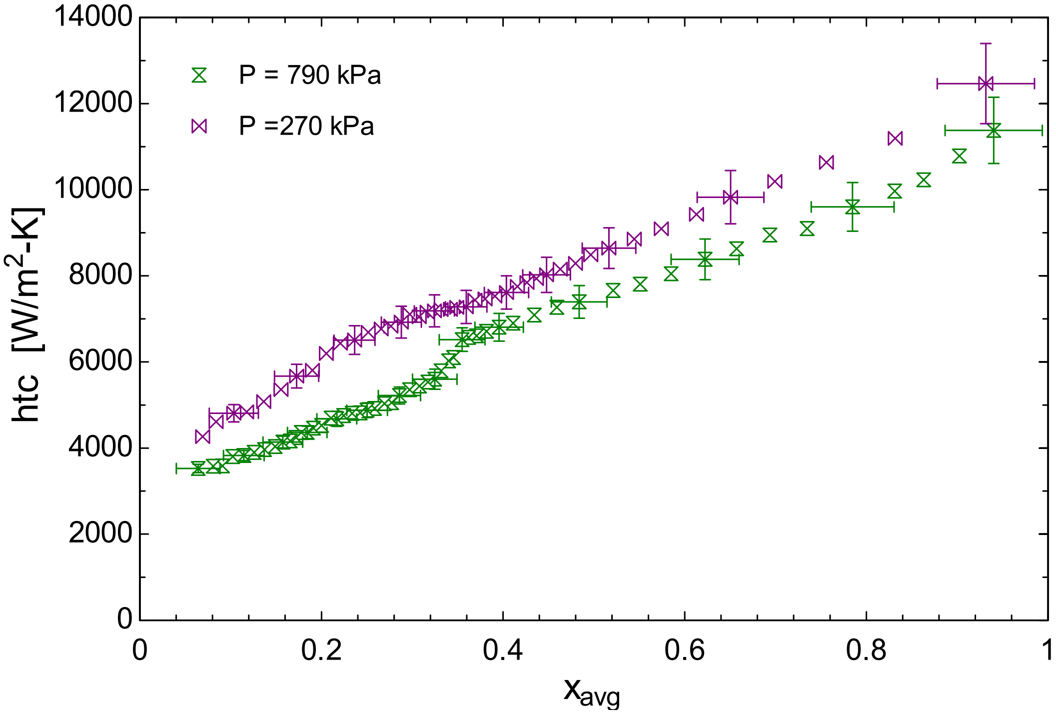

Figure 89. heat transfer coefficient as a function of average quality, pressure effect, binary mixture, *G* = 240 kg/m^2-s, *Q″* = 56 kW/m^2, *ID* = 1.5 mm, Runs 33 and 34

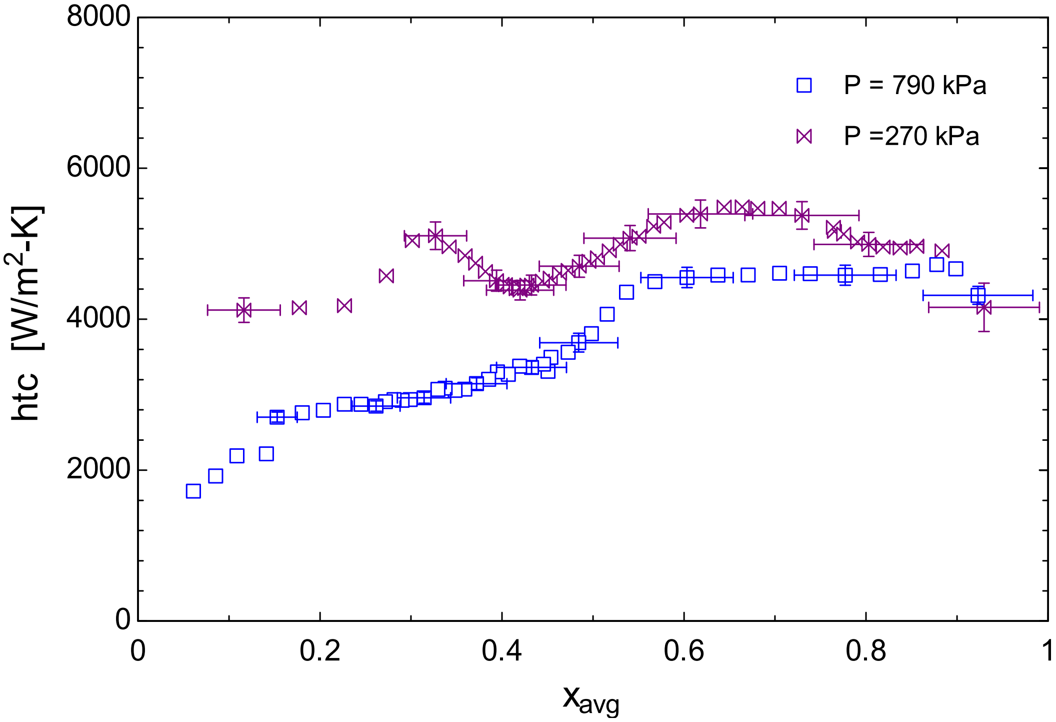

Figure 90. heat transfer coefficient as a function of average quality, pressure effect, hydrocarbon mixture (no dilution), *G* = 144 kg/m^2-s, *Q″* = 56 kW/m^2, *ID* = 1.5 mm, Runs 7 and 9

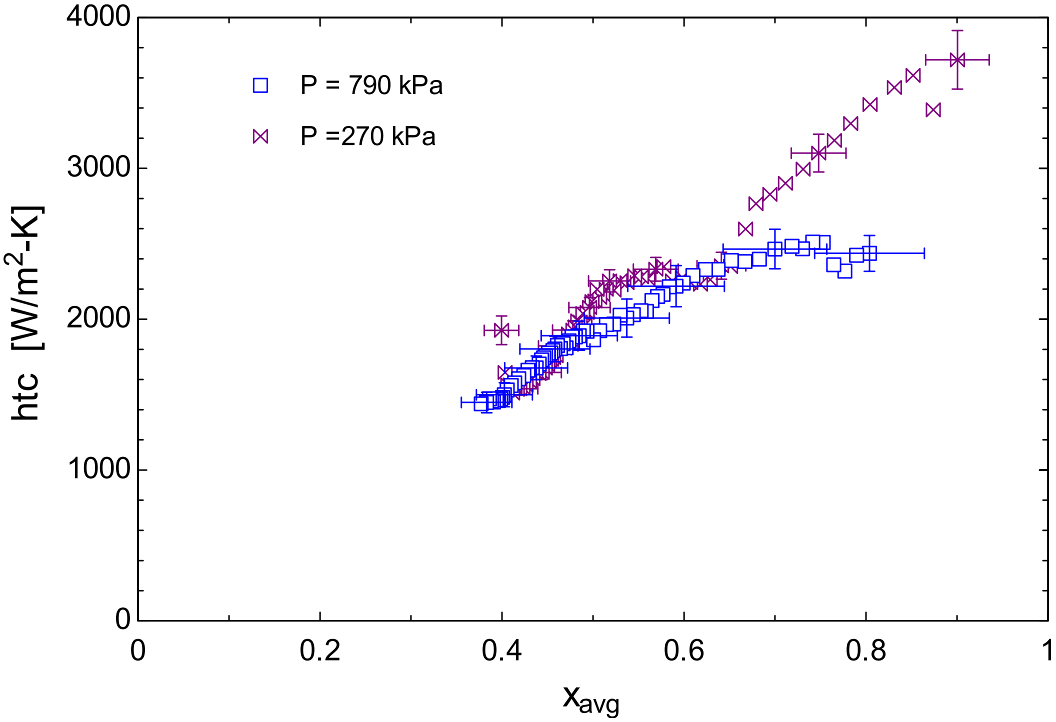

Figure 91. heat transfer coefficient as a function of average quality, pressure effect, synthetic refrigerant mixture (no dilution), $G = 144$ kg/m^2-s, $Q'' = 28$ kW/m^2, $ID = 1.5$ mm, Runs 20 and 21

The experimental results suggest that as the pressure is reduced, the heat transfer coefficient slightly increases. For the hydrocarbons mixtures, Figure 90 shows different trends for the two pressures analyzed. The difference in heat transfer coefficients with pressure tends to decrease for values of thermodynamic quality greater than 50%. The heat transfer coefficient is almost constant and approximately equal to 5000 W/m^2-K for the low pressure data, showing an initial peak where most of the methane is evaporated. In the high pressure data, the experimental data show two clear flat zones (i.e., two regions in which the heat transfer coefficient is constant). A heat transfer coefficient of approximately 3000 W/m^2-K exists when the quality is below 50% and it increases to approximately 4000 W/m^2-K when the quality is greater than 50%. The synthetic refrigerant mixtures show similar trends for both evaporating pressures. The main difference is seen when the quality is over 80% because the high pressure data seems to reach the dry out region before the low pressure data. In the case of the binary mixture, Figure 89 shows a similar trend for both evaporating pressures. In conclusion, changes in the evaporating pressures do not seem to have a significant effect on the heat transfer coefficient except in the low quality region of the hydrocarbons mixture. Most of the evaporating pressure effects may be related to changes in fluid properties.

5.3.4. Composition effects

The influence of the mixture composition on the heat transfer coefficient is studied by diluting the hydrocarbons and synthetic refrigerants mixtures and keeping the other test conditions constant. The hydrocarbons and the synthetic refrigerants mixtures are diluted using nitrogen and argon, respectively. The experimental heat transfer data for hydrocarbons mixture in the 3.0 mm test section is are shown in Figure 92. Figure 93 presents the current experimental data for the synthetic refrigerant mixtures in the 3.0 mm test section showing 0%, 20%, and 40% argon dilution.

Nitrogen, which is used to dilute the hydrocarbon mixtures, has a lower saturation temperature than methane. Methane is the lightest component of the hydrocarbons mixture. When the nitrogen is added to the hydrocarbons mixture, the two-phase region is significantly expanded and the temperature glide is increased by around 45 K, as shown in Table 12. The synthetic refrigerant mixture behaves in a similar manner when argon is added. The dew and bubble temperature for the synthetic refrigerants mixtures are shown in Table 13.

The dilution affects the properties of the mixture and the diluted mixture is expected to behave as a new fluid. A significant variation in the magnitude of the measured heat transfer coefficient for different compositions is observed, as reported by Nellis et al. [30]. In the hydrocarbon mixtures case, the 20% dilution using nitrogen reduces the heat transfer coefficient by approximately 15% and maintains a similar trend to the data without dilution. As the dilution increases (40%), the heat transfer coefficient increases in the low quality region (below 40%) coinciding with where most of the nitrogen is evaporated and showing a peak at low temperature. In the high quality region (over 40%), the heat transfer coefficient for 40% dilution is about 25% smaller than without dilution.

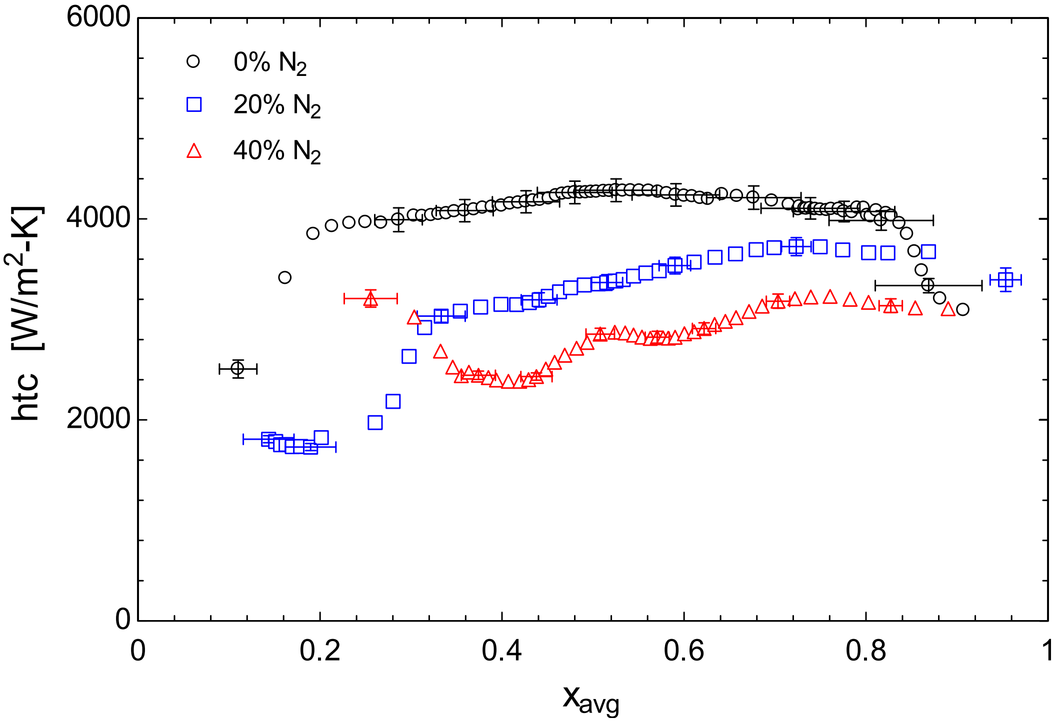

Figure 92. heat transfer coefficient as a function of average quality, Composition effect, hydrocarbon mixture, *G* = 144 kg/m^2-s, *P* = 790 kPa, *Q″* = 56 kW/m^2, *ID* = 3.0 mm, Runs 13, 14 and 15

In the synthetic refrigerant mixture, as 20% argon is added, the heat transfer coefficient is reduced by approximately 20% for qualities greater than 50%. The heat transfer coefficients for the 40% dilution case results in a reduction by approximately 40% compared with the mixture without dilution in the same range. At low temperature for the 20% and 40% dilution, a peak is observed, which is related to the region where most of the evaporation of argon occurs. The heat transfer coefficient for 20% and 40% dilution seem to be similar at low qualities.

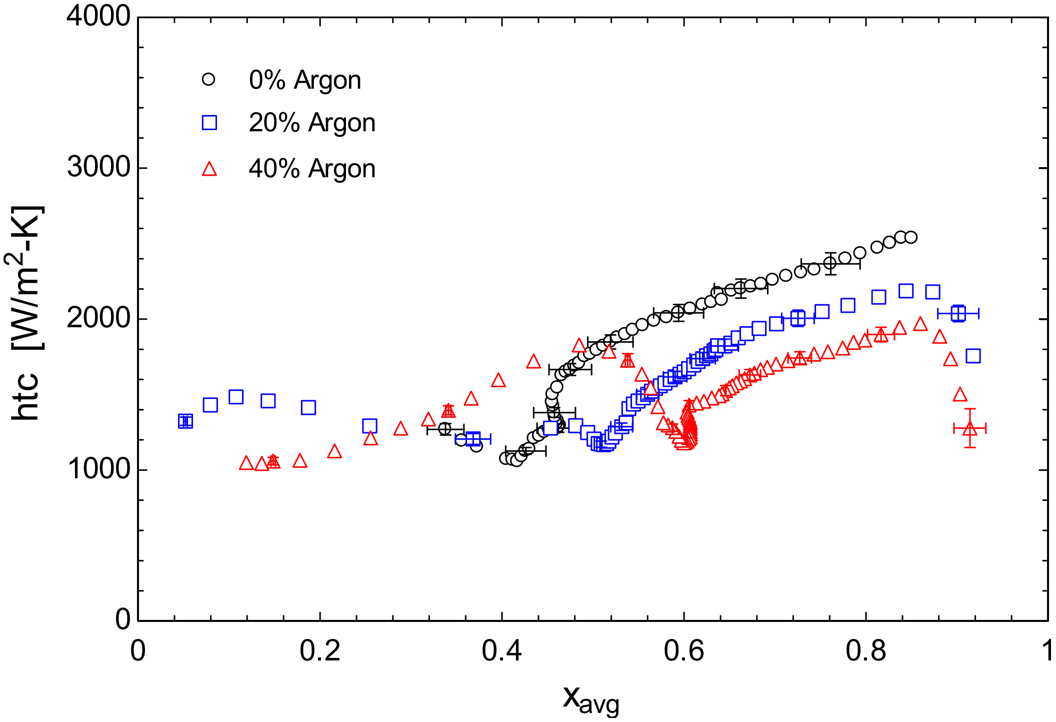

Figure 93. heat transfer coefficient as a function of average quality, Composition effect, synthetic refrigerant mixture, G = 144 kg/m^2-s, P = 790 kPa, Q'' = 28 kW/m^2, ID = 3.0 mm, Runs 27, 28 and 29

5.3.5. Tube size effects

It is believed that convection dominant the boiling process for the mixture tested; consequently, it is expected that the heat transfer coefficient increases as the diameter is reduced. As suggested by Eqs. (100) and (101), the measured heat transfer coefficient should be 25% greater in the 0.5 mm than the 1.5 mm test section and 15% greater in the 3.o mm than the 1.5 mm test section.

$$\frac{htc_{ID=0.5}}{htc_{ID=1.5}} = \left(\frac{1.5}{0.5}\right)^{0.2} \approx 1.25 \qquad (100)$$

$$\frac{htc_{ID=1.5}}{htc_{ID=2.9}}=\left(\frac{2.9}{1.5}\right)^{0.2}\approx 1.15 \qquad (101)$$

Figure 94, Figure 95 and Figure 96 show the measured heat transfer coefficient varying the diameter of the test section and keeping constant the other test condition for binary, hydrocarbon and synthetic refrigerants mixtures, respectively. Similar results are shown in Appendices C and D for the hydrocarbon and synthetic dilutions. The binary mixture show the expected result between the 0.5 and 1.5 mm data; however, the 3.0 mm data only follow the expected trend as the quality is greater than 50%. Figure 95 shows similar behavior for the hydrocarbon data. The synthetic refrigerant mixture data behave according to the trend suggested before.

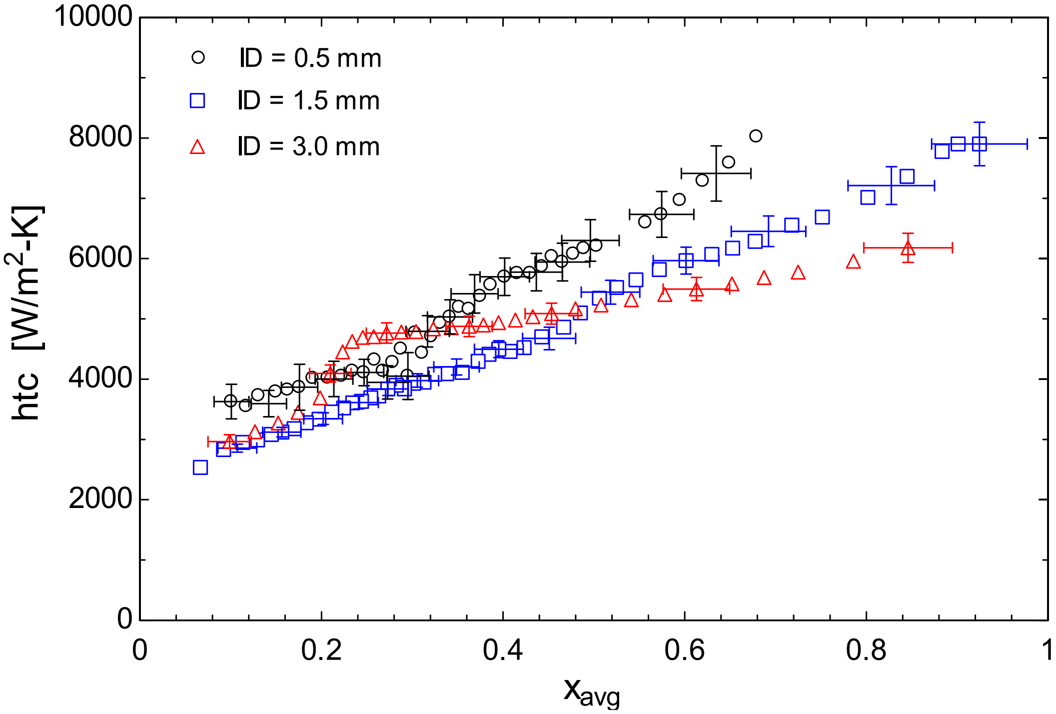

Figure 94. heat transfer coefficient as a function of average quality, Diameter effect, binary mixture, G = 144 kg/m^2-s, P = 790 kPa, Q'' = 56 kW/m^2, Runs 30, 35 and 37

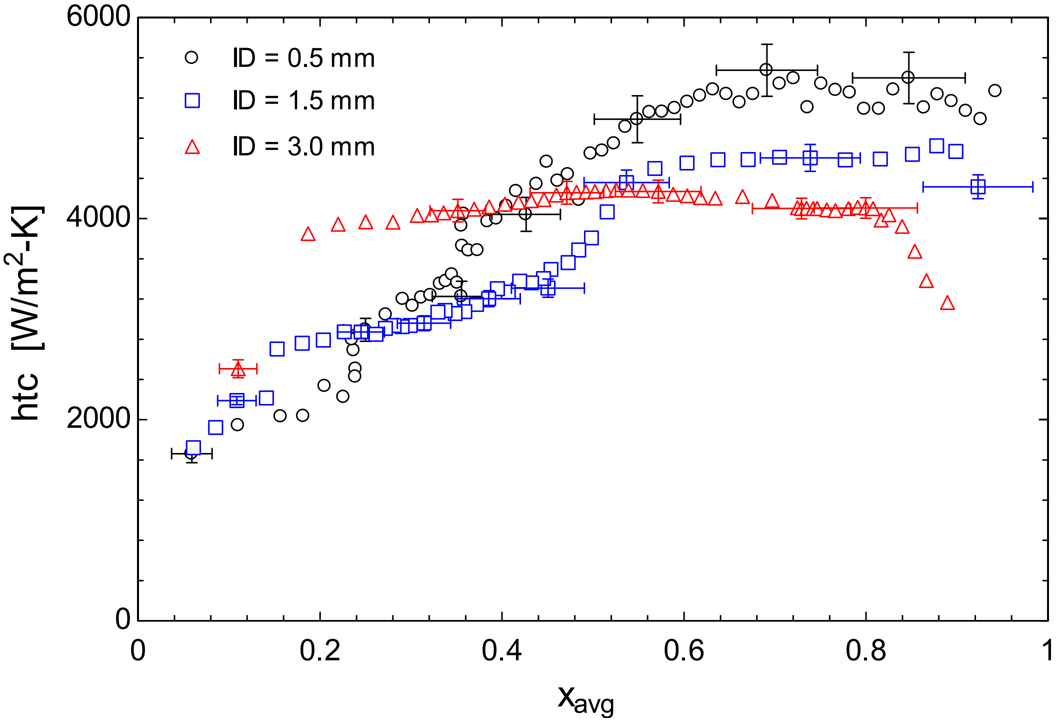

Figure 95. heat transfer coefficient as a function of average quality, Diameter effect, hydrocarbon mixture (no dilution), *G* = 144 kg/m^2-s, *P* = 790 kPa, *Q″* = 56 kW/m^2, Runs 1, 9 and 13

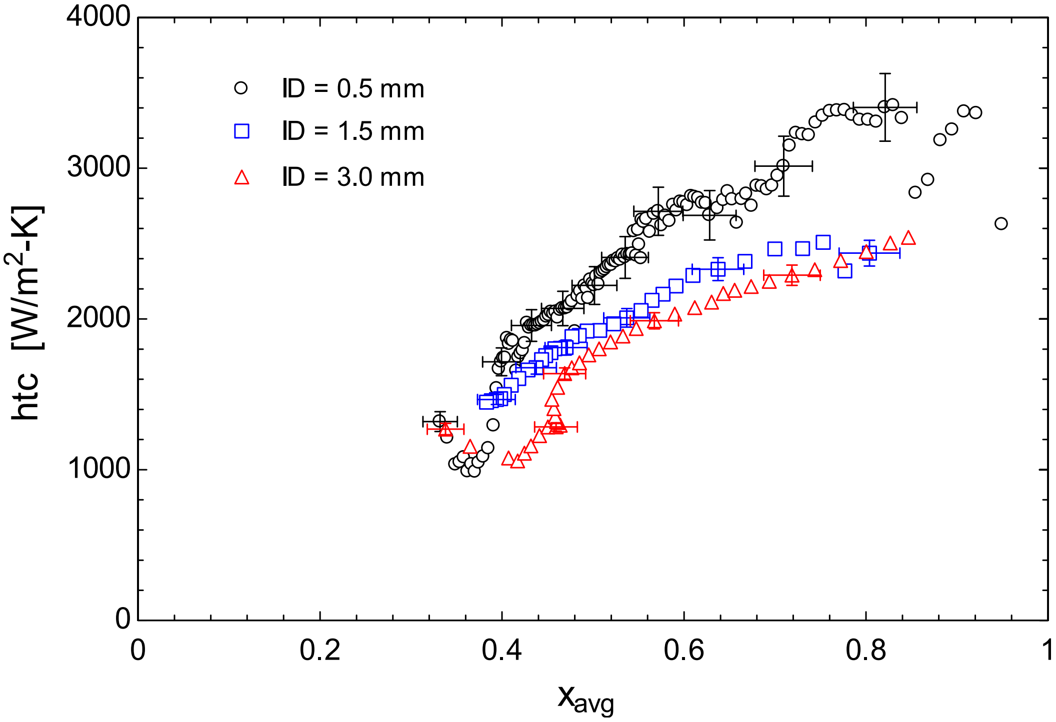

Figure 96. heat transfer coefficient as a function of average quality, Diameter effect, synthetic refrigerant mixture (no dilution), *G* = 144 kg/m^2-s, *P* = 790 kPa, *Q″* = 28 kW/m^2, , Runs 16, 21 and 27

The unexpected higher heat transfer coefficient for the binary and hydrocarbon mixtures in the 3.0 mm test section at qualities lower than 50% may be explained because a different flow regime induced by the small diameter. In the small diameters, the confined bubble regime may be dominant. As the diameter increases, the bubbles allow liquid flowing between the bubbles and the wall accelerating the flow and enhancement the heat transfer coefficient.

5.3.6. Roughness effects

The actual 1.5 mm test section has a RMS roughness of 0.86 μm and a relative roughness of 0.0006 as presented in Table 4 and Table 8. The old 1.5 mm test section has a RMS roughness of 2.56 μm and a relative roughness of 0.0017 according to Table 8. Figure 97 shows the results for the measured heat transfer coefficient both test section keeping the same test conditions: Hydrocarbon mixture, no dilution, $G = 144$ kg/m^2-s, $P = 270$ kPa, $\dot{Q}'' = 56$ kW/m^2.

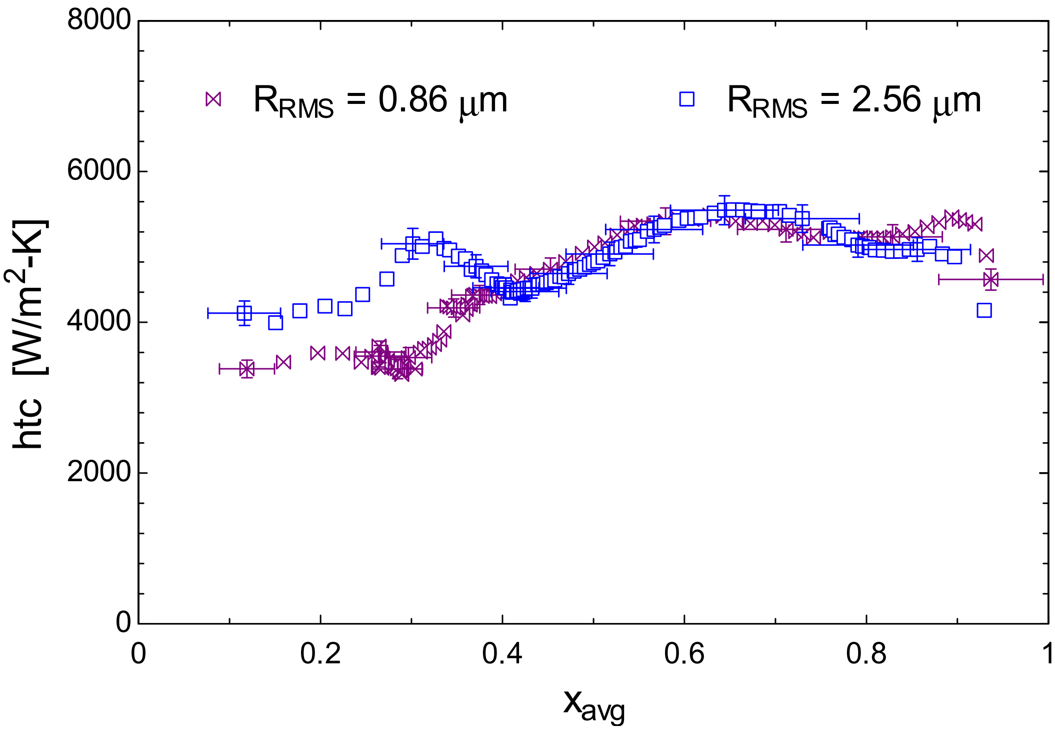

Figure 97. heat transfer coefficient as a function of average quality, Composition effect, hydrocarbon mixture, $G =$ 144 kg/m^2-s, $P = 270$ kPa, $Q'' = 56$ kW/m^2, $ID = 1.5$ mm, Runs 5 and 7

There is not a significant difference between the collected heat transfer coefficients in the two test sections when the thermodynamic quality is greater 40%. The old test section, which has a greater relative roughness, shows an enhancement of the heat transfer coefficient as the quality decreases to values below 40%.

5.4. Dimensionless number and nomenclature used in two-phase flow

Reynolds, Prandtl, Froude, and Weber number are frequently referred in the two-phase flow literature. They can be related with the mixture or two-phase fluid or for the vapor and liquid phases. When the dimensionless number is associated with mixture or two-phase fluid may be indicated either with no subscripts or subscripts as *mixt* or *2ph*. The liquid phase may be referred with the subscripts *l* or *lo*. The subscripts *l* means that only the liquid fraction of the two-phase flow is flowing on the tube. The subscripts *lo* (or liquid only) is used when it is assume that all of the two phase fluid behaves as liquid. The vapor phase is treated in the same manner than liquid phase. Table 15 shows the dimensionless number used in this report.

Table 15. Dimensionless number used in this report

Dimensionless number	**mixture/two-phase**	**liquid**	**liquid only**	**vapor**	**vapor only**
Reynolds	$Re=\frac{G\,ID}{\mu_{mixt}}$	$Re_l=\frac{G(1-x)\,ID}{\mu_l}$	$Re_{lo}=\frac{G\,ID}{\mu_l}$	$Re_v=\frac{G\,x\,ID}{\mu_v}$	$Re_{vo}=\frac{G\,ID}{\mu_v}$
Prandtl		$Pr_l=\frac{\mu_l\,Cp_l}{k_l}$		$Pr_v=\frac{\mu_v\,Cp_v}{k_v}$	
Froude	$Fr=\frac{G^2}{\rho_{mixt}{}^2\,g\,ID}$	$Fr_l=\frac{\left(G\left(1-x\right)\right)^2}{\rho_{l,}^2\,g\,ID}$	$Fr_{lo}=\frac{G^2}{g\,ID\,\rho_l^2}$		
Weber	$We=\frac{G^2\,ID}{\rho_{mixt}\,\sigma}$				$We_{vo}=\frac{G^2\,ID}{\rho_v\,\sigma}$

5.5. Heat transfer coefficient models

In general, boiling models for turbulent flow of pure fluids indicate that the heat transfer process in the two-phase zone is mainly explained by convective and nucleate boiling. Convective boiling is a phase change process that occurs at the vapor-liquid interface. Liquid evaporates to vapor at this boundary. This process can be understood as a single-phase turbulent forced convection [60]. Nucleate boiling can be understood as being similar to nucleate pool boiling in which there is generation and growth of vapor bubbles in the liquid-solid (wall tube) interface until they leave the wall due to buoyancy or pressure forces from the surrounding, flowing fluid. As heat flux increases, more nucleation sites are activated, generating more vapor bubbles. The heat flux associated with nucleation is higher because the generation, growth, and removal of vapor bubbles in the tube surface produces a strong fluid motion that continuously allow cold fluid to access the hot tube surface. Both nucleate and convective boiling mechanisms explain high heat transfer coefficients in boiling process [59].

There is not a general and accurate correlation to predict the local heat transfer coefficient (*htc*) for mixtures during the boiling process. Thome [60] suggested for non-azeotropic mixtures that the best approach is to utilize an accurate pure fluid correlation including modifications to take into account the mixture mass diffusion effect; consequently, previous work regarding to boiling of pure fluids are visited. However, one limitation of most of the existing boiling correlations for pure fluids is that they were developed using experiment data obtained on vertical tubes [11]. These correlations have been modified to be suitable for horizontal tubes. In vertical flow, there are few data collected at high qualities because the dry out occurs in the quality range between 50 and 75%. Consequently, the local heat transfer coefficient is not predicted adequately at high quality regions. Table 16 shows some of the well-known correlations that predict heat transfer coefficient for boiling flow of pure fluids.

A considerable number of heat transfer correlations of flow boiling for pure fluids have been proposed. Chen [28] provided one of the first general correlations for flow boiling. This correlation superimposes both mechanisms that could explain the boiling phenomenon by separately considering the contribution of nucleate (htc_n) and convective boiling (htc_c). Another superposition model has been proposed by Gungor and Winterton [61]. Gungor and Winterton [62] modified their previous correlation and proposed an enhancement model that is based in a liquid single-phase heat transfer coefficient with a two-phase enhancement factor. Liu and Winterton [63] provided an asymptotic model that is an improvement of the Gungor and Winterton [61] correlation.

Table 16. Boiling heat transfer correlations for pure fluids

Author	Equation	Comments
Chen [28]	$htc = htc_n + htc_c = htc_{nb}\, S_{Chen} + htc_l\, F_{Chen}$ $htc_{nb} = 0.00122\left(\frac{k_l^{0.79}\, Cp_l^{0.45}\, \rho_l^{0.49}}{\sigma^{0.5}\, \mu_l^{0.29}\, h_{lv}^{0.24}\, \rho_v^{0.24}}\right)\left(T_{wall} - T_{sat}\right)^{0.24}\left(P_{sat}\left(T_{wall}\right) - P_{sat}\right)^{0.75}$ $S_{Chen} = \left(1 + 2.53\times10^{-6}\left(Re_l\, F_{Chen}^{1.25}\right)^{1.17}\right)^{-1}$ $htc_l = 0.023\, Re_l^{0.8}\, Pr_l^{0.4}\, \frac{k_l}{ID}$ $F_{Chen} = \left(\frac{\left(dp/dz\right)_{2ph}}{\left(dp/dz\right)_l}\right)^{0.444}$	developed for water, methanol, cyclohexane, and pentane in vertical tubes
Gungor and Winterton [61]	$htc = E_{GW}\, htc_l + S_{GW}\, htc_{pool}$ $E_{GW} = 1 + 24000\, Bo^{1.16} + 1.37\, X_{tt}^{-0.86}$ $X_{tt} = \left(\frac{1-x}{x}\right)^{0.9}\left(\frac{\rho_v}{\rho_l}\right)^{0.5}\left(\frac{\mu_l}{\mu_v}\right)^{0.1}$ $S_{GW} = \left(1 + 1.15\times10^{-6}\, E_{GW}^{2}\, Re_l^{1.17}\right)^{-1}$ $htc_{pool} = 55 P_r^{0.12}\left(-log\left(P_r\right)\right)^{-0.55} M^{-0.5}\, q''^{0.67}$	developed for water, synthetic refrigerants, and alcohols in both horizontal and vertical tubes
Gungor and Winterton [62]	$htc = E_{new}\, htc_l$ $E_{new} = 1 + 3000\left(Bo\right)^{0.86} + 1.12\left(\frac{x}{1-x}\right)^{0.75}\left(\frac{\rho_l}{\rho_v}\right)^{0.41}$	
Liu and Winterton [63]	$htc = \sqrt{\left(E_{LW}\, htc_l\right)^2 + \left(S_{LW}\, htc_{pool}\right)^2}$ $E_{LW} = \left(1 + x\, Pr_l\left(\frac{\rho_l}{\rho_v} - 1\right)\right)^{0.35}$ $S_{LW} = \left(1 + 0.055 E_{LW}^{0.1}\, Re_l^{0.16}\right)^{-1}$	includes more empirical data from water, synthetic refrigerants, and hydrocarbons

The correlations presented in Table 16 for pure fluids are evaluated and compared with the measured heat transfer coefficients for the mixed refrigerants tested. The average absolute deviation (AAD) is used to evaluate each correlation. The AAD is defined in Eq. (102) as the ratio between the sum of the relative errors and the number of data point collected. The relative error is the ratio of the absolute difference between the measured (true value) and the predicted heat transfer coefficient divided by the true value:

$$AAD = \frac{1}{N}\sum\left(\frac{\left|htc_{measured} - htc_{predicted}\right|}{htc_{measured}}\right)100\% \tag{102}$$

Table 17 summarizes the AAD of the heat transfer coefficient predicted using existing boiling correlations for pure fluids. The results are shown for each diameter and for each mixture tested separated as binary, hydrocarbons, hydrocarbons dilution, synthetics and synthetics dilution. Also, the combined results for hydrocarbons and synthetic refrigerants mixtures are shown. Finally, the last column of Table 17 shows the combined result for each diameter and also for the combination of all diameters.

It is clear that the existing correlations for boiling pure fluids do not accurately predict the boiling heat transfer coefficient for mixtures. Chen [28], Gungor and Winterton [61] and [62] and Liu and Winterton [63] include in their models the contribution of nucleate boiling; however, the experimental data shows prevalence of convection boiling. Table 18 displays the deviations of the same correlations, but only taking into account the convective boiling contribution. Chen and Liu and Winterton convection models show better results. The convective part of Chen provides the best prediction with an AAD of 27%, and it especially is good relative to predicting the behavior of the hydrocarbons mixtures (dilution and no dilution) in the 1.5 mm test section (with an AAD below 16%). AADs over 30% are observed in the small test section for all the mixtures.

Table 17. AAD of heat transfer coefficient predicted using existing boiling heat transfer correlations for pure fluids

Correlations	**Binary**			**HC**			**HC+N$_2$**			**Syn**			**Syn+Ar**			**All data**			
	0.5	**1.5**	**3.0**	**0.5**	**1.5**	**3.0**	**0.5**	**1.5**	**3.0**	**0.5**	**1.5**	**3.0**	**0.5**	**1.5**	**3.0**	**0.5**	**1.5**	**3.0**	**All**
Chen	42%	15%	46%	65%	24%	71%	80%	31%	58%	132%	161%	34%	283%		201%	131%	298%	96%	210%
Gungor and Winterton	368%	266%	202%	486%	268%	248%	675%	652%	455%	385%	294%	318%	1340%	863%	881%	695%	426%	487%	504%
Gungor and Winterton 2	115%	94%	54%	155%	91%	62%	272%	279%	202%	134%	97%	98%	458%	305%	320%	246%	156%	173%	182%
Liu and Winterton	163%	139%	130%	239%	131%	172%	286%	340%	291%	144%	120%	158%	262%	285%	296%	228%	187%	227%	207%

Table 18. AAD of heat transfer coefficient predicted using the convective contribution of existing boiling heat transfer correlations for pure fluids

Correlations	**Binary**			**HC**			**HC+N$_2$**			**Syn**			**Syn+Ar**			**All data**			
	0.5	**1.5**	**3.0**	**0.5**	**1.5**	**3.0**	**0.5**	**1.5**	**3.0**	**0.5**	**1.5**	**3.0**	**0.5**	**1.5**	**3.0**	**0.5**	**1.5**	**3.0**	**All**
Chen	39%	18%	29%	37%	16%	23%	29%	14%	21%	45%	37%	28%	35%	35%	31%	37%	23%	26%	**27%**
Gungor and Winterton	115%	79%	43%	149%	84%	53%	293%	310%	228%	136%	94%	89%	992%	535%	594%	372%	190%	256%	249%
Liu and Winterton	38%	28%	47%	43%	25%	41%	34%	23%	34%	35%	31%	32%	33%	30%	28%	36%	27%	35%	31%

Table 19 shows some of the correlations available for boiling mixtures in the literature. Some of the pure fluid boiling correlations have been empirically evaluated, and they have been modified including coefficients that take into account some mixing effects. Most of these correlations have been validated for binary mixtures under limited conditions. The binary data used to validate these correlations have been obtained in large channels, for mixtures with small temperature glides and close to room temperature. Bennett and Chen [64] is one of these correlations, which was proposed to predict heat transfer coefficient for binary mixtures. The Bennett and Chen correlation is based on the Chen correlation.

Mishra et al. [54] proposed the correlation shown in Eq. (103):

$$htc = C\, htc_l \left(\frac{1}{X_{tt}} \right)^m Bo^n \tag{103}$$

Mishra correlated their experimental data with the liquid single-phase heat transfer coefficient and introduced an enhancement factor that take into account effects of the boiling multi-component mixture. The enhancement factor is defined as a function of the boiling number (*Bo*) and the Lockhart-Martinelli coefficient (X_{tt}) both phase turbulent. The coefficients *C*, *m* and *n* were experimentally defined for each mixture evaluated.

Table 19. Boiling heat transfer correlations for mixtures

Author	Equation	Comments
Bennett and Chen [64]	$htc = htc_{nb}\, S_{Chen} + htc_l\, F_{bennett}$ $F_{bennett} = F_{Chen}\left(\frac{Pr_l + 1}{2}\right)^{0.444}$	Validated with ethylene glycol-water mixture flowing in a vertical electrically heated test section
Mishra et al. [54]	$htc = C\, htc_l \left(\frac{1}{X_{tt}}\right)^m Bo^n$ $Bo = \frac{q''}{G\, h_{lv}}$	Horizontal test section. Mixture 1: R-12 (23–27%) and R-22 (77–73%), C =5.62, m=0.23, n=0.5. Mixture 2: R-12 (41–48%) and R-22 (59–52%), C=21.75, m=0.29, n=0.23.
Kandlikar [65]	$htc = max(htc_B, htc_C)$ if $V_1 < 0.03$ $htc_B = htc_l\left(0.6683\, Co^{-0.2} + 1058\, Bo^{0.7}\right)$ $htc_C = htc_l\left(1.136\, Co^{-0.9} + 667.2\, Bo^{0.7}\right)$ $htc = htc_l\left(1.136\, Co^{-0.9} + 667.2\, Bo^{0.7}\right)$ if $0.03 < V_1 < 0.2$ & $Bo > 0.0001$ $htc = htc_l\left(1.136\, Co^{-0.9} + 667.2\, Bo^{0.7}\, F_D\right)$ if $0.03 < V_1 < 0.2$ & $Bo \leq 0.0001$ or $V_1 \geq 0.2$ $Co = \left(\frac{\rho_v}{\rho_l}\right)^{0.5}\left(\frac{1-x}{x}\right)^{0.8}$ $V_1 = \frac{cp_l}{h_{lv}}\left(\frac{\kappa}{D}\right)^{0.5}\frac{dT}{dx_1}\left(y_1 - x_1\right)$ $F_D = 0.678\left(1 - \frac{Cp_l}{h_{lv}}\left(\frac{\kappa}{D}\right)^{0.5}\frac{dT}{dx_1}\left(y_1 - x_1\right)\right)^{-1}$	Validated over 2500 data points for binary mixtures R-12/R-22, R-22/R-114, R-22/R-152a and R-132a/R-123. It includes a correction factor for horizontal test sections.
Granryd [1]	$\frac{1}{htc} = \frac{1}{htc_l\, F\left(X_{tt}\right)} + \frac{x\, Cp_v}{htc_v\left(\frac{\partial h}{\partial T}\right)_P}\frac{x}{C_{lv}}$ $C_{lv} = 2$ $F\left(X_{tt}\right) = 2.37\left(0.29 + \frac{1}{X_{tt}}\right)^{0.85}$	
Little [2]	$\frac{1}{htc} = \frac{1}{htc_{film,little}} + \frac{x\, Cp_v}{htc_{lv}\left(\frac{\partial h}{\partial T}\right)_P}\frac{x\, Cp_v}{(1-x)\, Cp_l + x\, Cp_v}$ $htc_{l,film} = 0.023\left(\frac{Re_l}{1+\sqrt{\alpha}}\right)^{0.8} Pr_l^{0.4}\frac{k_l}{ID\left(1-\sqrt{\alpha}\right)}$ $htc_{lv} = 0.023\left(\frac{Re_v}{\sqrt{\alpha}}\right)^{0.8} Pr_v^{0.4}\frac{k_v}{ID\sqrt{\alpha}}$ $\alpha = \left(1 + \frac{(1-x)\,\rho_v}{x\,\rho_l}\sqrt{1 - x\left(1 - \frac{\rho_l}{\rho_v}\right)}\right)^{-1}$	

Kandlikar [65] developed a correlation for flow boiling with binary mixtures. This correlation includes the fundamentals of bubble growth phenomenon and the effect of liquid and vapor concentration on the interphase. The correlation defines three regions: one region includes nucleation boiling, another region with moderate suppression of nucleate boiling, and a region with severe suppression of nucleate boiling.

Little [2] and Granryd [1] models are similar to model proposed by Silver [66] and Bell and Ghaly [67]. These models are based on annular flow, which is characterized by the presence of separated liquid and vapor phase flows: a liquid film flowing along the wall and vapor flowing on the center of the tube surrounding by the liquid film. The correlation proposed by Silver [66] and Bell and Ghaly [67] was developed for condensing mixtures. This correlation is given by Eq. (104):

$$\frac{1}{htc} = \frac{1}{htc_{film}} + \frac{x\,Cp_v}{htc_v \left(\frac{\partial h}{\partial T}\right)_P} \tag{104}$$

A specific correlation to calculate the liquid film (htc_{film}) and the vapor (htc_v) heat transfer coefficients is not provided. Ardhapurkar [68] proposed to calculate the film heat transfer coefficient using a modified version of Gungor and Winterton [62] with the correction factor for mixtures proposed by Thome and Shakir [69]. Ardhapurkar compared his correlation to experimental data obtained from Nellis et al.[30].

Eq. (105) shows the correlation proposed by Granryd [1]:

$$\frac{1}{htc} = \frac{1}{htc_l\, 2.37\left(0.29 + \frac{1}{X_{tt}}\right)^{0.85}} + \frac{x^2\,Cp_v}{2\,htc_v \left(\frac{\partial h}{\partial T}\right)_P} \tag{105}$$

The heat transfer coefficients for the liquid and vapor phase are calculated using Dittus and Boelter [26] correlation. Vapor and liquid components are assumed to flow in separate tubes. The first term, corresponding to the liquid film, includes an enhancement factor that is a function of Lockhart and Martinelli coefficient assuming liquid and vapor phase are both in a turbulent flow regime. In addition, another enhancement factor equal to 2 is introduced for the vapor component (second term) to take into account the improvement due to interface effects (vapor/liquid). Granryd validated his correlation against Jung [13] data for mixtures of R-12/R-152 and R-22/R-114.

Little [2] proposed a correlation that predicts with reasonable agreement heat transfer coefficient (*htc*) of boiling zeotropic mixtures flowing on horizontal tubes. Little's model was validated using experimental data presented by Nellis et al. [30] for nitrogen-hydrocarbon mixtures. However, it is not clearly shown how the correlation is obtained and how it should be applied. Appendix D shows a detailed heat transfer model that arrives to the same correlation proposed by Little. The correlation for the mixture heat transfer coefficient proposed by Little is shown in Eq. (106).

$$\frac{1}{htc} = \frac{1}{htc_{l,film}} + \frac{x^2\, Cp_v^{\,2}}{htc_{lv}\left(\dfrac{\partial h}{\partial T}\right)_P Cp_b} \tag{106}$$

The Dittus and Boelter [26] correlation is recommended for determining the single-phase heat transfer coefficients between the liquid film and the wall ($htc_{l,film}$) and between the core vapor and the liquid film (htc_{lv}) components as shown in Table 19. The parameters Cp_v and Cp_b are the specific heat for the vapor phase and for the mixture. Cp_b is defined as the weighted average of the liquid and vapor phase specific heat as shown in Eq. (107).

$$Cp_b = Cp_l\left(1-x\right)+Cp_v\,x \tag{107}$$

where x is the thermodynamic quality. $\left(\frac{\partial h}{\partial T}\right)_P$ is the apparent heat capacity of the mixture, which is the partial derivative of the mixture enthalpy with respect to temperature at constant pressure. The apparent specific heat of the mixture includes both the sensible and latent heat contributions. In addition, Little recommends the Chisholm void fraction model [70] be used to determine hydraulic diameters of the liquid and vapor fractions.

Table 20 displays the AAD for the mixture correlations shown in Table 19 in order to understand their applicability to the conditions and mixtures tested. As expected, the Bennett and Chen [64] correlation does not work well predicting the experimental data because it is based on Chen [28], which is a superposition model that adds the effects of convective and nucleate boiling, and the current experimental data is dominated by convective boiling. The Mishra [54] approach presents clear limitations because each mixture needs to define new experimental coefficients. The Mishra correlation is fitted against the experimental data presented in this paper, the experimentally-determined coefficient that best fits the data are C = 1.96, m = 0.7, n = 0. The value of zero for the coefficient n ($n=0$) suggests that play any important role in the data collected. The Mishra correlation seems to accurately predict the data well except for the dilutions of the hydrocarbons and synthetic mixtures data collected on the small test section of 0.5 mm. A prediction with an AAD of 18% seems to be good given the simplicity of the correlation. The Kandlikar correlation [65] does not seem to be suitable for predicting the heat transfer coefficient of the tested mixtures. The three correlations based on Silver [66], Bell and Ghaly [67] seem to work well to predict the experimental data. Granryd [1] shows the best agreement and Silver [66], Bell and Ghaly [67] has the worst performance. The

AAD for all the experimental data using Granryd is 15.0%. The greatest deviation is observed when the hydrocarbons and synthetic dilutions data are predicted on the 0.5 mm test section. Granryd seems to provide more accurate predictions for the experimental data as the diameter of the test section increases (Little [2] performs well with an AAD of 18%). Also for Little, the 0.5 mm test section data seems to be most difficult to predict.

Figure 98 to Figure 100 show four plots of the predicted Nusselt as a function of the experimental Nusselt. These plots show the results of the best four correlations for experimental data shown in this paper: Granryd, Little, Mishra and convective Chen. The plots are all on a log-log scale. In each plot the ±25% error lines are shown. It is clear that convective Chen correlation is less accurate than the other three selected models. Mishra and Little show the greatest dispersion as the Nusselt number is reduced below 100. Little seems to be the most accurate correlation for Nusselt number greater than 100. Granryd is the most accurate heat transfer coefficient correlation to predict all the experimental data.

Table 20. AAD of heat transfer coefficient predicted using the existing boiling heat transfer correlations for mixtures

Correlations	**Binary**			**HC**			**HC+N_2**			**Syn**			**Syn+Ar**			**All data**			
	0.5	**1.5**	**3.0**	**0.5**	**1.5**	**3.0**	**0.5**	**1.5**	**3.0**	**0.5**	**1.5**	**3.0**	**0.5**	**1.5**	**3.0**	**0.5**	**1.5**	**3.0**	**All**
Bennett &Chen	33%	30%	36%	70%	38%	64%	84%	44%	53%	117%	148%	29%	284%		197%	129%	303%	90%	210%
Mishra	22%	17%	31%	12%	9%	22%	34%	21%	11%	13%	11%	13%	38%	26%	12%	25%	15%	16%	18%
Kandlikar 2	69%	63%	30%	110%	75%	43%	180%	165%	110%	87%	69%	71%	137%	111%	41%	126%	94%	61%	93%
Granryd	11%	13%	12%	31%	13%	9%	34%	19%	7%	11%	8%	9%	35%	19%	7%	26%	14%	8%	15%
Little	19%	28%	8%	36%	17%	11%	27%	27%	17%	15%	9%	13%	30%	14%	12%	26%	18%	13%	18%
SBG	23%	19%	27%	20%	29%	30%	25%	29%	41%	37%	38%	35%	24%	32%	36%	27%	31%	35%	31%

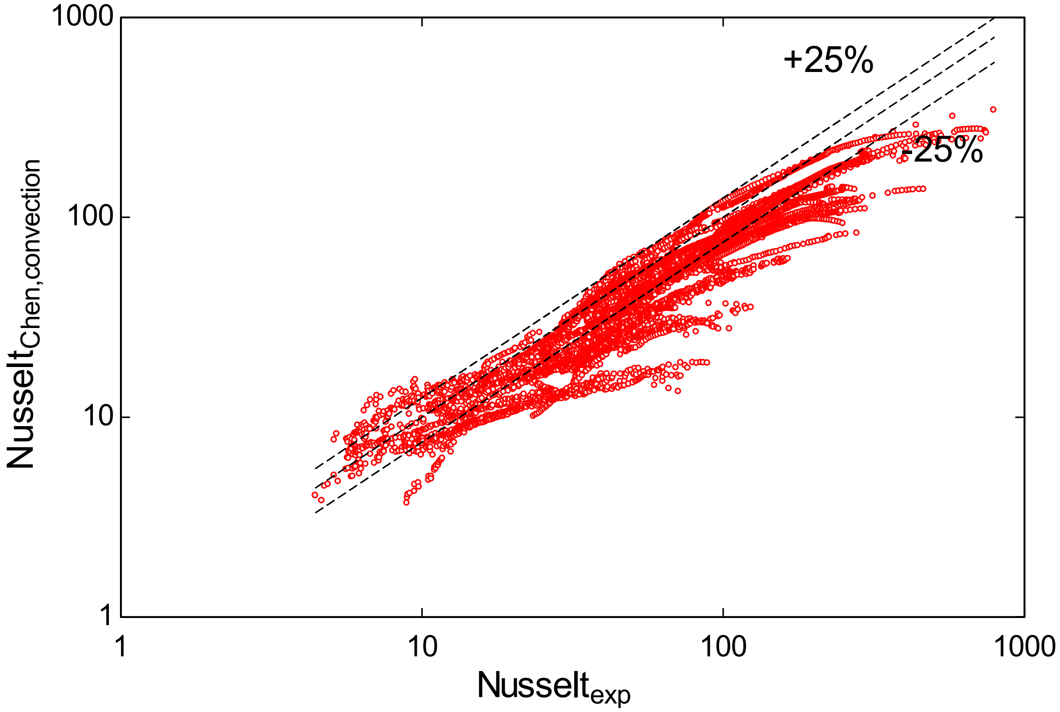

Figure 98. Predicted Nusselt number as a function of experimental Nusselt number using Chen correlation (only convection contribution).

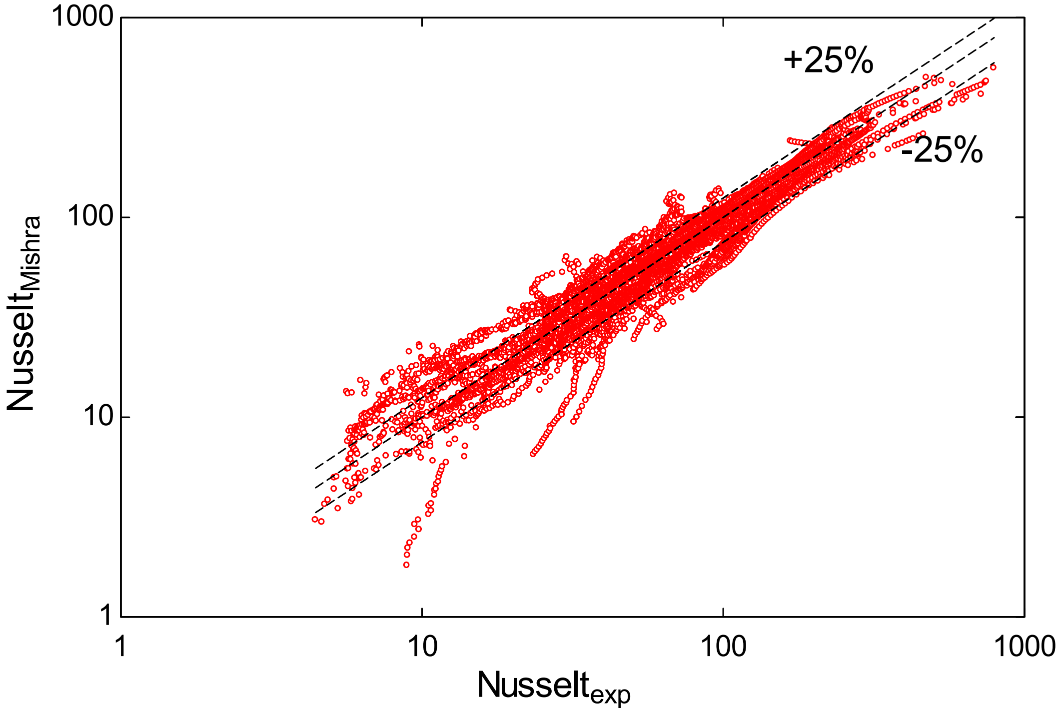

Figure 99. Predicted Nusselt number as a function of experimental Nusselt number using Mishra correlation.

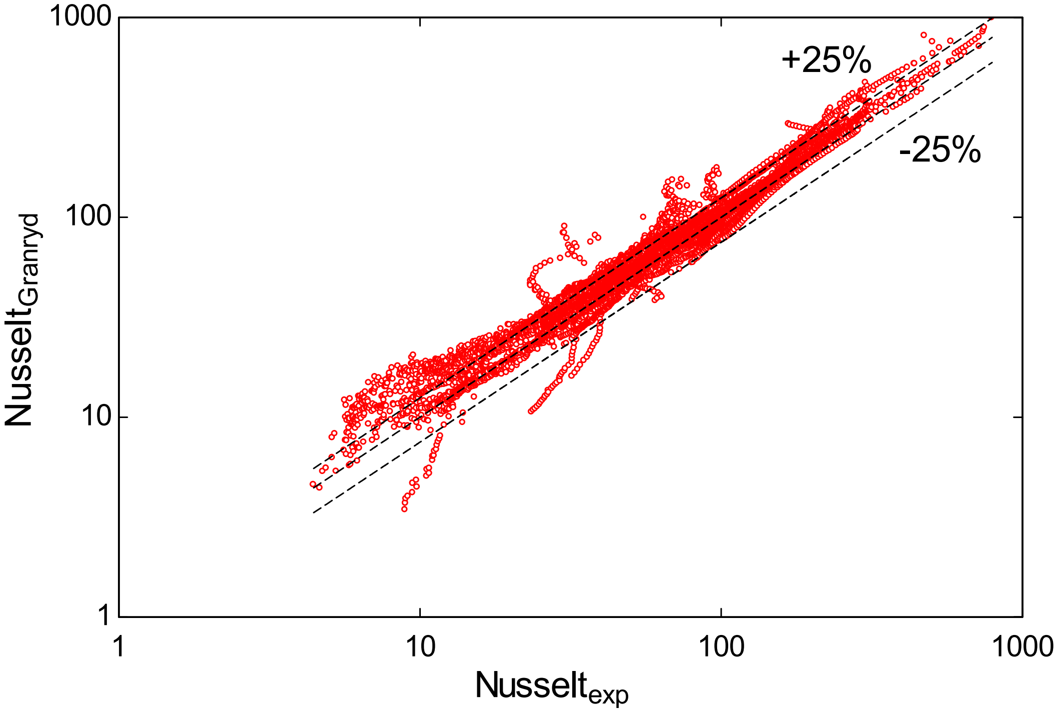

Figure 100. Predicted Nusselt number as a function of experimental Nusselt number using Granryd correlation.

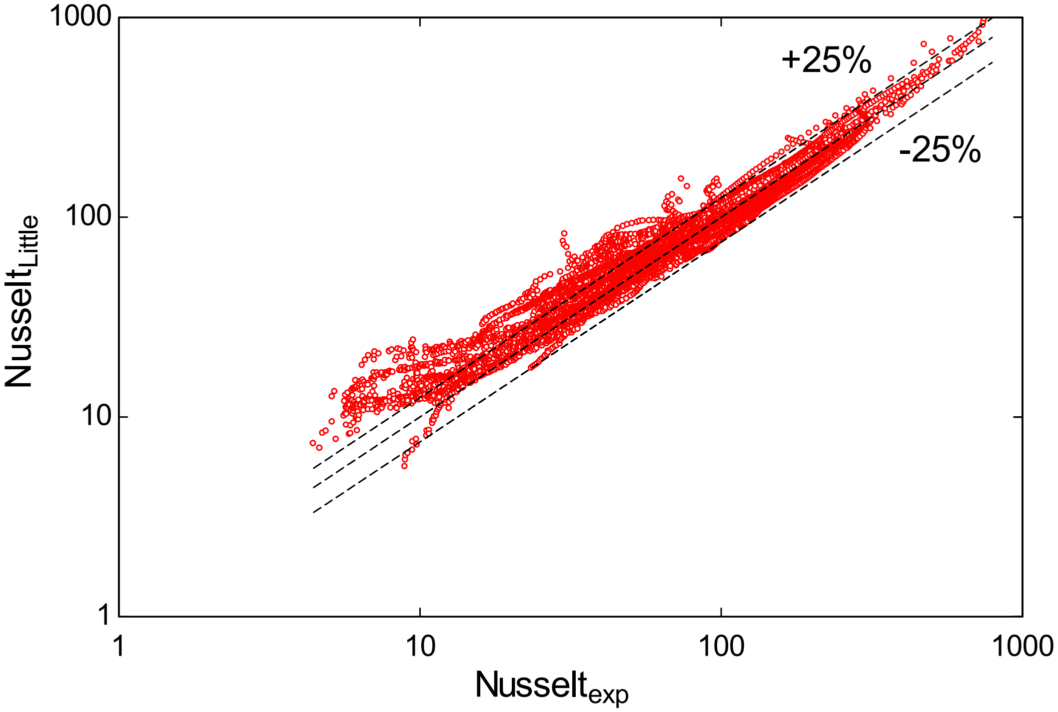

Figure 101. Predicted Nusselt number as a function of experimental Nusselt number using Little correlation.

In summary, the convective component of Chen correlation produce the worse prediction of the four selected heat transfer models. Also, Granryd, Little and Mishra predict the experimental data very well. The best agreement is obtained using Granryd with an AAD of 15.0% and the second best is given by Little with an AAD of 18%; consequently, the calculated heat transfer coefficient using correlations from the literature provide reasonable predictions.

Granryd and Little seem to be the best predictor models. Figure 102 and Figure 103 show the relative errors as a function of quality for Granryd and Little correlations, respectively. A solid line indicates the average relative error as a function of quality. Partial dryout increment the average relative error as the average quality increases over 80%. However, the relative error increases faster in the prediction done using Granryd. Little seems to be more accurate for high qualities. On the other hand, Little is less accurate as the average quality is reduced below 40%. Little seems to predict reasonable well the data between 40% and 100% of thermodynamic quality where the average error is below 20%. Granryd shows good prediction in all of the range, but it is especially good for qualities between 10% and 80% showing average relative error below 20%.

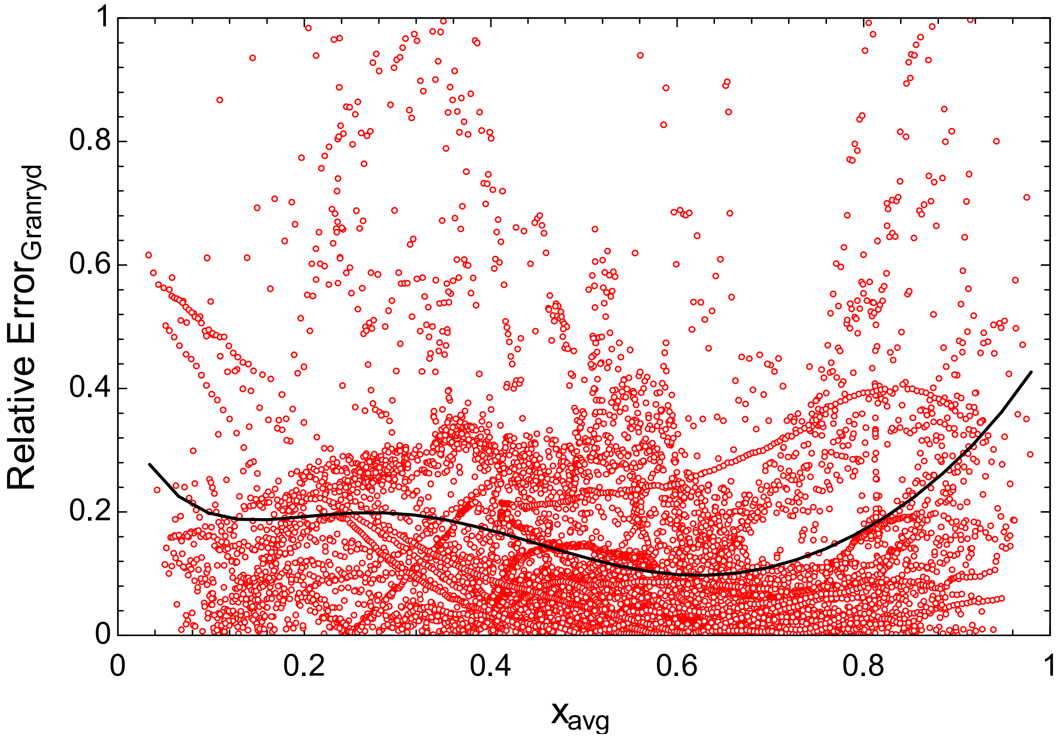

Figure 102. Relative error of the prediction as a function of average quality using Granryd correlation.

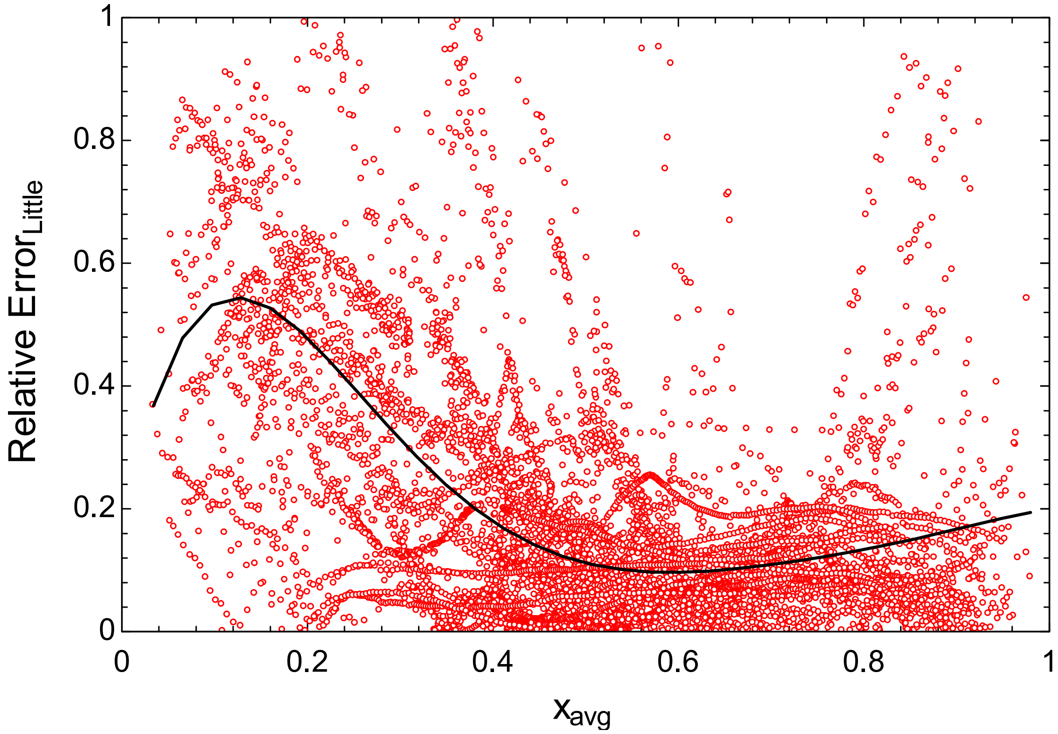

Figure 103. Relative error of the prediction as a function of average quality using Little correlation.

Table 21 shows the fraction of the empirical data predicted using Little and Granryd with relative error lower than 10, 20, 25, 30 and 50%. In general, about 80% of the experimental data is predicted with relative error lower than 30% using both correlations. Granryd works extremely well with the data collected for the 1.5 and 3.0 test sections predicting more than 90% with a relative error lower than 30%. As the diameter decreases, the prediction becomes less accurate. 97% of the data for 3.0 mm, 91% for 1.5 mm and 69% for 0.5 mm are calculated with a relative error lower than 30% using Granryd. Little includes 91%, 82% and 73% for the 3.0, 1.5 and 0.5 mm, respectively. Little predicts more data with a relative error lower than 30% in the 0.5 mm test section.

Table 21. % of experimental data for different % of relative error

Models		**% of experimental data with a relative error lower than**				
		10%	**20%**	**25%**	**30%**	**50%**
Granryd	0.5 mm	32%	53%	62%	69%	85%
	1.5 mm	51%	74%	82%	91%	98%
	3.0 mm	72%	92%	96%	97%	100%
	All data	52%	74%	81%	87%	95%
Little	0.5 mm	44%	64%	70%	73%	83%
	1.5 mm	44%	71%	78%	82%	92%
	3.0 mm	57%	83%	88%	91%	97%
	All data	47%	73%	79%	82%	91%

5.6. Models evaluation using Nellis et al. [47]

Nellis et al. [30] presented experimental heat transfer coefficient data for six sets of evaporating zeotropic mixtures on a horizontal test section with an inner diameter of 0.835 mm. The zeotropic mixtures are formed by different compositions of nitrogen, methane, ethane, propane and isobutane. The test conditions include variation of mass fluxes between 200 and 900 kg/m^2-s, evaporating pressures between 400 and 1400 kPa with a constant heat flux of 80 kW/m^2 for all test conditions. Little correlation was validated using Nellis et al. data.

Little and Granryd models are used to predict Nellis et al. data. Figure 104 shows a log/log plot of the predicted versus the empirical Nusselt number. Also, the 25% error lines are indicated.

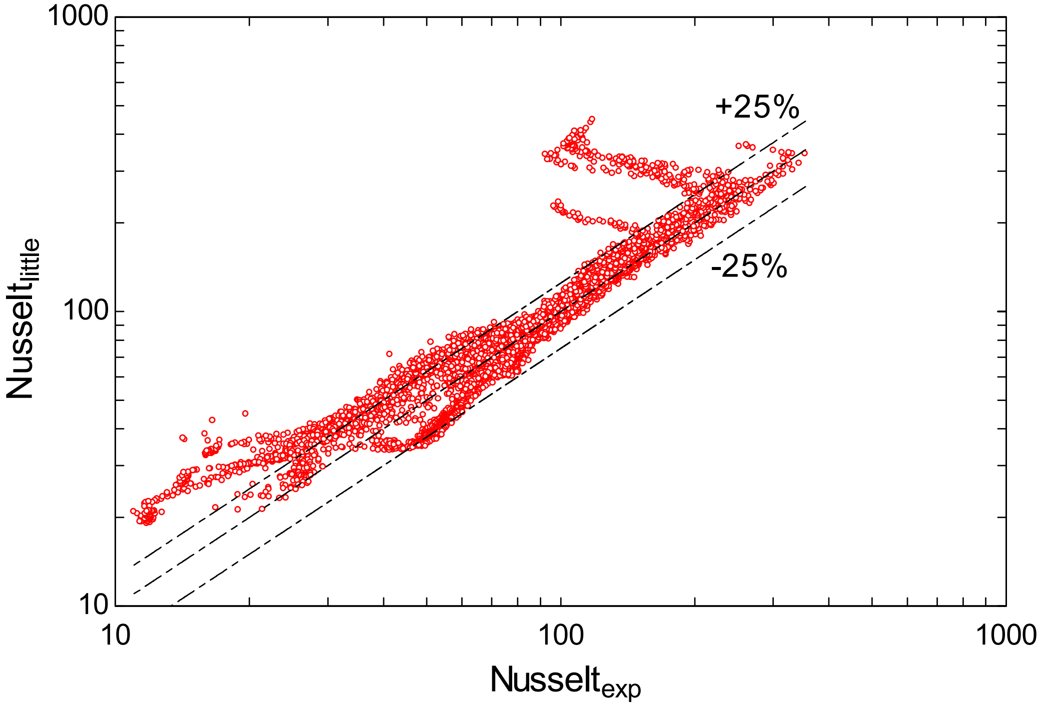

Figure 104. Predicted Nusselt number using Little as a function of experimental Nusselt number obtained by Nellis et al. [47]

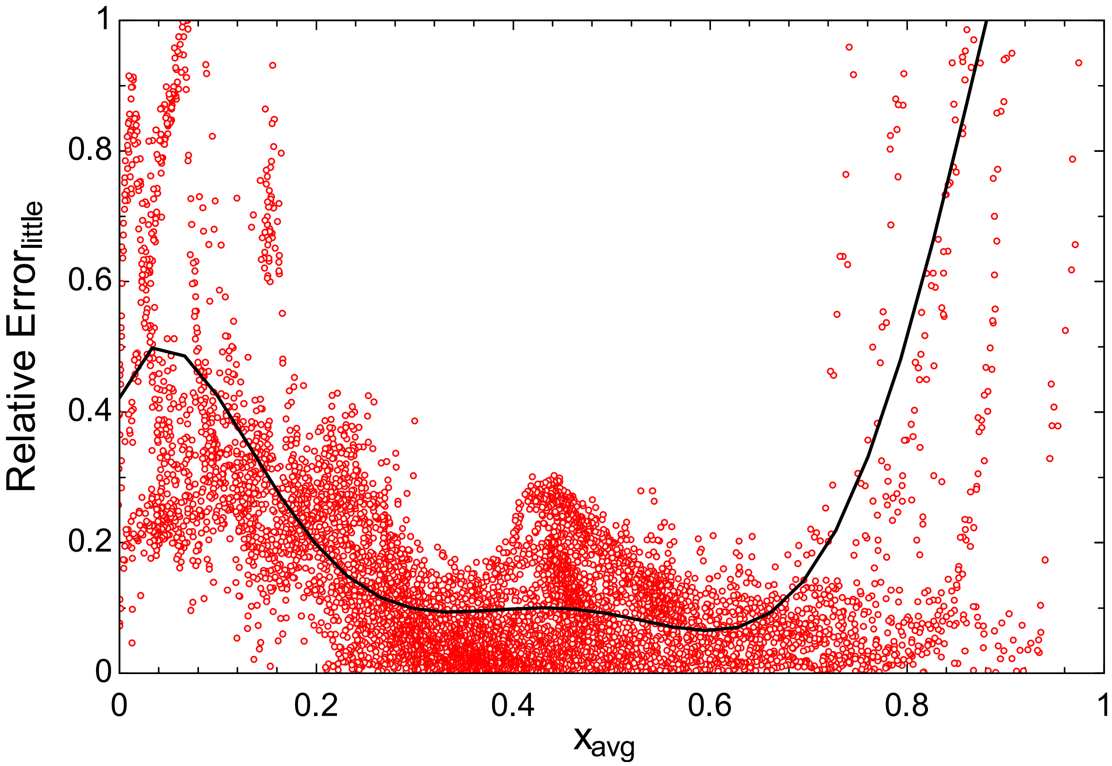

Figure 105. Relative error of the prediction as a function of average quality for Nellis et al. data using Little correlation.

Figure 104 indicates that Little model predicts Nellis experimental data well. At low and high Nusselt numbers, the correlation shows greater errors. The excessive error at high Nusselt number is related with partial dryout of the mixture flowing within the tube. Figure 105 shows that the dryout appears when thermodynamic qualities are greater than 70%. At the low quality region, the Nusselt number is over predicted as displayed on the low end of Figure 105 (left). The relative error as a function of quality shown in Figure 105 helps to visualize how the relative error increases as quality decreases below 30%. Increased relative error at low qualities occurs because Little is based on annular flow and it is less likely to have annular flow at low qualities. The minimum relative errors are observed between 30% and 70% of thermodynamic qualities.

The Little correlation has an AAD of 19% for the Nellis data and it is able to predict 87% of Nellis data with a relative error lower than 30% according to Table 22.

Figure 106 shows the predicted Nusselt number using the Granryd correlation as a function of the experimental Nusselt number obtained by Nellis. Most of the data fall within the ±25% error lines.

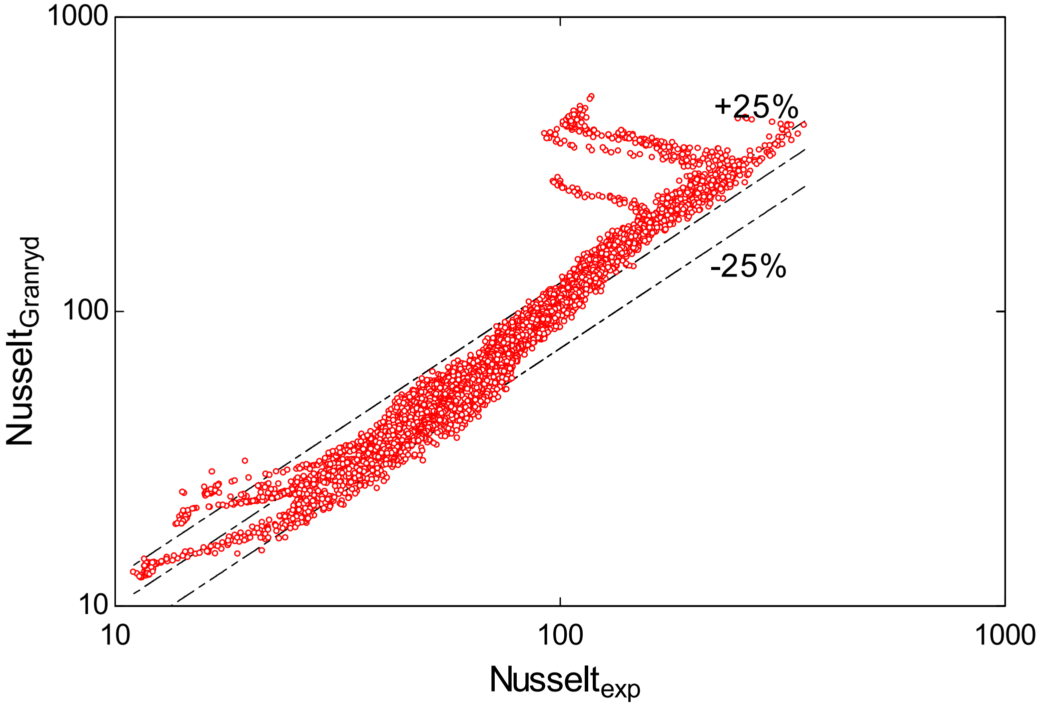

Figure 106. Predicted Nusselt number using Granryd as a function of experimental Nusselt number obtained by Nellis et al. [47]

Figure 107 shows the relative error using Granryd as a function of average quality. The behavior is similar to what was seen for the actual experimental data. It shows a low average relative error for low qualities and the error keeps low up to 70% of average quality. The error grows faster than Little at high quality values.

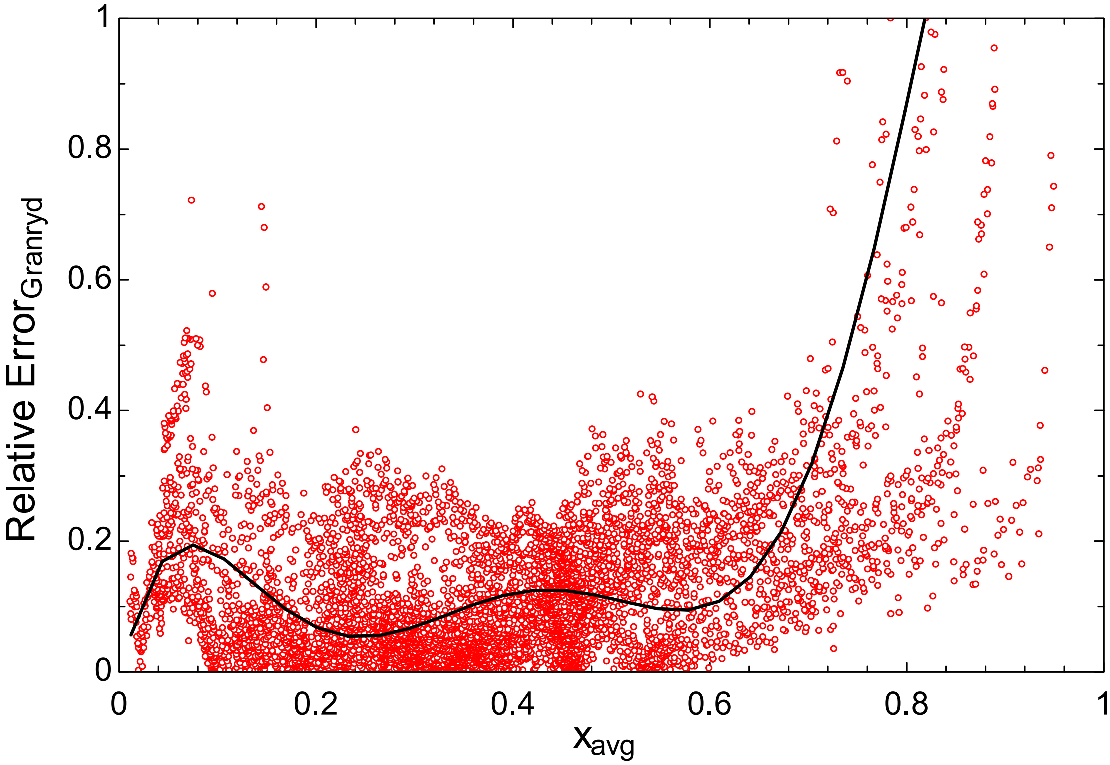

Figure 107. Relative error of the prediction as a function of average quality for Nellis et al. data using Granryd correlation

Nellis et al. data is predicted with an AAD of 18% using Granryd model. Table 22 shows that Granryd is able to predict 92% of Nellis data with a relative error lower than 30%.

Table 22. % of experimental data for different % of relative error

Models	**% of experimental data with a relative error lower than**				
	10%	**20%**	**25%**	**30%**	**50%**
Granryd	50%	76%	86%	92%	96%
Little	47%	72%	80%	87%	94%

5.7. Model generalization

The Nellis data were obtained in a test section with an inner diameter of 0.835 mm, which is between the small (0.5 mm) and medium (1.5 mm) diameter tested in this research; however, the prediction of Nellis data seems to be slightly better using Little and Granryd correlations. One reason that could explain this result is that the mass fluxes tested by Nellis are greater. A low mass flux may produce laminar flow even at high qualities, which may not be well modeled. This hypothesis might be reinforced if the diameter is reduced. Figure 108 and Figure 109 show the relative error of the combined data (Nellis et al. and the actual data) as a function of the factor $Re\,x/(1-x)$ using Little and Granryd, respectively. $Re\,x/(1-x)$ is low when the Reynolds number of the mixture is low (laminar condition) or the quality is low (no annular flow). A clear trend is observed for Little calculation (Figure 108) when the factor decreases the high relative error increases. Peaks of relative error greater than 50% are observed when the factor is lower than 500. Also, the dryout region is clear when the factor is greater than 40000.

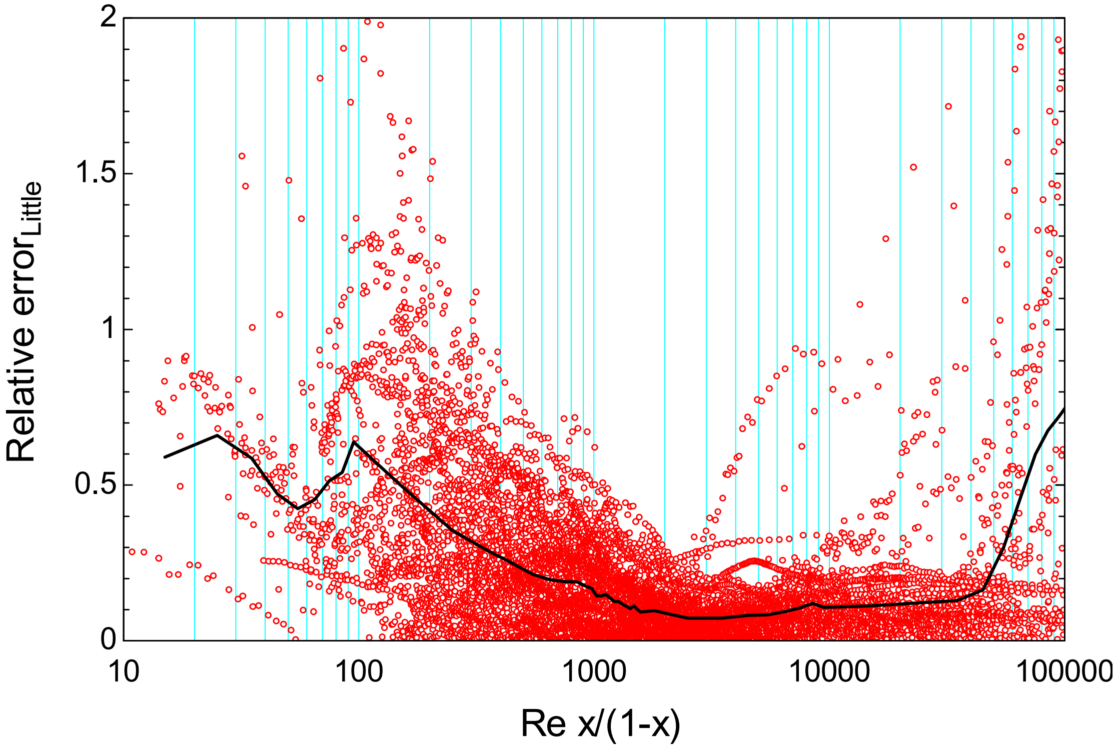

Figure 108. Relative error of all data combined using Little, Nellis et al and actual data, as a function of Re x/(1-x).

The same trend is observed in Figure 109 for Granryd correlation; however, the increment in the relative error is not as dramatically as using Little when the factor $Re\,x/(1-x)$ is reduced below 500. Even though Granryd predicts better heat transfer coefficient at low Reynolds number and low qualities, Granryd is less accurate when $Re\,x/(1-x)$ is lower than 500.

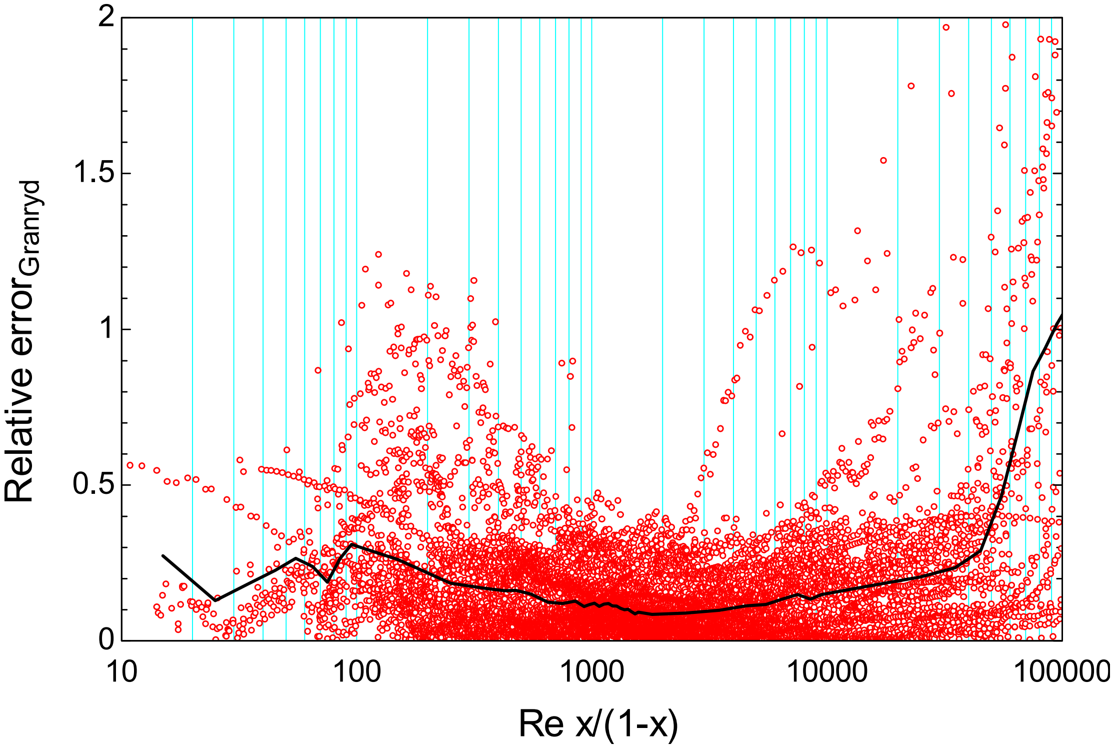

Figure 109. Relative error of all data combined using Granryd, Nellis et al and actual data, as a function of Re x/(1-x).

Figure 110 presents the fraction of data with relative error lower than 25% as a function of the factor $Re\,x/(1-x)$. Little correlation shows a clear transition when the factor $Re\,x/(1-x)$ is around 500. 60% or less of the data is predicted with relative error lower than 25% for factor values lower than 500 using Little correlation. On the other hand, at least 80% of data is predicted with a relative error lower than 25% when the factor is greater than 500. A value of 500 for this factor is suggested as the limit for use of the Little correlation with reasonable accuracy. Granryd is clearly better predicting heat transfer coefficient for low $Re\,x/(1-x)$ values because at least 70% of the data show relative error low than 25%. When the factor increase up to values close to 2000 or higher, Little predictions are slightly better than Granryd.

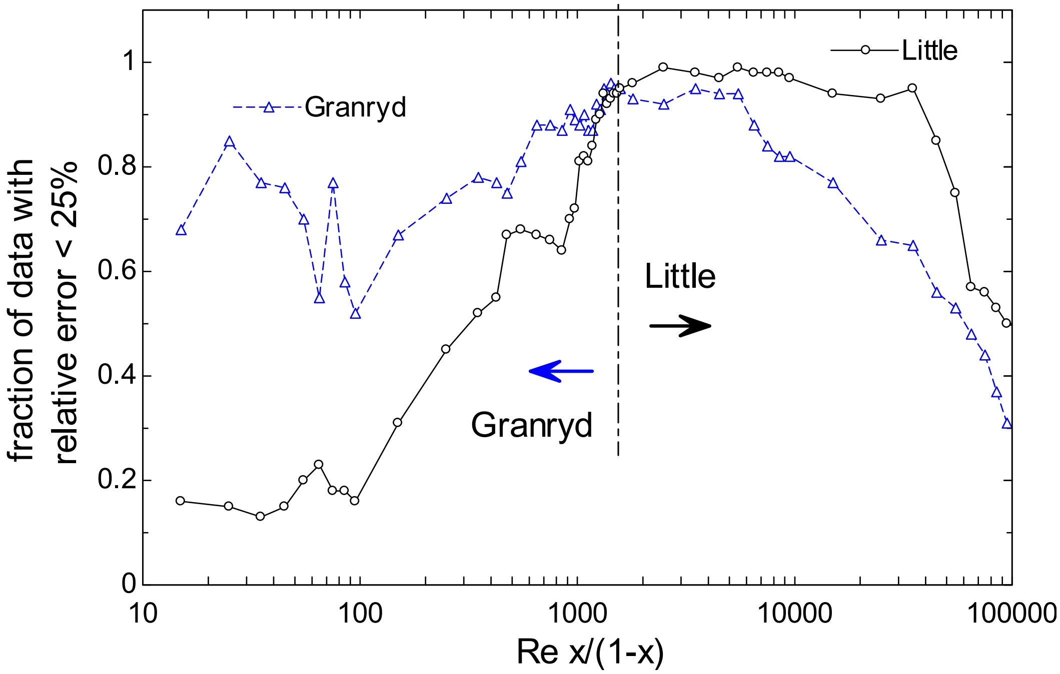

Figure 110. Fraction of data with relative error lower than 25% as a function of Re x/(1-x).

6. FRICTIONAL PRESSURE DROP

6.1. Literature review

Some reported studies such as Ould Didi et al. [71], Greco and Vanoli [72], Jung and Radermacher [73] and Sami and Duong [74] include pressure drop information for zeotropic mixtures with small temperature glides and nearly-azeotropic mixtures that change phase at temperatures close to room temperature in conventional channels. Ould Didi et al. [71] report two-phase frictional pressure drop data measured in horizontal tubes (D_H = 10.92 and 12.00 mm) while evaporating five refrigerants (R-134a, R-123, R-402a, R-404a and R-502) as a function of mass flux (100 - 500 kg/m^2-s) and thermodynamic quality (0.04 to 1.0). Ould Didi et al. concluded that Müller-Steinhagen and Heck [6] and Gronnerud [75] methods provide the best predictions for their data. Greco and Vanoli [72] describe an experimental study of the frictional pressure drop for boiling R-22, R-507, R-404A, R-134a, R-407C and R-410A in a horizontal tube (D_H = 6 mm). The pressure drop is provided as a function of mass flux (280–1080 kg/m^2-s) while the evaporating pressure is fixed at 7.0 bar. Chawla's [76] friction correlation shows the best-fit to their experimental data.

Jung and Radermacher [73] report pressure drop data collected during boiling of pure and mixed refrigerants of R-22, R-114, R-12, and R-152a in a horizontal test section. The heat flux and mass flux vary from 10–45 kW/m^2 and 230–720 kg/m^2-s, respectively. Jung and Radermacher reported good correlation between the Lockhart and Martinelli parameter and pressure drop with both pure and mixed refrigerants. Also, Jung and Radermacher proposed a correlation that predicts their experimental data with a mean deviation of 8.4%. Sami and Duong [74] present empirical data for a boiling mixture R-22/R-114 in the annuli of a horizontal enhanced surface tubing evaporator with 17.3, 28.6, and 32.3 mm for the inner , envelope and an outer diameters, respectively. Heat flux ranged between 5 and 25 kW/m^2 while the mass flux varied between 180 and 290 kg/m^2-s at a pressure of 570 kPa. A correlation is proposed to predict pressure drop of their R-22/R-114 (zeotropic refrigerant) mixture.

One of the few studies that involve conditions similar to those described here is reported by Baek et al. [77]. They report pressure drop data during boiling for what they called “macro heat exchangers” (D_H = 1.58 mm) and “micro heat exchangers” (D_H = 0.34 mm) installed in a mixed refrigerant Joule-Thomson system using two-phase zeotropic mixtures as a function of mass flux. A four component mixture formed by Argon, R-14, R-23, and R-218 (0.26/0.21/0.21/0.32 molar composition) and a five component mixture formed by Argon, R-14, R-23, R-218, and R-134a (0.34/0.22/0.10/0.15/0.19 molar composition) were tested over a temperature range between 70 and 210 K and an evaporating pressure of 200 kPa. The pressure drop that is reported takes into account the pressure difference between the inlet and the outlet of the heat exchangers. Baek et al. [77] concluded that the frictional pressure drop for the zeotropic mixtures tested while operating at cryogenic temperatures can be predicted with the Qu and Mudawar [78] and Sami and Duong [74] correlations for macro and micro heat exchangers, respectively. However, their global measurement of the frictional pressure drop does not allow a fundamental understanding of two-phase frictional pressure drop phenomenon because it does not provide details on the local pressure drop, which limits the application of their conclusion to systems that have different operating conditions.

6.2. Experimental data description

One of the objectives of this study is to present the results of experimental frictional pressure drop data obtained from boiling zeotropic mixtures. Two horizontal test sections are used with inner diameters *ID* = 0.5 mm and *ID* = 1.5 mm. The majority of the pressure drop data were collected together with heat transfer coefficients measurements; however, some data were obtained under adiabatic conditions.

Table 23 through Table 27 provide mixture composition and test conditions for each set of data collected. Figure 111 to Figure 115 show the corresponding measured frictional pressure drop obtained during boiling for each corresponding zeotropic mixture.

Table 23. Hydrocarbon mixture, composition and test conditions.

Run	Mixture & Composition (by volume)	Condition	P kPa	G kg/s-m^2	$\dot{Q}''$ kW/m^2	ID mm	T_{bubble} K	T_{dew} K	ΔT_{glide} K
HC-1	$CH_4/C_2H_6/C_3H_8$ (0.45/0.35/0.20)	Diabatic	787±3	143±12	56.5±1.4	0.5	160	246	86
HC-2	$CH_4/C_2H_6/C_3H_8$ (0.45/0.35/0.20)	Adiabatic	779±3	242±12		0.5	160	246	86
HC-3	$CH_4/C_2H_6/C_3H_8$ (0.45/0.35/0.20)	Diabatic	785±3	143±1	56.9±0.2	1.5	160	246	86
HC-4	$CH_4/C_2H_6/C_3H_8$ (0.45/0.35/0.20)	Adiabatic	789±3	144±1		1.5	160	246	86
HC-5	$CH_4/C_2H_6/C_3H_8$ (0.45/0.35/0.20)	Diabatic	265±3	239±2	56.7±0.2	1.5	135	221	86
HC-6	$CH_4/C_2H_6/C_3H_8$ (0.45/0.35/0.20)	Diabatic	269±3	144±1	57.0±0.2	1.5	135	221	86

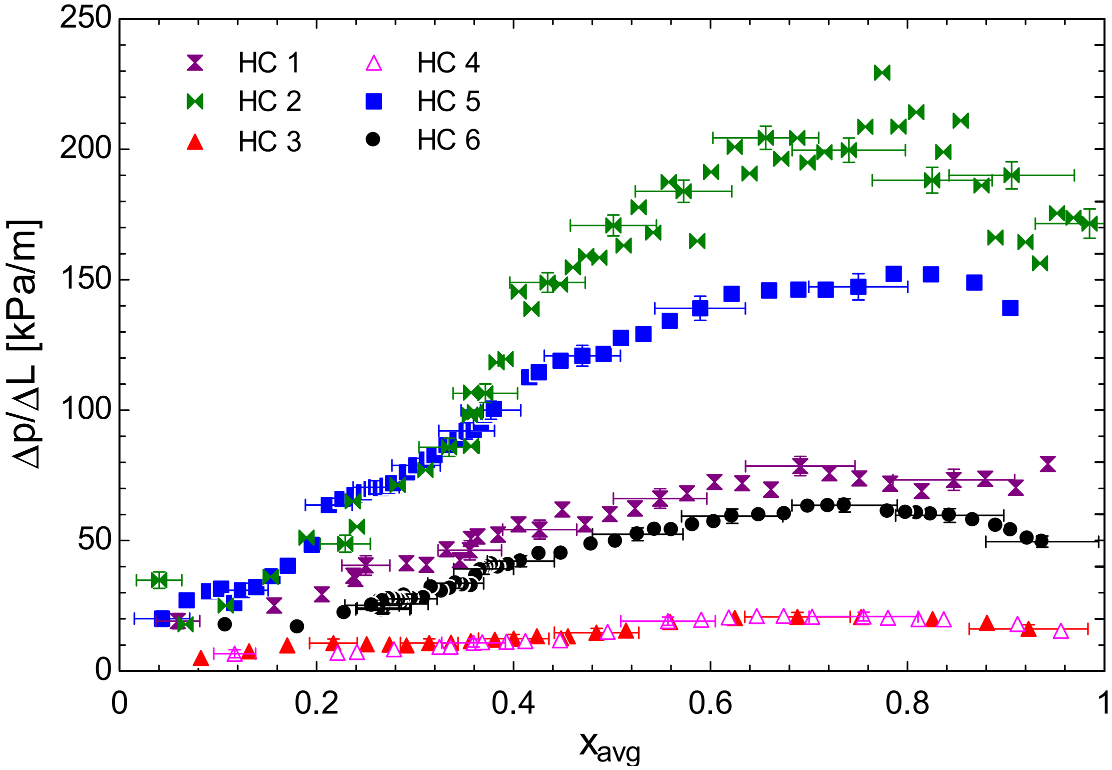

Figure 111. Frictional pressure drop for hydrocarbons mixture as a function thermodynamic average quality

Table 24. Hydrocarbon diluted with nitrogen mixture, composition and test conditions.

Run	Mixture & Composition (by volume)	Condition	P kPa	G kg/s-m^2	$\dot{Q}''$ kW/m^2	ID mm	T_{bubble} K	T_{dew} K	ΔT_{glide} K
HC-N_2 1	$CH_4/C_2H_6/C_3H_8/N_2$ (0.36/0.28/0.16/0.20)	Diabatic	788±3	145±12	56.6±1.4	0.5	105	240	135
HC-N_2 2	$CH_4/C_2H_6/C_3H_8/N_2$ (0.36/0.28/0.16/0.20)	Diabatic	787±3	143±1	56.5±0.2	1.5	105	240	135
HC-N_2 3	$CH_4/C_2H_6/C_3H_8/N_2$ (0.27/0.21/0.12/0.40)	Diabatic	786±3	145±12	56.6±1.4	0.5	103	232	129
HC-N_2 4	$CH_4/C_2H_6/C_3H_8/N_2$ (0.27/0.21/0.12/0.40)	Diabatic	786±3	143±1	56.8±0.2	1.5	103	232	129

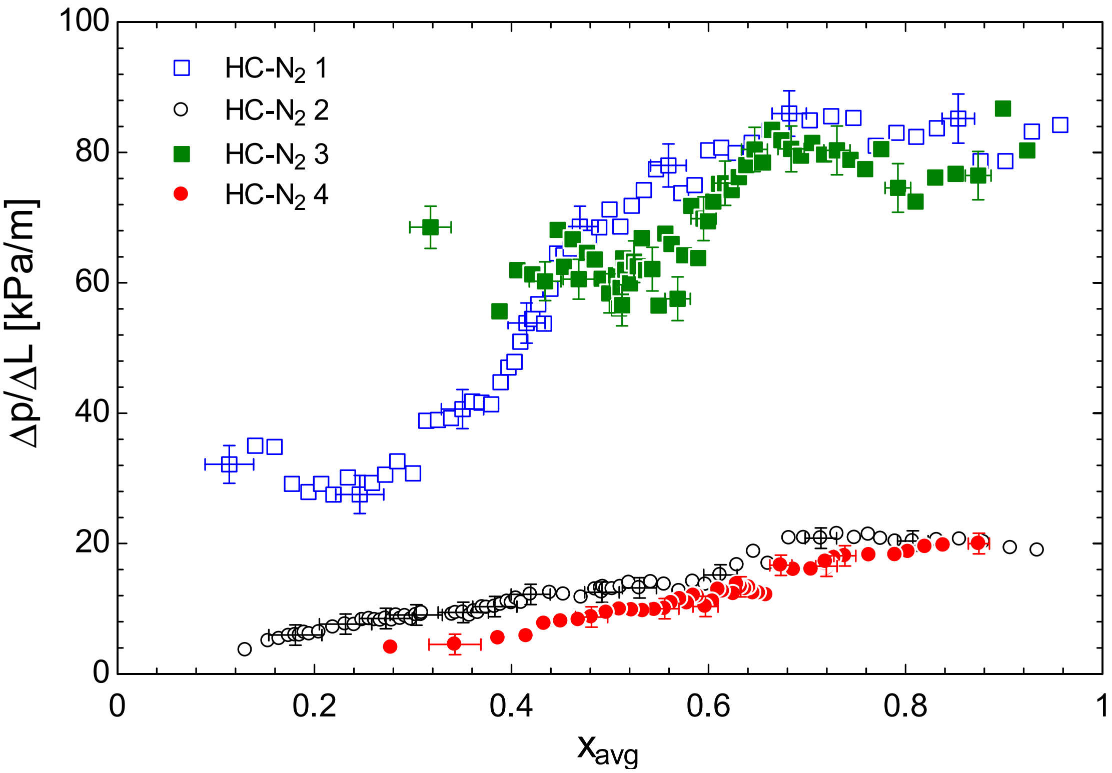

Figure 112. Frictional pressure drop for hydrocarbon mixtures diluted with nitrogen as a function thermodynamic average quality

Table 25. Synthetic mixture, composition and test conditions

Run	Mixture & Composition (by volume)	Condition	P kPa	G $kg/s\text{-}m^2$	$\dot{Q}''$ kW/m^2	ID mm	T_{bubble} K	T_{dew} K	ΔT_{glide} K
Syn 1	R-14/R-23/R-32/R-134a (0.35/0.15/0.15/0.35)	Diabatic	789±3	145±12	27.8±1.0	0.5	186	275	89
Syn 2	R-14/R-23/R-32/R-134a (0.35/0.15/0.15/0.35)	Diabatic	788±3	145±12	41.7±1.2	0.5	186	275	89
Syn 3	R-14/R-23/R-32/R-134a (0.35/0.15/0.15/0.35)	Diabatic	790±3	143±1	27.8±0.2	1.5	186	275	89
Syn 4	R-14/R-23/R-32/R-134a (0.35/0.15/0.15/0.35)	Diabatic	790±3	144±1	41.8±0.2	1.5	186	275	89
Syn 5	R-14/R-23/R-32/R-134a (0.35/0.15/0.15/0.35)	Diabatic	788±3	242±2	27.8±0.2	1.5	186	275	89
Syn 6	R-14/R-23/R-32/R-134a (0.35/0.15/0.15/0.35)	Diabatic	271±3	145±1	27.8±0.2	1.5	159	248	89

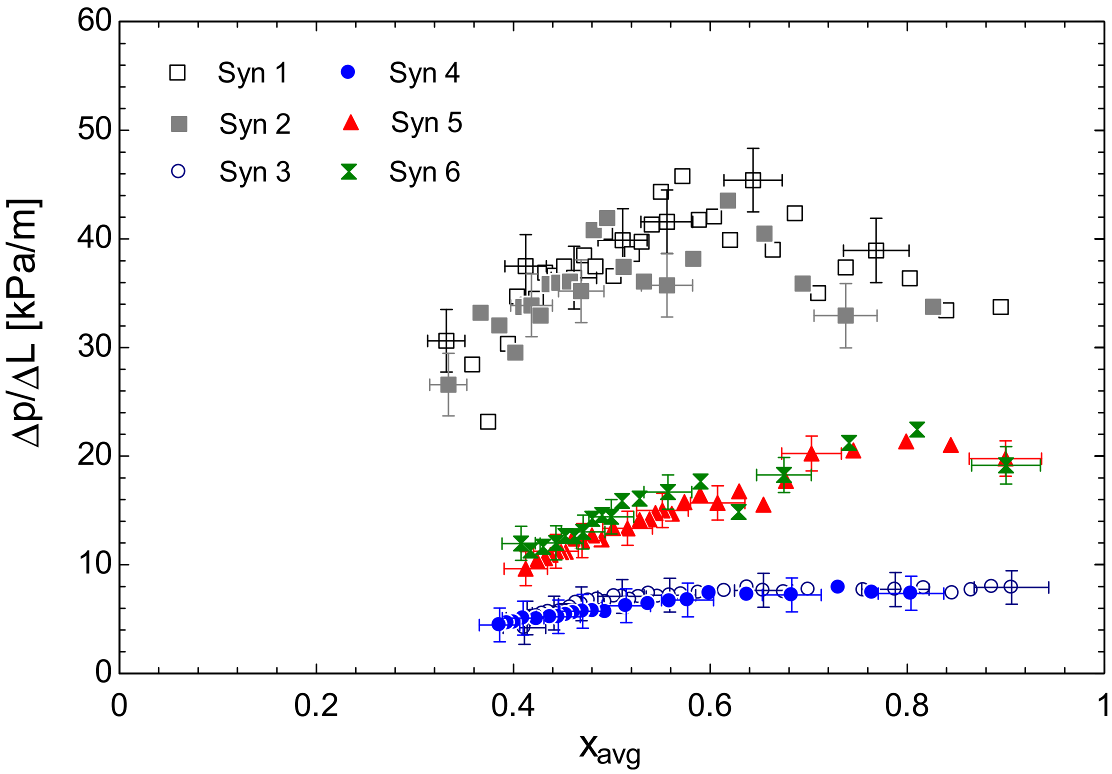

Figure 113. Frictional pressure drop for synthetic mixtures as a function thermodynamic average quality

Table 26. Synthetic mixtures diluted with argon, composition and test conditions.

Run	Mixture & Composition (by volume)	Condition	*P* *kPa*	*G* *kg/s-m*^{2}	$\dot{Q}''$ *kW/m*^{2}	*ID* *mm*	T_{bubble} *K*	T_{dew} *K*	ΔT_{glide} *K*
Syn-Ar 1	R-14/R-23/R-32/R-134a/Ar (0.28/0.12/0.12/0.28/0.20)	Diabatic	788±3	144±12	27.8±1.0	0.5	153	268	115
Syn-Ar 2	R-14/R-23/R-32/R-134a/Ar (0.28/0.12/0.12/0.28/0.20)	Diabatic	789±3	144±1	27.8±0.2	1.5	153	268	115
Syn-Ar 3	R-14/R-23/R-32/R-134a/Ar (0.21/0.09/0.09/0.21/0.40)	Diabatic	788±3	143±12	27.8±1.0	0.5	129	261	132
Syn-Ar 4	R-14/R-23/R-32/R-134a/Ar (0.21/0.09/0.09/0.21/0.40)	Diabatic	789±3	143±1	27.9±0.2	1.5	129	261	132

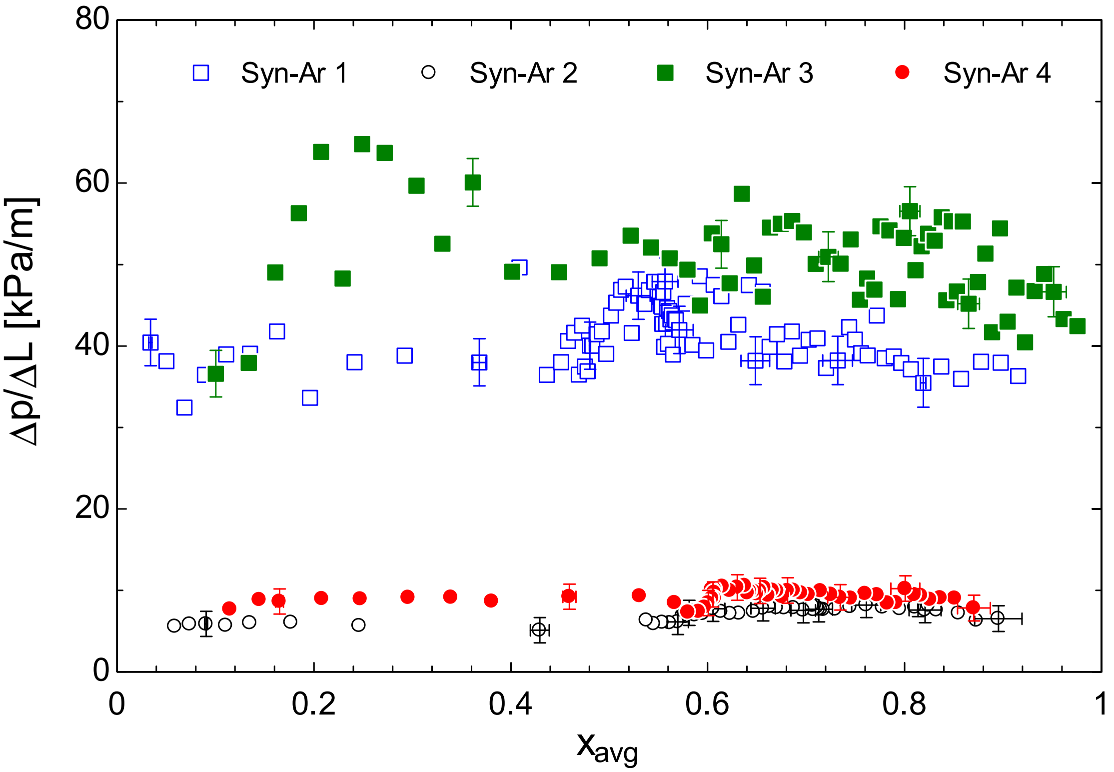

Figure 114. Frictional pressure drop for synthetic mixtures diluted with argon as a function thermodynamic average quality

Table 27. Binary mixture, composition and test conditions.

Run	Mixture & Composition (by volume)	Condition	*P* *kPa*	*G* *kg/s-m*^{2}	$\dot{Q}''$ *kW/m*^{2}	*ID* *mm*	T_{bubble} *K*	T_{dew} *K*	ΔT_{glide} *K*
Bin-1	CH_4/C_2H_6 (0.60/0.40)	Diabatic	784±3	145±12	55.9±1.4	0.5	155	208	53
Bin-2	CH_4/C_2H_6 (0.60/0.40)	Diabatic	789±3	142±12	86.3±1.7	0.5	155	208	53
Bin-3	CH_4/C_2H_6 (0.60/0.40)	Diabatic	788±3	145±1	56.8±0.2	1.5	155	208	53
Bin-4	CH_4/C_2H_6 (0.60/0.40)	Diabatic	786±3	242±2	56.9±0.2	1.5	155	208	53
Bin-5	CH_4/C_2H_6 (0.60/0.40)	Diabatic	785±3	242±2	85.4±0.3	1.5	155	208	53
Bin-6	CH_4/C_2H_6 (0.60/0.40)	Diabatic	266±3	241±2	56.7±0.2	1.5	132	185	53

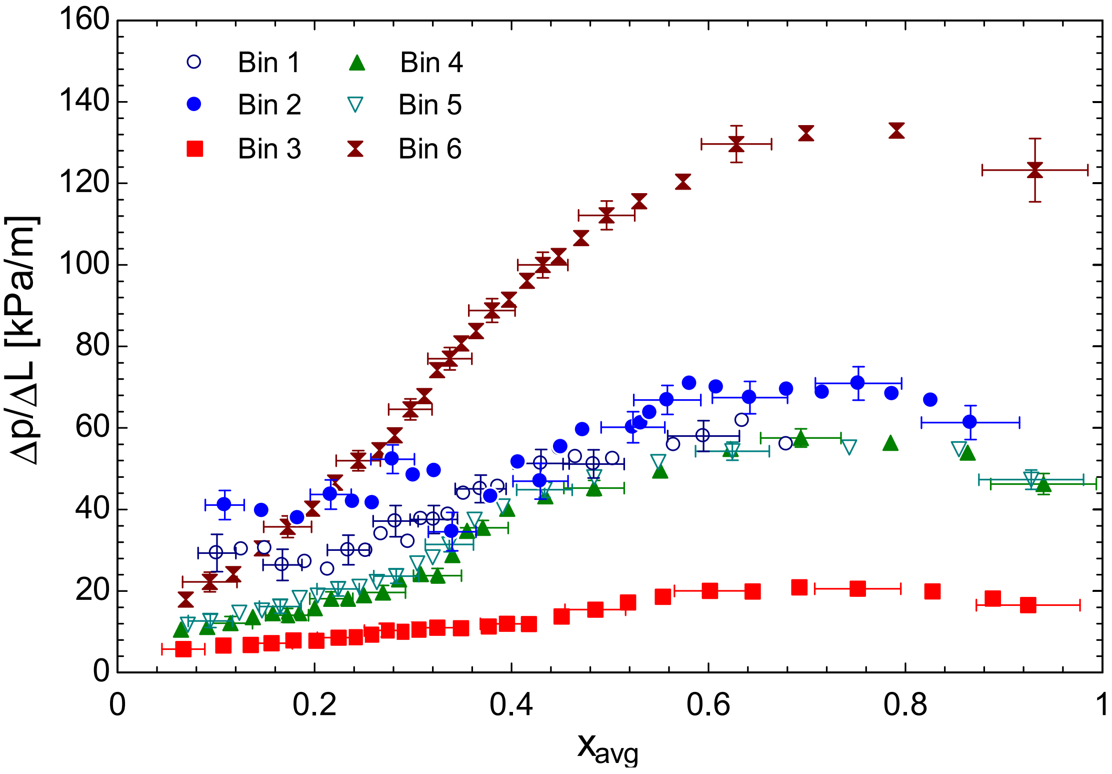

Figure 115. Frictional pressure drop for the binary mixture as a function thermodynamic average quality

As an exercise to qualitatively understand how the experimental data of zeotropic mixture behave, we assume that a homogeneous model is sufficient to describe zeotropic mixtures. The homogeneous theory treats two-phase flow as a pseudo single phase fluid as shown by equation (110). The homogeneous model suggests that the frictional pressure drop can be explained as a function of mass flux, friction factor, inside diameter, and mixture density. The pressure drop increases because mass flux (*G*) and friction factor (*f*) increase, and diameter (*ID*) and mixture density (ρ_{mixt}) are reduced. Mass flux and diameters effects are clear if the experimental data is observed because they follow the trends suggested by the homogeneous model. The mixture density may be affected by composition and evaporating pressure. The density of the vapor fraction is proportional to evaporating pressure (Table 11); consequently, as the pressure is reduced, the mixture density decreases increasing the pressure drop. This behavior can also be observed in the experimental data. The friction factor effect is the most complicated to observe because it is a function of the Reynolds number and relative roughness. If the flow is turbulent during the entire phase change, between $x = 0$ and 100% (qualities), the pressure drop behavior can be separated into two regions: $x = 0$ to 85%, and $x = 85\%$ to 100%. In the $x = 0$ to 85% region, the pressure drop increases with increasing vapor fraction reaching a maximum at around 85%. This trend is influenced mostly by mixture density. The mixture density decreases as more liquid is evaporated resulting in increase in mixture velocity and pressure drop. In this region, the two-phase friction factor slowly decreases proportional to $Re^{-1/4}$. As the quality increases, mixture density and friction factor compete in their effect on pressure drop. When the quality is greater than 85%, the friction factor dominates because the mixture viscosity approaches the viscosity of vapor alone, increasing the Reynolds number; therefore, the friction factor and the pressure drop decreases, similar as described by Muller-Steinhagen and Heck [6].

This situation is observed in most of the 1.5 mm data. Difficulties in interpreting that data start when part of the two-phase region is laminar because the friction factor is proportional to $Re^{-1} \propto \mu_{2ph}$; therefore, friction factor and mixture density compete as the dominant mechanisms. This situation produces high pressure drop at low qualities because μ_{2ph} is close to the liquid viscosity at low qualities increasing the friction factor and the pressure drop even though the flow velocity is low. This phenomenon is observed even at the small diameter (0.5 mm data), and it is clearly observed in the synthetic dilution data that basically shows a constant pressure drop as a function of quality. Also, this behavior is partially observed for both the binary and hydrocarbon dilution data. In addition, as can be seen in Figure 112 and Figure 114 for the diluted hydrocarbon and the diluted synthetic mixtures, respectively, the frictional pressure drop is similar for 20% and 40% dilution; consequently, frictional pressure drop is a weak function of the mixture composition

6.3. Friction factor

The friction factor for all of the correlations is defined in the laminar region as:

$$f = \frac{64}{Re} \tag{108}$$

The laminar region is defined by a Reynolds number lower than 1187. This limit is similar to Müller-Steinhagen and Heck [6] criterion. The turbulent friction factor is given by Zigrang and Silvester when Reynolds numbers are greater than 3000.

$$f = \left(-2\,log\left(\frac{relrough}{3.7} - \frac{5.02}{Re} log\left(\frac{relrough}{3.7} + \frac{13}{Re} \right) \right) \right)^{-2} \tag{109}$$

The friction factor on the transition region, $1187 \leq Re \leq 3000$, is found using linear interpolation between the laminar and turbulent models.

6.4. Frictional pressure drop models comparison

Researchers of two-phase flow have developed several correlations to predict frictional pressure drop. Most of the general two-phase frictional pressure drop correlations have been developed for conventional size channels and pure fluids. There have been some attempts to adjust and modify them for application to pure fluids flowing in mini-channels. Only a few correlations have been reported for mixtures flowing in conventional channels. Many of the proposed models may be grouped in homogeneous and separated flow theories. Homogeneous model treats two-phase flow as a pseudo single phase fluid (Eq. (110)).

$$\left(\frac{dp}{dz}\right)_{2ph} = f_{2ph} \frac{G^2}{2\, ID\, \rho_{mixt}} \tag{110}$$

The friction factor is determined using conventional friction factor correlations with the two-phase Reynolds number shown in Eq. (111).

$$Re_{2ph} = \frac{G\, ID}{\mu_{2ph}} \tag{111}$$

Many authors have defined different correlations to predict the two-phase viscosity (μ_{2ph}), which is required to calculate the two-phase Reynolds number, as an arrangement of liquid and vapor viscosity. Some of the homogeneous models are shown in Table 28. Cicchitti et al. [5] and McAdams et al. [79] are responsible for the most well-known homogeneous models. Awad and Muzychka [3] propose four models to predict the two-phase viscosity based on the analogy used to calculate the thermal conductivity of a composite of two materials.

Table 28. Homogeneous models

Author	Equation	Comments
Cicchitti et al. [5]	$\mu_{2ph}=(1-x)\mu_{l,mixt}+x\mu_{v,mixt}$	Mass average model
McAdams et al. [79]	$\mu_{2ph}=\left(\frac{x}{\mu_{v,mixt}}+\frac{1-x}{\mu_{l,mixt}}\right)^{-1}$	Mass averaged the reciprocal of the liquid and vapor viscosities
Dukler et al. [80]	$\mu_{2ph}=\rho_{mixt}\left(\frac{x}{\rho_{v,mixt}}\mu_{v,mixt}+\frac{(1-x)}{\rho_{l,mixt}}\cdot\mu_{l,mixt}\right)$	Obtained from the mass averaged kinematic viscosity
Davidson et al. [81]	$\mu_{2ph}=\mu_{l,mixt}\left(1+x\left(\frac{\rho_{l,mixt}}{\rho_{v,mixt}}-1\right)\right)$	Empirical correlation. It does not approach to the vapor viscosity when the quality is 1.
Beattie and Whalley [82]	$\mu_{2ph}=\mu_{l,mixt}\cdot(1-\alpha_h)(1+2.5\,\alpha_h)+\mu_{v,mixt}\,\alpha_h$ $\alpha_h=\frac{x\rho_{l,mixt}}{x\rho_{l,mixt}+(1-x)\rho_{v,mixt}}$	Hybrid model that combine an annular and bubble flow correlation.
Lin et al. [83]	$\mu_{2ph}=\frac{\mu_{l,mixt}\,\mu_{v,mixt}}{\mu_{v,mixt}+x^{1.4}\left(\mu_{l,mixt}-\mu_{v,mixt}\right)}$	Modification of the McAdams model. Add an exponent to the quality to take into account slip between the vapor and liquid phase.
Awad and Muzychka [3] (Definition 1)	$\mu_{2ph}=\mu_{l,mixt}\frac{2\mu_{l,mixt}+\mu_{v,mixt}-2\left(\mu_{l,mixt}-\mu_{v,mixt}\right)x}{2\mu_{l,mixt}+\mu_{v,mixt}+\left(\mu_{l,mixt}-\mu_{v,mixt}\right)x}$	Analogy of Maxwell-Euken for effective thermal conductivity on two-component porous material. Liquid viscosity greater than vapor viscosity
Awad and Muzychka [3] (Definition 2)	$\mu_{2ph}=\mu_{v,mixt}\frac{2\mu_{v,mixt}+\mu_{l,mixt}-2\left(\mu_{v,mixt}-\mu_{l,mixt}\right)(1-x)}{2\mu_{v,mixt}+\mu_{l,mixt}+\left(\mu_{v,mixt}-\mu_{l,mixt}\right)(1-x)}$	Also based on analogy of Maxwell-Euken equation. Vapor viscosity is greater than liquid viscosity.
Awad and Muzychka [3] (Definition 3)	$\mu_{2ph}=0.25\left(\begin{array}{l}(3x-1)\mu_{v,mixt}+(2-3x)\mu_{l,mixt}\\+\sqrt{\left((3x-1)\mu_{v,mixt}+(2-3x)\mu_{l,mixt}\right)^2+8\mu_{l,mixt}\,\mu_{v,mixt}}\end{array}\right)$	Based on the “effective medium theory”
Awad and Muzychka [3] (Definition 4)	$\mu_{2ph}=\frac{1}{2}\left(\begin{array}{l}\mu_{l,mixt}\frac{2\mu_{l,mixt}+\mu_{v,mixt}-2\left(\mu_{l,mixt}-\mu_{v,mixt}\right)x}{2\mu_{l,mixt}+\mu_{v,mixt}+\left(\mu_{l,mixt}-\mu_{v,mixt}\right)x}\\+\mu_{v,mixt}\frac{2\mu_{v,mixt}+\mu_{l,mixt}-2\left(\mu_{v,mixt}-\mu_{l,mixt}\right)(1-x)}{2\mu_{v,mixt}+\mu_{l,mixt}+\left(\mu_{v,mixt}-\mu_{l,mixt}\right)(1-x)}\end{array}\right)$	Average of definition 1 and 2

Separated flow models consider the contribution on the frictional pressure drop of the liquid and vapor streams as if they flowed in separate tubes. The first approach, suggested by Lockhart and Martinelli [84], assumes that only a fraction of the mass flow rate flows in each tube. The liquid and vapor fractions flow in the liquid and vapor streams, respectively. In general, most of the correlations based on this approach may be expressed as the product of liquid frictional pressure drop times a two-phase friction multiplier ($\phi^2{}_l$) as shown in Eq. (112).

$$\left(\frac{dp}{dz}\right)_{2ph} = \left(\frac{dp}{dz}\right)_l \phi^2{}_l = f_l \frac{\left(G(1-x)\right)^2}{2\,ID\,\rho_{l,mixt}} \phi^2{}_l \tag{112}$$

Lockhart and Martinelli [84] proposed a graphical method to predict frictional pressure drop as a function of a parameter *X*. The dimensionless parameter *X*, also known as Lockhart and Martinelli coefficient, is defined as the square root of the ratio of the frictional pressure drop of the liquid over the vapor according to:

$$X = \sqrt{\left(\frac{dp}{dz}\right)_l \Big/ \left(\frac{dp}{dz}\right)_v} \tag{113}$$

This method separates the flow into four types: (1) liquid and vapor both laminar, (2) laminar liquid and turbulent vapor, (3) turbulent liquid and laminar vapor, and (4) liquid and vapor both turbulent. Chisholm [85] converted Lockhart and Martinelli charts into a correlation, which is a function of *X* and the Chisholm parameter, *C*. *C* is defined for each flow condition. The two-phase multiplier, $\phi^2{}_l$, in this case is given by:

$$\phi^2{}_l = 1 + \frac{C}{X} + \frac{1}{X^2} \tag{114}$$

The physical meaning may be noted if equation (112) is expanded and combined with eqns. (113) and (114). The frictional two-phase pressure drop definition results as the sum of liquid, vapor and the interphase contributions.

$$\left(\frac{dp}{dz}\right)_{2ph}=\left(\frac{dp}{dz}\right)_{l}+\left(\frac{dp}{dz}\right)_{int}+\left(\frac{dp}{dz}\right)_{v}=\left(\frac{dp}{dz}\right)_{l}+C\sqrt{\left(\frac{dp}{dz}\right)_{l}\left(\frac{dp}{dz}\right)_{v}}+\left(\frac{dp}{dz}\right)_{v} \qquad (115)$$

According to the Lockhart and Martinelli flow definitions, most of the experimental data is located in the laminar liquid and turbulent vapor condition as shown in Figure 116. There are some data in the liquid and vapor both turbulent region and few data in the liquid and vapor both laminar region. The data distribution suggests that the Chisholm parameter *C* that is most appropriate for the actual data is *C* = 12, which leads to an AAD of 45%; however, for the actual experimental data, the best fit is obtained with a C = 7, which reduces the AAD to 18%. Figure 117 shows the ratio of the experimental and the liquid frictional pressure drop as a function of the Lockhart and Martinelli coefficient.

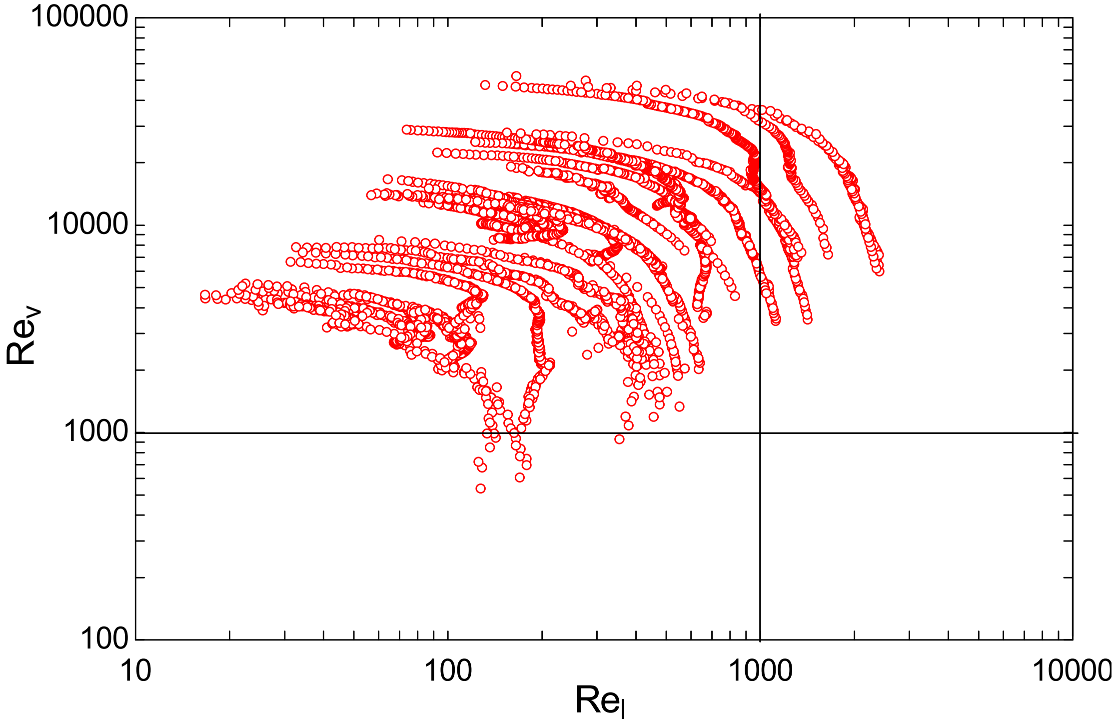

Figure 116. Distribution of experimental data according to Lockhart and Martinelli flow conditions

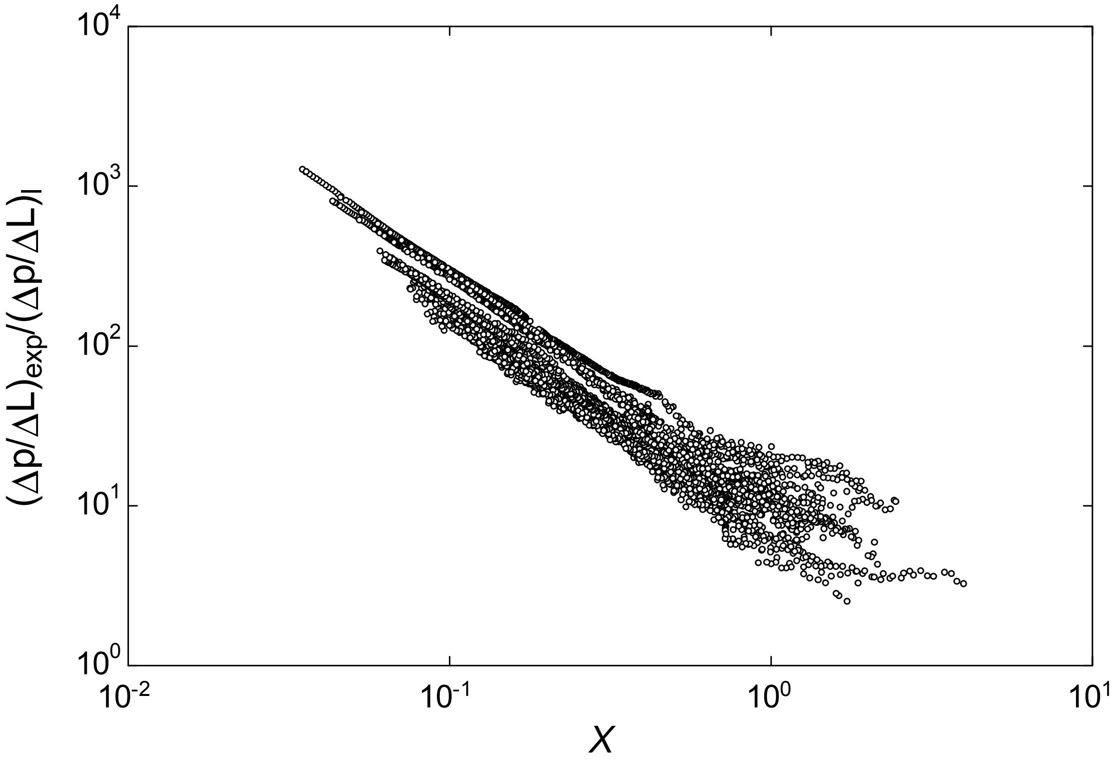

Figure 117. Experimental-liquid frictional pressure drop ratio as a function of Lockhart and Martinelli coefficient

Because the Chisholm parameter C seems to change as the flow condition changes, it may not be a constant. Many correlations are based on the Lockhart and Martinelli proposition, and they try to predict the Chisholm parameter C as shown in

Table **29**. Correlations [26] to [31] have been proposed for use with mini-channels with two-phase pure fluids. Mishima and Hibiki [7] say that C is a function of the channel diameter and decreases as the diameter decreases. This statement seems to be true because the best curve fit with the experimental data is obtained with $C = 6$ and $C = 7.6$ on the 0.5 and 1.5 mm test section, respectively. Mishima and Hibiki equation predicts $C = 3.2$ and 8.2 for the 0.5 and 1.5 mm test section, respectively. This correlation shows a reasonable agreement with 1.5 mm, but it seems to decrease too fast for the small diameter.

Table 29. Separated flow models, $\phi^2{}_l$ or $\phi^2{}_v$ multiplier

Author	Equation	Comments
Lockhart and Martinelli [84]	$\phi^2{}_l = 1 + \frac{C}{X} + \frac{1}{X^2}$ $C = 5$ laminar liquid/laminar vapor $C = 10$ turbulent liquid/laminar vapor $C = 12$ laminar liquid/turbulent vapor $C = 20$ turbulent liquid/turbulent vapor	Simultaneous flow of air with liquids as benzene, kerosene, water and oils. Tubes with diameters between 1.5 to 25.8 mm.
Mishima and Hibiki [7]	$C = 21\left(1 - exp\left(-319\,ID\right)\right)$	Air/water, ammonia, and R-113/N$_2$. Tubes with diameters between 1 to 4 mm
Kawahara et al. [86]	$C = 0.24$	Water and N$_2$. 100 micrometer tube
Qu and Mudawara [78]	$C = 21\left(1 - exp\left(-319\,ID\right)\right)\left(0.00418\,G + 0.0613\right)$	Water. Square multi channels 231 x 713 micrometers
Sun and Mishima [4]	$C = 26 \cdot \left(1 + Re_l / 1000\right) \cdot \left(1 - exp\left(-\frac{0.153}{0.27 \cdot La + 0.8}\right)\right)$ $\phi^2{}_l = 1 + \frac{C}{X^{1.19}} + \frac{1}{X^2}$ $C = 1.79 \cdot \left(Re_v / Re_l\right)^{0.4} \cdot \left(\frac{1-x}{x}\right)^{0.5}$	R-123, R-134a, R-22, R-236ea, R-245fa, R-404a, R-407C, R-410a, R-507, CO2, water and air. Channels with hydraulic diameter ranges from 0.506 to 12 mm.
Lee et al. [87]	$C = 121.6\left(1 - exp\left(-22.7\,Bo\right)\right)x^{1.85}$	Water, n-pentane, ammonia, CO$_2$, R-410a, R-134a, R-12 and R-22. Hidraulic diameter 0.35, 0.81, 0.89, 1.46, 2, 2.46, 8 and 13.8 mm
Hwang and Kim [88]	$C = 0.227\,Re_{lo}{}^{0.452}\,X^{-0.32}\,La^{-0.82}$	R-134. Tubes with inner diameters of 0.244, 0.430, and 0.792 mm. .
Gronnerud [75]	$\phi^2{}_{l,G} = 1 + f_{Fr}\left(x + 4\left(x^{1.8} - x^{10}\,f_{Fr}{}^{0.5}\right)\right)\left(\frac{\rho_{l,mixt} / \rho_{v,mixt}}{\left(\mu_{l,mixt} / \mu_{v,mixt}\right)^{0.25}} - 1\right)$ $f_{Fr} = \begin{cases} Fr_{lo}^{0.3} + 0.0055 \cdot \left(ln\left(1/Fr_{lo}\right)\right)^2 & if\ Fr_{lo} < 1 \\ 1 & if\ Fr_{lo} \geq 1 \end{cases}$	
Chawla [76]	$\phi^2{}_{v,Chawla} = \left(1 + \frac{1-x}{x\,e_c\,\rho_{l,mixt} / \rho_{v,mixt}}\right)^{19/8}$ $e_c = \left(\frac{1}{e_{c1}{}^3} + \frac{1}{e_{c2}{}^3}\right)^{-1/3}$ $log\left(e_{c1}\right) = 0.9592 + log\left(B\right)$ $log\left(e_{c2}\right) = \left(0.1675 - 0.055\,log\left(relrough\right)\right)log\left(B\right) - 0.67$ $B = \frac{1-x}{x}\left(Re_l\,Fr_l\right)^{-1/6}\left(\frac{\rho_{v,mixt}}{\rho_{l,mixt}}\right)^{0.9}\left(\frac{\mu_{v,mixt}}{\mu_{l,mixt}}\right)^{0.5}$	

Kawahara et al. [86] reported a C value of 0.24 for their data. This small value agrees with Mishima and Hibiki observation that C decreases as the diameter decreases. Qu and Mudawara [78] propose to add to the Mishima and Hibiki [7] correlation a factor that is a function of the mass flux. According to the results showing on Table 31, Qu and Mudawara perform worse than those Mishima and Hibiki for the actual data; consequently mass flux does not seem to be relevant to predict C. Sun and Mishima [4] present two equations. One is valid when both the liquid and vapor are laminar; in that case, they propose a correlation for C that is a function of Laplace number (La). When the liquid or vapor or both are turbulent, Sun and Mishima propose a new multiplier ($\phi^2{}_l$) and C factor, which is a function of quality and the ratio of liquid and vapor Reynolds numbers. As shown in Figure 116, most of the data have at least the vapor component turbulent; consequently, only the turbulent proposition is tested. Lee et al. [87] and Hwang and Kim [88] propose Chisholm parameter correlations that are a function of dimensionless number used to characterize mini-channels. This approach does not seem to work well with the experimental data presented.

The second approach based on the separated flow theory, similar to that used by Chisholm [89], implies that the whole mass flow rate flows in both the liquid and vapor tubes. In this case, the correlations relate the frictional pressure drop of the whole mass flow rate as a liquid and a two-phase friction multiplier $\phi^2{}_{lo}$ as shown in Eq. (116).

$$\left(\frac{dp}{dz}\right)_{2ph} = \left(\frac{dp}{dz}\right)_{lo} \phi^2{}_{lo} = f_{lo} \frac{G^2}{2\, ID\, \rho_{l,mixt}} \phi^2{}_{lo} \tag{116}$$

Chisholm [89] transformed the graphical procedure of Baroczy [90] into a correlation that is a function of a physical properties coefficient ($\varGamma$) . The coefficient $\varGamma$ is similar to the Lockhart Martinelli coefficient; however, it represents the ratio between vapor and liquid (instead liquid and vapor for X), and it is based on the idea that the whole fluid behaves as liquid and vapor and not simply the individual fractions. The coefficient $\varGamma$ is shown by Eq. (117).

$$\varGamma = \sqrt{\frac{\left(\frac{dp}{dz}\right)_{vo}}{\left(\frac{dp}{dz}\right)_{lo}}} \tag{117}$$

Table 30 shows some of the existing correlations that predict the two-phase friction multiplier $\phi^2{}_{lo}$

Table 30. Separated flow models, ϕ^2_{lo} multiplier

Author	Equation	Comments
Chisholm [91]	$\phi^2_{lo,Chisholm} = 1 + \left(\Gamma^2 - 1\right)\left(B x^{0.875}\left(1-x\right)^{0.875} + x^{1.75}\right)$ $B = 4.8$ if $\Gamma \leq 9.5$ & $G \leq 500\left[kg/m^2 s\right]$ $B = 2400/G$ if $\Gamma \leq 9.5$ & $500 < G < 1900\left[kg/m^2 s\right]$ $B = 55/G^{0.5}$ if $\Gamma \leq 9.5$ & $G \geq 1900\left[kg/m^2 s\right]$ $B = 520/\left(\Gamma G^{0.5}\right)$ if $9.5 < \Gamma < 28$ & $G \leq 600\left[kg/m^2 s\right]$ $B = 21/\Gamma$ if $9.5 < \Gamma < 28$ & $G > 600\left[kg/m^2 s\right]$ $B = \Gamma^2 G^{0.5}$ if $\Gamma \geq 28$	
Friedel [92]	$\phi^2_{lo,Friedel} = \left(1-x\right)^2 + x^2 \Gamma^2 + \dfrac{3.24 x^{0.78}\left(1-x\right)^{0.224}}{{Fr_{2ph}}^{0.045}\,{We_{2ph}}^{0.035}}\left(\dfrac{\rho_{l,mixt}}{\rho_{v,mixt}}\right)^{0.91}\left(\dfrac{\mu_{v,mixt}}{\mu_{l,mixt}}\right)^{0.19}\left(1-\dfrac{\mu_{v,mixt}}{\mu_{l,mixt}}\right)^{0.7}$	
Chen et al. [93]	$\phi^2_{lo,Chen} = \phi^2_{lo,Friedel}\,\Omega$ $\Omega = 0.0333\dfrac{{Re_{lo}}^{0.45}}{{Re_v}^{0.09}\left(1+0.4\,exp\left(-Eo/4\right)\right)}$ for $Eo < 10$ $\Omega = \dfrac{{We_{2ph}}^{0.2}}{2.5 + 0.015\,Eo}$ for $Eo \geq 10$	
Zhang and Webb [94]	$\phi^2_{lo,Z\&W} = \left(1-x\right)^2 + 2.87 x^2\left(\dfrac{P_c}{P}\right) + 1.68 x^{0.8}\left(1-x\right)^{0.25}\left(\dfrac{P_c}{P}\right)^{1.64}$	
Tran et al. [95]	$\phi^2_{lo,Tran} = 1 + \left(4.3\Gamma^2 - 1\right)\left(Eo^{-0.5}\cdot x^{0.875}\cdot\left(1-x\right)^{0.875} + x^{1.75}\right)$	
Müller-Steinhagen and Heck [6]	$\phi^2_{lo,MS\&H} = \left(1 + 2x\left(\Gamma^2 - 1\right)\right)\left(1-x\right)^{1/3} + \Gamma^2 x^3$	
Sami and Duong [74]	$\phi^2_{lo,S\&D} = 8.41\left(1-x\right)^{1.764} {X_{tt}}^{-1.24}$	
Jung and Radermacher [73]	$\phi^2_{lo,J\&R} = 30.78 x^{1.323}\left(1-x\right)^{0.477}\left(\dfrac{P_{avg}}{P_c}\right)^{-0.7232}$	
Souza and Pimenta [96]	$\phi^2_{lo,S\&P} = 1 + \left(\Gamma^2 - 1\right)x^{1.75}\left(1 + 0.9524\,\Gamma X^{0.4126}\right)$	
Cavallini et al. [97]	$\phi^2_{lo,C} = \left(1-x\right)^2 + x^2\Gamma^2 + 1.262 x^{0.6978}\dfrac{H}{{We_{vo}}^{0.1458}}$ $H = \left(\dfrac{\rho_{l,mixt}}{\rho_{v,mixt}}\right)^{0.3278}\left(\dfrac{\mu_{v,mixt}}{\mu_{l,mixt}}\right)^{-1.181}\left(1-\dfrac{\mu_{v,mixt}}{\mu_{l,mixt}}\right)^{3.477}$	

The frictional pressure drop data are compared with the existing correlations show in Tables 7, 8 and 9. The AADs of the experimental data against the reported correlations are shown in Table 31. The results are delineated by mixture and by tube diameter. The Müller-Steinhagen and Heck correlation [6], one of the most referenced correlation on the literature, shows good agreement for all of the mixtures flowing on the 1.5 mm test section. Also, Müller-Steinhagen and Heck predicts hydrocarbons and their dilutions on the 0.5 mm test section; however, the prediction for synthetic refrigerants and their dilutions do not seem to be good enough. The poor correlation for synthetic mixture is likely due to the Müller-Steinhagen and Heck being based on the assumption that most fluids behave similarly as a function of quality; however, as the diameter is reduced, most of two-phase region of the synthetic dilution mixture is in a laminar flow condition incrementing the pressure drop at low qualities.

Table 31. AADs of the experimental data against the reported correlations

Correlations	**Binary**		**HC**		**HC+N2**		**Syn**		**Syn+Ar**		**All data**		
	0.5	**1.5**	**0.5**	**1.5**	**0.5**	**1.5**	**0.5**	**1.5**	**0.5**	**1.5**	**0.5**	**1.5**	**All**
Homogeneous													
Cicchitti	21%	14%	29%	10%	**30%**	15%	19%	20%	**30%**	12%	26%	**14%**	**18%**
McAdams	33%	37%	28%	40%	47%	42%	62%	46%	60%	44%	46%	42%	44%
Dukler	39%	43%	32%	46%	49%	44%	64%	48%	61%	46%	49%	46%	47%
Davidson													
Beattie & Whalley	30%	34%	27%	39%	39%	34%	57%	39%	55%	39%	42%	38%	39%
Lin	28%	31%	26%	35%	44%	39%	61%	43%	58%	42%	44%	39%	40%
Awad & Muzychka 1	17%	15%	24%	10%	20%	15%	17%	19%	21%	14%	20%	15%	**17%**
Awad & Muzychka 2	24%	28%	24%	31%	40%	35%	58%	38%	55%	38%	41%	34%	37%
Awad & Muzychka 3	18%	17%	27%	14%	27%	21%	**30%**	23%	**30%**	27%	28%	20%	**23%**
Awad & Muzychka 4	16%	19%	19%	15%	24%	22%	**36%**	23%	**32%**	24%	26%	20%	**22%**
Separated flow													
Lockhart & Martinelli	70%	32%	73%	19%	71%	44%	46%	40%	54%	49%	63%	35%	45%
Mishima & Hibiki	30%	19%	25%	28%	28%	14%	42%	9%	39%	20%	32%	18%	**23%**
Kawahara	62%	72%	55%	71%	61%	63%	70%	65%	66%	58%	62%	66%	65%
Qu & Mudawara	41%	25%	28%	38%	39%	18%	52%	18%	49%	16%	41%	24%	30%
Sun & MIshima	18%	21%	25%	19%	23%	15%	9%	12%	17%	22%	**19%**	17%	**18%**
Lee	112%	81%	143%	90%	191%	264%	274%	270%	416%	427%	231%	224%	226%
Hwang & Kim	41%	18%	31%	34%	44%	32%	51%	31%	56%	170%	44%	53%	50%
Gronnerud	39%	44%	45%	31%	56%	25%	44%	26%	63%	22%	51%	28%	36%
Chawla	83%	125%	147%	81%	62%	115%	18%	42%	21%	32%	70%	74%	72%
Friedel	71%	13%	69%	15%	102%	22%	100%	50%	121%	63%	93%	33%	55%
Chen	66%	65%	66%	74%	69%	71%	73%	66%	104%	77%	75%	71%	73%
Zhang and Webb	129%	72%	140%	158%	412%	178%	183%	189%	92%	27%	205%	141%	164%
Chisholm	89%	96%	105%	80%	32%	43%	22%	36%	25%	26%	53%	54%	54%
Tran	506%	186%	565%	184%	338%	160%	112%	96%	87%	99%	320%	143%	206%
Müller-Steinhagen & Heck	16%	10%	19%	13%	21%	19%	**42%**	17%	**38%**	23%	28%	17%	**21%**
Sami & Duong	30%	32%	41%	54%	37%	45%	48%	46%	55%	56%	43%	48%	46%
Jung & Radermacher	169%	48%	166%	43%	432%	190%	310%	185%	227%	103%	272%	119%	173%
Cavallini	203%	60%	265%	125%	760%	319%	703%	453%	884%	427%	588%	291%	396%
Souza & Pimenta	45%	57%	42%	45%	65%	58%	77%	60%	79%	68%	62%	56%	58%

In Table 31, it is noted that the best homogeneous models are the correlations of Cicchitti [5] and the first definition of Awad and Muzychka [3] with overall predictions of AAD = 18% and AAD = 17%, respectively. The Cicchitti model predicts the data flowing in the 1.5 mm (AAD = 14%) better than in the 0.5 mm test section (AAD = 26%). The Awad and Muzychka 1 correlation is more consistent than Cicchitti for all of the mixtures and diameters (AAD = 15% for 1.5 mm and AAD = 20% for 0.5 mm). Mishima and Hibiki [7] and Sun and Mishima [4] have the best predictions for the separated flow models presented in Table 29. Mishima and Hibiki [7] show an overall AAD = 23%,; however, the prediction for the 0.5 mm test section is not as good as it is for the 1.5 mm test section. Sun and Mishima [4] is more consistent showing AAD = 19%, 17% and 18% for the 0.5 mm, 1.5 mm and overall data.

Figure 118 to Figure 121 show the best four correlations for prediction of two-phase frictional pressure drop during boiling of zeotropic mixtures flowing in horizontal mini-channels. Cicchitti [5], Awad and Muzychka (definition 1) [3], Sun and Mishima [4] and Müller-Steinhagen and Heck [6] predictions are plotted against the collected data in log-log plot with ±25% lines shown.

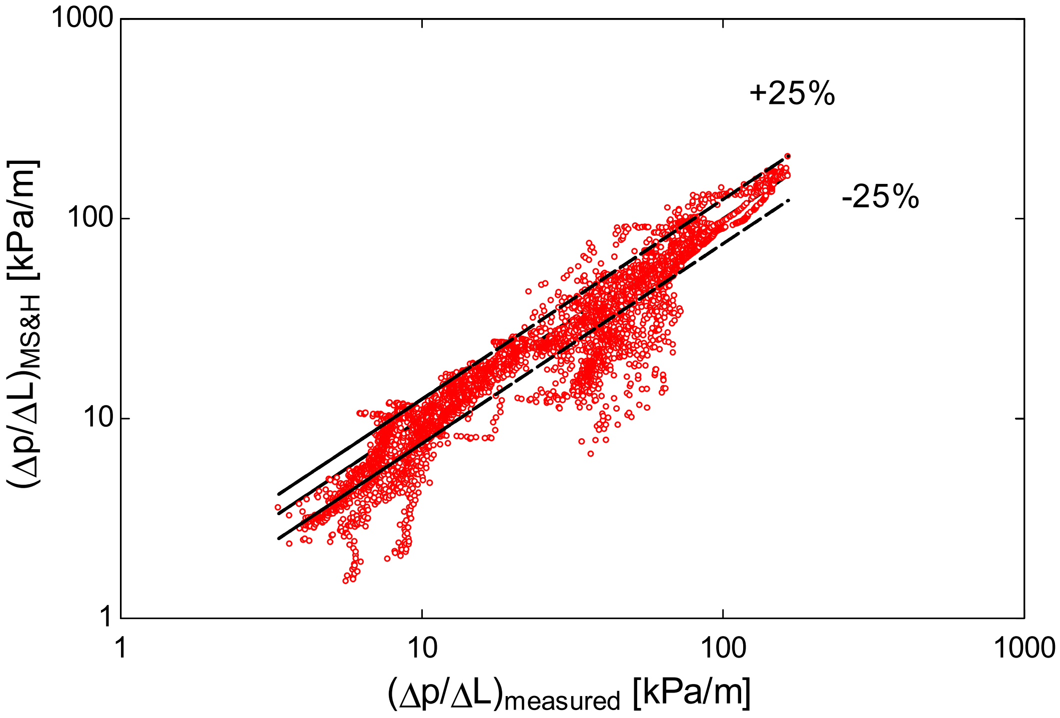

Figure 118. Measured vs predicted frictional pressure drop using Müller-Steinhagen and Heck correlation

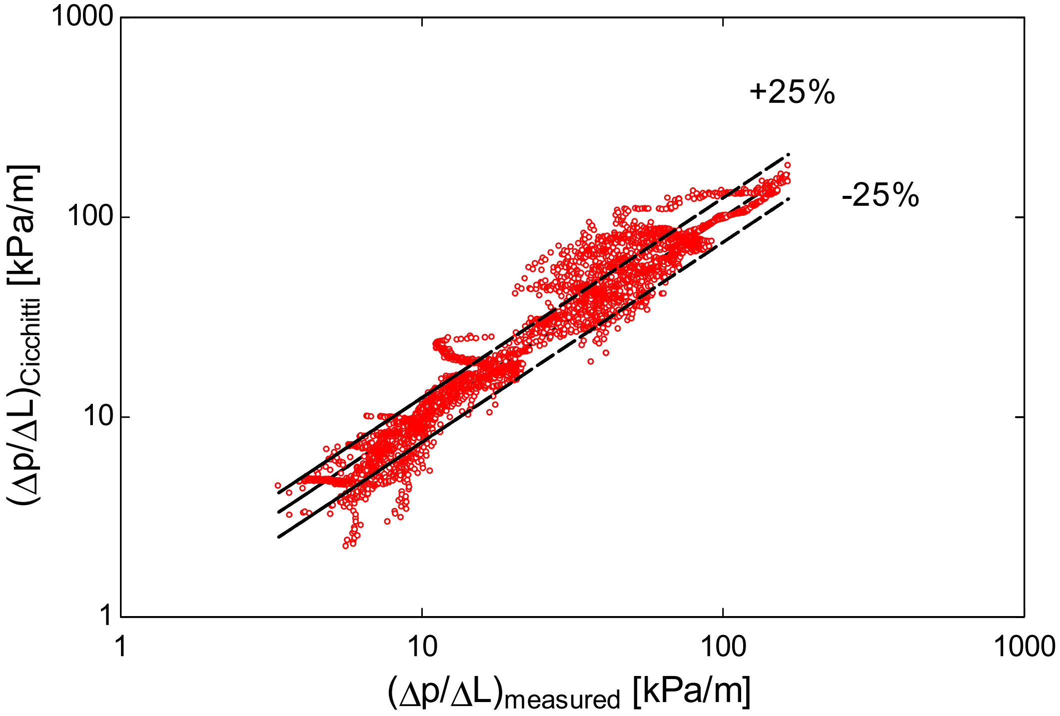

Figure 119. Measured vs predicted frictional pressure drop using Cicchitti homogeneous model

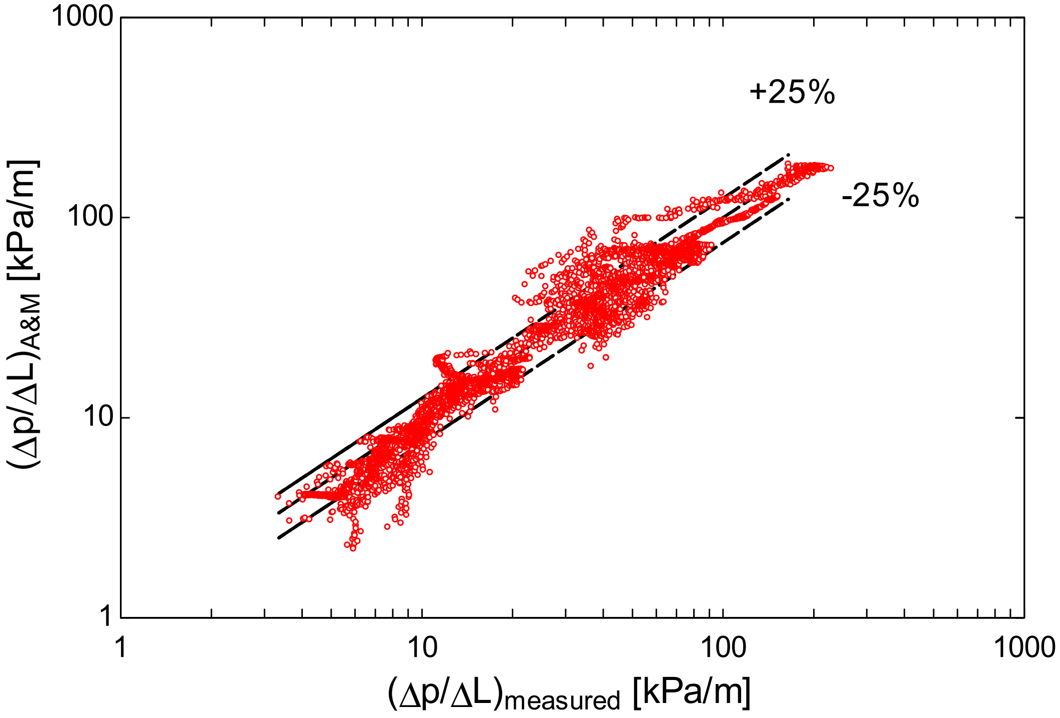

Figure 120. Measured vs predicted frictional pressure drop using Awad and Muzychka homogeneous model

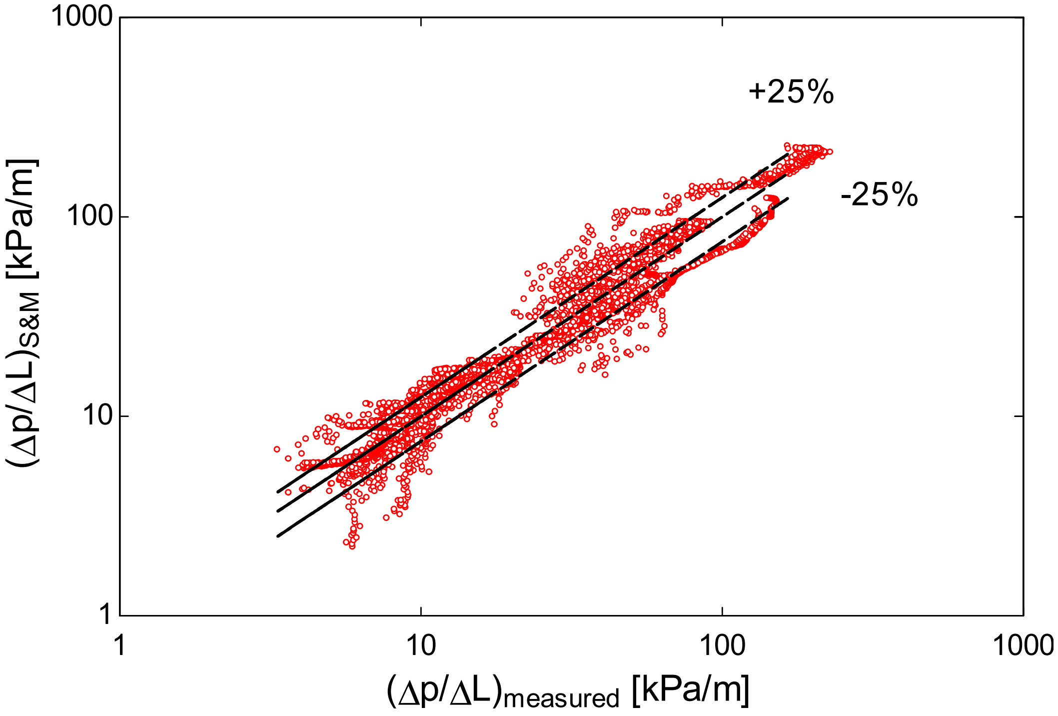

Figure 121. Measured vs predicted frictional pressure drop using Sun and Mishima correlation

Figure 122 shows the relative error of the Awad and Muzychka (definition 1) homogeneous model, the best correlation identified by this work, as a function of the average thermodynamic quality. When the quality is greater than 50%, the frictional pressure drop prediction improves keeping the relative errors peaks below 40%. The error in the prediction of the frictional pressure drop increases as the quality decreases. When the quality is between 25 and 50% the relative errors peaks increase up to 75%, and a greater dispersion is observed between qualities of 0 and 25%.

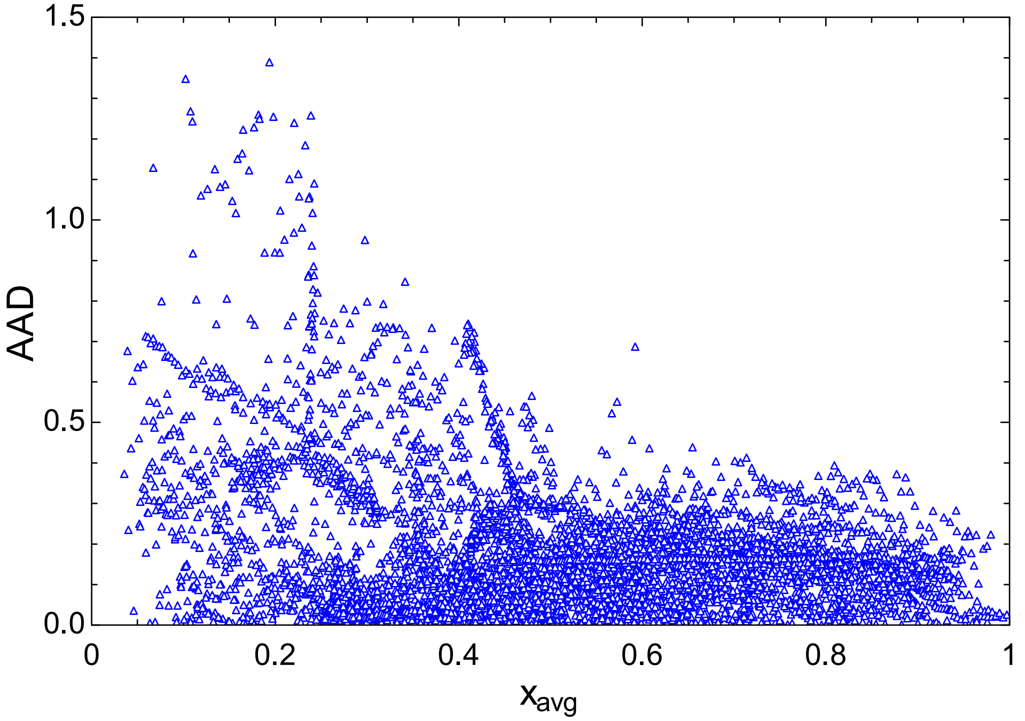

Figure 122. AAD of Awad and Muzychka model as a function of average thermodynamic quality

Cicchitti is the best model for prediction of the data collected in the 1.5 mm test section. Sun and Mishima show the best prediction for the 0.5 mm test section. The Awad and Muzychka (definition 1) correlation has the overall better prediction. Awad and Muzychka (definition 1) predict 86% of the experimental data with a relative error lower than 30%. Awad and Muzychka (definition 1) perform better than Sun and Mishima and Cicchitti in that they only predict 83% of the data points with a relative error lower than 30%, according to Table 32.

Table 32. % of experimental data for different % of relative error

Models	**% of experimental data with a relative error lower than**				
	10%	**20%**	**25%**	**30%**	**50%**
Cicchitti	43%	72%	79%	83%	92%
Awad & Muzychka	39%	72%	81%	86%	96%
Sun & Mishima	40%	65%	74%	82%	96%
Müller-Steinhagen & Heck	31%	62%	70%	77%	92%

7. CONCLUSIONS AND RECOMMENDATIONS FOR FUTURE WORK

7.1. Experimental test facility

An experimental test facility able to measure heat transfer coefficient for zeotropic mixtures during boiling have been designed and built. The test facility is also able to measure pressure drop under diabatic and adiabatic conditions. The design process that includes component and instrumentation selection that allow to measured heat transfer coefficient with the required accuracy is presented. The actual test facility is described and it is able to fulfill with the design parameters. Accurate measurements of inner diameter of the test section and surface roughness are performed and reported. Also, it is indicated the reduction data procedure and the uncertainty analysis of the measurement.

The heat transfer measurement was validated testing single-phase pure nitrogen and comparing the heat transfer coefficient measurement with values predicted using well-known single-phase correlations. In addition, it is verified the repetition of the measurement testing a selected mixture while the system is cooled and when is warmed under the same tested conditions. Also, the isothermal copper block assumption is verified. The pressure drop measurement has been calibrated using single-phase pure nitrogen and well-known friction factor correlation for turbulent single-phase. The pressure drop measurement is validated testing superheated single-phase vapor of the tested mixtures and comparing with appropriate frictional pressure drop correlation.

In conclusion, the experimental test facility shown in this report is able to measure heat transfer coefficient and pressure drop of boiling zeotropic mixtures in a horizontal test section.

The heat transfer coefficient measurements have been shown to be accurate (with an uncertainty lower than 10%) and repeatable.

7.2. Heat transfer coefficients

The experimental test facility described in this document provides local heat transfer coefficient data for zeotropic mixtures for a range of temperatures between 100 K and room temperature with an uncertainty lower than 10%. Five mixtures are tested: A methane, ethane, and propane mixture (hydrocarbon mixtures) with molar composition of 45%, 35% and 20%, respectively. The hydrocarbon mixture is diluted with 20% and 40% of nitrogen. A synthetic refrigerant mixture (35% R-14, 15% R-23, 15% R-32, and 35% R-134a) is tested. The synthetic refrigerant mixture diluted using argon also is measured. The fifth mixture is a binary mixture formed by methane and ethane, 40% and 60% by volume. Most of the experimental data obtained with this test facility are representative of the boiling of mixtures in the range of thermodynamic qualities between 10 and 90%. It is considered a two-phase measurement when the inlet and the outlet of the test section are in presence of two-phase flow avoiding disturbed by the presence of subcooled liquid in the inlet and superheated vapor at the outlet of the test section. Dry out is observed to occur when the quality at the outlet of the test section is over 85%. For some mixtures and condition, a dry out around a quality of 80% at the outlet condition is observed. The concentration of the mixture changes as the mixture moves through two-phase region because some of the component condenses out of circulation; consequently, the mixture composition is sample periodically during the test.

The heat transfer coefficient for the 0.5, 1.5, and 3.0 mm test section and for the mixtures tested is dominated by convective boiling for all of the gas mixtures tested, independent of heat flux. Decreasing the evaporating pressure moves the two-phase region to the coldest zone, but the temperature glide is constant. The evaporating pressure does not seem to have a big impact in synthetic refrigerant and binary mixtures because they exhibit a similar trend. However, the experimental results suggest that as the pressure is reduced, the heat transfer coefficient increases slightly. The heat transfer coefficient increment may be related to changes in fluid properties as fluid liquid viscosity than seem to be more affected by pressure changes. In the case of hydrocarbons mixture, changes of evaporating pressures seem to have a significant effect on the heat transfer coefficient only in the low quality region. Dilution of both hydrocarbon and synthetic refrigerant mixtures increases the temperature glide, and deteriorates the heat transfer coefficient. The temperature glide may be increased up to 50 K and the heat transfer coefficient is reduced about 20% and 40% for the 20% and 40% dilution, respectively. As the convective boiling is dominant, it is expected an increment of the heat transfer coefficient as the diameter is reduced. Binary and hydrocarbon mixtures show an unexpected behavior for the data collected in the 3.0 mm test section because the heat transfer coefficient is higher in the 3.0 mm for qualities lower than 50%. This phenomenon may be explained because the 3.0 mm test section is big enough to allow liquid flowing between the bubbles and the wall accelerating the flow and producing an enhancement of the heat transfer coefficient. The surface roughness seems to have an impact in the heat transfer coefficient as the thermodynamic quality is reduced to values below 40%. At high qualities, when annular flow is supposed to be present, the change of surface roughness does not produce any significant effect on the heat transfer coefficient.

The usefulness of currently available correlations for heat transfer is evaluated. Traditional heat transfer correlation for boiling of pure fluids as Chen, Liu and Winterton, and Gungor and Winterton are not suitable to predict the heat transfer coefficient of the mixtures tested. The pure fluids models include the superposition of nucleate and convection boiling, but the boiling process of the mixtures tested is dominated by convective boiling. The evaluation of the traditional model, but only taking into account the convection component seems to work better, especially the model of Chen. Models developed to predict boiling of binary mixtures as Kandlikar and Bennett and Chen also do not show reasonable results in comparison with the experimental data. The annular models based on Silver, Bell and Ghally provide a good prediction of the experimental data. The Granryd correlation provides the best prediction the current data with an AAD of around 15% and predicting more than 87% of the data points with a relative error lower than 30%. Granryd makes a good job with 1.5 and 3.0 test sections predicting more than 90% within 30%. As the diameter decreases, the prediction becomes less accurate. 97% of the data for 3.0 mm, 91% for 1.5 mm and 69% for 0.5 mm are calculated with a relative error lower than 30% using Granryd. The Little correlation is the second best with an AAD of 18% and predicting 82% of the data within 30%. Also, Granryd and Little accuracy is verified by comparing with the data provided by Nellis et al. [30]. Both models show good agreement with Nellis data having AADs of 18% for Granryd and 19% for Little.

Little shows poor performance to predict heat transfer data for lower qualities and lower Reynolds number predicting less than 50% of the data with 25% of relative error. Granryd is clearly better predicting heat transfer coefficient in that range because it is able to predict at least 70% of the data with a relative error low than 25%. In conclusion, Granryd correlation is recommended to be used to predict heat transfer coefficient of zeotropic mixtures because its prediction are less dependent of flow conditions.

7.3. Frictional pressure drop

A large set of frictional pressure drop data for boiling zeotropic mixtures with large temperature glides flowing in horizontal tubes of 0.5 mm and 1.5 mm diameters have been collected. The Rouhani-Axelsson void fraction model works well as an input to estimate the acceleration term of the pressure drop for the mixtures tested. The experimental data show a significant impact of reducing the diameter because a part of the two-phase region becomes laminar, incrementing the friction factor and the pressure drop at low qualities. Composition of the mixture does not seem to be a key factor in the frictional pressure drop.

The Lee et al. [87], Hwang and Kim [88], Chen et al. [93] and Tran et al. [95] correlations include as a parameter the Eotvos, Bond or Laplace number to take into account the different behavior that should present in the flow flowing in mini-channels. These correlations show poor results, especially Lee et al. [87], and Tran et al. [95]. For the mixture tested, the frictional pressure drop during boiling does not seem to be a function of one of these dimensionless numbers or at least not in the way that these correlations proposed.

It is necessary to include some mixture properties to adequately predict frictional pressure drop for zeotropic mixtures with large temperature glide. The Zhang and Webb [94] and Jung and Radermacher [73] correlations are only a function of quality, and evaporative and critical pressures. Zhang and Webb [94] and Jung and Radermacher [73] show AADs of 164% and 173%, respectively.

The Chisholm parameter *C* shows some dependence on channel diameter as suggested by Mishima and Hibiki [7]. Also, *C* appears to be a function of quality and the ratio of liquid and vapor viscosity according to the correlation proposed by Sun and Mishima [4].

Awad and Muzychka (definition 1) [3] show the best prediction for the overall experimental data with an AAD of 17% and the second best is Sun and Mishima [4] (AAD = 18%). Cicchitti et al. [5] provide the best prediction of the data collected in the 1.5 mm test section with an AAD of 14% and Sun and Mishima [4] has the top performance for the 0.5 mm test section. Müller-Steinhagen and Heck [6] and Mishima and Hibiki [7] correlations have a reasonable agreement with the experimental data, but this agreement is better with the data collected on the 1.5 mm test section. We recommend the use of the Awad and Muzychka (definition 1) [3] homogeneous model because it requires only liquid and vapor viscosity, quality and mixture density. Also, the Awad and Muzychka (definition 1) correlation predicts more data with low relative error.

7.4. Future work

Surface roughness seems to play a significant role in the heat transfer coefficient at low qualities values. Flow regime may change as different diameter and mixtures are tested during boiling. Some experimental results suggest that flow regime influence heat transfer coefficient. It will be a real input to the state of the art of multi-phase multi-component flow designing an experiment that allows visualizing flow regimes and relates these results with some flow parameters.

It is suggested to use the actual experimental facility to measure heat transfer coefficient and frictional pressure drop for boiling zeotropic multi-component mixtures varying the inclination of the test section. The inclination of the test section may be gradually varied from horizontal (0 degrees) to vertical (90 degrees). This measurement does not require any major modifications. Also, it is possible to test different channel geometries.

This study has provided experimental data for heat transfer coefficient and frictional pressure drop for boiling zeotropic mixtures. Heat transfer coefficient and frictional pressure drop correlations have been validated for the tested mixtures and geometries. Some applications as Joule-Thomson cycles involve heat exchanger that in one side has boiling mixture and in the other has condensing mixtures. Also, there are limited data and correlations to predict heat transfer coefficient for condensing zeotropic mixtures. It is required to measure heat transfer coefficient during condensation.

Some problems have been experienced during the collection of experimental data because of the freezing of zeotropic mixtures in the coldest location of the experimental facility. It will be useful for optimization techniques of the mixture to know which the freezing points of zeotropic mixtures are, and how freezing point may be predicted.

8. REFERENCES

[1] E. Granryd, Heat transfer in flow evaporation of non azeotropic refrigerant mixtures - A theoretical approach, in: Proc. 18th Int. Congr. Refrig., 1991: pp. 1330–1334.

[2] W.A. Little, HEAT TRANSFER EFFICIENCY OF KLEEMENKO CYCLE HEAT EXCHANGERS, in: AIP Conf. Proc., AIP Publishing, 2008: pp. 606–613. doi:10.1063/1.2908605.

[3] M.M. Awad, Y.S. Muzychka, Effective property models for homogeneous two-phase flows, Exp. Therm. Fluid Sci. 33 (2008) 106–113. doi:10.1016/j.expthermflusci.2008.07.006.

[4] L. Sun, K. Mishima, Evaluation analysis of prediction methods for two-phase flow pressure drop in mini-channels, Int. J. Multiph. Flow. 35 (2009) 47–54. doi:10.1016/j.ijmultiphaseflow.2008.08.003.

[5] A. Cicchitti, C. Lombardi, M. Silvestri, G. Soldaini, R. Zavattarelli, Two-phase cooling experiments: pressure drop, heat transfer and burnout measurements, Centro Informazioni Studi Esperienze, Milan, 1959. http://www.osti.gov/scitech/biblio/4181977 (accessed March 18, 2015).

[6] H. Müller-Steinhagen, K. Heck, A simple friction pressure drop correlation for two-phase flow in pipes, Chem. Eng. Process. Process Intensif. 20 (1986) 297–308. doi:10.1016/0255-2701(86)80008-3.

[7] K. Mishima, T. Hibiki, Some characteristics of air-water two-phase flow in small diameter vertical tubes, Int. J. Multiph. Flow. 22 (1996) 703–712. doi:10.1016/0301-9322(96)00010-9.

[8] W. Li, X. Feng, L.J. Yu, J. Xu, Effects of evaporating temperature and internal heat exchanger on organic Rankine cycle, Appl. Therm. Eng. 31 (2011) 4014–4023. doi:10.1016/j.applthermaleng.2011.08.003.

[9] H. Chen, D.Y. Goswami, M.M. Rahman, E.K. Stefanakos, A supercritical Rankine cycle using zeotropic mixture working fluids for the conversion of low-grade heat into power, Energy. 36 (2011) 549–555. doi:10.1016/j.energy.2010.10.006.

[10] X.D. Wang, L. Zhao, Analysis of zeotropic mixtures used in low-temperature solar Rankine cycles for power generation, Sol. Energy. 83 (2009) 605–613. doi:10.1016/j.solener.2008.10.006.

[11] L. Cheng, D. Mewes, Review of two-phase flow and flow boiling of mixtures in small and mini channels, Int. J. Multiph. Flow. 32 (2006) 183–207. doi:10.1016/j.ijmultiphaseflow.2005.10.001.

[12] J. Chen, J. Yu, Performance of a new refrigeration cycle using refrigerant mixture R32/R134a for residential air-conditioner applications, Energy Build. 40 (2008) 2022–2027. doi:10.1016/j.enbuild.2008.05.003.

[13] D.S. Jung, M. McLinden, R. Radermacher, D. Didion, Horizontal flow boiling heat transfer experiments with a mixture of R22/R114, Int. J. Heat Mass Transf. 32 (1989) 131–145. doi:10.1016/0017-9310(89)90097-5.

[14] V.S. Chakravarthy, R.K. Shah, G. Venkatarathnam, A Review of Refrigeration Methods in the Temperature Range 4–300 K, J. Therm. Sci. Eng. Appl. 3 (2011) 020801–020801. doi:10.1115/1.4003701.

[15] W.A. Little, Recent development in Joule–Thomson cooling: gases, coolers, and compressors., Proc. 5th Int. Cryocooler Conf. (1998) 3–11.

[16] E.C. Luo, M.Q. Gong, Y. Zhou, J.T. Liang, L. Zang, Mixed-refrigerant Joule-Thomson cryoccolers in CL/CAS, in: Adv. Cryog. Eng., 2000: pp. 299–306.

[17] M. Boiarski, A. Khatri, V. Kovalenko, Design Optimization of the Throttle-Cycle Cooler with Mixed Refrigerant, in: R.G.R. Jr (Ed.), Cryocoolers 10, Springer US, 2002: pp. 457–465. http://link.springer.com/chapter/10.1007/0-306-47090-X_54 (accessed October 10, 2014).

[18] F. Keppler, G. Nellis, S.A. Klein, Optimization of the Composition of a Gas Mixture in a Joule-Thomson Cycle, HVACR Res. 10 (2004) 213–230. doi:10.1080/10789669.2004.10391100.

[19] W.A. Little, Method for efficient counter-current heat exchange using optimized mixtures, 5,644,502, 1997.

[20] M.Q. Gong, E.C. Luo, Y. Zhou, J.T. Liang, L. Zhang, Optimum composition calculation for multicomponent cryogenic mixture used in Joule-Thomson refrigerators, in: Adv. Cryog. Eng. Vol. 45 Parts B, Springer Science & Business Media, 2000: pp. 283–290.

[21] A. Alexeev, C. Haberstroh, H. Quack, Further Development of a Mixed Gas Joule Thomson Refrigerator, in: P. Kittel (Ed.), Adv. Cryog. Eng., Springer US, 1998: pp. 1667–1674. http://link.springer.com/chapter/10.1007/978-1-4757-9047-4_209 (accessed October 10, 2014).

[22] H. Skye, G. Nellis, S. Klein, Modeling and Optimization of a Cascaded Mixed Gas Joule-Thompson Cryoprobe System, ASHRAE Trans. 115 (2009) 966–983.

[23] G. Nellis, S. Klein, Heat Transfer, Cambridge University Press, New York, 2008.

[24] F.P. Incropera, Fundamentals of heat and mass transfer, John Wiley & Sons, 2011. https://books.google.com/books?hl=en&lr=&id=vvyIoXEywMoC&oi=fnd&pg=PR21&dq=heat+transfer+incropera&ots=8IppMZcXGa&sig=nbWP8anZjlLW3dprBl7reg8n3lM (accessed April 17, 2015).

[25] E.W. Lemmon, Huber, Marcia L., McLiden, Mark O., REFPROP, NIST Standard Reference Database 23, 2014.

[26] Dittus, F.W., Boelter, L.M.K., Heat transfer in automobile radiators of the tubular type, Univ Californ Publ Eng. (1930) 443–461.

[27] Lakeshore, PT-100 Series Platinum RTDs, 2013. http://www.lakeshore.com/Documents/ LSTC_Platinum_l.pdf.

[28] J.C. Chen, Correlation for Boiling Heat Transfer to Saturated Fluids in Convective Flow, Ind. Eng. Chem. Process Des. Dev. 5 (1966) 322–329. doi:10.1021/i260019a023.

[29] H.E. Sostmann, J.P. Tavener, Fundamentals of Thermometry Part V, Isotech J. Thermom. Online Ref. Www Its-90 Com. (1990). http://www.isotechna.com/v/vspfiles/pdf_articles/Industrial%20(Use)%20Platinum%20Resistance%20Thermometers%20and%20Common%20Errors%20in%20Industrial%20Temperature%20Measurement.pdf (accessed April 18, 2015).

[30] G. Nellis, C. Hughes, J. Pfotenhauer, Heat transfer coefficient measurements for mixed gas working fluids at cryogenic temperatures, Cryogenics. 45 (2005) 546–556. doi:10.1016/j.cryogenics.2005.05.002.

[31] S.Z. Rouhani, E. Axelsson, Calculation of void volume fraction in the subcooled and quality boiling regions, Int. J. Heat Mass Transf. 13 (1970) 383–393. doi:10.1016/0017-9310(70)90114-6.

[32] P.F. Dunn, Measurement and Data Analysis for Engineering and Science, Second Edition, CRC Press, 2010.

[33] Endress + Hauser, Technical Information Proline Promass 80A, 83A Coriolis Mass Flow Measuring System The single-tube system for highly accurate measurement of very small flows, 2012. https://portal.endress.com/wa001/dla/5000000/0158/000/07/TI00054DEN_1312.pdf.

[34] Setra, Model 204 High Accuracy Gauge & Absolute Pressure Transducers, 2013. http://www.setra.com/Products/Pressure/Absolute-Pressure/Model-204-Data-Sheet.aspx.

[35] Setra, Model 204D DIFFERENTIAL PRESSURE High Accuracy Differential Pressure, 2013. http://www.setra.com/Products/Pressure/Differential-Pressure/Model-204D-Data-Sheet.aspx.

[36] Omega, Micro-Machined Silicon Transducers wet/dry differential Pressure Models, 2015. http://www.omega.com/Pressure/pdf/PX409-WDDIF.pdf.

[37] H. Skye, Modeling, Experimentation and Optimization for a Mixed Gas Joule-Thomson Cycle with Precooling for Cryosurgery, University of Wisconsin-Madison, 2011.

[38] Campbell Scientific, Inc., Operator's Manual, CR23X Micrologger, 2006. http://s.campbellsci.com/documents/us/manuals/cr23x.pdf.

[39] S.A. Klein, Engineering Equation Solver, F-Chart Software, 2014.

[40] Gnielinski, V., New equations for heat and mass transfer in turbulent pipe and channel flow, Int. Chem. Eng. 16 (1976) 359–368.

[41] D.J. Zigrang, N.D. Sylvester, Explicit approximations to the solution of Colebrook's friction factor equation, AIChE J. 28 (1982) 514–515. doi:10.1002/aic.690280323.

[42] Alternatives / SNAP | US EPA, (n.d.). http://www.epa.gov/ozone/snap/ (accessed April 9, 2015).

[43] R.K. Shah, Classification of heat exchangers, in: Heat Exch. Therm.-Hydraul. Fundam. Des., Hemisphere Publishing Corp, Washington, 1986: pp. 9–46.

[44] S.S. Mehendale, A.M. Jacobi, R.K. Shah, Fluid Flow and Heat Transfer at Micro- and Meso-Scales With Application to Heat Exchanger Design, Appl. Mech. Rev. 53 (2000) 175–193. doi:10.1115/1.3097347.

[45] S.G. Kandlikar, Fundamental issues related to flow boiling in minichannels and microchannels, Exp. Therm. Fluid Sci. 26 (2002) 389–407. doi:10.1016/S0894-1777(02)00150-4.

[46] K.A. Triplett, S.M. Ghiaasiaan, S.I. Abdel-Khalik, D.L. Sadowski, Gas–liquid two-phase flow in microchannels Part I: two-phase flow patterns, Int. J. Multiph. Flow. 25 (1999) 377–394. doi:10.1016/S0301-9322(98)00054-8.

[47] N. Brauner, D.M. Maron, Identification of the range of "small diameters" conduits, regarding two-phase flow pattern transitions, Int. Commun. Heat Mass Transf. 19 (1992) 29–39. doi:10.1016/0735-1933(92)90061-L.

[48] P.A. Kew, K. Cornwell, Correlations for the prediction of boiling heat transfer in small-diameter channels, Appl. Therm. Eng. 17 (1997) 705–715. doi:10.1016/S1359-4311(96)00071-3.

[49] F.J. Schwartz, Measurement of heat transfer coefficient for mixtures, University of Wisconsin-Madison, 2015.

[50] M.Q. Gong, J.F. Wu, E.C. Luo, Y.F. Qi, Q.G. Hu, Y. Zhou, Study on the overall heat transfer coefficient for the tube-in-tube heat exchanger used in mixed-gases coolers, in: AIP Conf. Proc., AIP Publishing, 2002: pp. 1483–1490. doi:10.1063/1.1472181.

[51] P.M. Ardhapurkar, A. Sridharan, M.D. Atrey, Experimental investigation on temperature profile and pressure drop in two-phase heat exchanger for mixed refrigerant Joule–Thomson cryocooler, Appl. Therm. Eng. 66 (2014) 94–103. doi:10.1016/j.applthermaleng.2014.01.067.

[52] L. Zhang, E. Hihara, T. Saito, J.-T. Oh, Boiling heat transfer of a ternary refrigerant mixture inside a horizontal smooth tube, Int. J. Heat Mass Transf. 40 (1997) 2009–2017. doi:10.1016/S0017-9310(96)00301-8.

[53] K. Stephan, Two-phase heat exchange for new refrigerants and their mixtures, Int. J. Refrig. 18 (1995) 198–209. doi:10.1016/0140-7007(95)90315-Q.

[54] M.P. Mishra, H.K. Varma, C.P. Sharma, Heat transfer coefficients in forced convection evaporation of refrigerants mixtures, Lett. Heat Mass Transf. 8 (1981) 127–136. doi:10.1016/0094-4548(81)90034-5.

[55] R.G. SARDESAI, R.A.W. SHOCK, D. BUTTERWORTH, Heat and Mass Transfer in Multicomponent Condensation and Boiling, Heat Transf. Eng. 3 (1982) 104–114. doi:10.1080/01457638108939589.

[56] J.Y. Shin, M.S. Kim, S.T. Ro, Experimental study on forced convective boiling heat transfer of pure refrigerants and refrigerant mixtures in a horizontal tube, Int. J. Refrig. 20 (1997) 267–275. doi:10.1016/S0140-7007(97)00004-2.

[57] T. Inoue, M. Monde, Y. Teruya, Pool boiling heat transfer in binary mixtures of ammonia/water, Int. J. Heat Mass Transf. 45 (2002) 4409–4415. doi:10.1016/S0017-9310(02)00153-9.

[58] D. STEINER, J. TABOREK, Flow Boiling Heat Transfer in Vertical Tubes Correlated by an Asymptotic Model, Heat Transf. Eng. 13 (1992) 43–69. doi:10.1080/01457639208939774.

[59] J.G. Collier, J.R. Thome, Convective Boiling and Condensation, Oxford University Press, 1994.

[60] J.R. Thome, Boiling of new refrigerants: a state-of-the-art review, Int. J. Refrig. 19 (1996) 435–457. doi:10.1016/S0140-7007(96)00004-7.

[61] K.E. Gungor, R.H.S. Winterton, A general correlation for flow boiling in tubes and annuli, Int. J. Heat Mass Transf. 29 (1986) 351–358. doi:10.1016/0017-9310(86)90205-X.

[62] K.E. Gungor, R.H.S. Winterton, Simplified general correlation for saturated flow boiling and comparisons of correlations with data, Chem. Eng. Res. Des. 65 (1987) 148–156.

[63] Z. Liu, R.H.S. Winterton, A general correlation for saturated and subcooled flow boiling in tubes and annuli, based on a nucleate pool boiling equation, Int. J. Heat Mass Transf. 34 (1991) 2759–2766. doi:10.1016/0017-9310(91)90234-6.

[64] D.L. Bennett, J.C. Chen, Forced convective boiling in vertical tubes for saturated pure components and binary mixtures, AIChE J. 26 (1980) 454–461. doi:10.1002/aic.690260317.

[65] S.G. Kandlikar, Boiling Heat Transfer With Binary Mixtures: Part II—Flow Boiling in Plain Tubes, J. Heat Transf. 120 (1998) 388–394. doi:10.1115/1.2824262.

[66] L. Silver, Gas cooling with aqueous condensation, Trans Inst Chem Eng. 25 (n.d.) 30–42.

[67] K.J. Bell, M.A. Ghaly, An approximate generalized design method for multicomponent/partial condensation, AIChE Symp. 39 (1972) 72–79.

[68] P.M. Ardhapurkar, A. Sridharan, M.D. Atrey, Flow boiling heat transfer coefficients at cryogenic temperatures for multi-component refrigerant mixtures of nitrogen–hydrocarbons, Cryogenics. 59 (2014) 84–92. doi:10.1016/j.cryogenics.2013.11.006.

[69] J.R. Thome, S. Shakir, A new correlation for nucleate pool boiling of aqueous mixtures, (1987). http://inis.iaea.org/Search/search.aspx?orig_q=RN:19081732 (accessed January 9, 2015).

[70] D. Chisholm, Void Fraction during Two-Phase Flow, J. Mech. Eng. Sci. 15 (1973) 235–236. doi:10.1243/JMES_JOUR_1973_015_040_02.

[71] M.B. Ould Didi, N. Kattan, J.R. Thome, Prediction of two-phase pressure gradients of refrigerants in horizontal tubes, Int. J. Refrig. 25 (2002) 935–947. doi:10.1016/S0140-7007(01)00099-8.

[72] A. Greco, G.P. Vanoli, Experimental two-phase pressure gradients during evaporation of pure and mixed refrigerants in a smooth horizontal tube. Comparison with correlations, Heat Mass Transf. 42 (2006) 709–725. doi:10.1007/s00231-005-0020-7.

[73] D.S. Jung, R. Radermacher, Prediction of pressure drop during horizontal annular flow boiling of pure and mixed refrigerants, Int. J. Heat Mass Transf. 32 (1989) 2435–2446. doi:10.1016/0017-9310(89)90203-2.

[74] S.M. Sami, T.N. Duong, Flow boiling characteristics of refrigerant mixture R22/R114 in the annulus of enhanced surface tubing, Int. J. Energy Res. 16 (1992) 241–252. doi:10.1002/er.4440160307.

[75] R. Grönnerud, Investigation of liquid hold-up, flow-resistance and heat transfer in circulation type evaporators, part iv: two-phase flow resistance in boiling refrigerants, Bull L'Inst Froid Annexe. 1 (1972).

[76] J.M. Chawla, Reibungsdruckabfall bei der Strömung von Flüssigkeits/Gas-Gemischen in waagrechten Rohren, Chem. Ing. Tech. 44 (1972) 58–63. doi:10.1002/cite.330440111.

[77] S. Baek, S. Jeong, G. Hwang, Pressure drop characteristics of cryogenic mixed refrigerant at macro and micro channel heat exchangers, Cryogenics. 52 (2012) 689–694. doi:10.1016/j.cryogenics.2012.06.012.

[78] W. Qu, I. Mudawar, Measurement and prediction of pressure drop in two-phase micro-channel heat sinks, Int. J. Heat Mass Transf. 46 (2003) 2737–2753. doi:10.1016/S0017-9310(03)00044-9.

[79] W.H. McAdams, W.K. Woods, L.C. Heroman, Vaporization inside horizontal tubes-II-benzene-oil mixtures, Trans ASME. 64 (1942) 193–200.

[80] A.E. Dukler, M. Wicks, R.G. Cleveland, Frictional pressure drop in two-phase flow: A. A comparison of existing correlations for pressure loss and holdup, AIChE J. 10 (1964) 38–43. doi:10.1002/aic.690100117.

[81] W.F. Davidson, P.H. Hardie, C.G.R. Humphreys, A.A. Markson, A.R. Mumford, T. Ravese, Studies of heat transmission through boiler tubing at pressures from 500 to 3300 pounds, Trans ASME. 65 (1943) 553–591.

[82] D.R.H. Beattie, P.B. Whalley, A simple two-phase frictional pressure drop calculation method, Int. J. Multiph. Flow. 8 (1982) 83–87. doi:10.1016/0301-9322(82)90009-X.

[83] S. Lin, C.C.K. Kwok, R.-Y. Li, Z.-H. Chen, Z.-Y. Chen, Local frictional pressure drop during vaporization of R-12 through capillary tubes, Int. J. Multiph. Flow. 17 (1991) 95–102. doi:10.1016/0301-9322(91)90072-B.

[84] R.W. Lockhart, R.C. Martinelli, Proposed correlation of data for isothermal two-phase, two-component flow in pipes, Chem Eng Prog. 45 (1949) 39–48.

[85] D. Chisholm, A theoretical basis for the Lockhart-Martinelli correlation for two-phase flow, Int. J. Heat Mass Transf. 10 (1967) 1767–1778. doi:10.1016/0017-9310(67)90047-6.

[86] A. Kawahara, P.M.-Y. Chung, M. Kawaji, Investigation of two-phase flow pattern, void fraction and pressure drop in a microchannel, Int. J. Multiph. Flow. 28 (2002) 1411–1435. doi:10.1016/S0301-9322(02)00037-X.

[87] H.J. Lee, D.Y. Liu, Y. Alyousef, S. Yao, Generalized Two-Phase Pressure Drop and Heat Transfer Correlations in Evaporative Micro/Minichannels, J. Heat Transf. 132 (2010) 041004–041004. doi:10.1115/1.4000861.

[88] Y.W. Hwang, M.S. Kim, The pressure drop in microtubes and the correlation development, Int. J. Heat Mass Transf. 49 (2006) 1804–1812. doi:10.1016/j.ijheatmasstransfer.2005.10.040.

[89] D. Chisholm, Pressure gradients due to friction during the flow of evaporating two-phase mixtures in smooth tubes and channels, Int. J. Heat Mass Transf. 16 (1973) 347–358. doi:10.1016/0017-9310(73)90063-X.

[90] C.J. Baroczy, SYSTEMATIC CORRELATION FOR TWO-PHASE PRESSURE DROP., in: Chem Eng Progr Symp Ser 62 No 64 232-49 1966, Atomics International, Canoga Park, Calif., 1966. http://www.osti.gov/scitech/biblio/4300603 (accessed March 29, 2015).

[91] D. Chisholm, Two-phase flow in pipelines and heat exchangers, George Godwin London, 1983. http://www.opengrey.eu/item/display/10068/680408 (accessed March 19, 2015).

[92] L. Friedel, Improved friction pressure drop correlations for horizontal and vertical two-phase pipe flow, in: Eur. Two-Phase Flow Group Meet. Pap. E, 1979: p. 1979.

[93] I.Y. Chen, K.-S. Yang, Y.-J. Chang, C.-C. Wang, Two-phase pressure drop of air–water and R-410A in small horizontal tubes, Int. J. Multiph. Flow. 27 (2001) 1293–1299. doi:10.1016/S0301-9322(01)00004-0.

[94] M. Zhang, R.L. Webb, Correlation of two-phase friction for refrigerants in small-diameter tubes, Exp. Therm. Fluid Sci. 25 (2001) 131–139. doi:10.1016/S0894-1777(01)00066-8.

[95] T.N. Tran, M.-C. Chyu, M.W. Wambsganss, D.M. France, Two-phase pressure drop of refrigerants during flow boiling in small channels: an experimental investigation and correlation development, Int. J. Multiph. Flow. 26 (2000) 1739–1754. doi:10.1016/S0301-9322(99)00119-6.

[96] A. Lobo de Souza, M. de Mattos Pimenta, Prediction of pressure drop during horizontal two-phase flow of pure and mixed refrigerants, ASME-Publ.-FED. 210 (1995) 161–172.

[97] A. Cavallini, G. Censi, D. Del Col, L. Doretti, G.A. Longo, L. Rossetto, Condensation of halogenated refrigerants inside smooth tubes, HVACR Res. 8 (2002) 429–451.

[98] N. Kattan, J.R. Thome, D. Favrat, Flow Boiling in Horizontal Tubes: Part 3—Development of a New Heat Transfer Model Based on Flow Pattern, J. Heat Transf. 120 (1998) 156–165. doi:10.1115/1.2830039.

Appendix A: Numerical model of conduction on the test section

A numerical model of the thermal behavior of the test section is formulated to evaluate the effect of assuming an isothermal wall tube in the calculation of the heat transfer coefficient. A finite element method in cylindrical coordinates is used to develop the numerical model. Triangular elements are used, and linear basis functions. The purpose of the numerical model is to find an approximate solution of a given boundary-value problem. The basis of this method is the representation of the region of calculation by a finite number of subvolumes, where a spaced grid of nodes replaces a conduction region. These nodes are the location where the solution is computed. The left side of Figure 123 shows a two-dimensional region subdivided into finite elements. The mesh of the test section is generated using the packed model provided by Matlab. The original mesh is refined to improve the representation of the solution, which is shown in the right side of Figure 123. The region is formed by two subregions: copper block and stainless steel tube.

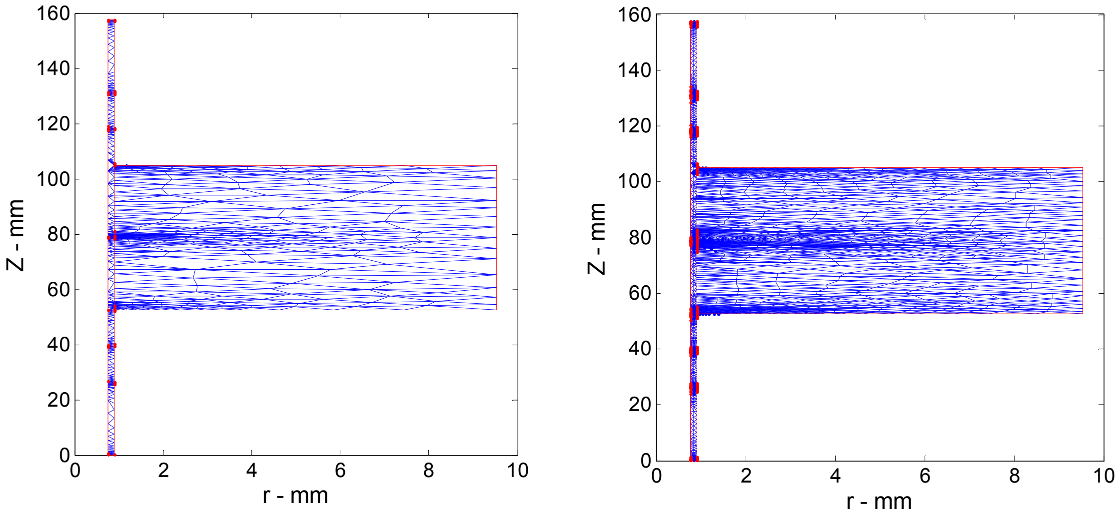

Figure 123. Mesh of the test section. Original (right) and refined (left)

This is a steady state problem two dimensional problem in cylindrical coordinates. The governing equation of the system is given by Eq. (118):

$$\frac{1}{r}\frac{\partial\left(k\,r\,T_r\right)}{\partial r}+\frac{\partial\left(k\,T_z\right)}{\partial z}=0 \tag{118}$$

The finite element model using cylindrical coordinate is described by Myers (1987). The boundary conditions that define this problem are shown in Figure 124. They include $\dot{Q}_{fluid}$, which is applied at the outer surface of the copper block (S_3). $\dot{Q}_{fluid}$ is obtained according to Eq. (61). $\dot{Q}_{fluid}$ is the result to subtract the radiation and conduction losses from $\dot{Q}_{applied}$. The gas mixture flowing inside of the tube removes heat from the inner wall tube (S_6). In addition, it is assumed that there are no radiation losses between the copper, the stainless steel tube and the surroundings because they were discount previously. Consequently, the others surfaces (S_1, S_2, S_4, and S_5) are assumed to be adiabatic

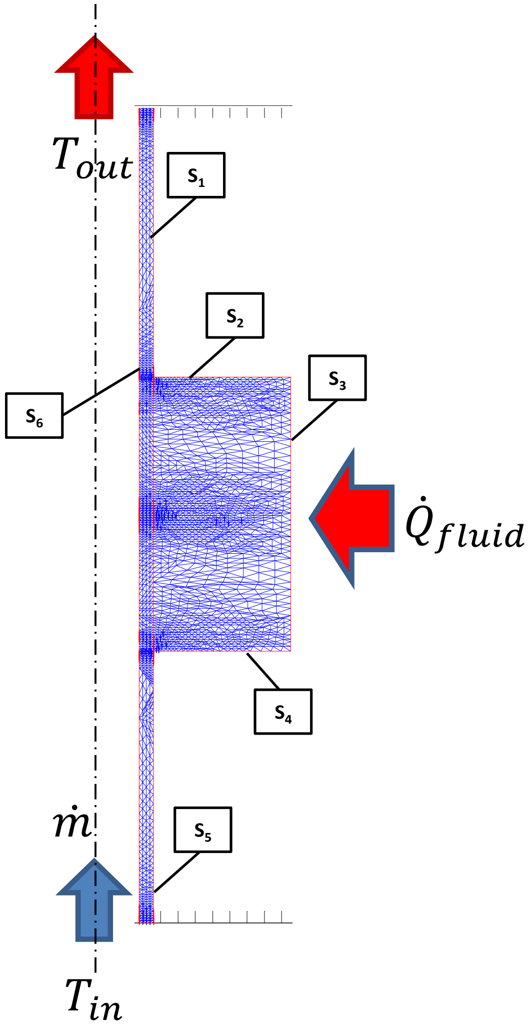

Figure 124. Boundary conditions

Two set of data are required to solve this problem. One of the files, called the geometry file, contains information related with the sub-regions, boundary segments and the sub-volumes. This information is summarized in three matrices (point, element and triangular). The other file is the input data file, which is formed by the temperature and pressure in the inlet and outlet of the test section, $\dot{Q}_{fluid}$, mass flow rate, mixture and composition, thermal conductivity of copper and stainless steel (SS304) as a function of temperature, the calculated heat transfer coefficient using the isothermal wall assumption. Figure 125 shows a schematic summarizing how the problem is solved:

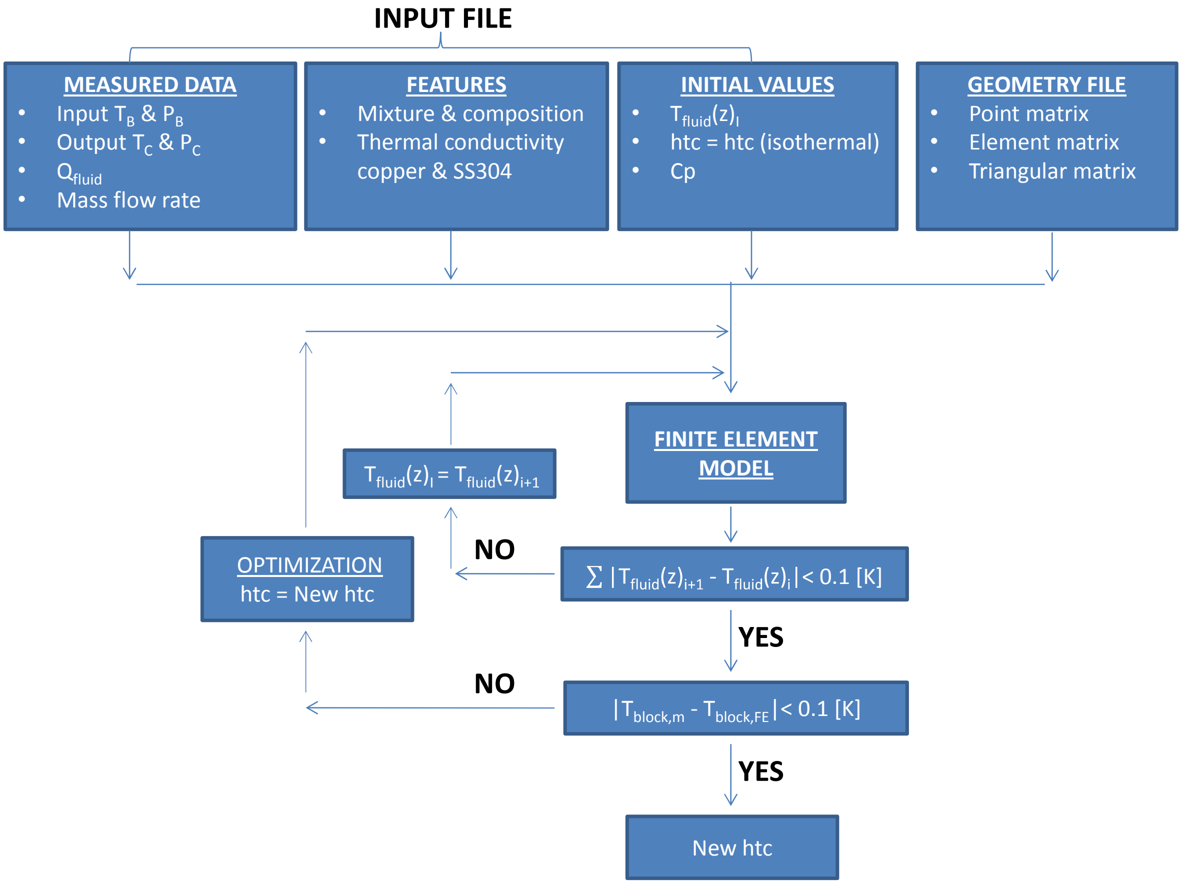

Figure 125. Schematic summary how the problem is solved

Initial values for the fluid temperature, heat transfer coefficient, and specific heat of the gas mixture are estimated: The fluid temperature is assumed to be constant and equal to (T_B) in the tube up to where the copper block is located. A constant gradient is assumed in the copper block achieving the outlet temperature (T_C) where the block copper finishes. T_C Is kept constant up to the end of the tube. The initial heat transfer is assumed to be equal to the heat transfer coefficient calculated assuming isothermal wall. The specific heat of the gas mixture, as a first approach, is kept constant through the whole test section, and it is the measured average specific heat. The measured average specific heat of the fluid is given by:

$$\overline{Cp_{fluid}} = \frac{\dot{Q}_{fluid}}{\dot{m}\left(T_{out} - T_{in}\right)} \tag{119}$$

Solving the finite element model, the temperatures in each node of the copper block and the stainless steel tube are known. Performing an energy balance in each element of the inner wall tube the new temperature profile for the fluid through the tube is obtained. This loop is repeated to minimize the temperature profile and the new temperature profile for the fluid according to:

$$\Sigma\left|T_{fluid}\left(z\right)_{i+1} - T_{fluid}\left(z\right)_{i}\right| < 0.1\left[K\right] \tag{120}$$

In addition, the new local specific heat for the mixture is calculated using REFPROP after each iteration. The specific heat for the mixture is given by

$$Cp = \left(\frac{\partial h}{\partial T}\right)_p \tag{121}$$

The specific heat for the mixture is a function of the local fluid temperature and pressure. A linear pressure drop is assumed in the test section. The calculated specific heat using REFPROP is corrected to match the measured average specific heat.

$$\overline{Cp_{fluid}} = \frac{\int_0^{3L}\left(\frac{\partial h}{\partial T}\right)_p dT}{T_{out} - T_{in}} \tag{122}$$

Once the fluid temperature fulfills the criterion indicated above, a new heat transfer coefficient is proposed. The iterative process continues up to minimize the difference between the calculated and measured block average temperature. The optimization is performed using the bisection method. The lower and upper limit are $0.75\,htc_{isothermal}$ and $1.25\,htc_{isothermal}$ respectively. When the minimization is achieved the new heat transfer coefficient is obtained. As an example, Figure 126 shows the numerical result for the wall tube and fluid temperature as a function of axial position (z-coordinate).

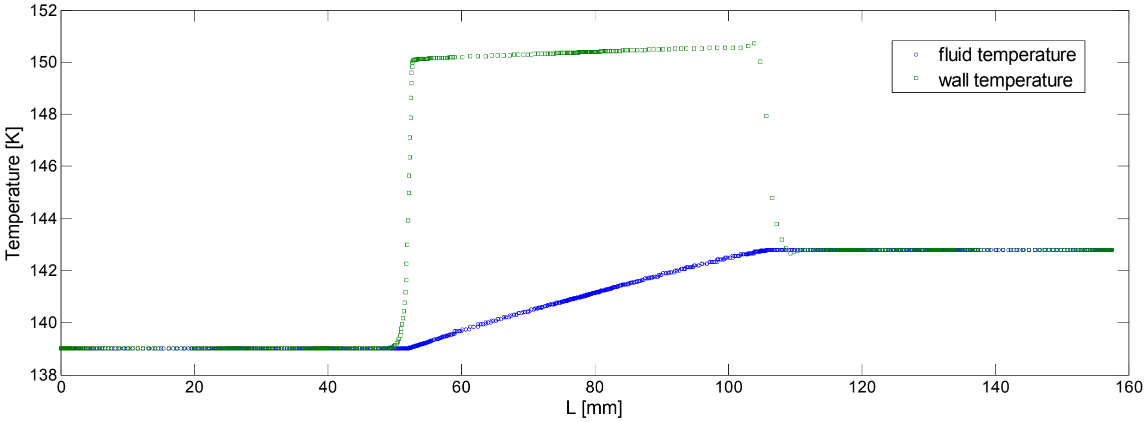

Figure 126. Wall tube and fluid temperature as a function of axial position (z-coordinate)

Appendix B: Binary mixture experimental data

B.1 Diameter effect

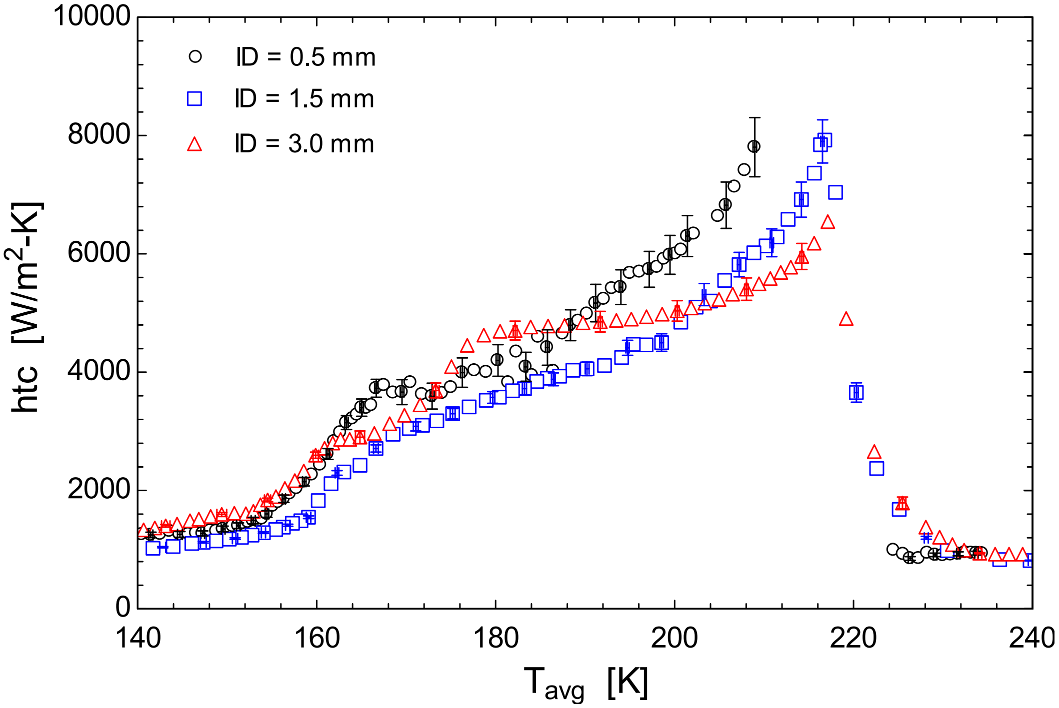

Figure 127. heat transfer coefficient as a function of average temperature, Diameter effect, binary mixture, *G* = 144 kg/m^2-s, *P* = 790 kPa, *Q″* = 56 kW/m^2, Runs 30,35 and 37

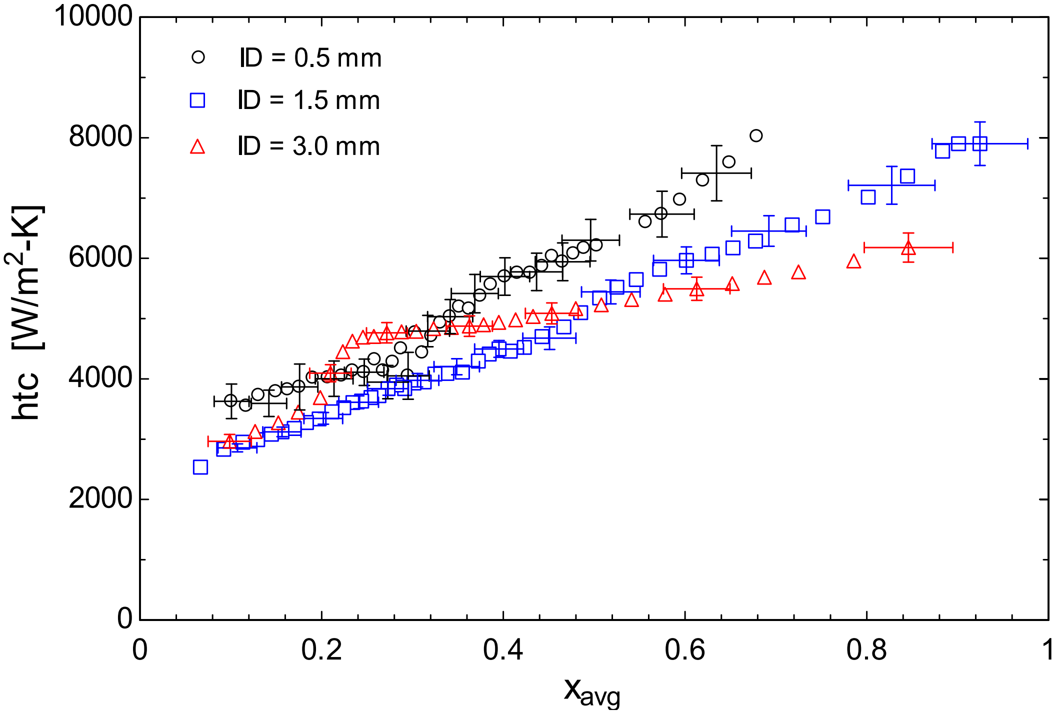

Figure 128. heat transfer coefficient as a function of average quality, Diameter effect, binary mixture, *G* = 144 kg/m^2-s, *P* = 790 kPa, *Q″* = 56 kW/m^2, Runs 30,35 and 37

B.2 Heat flux effect, *ID* = 0.5 mm

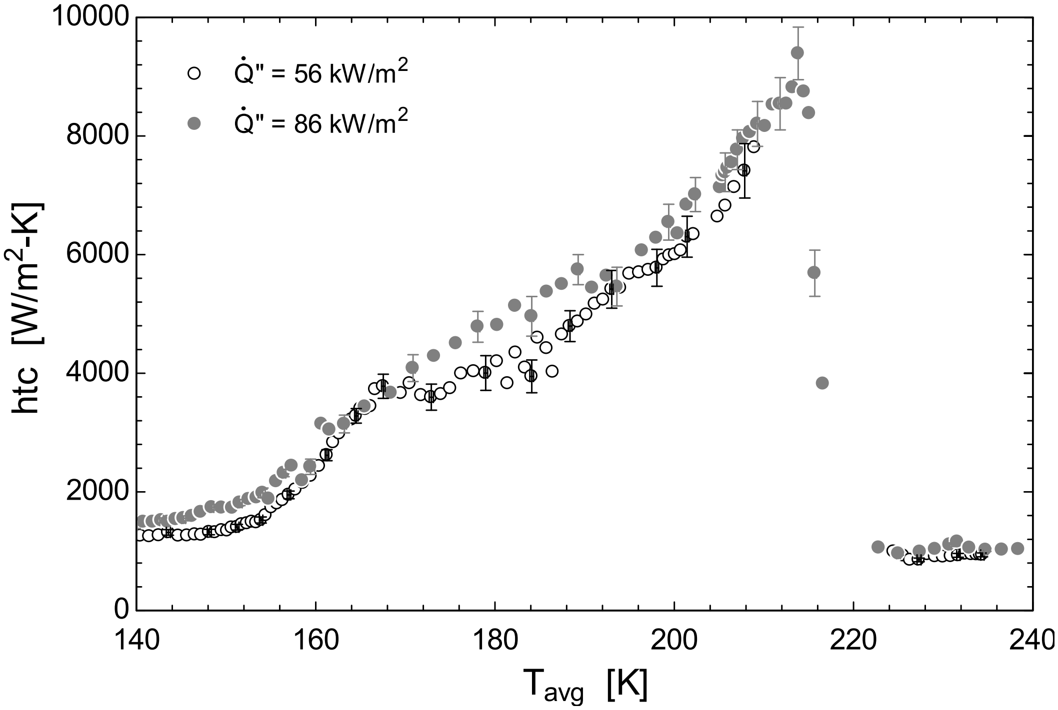

Figure 129. heat transfer coefficient as a function of average temperature, heat flux effect, binary mixture, *G* = 144 kg/m^2-s, *P* = 790 kPa, *ID* = 0.5 mm, Runs 30 and 31

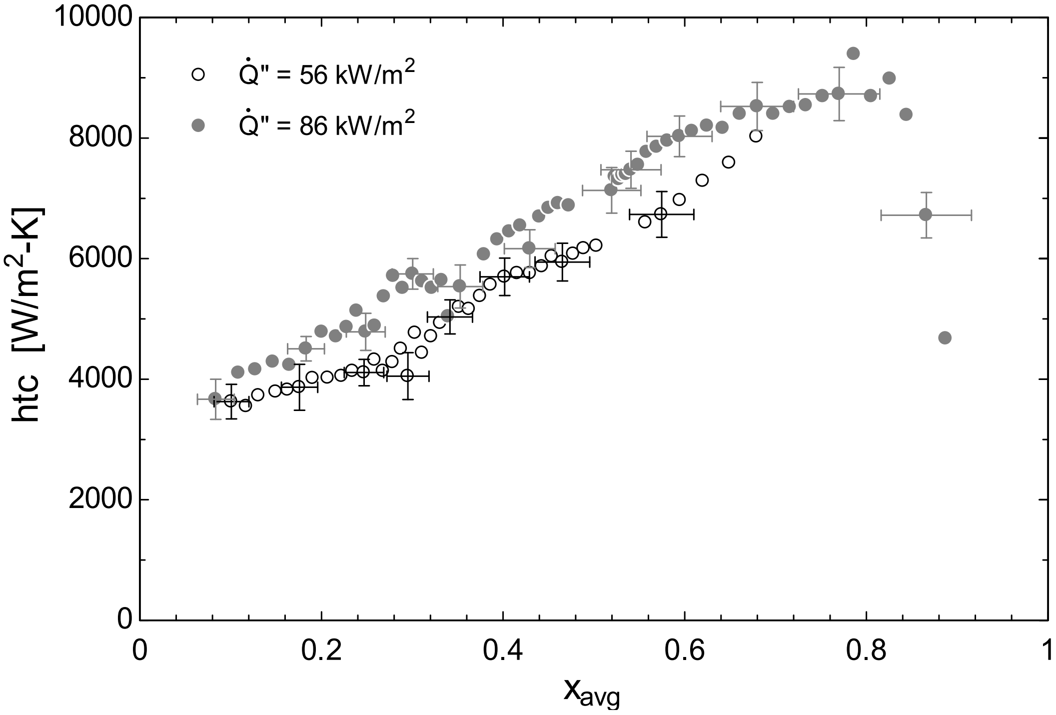

Figure 130. heat transfer coefficient as a function of average quality, heat flux effect, binary mixture, *G* = 144 kg/m^2-s, *P* = 790 kPa, *ID* = 0.5 mm, Runs 30 and 31

B.3 Heat flux effect, *ID* = 1.5 mm

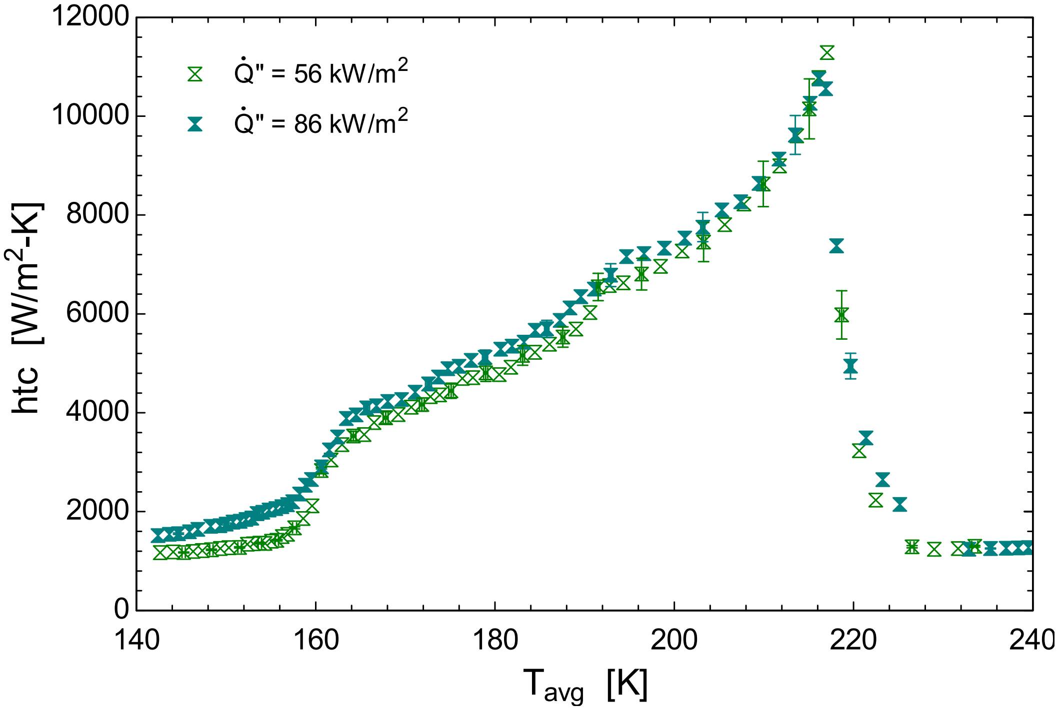

Figure 131. heat transfer coefficient as a function of average temperature, heat flux effect, binary mixture, *G* = 240 kg/m^2-s, *P* = 790 kPa, *ID* = 1.5 mm, Runs 32 and 33

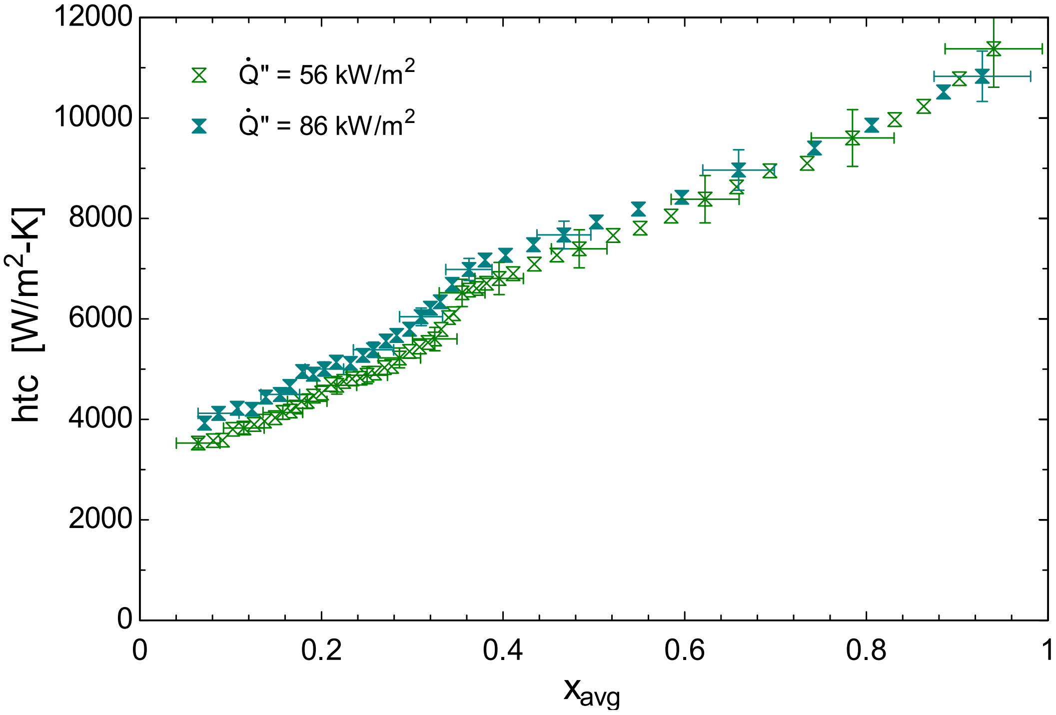

Figure 132. heat transfer coefficient as a function of average quality, heat flux effect, binary mixture, *G* = 240 kg/m^2-s, *P* = 790 kPa, *ID* = 1.5 mm, Runs 32 and 33

B.4 Heat flux effect, *ID* = 3.0 mm

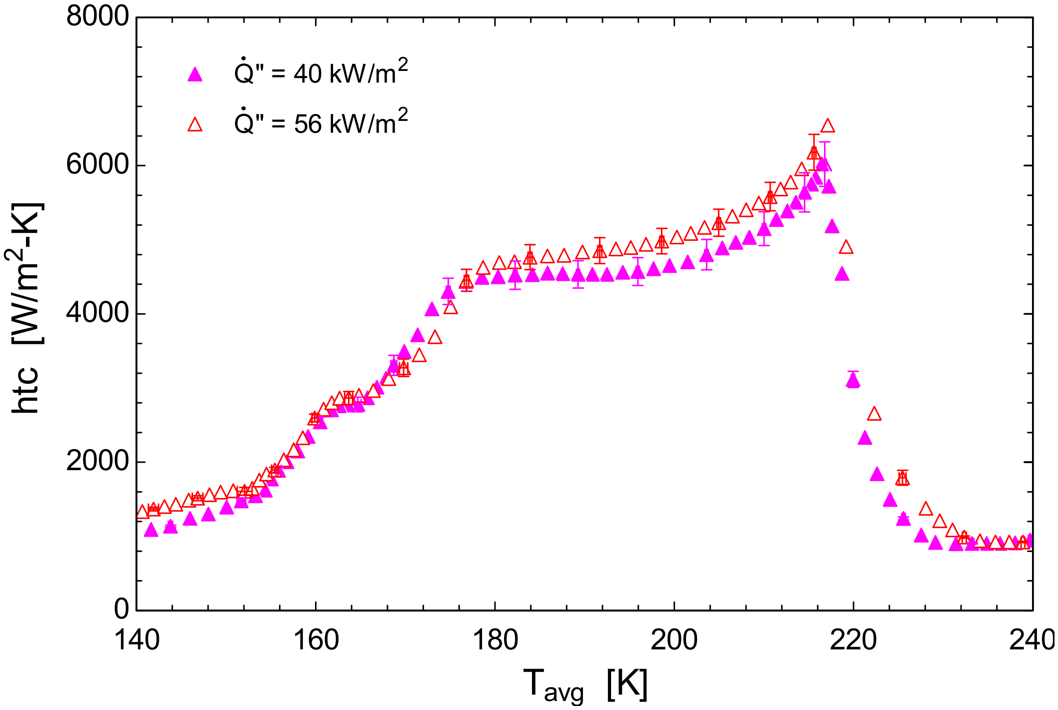

Figure 133. heat transfer coefficient as a function of average temperature, heat flux effect, binary mixture, *G* = 144 kg/m^2-s, *P* = 790 kPa, *ID* = 3.0 mm, Runs 36 and 37

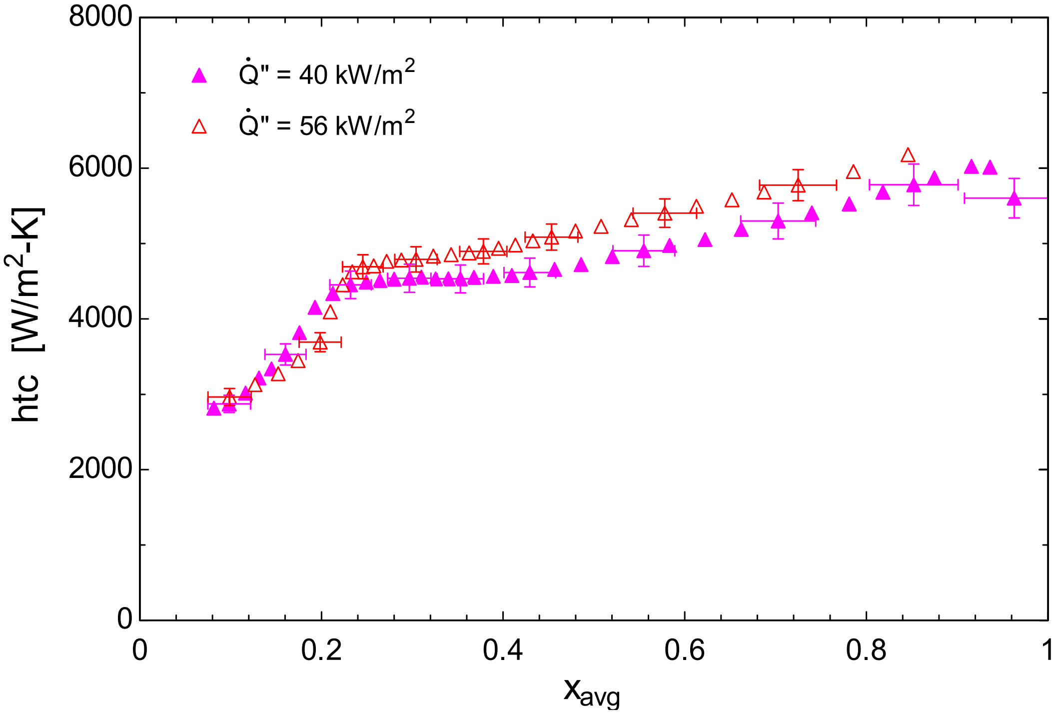

Figure 134. heat transfer coefficient as a function of average quality, heat flux effect, binary mixture, *G* = 144 kg/m^2-s, *P* = 790 kPa, *ID* = 3.0 mm, Runs 36 and 37

B.5 Pressure effect

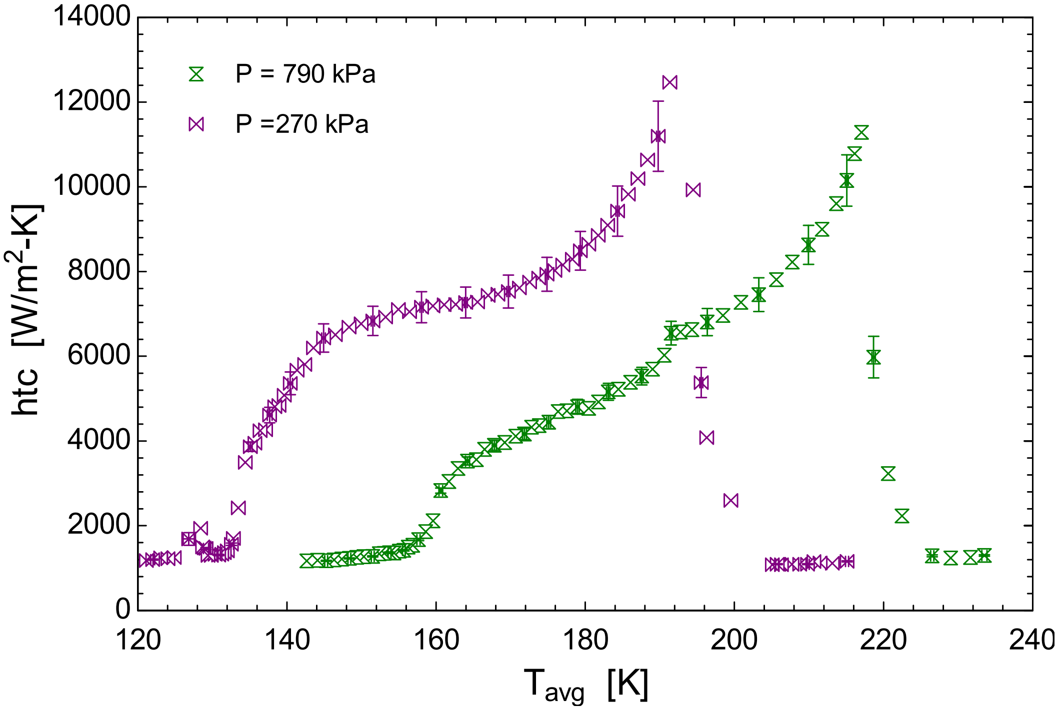

Figure 135. heat transfer coefficient as a function of average temperature, pressure effect, binary mixture, $G = 240$ kg/m^2-s, $Q'' = 56$ kW/m^2, $ID = 1.5$ mm, Runs 33 and 34

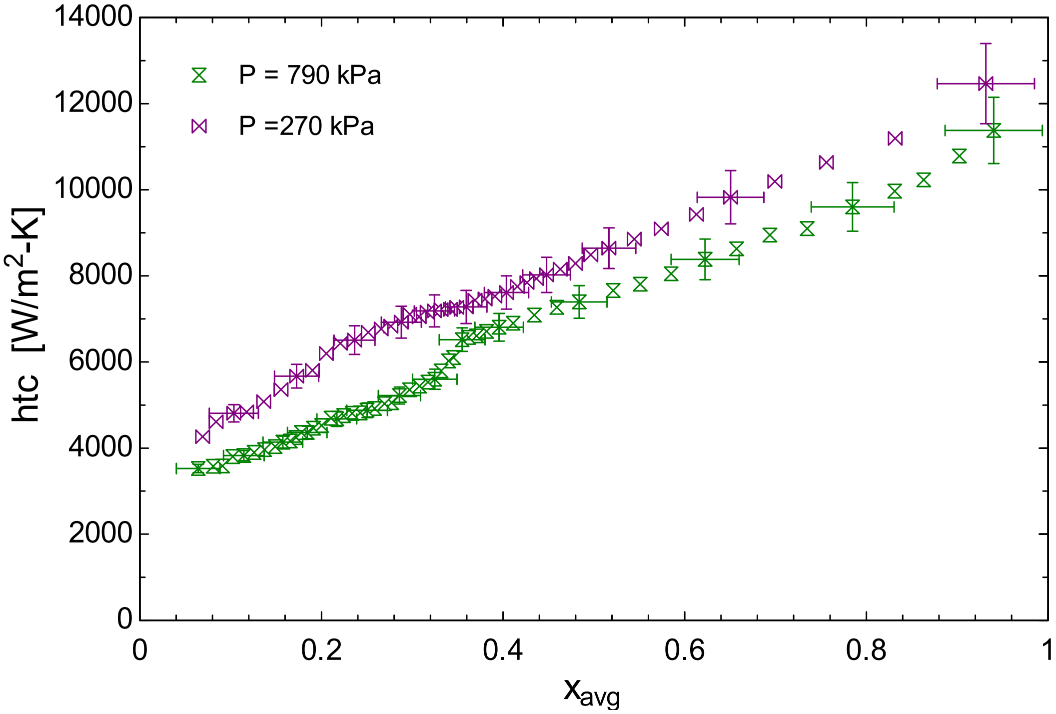

Figure 136. heat transfer coefficient as a function of average quality, pressure effect, binary mixture, $G = 240$ kg/m^2-s, $Q'' = 56$ kW/m^2, $ID = 1.5$ mm, Runs 33 and 34

B.6 Mass flux effect

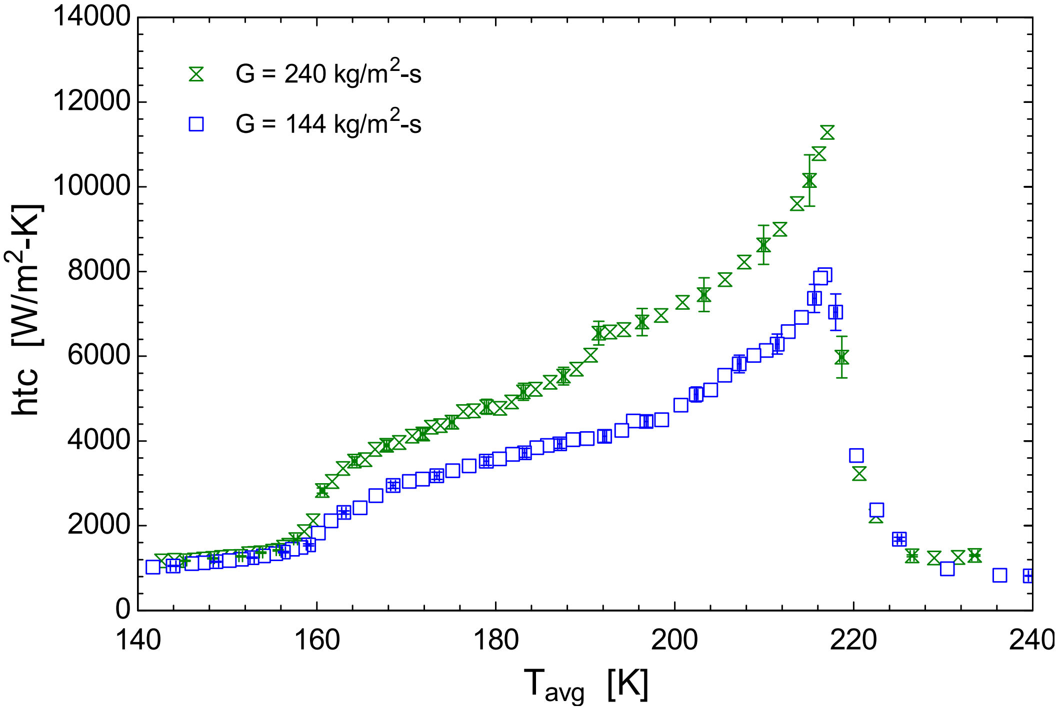

Figure 137. heat transfer coefficient as a function of average temperature, mass flux effect, binary mixture, *P* = 790 kPa, *Q″* = 56 kW/m^2, *ID* = 1.5 mm, Runs 33 and 35

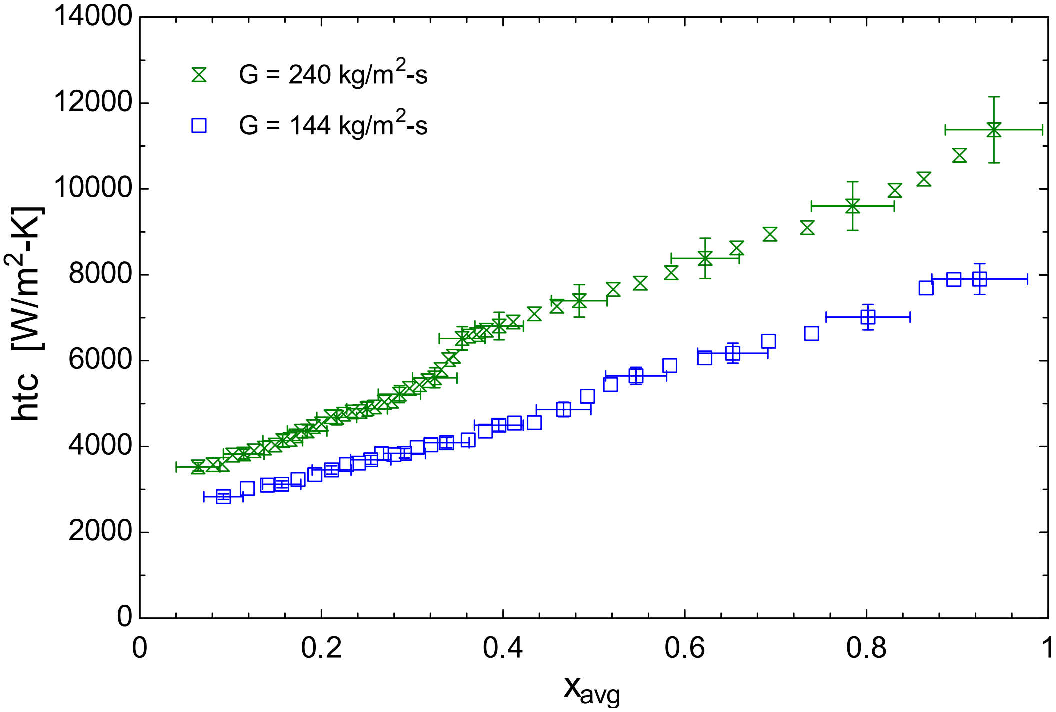

Figure 138. heat transfer coefficient as a function of average quality, mass flux effect, binary mixture, *P* = 790 kPa, *Q″* = 56 kW/m^2, *ID* = 1.5 mm, Runs 33 and 35

Appendix C: Hydrocarbons mixture experimental data

C.1 Diameter effect (0% N_2)

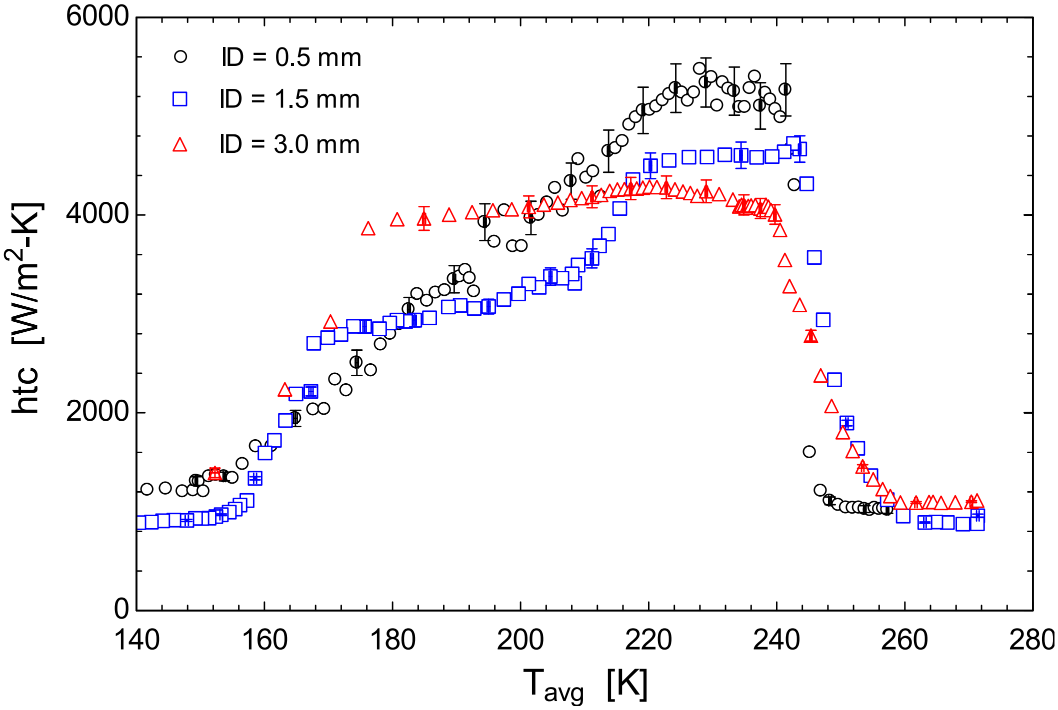

Figure 139. heat transfer coefficient as a function of average temperature, Diameter effect, hydrocarbon mixture (no dilution), G = 144 kg/m^2-s, P = 790 kPa, Q'' = 56 kW/m^2, Runs 1, 9 and 13

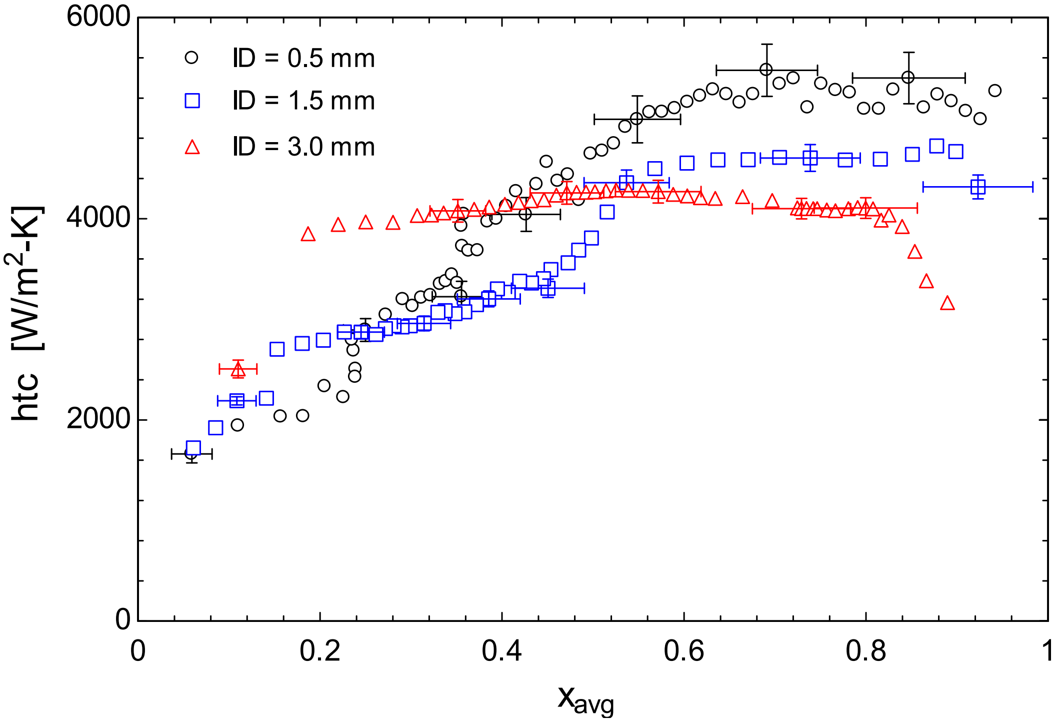

Figure 140. heat transfer coefficient as a function of average quality, Diameter effect, hydrocarbon mixture (no dilution), G = 144 kg/m^2-s, P = 790 kPa, Q'' = 56 kW/m^2, Runs 1, 9 and 13

C.2 Diameter effect (20% N_2)

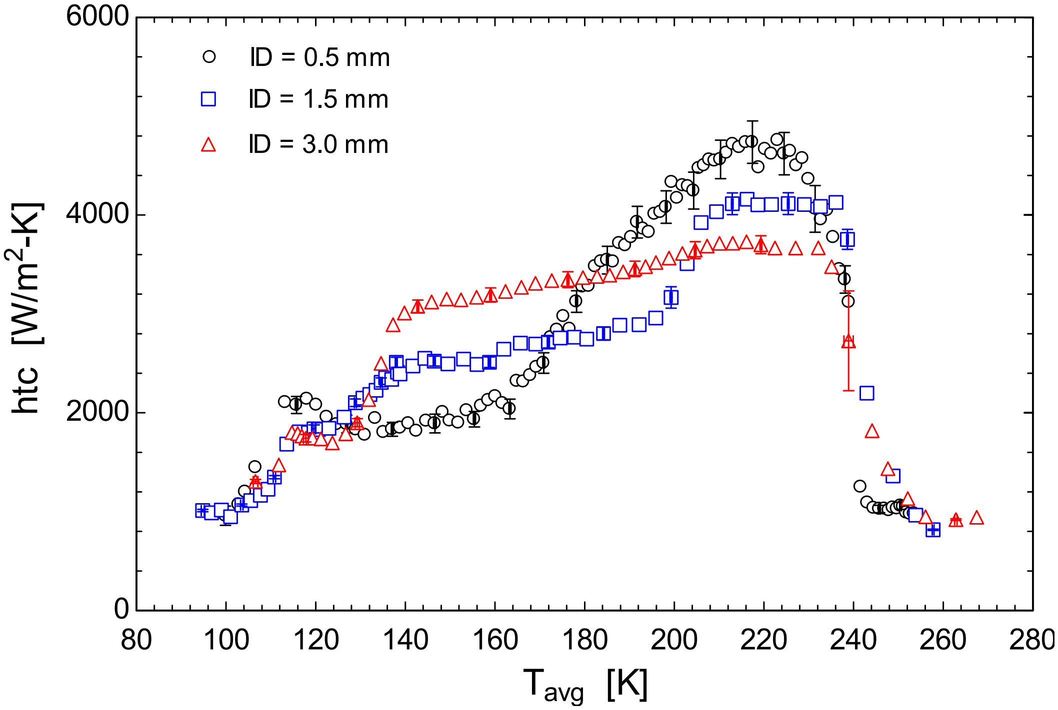

Figure 141. heat transfer coefficient as a function of average temperature, Diameter effect, hydrocarbon mixture (20% dilution), G = 144 kg/m^2-s, P = 790 kPa, Q'' = 56 kW/m^2, Runs 3, 10 and 14

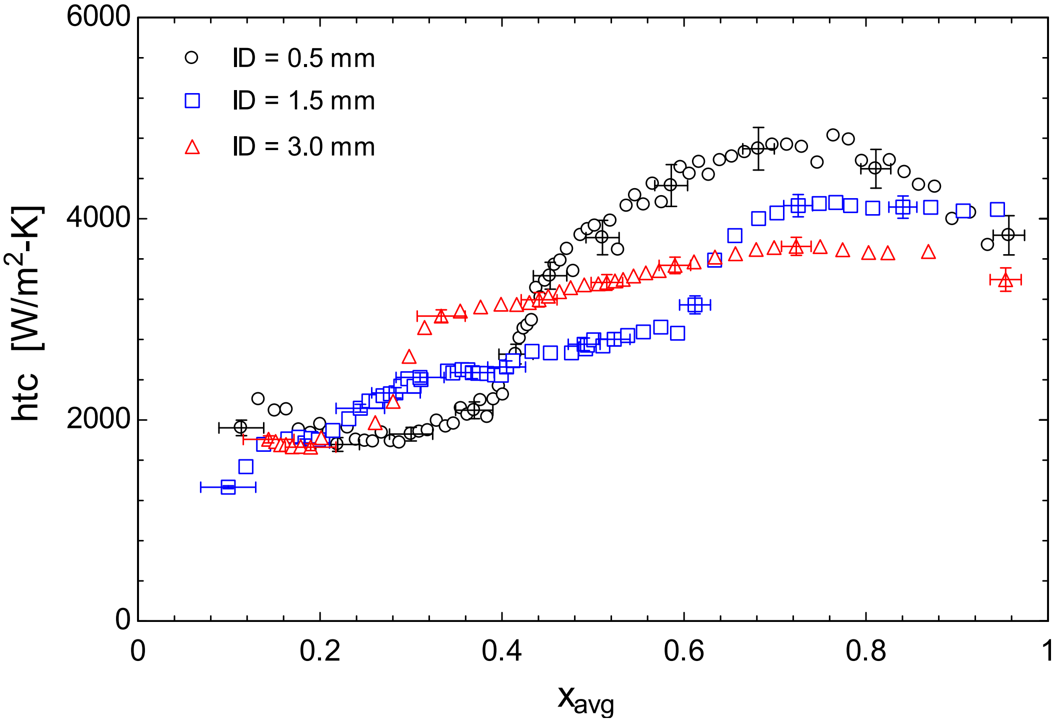

Figure 142. heat transfer coefficient as a function of average quality, Diameter effect, hydrocarbon mixture (20% dilution), G = 144 kg/m^2-s, P = 790 kPa, Q'' = 56 kW/m^2, Runs 3, 10 and 14

C.3 Diameter effect (40% N_2)

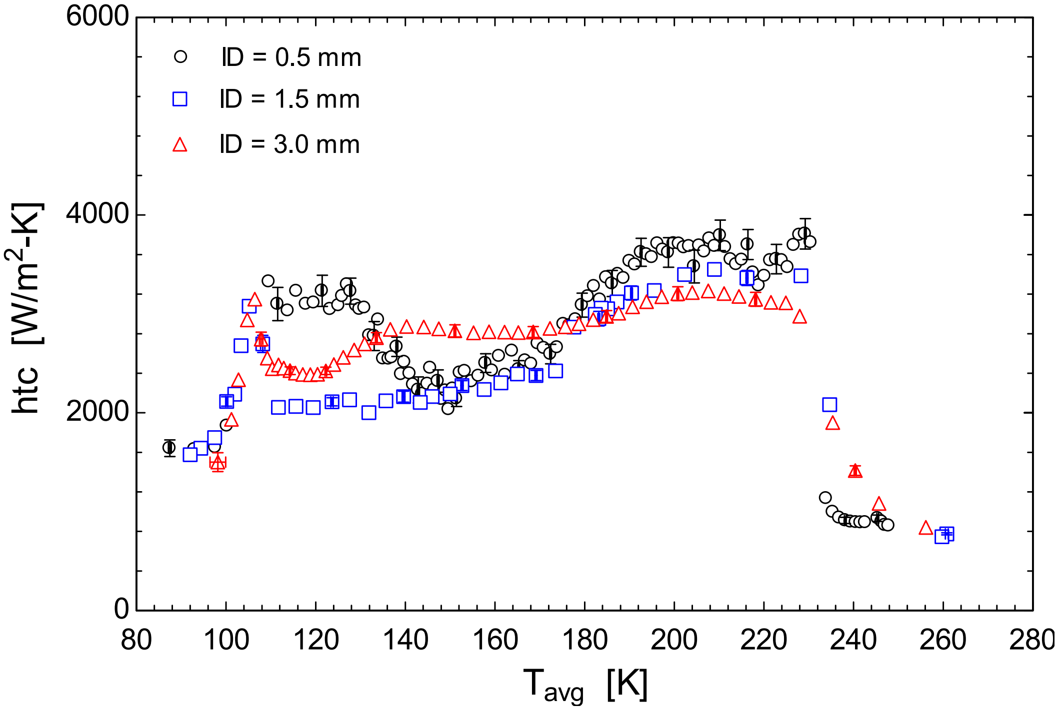

Figure 143. heat transfer coefficient as a function of average temperature, Diameter effect, hydrocarbon mixture (40% dilution), $G = 144$ kg/m^2-s, $P = 790$ kPa, $Q'' = 56$ kW/m^2, Runs 4, 11 and 15

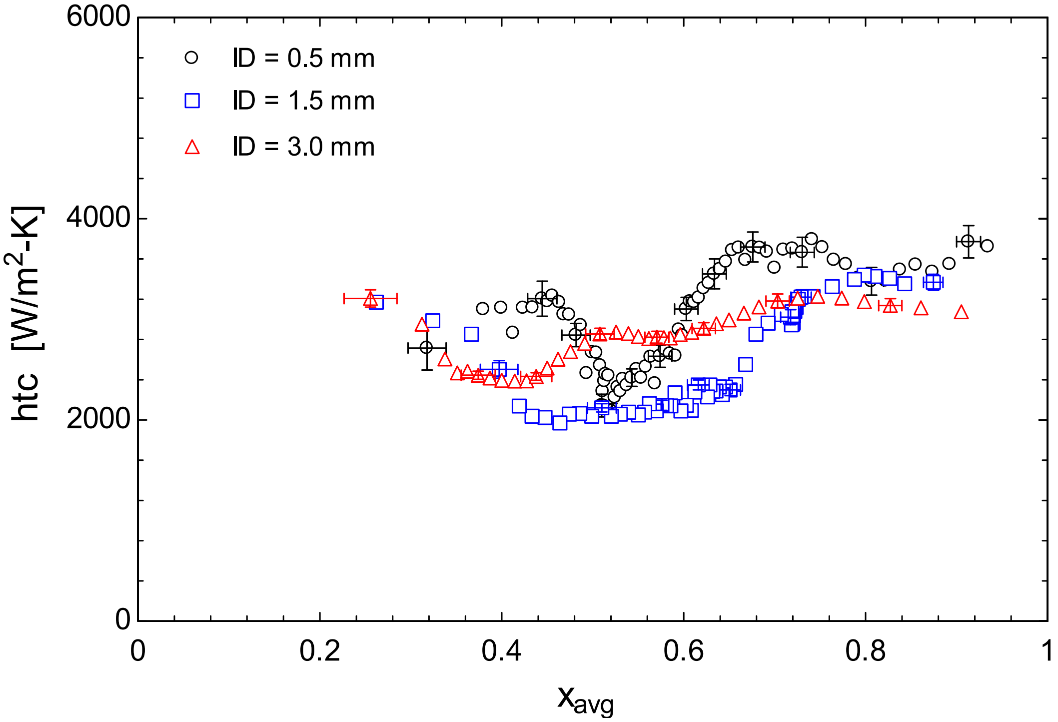

Figure 144. heat transfer coefficient as a function of average quality, Diameter effect, hydrocarbon mixture (40% dilution), $G = 144$ kg/m^2-s, $P = 790$ kPa, $Q'' = 56$ kW/m^2, Runs 4, 11 and 15

C.4 Heat flux effect (0.5 mm)

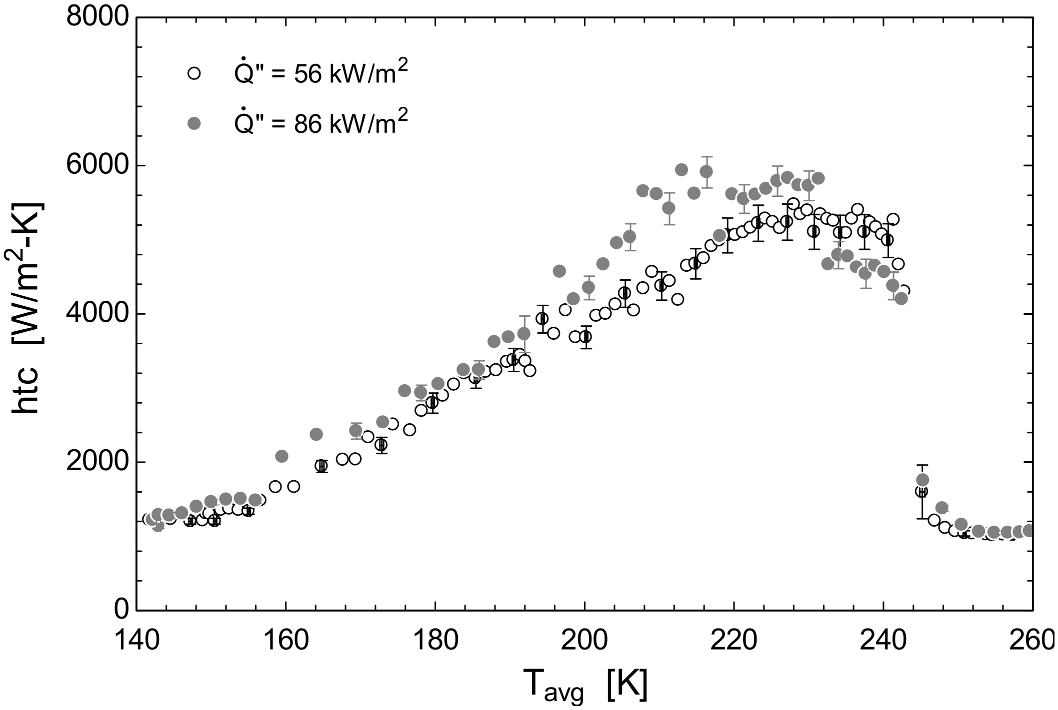

Figure 145. heat transfer coefficient as a function of average temperature, heat flux effect, hydrocarbon mixture (No dilution), *G* = 144 kg/m^2-s, *P* = 790 kPa, *ID* = 0.5 mm, Runs 1 and 2

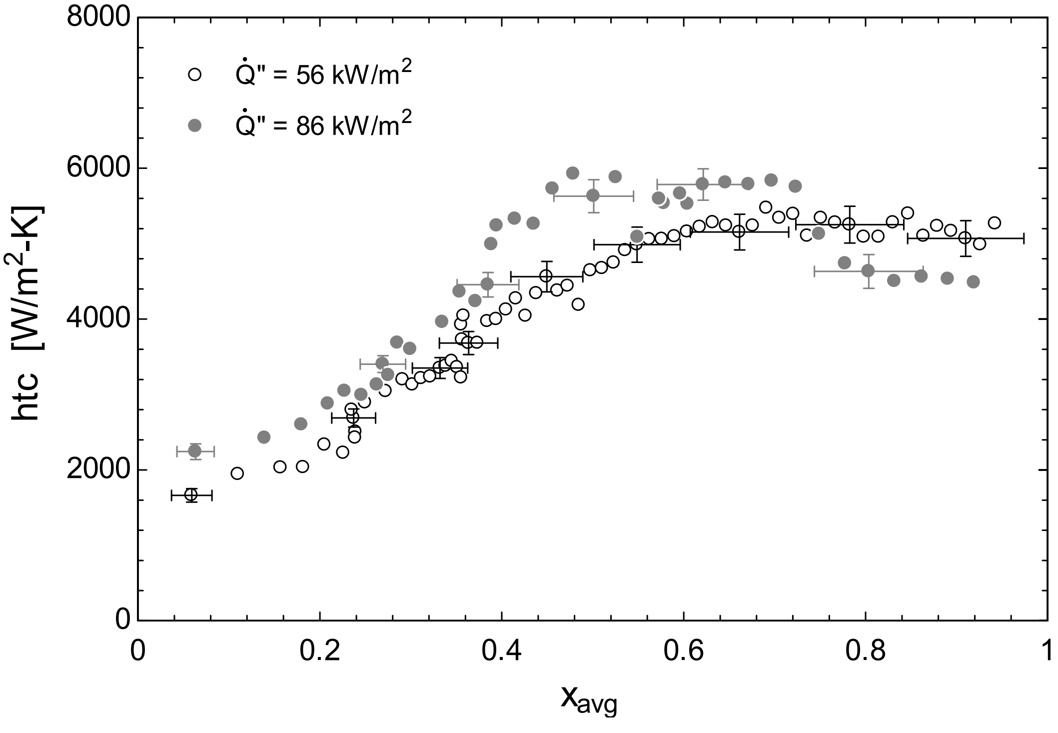

Figure 146. heat transfer coefficient as a function of average quality, heat flux effect, hydrocarbon mixture (No dilution), *G* = 144 kg/m^2-s, *P* = 790 kPa, *ID* = 0.5 mm, Runs 1 and 2

C.5 Heat flux effect (1.5 mm)

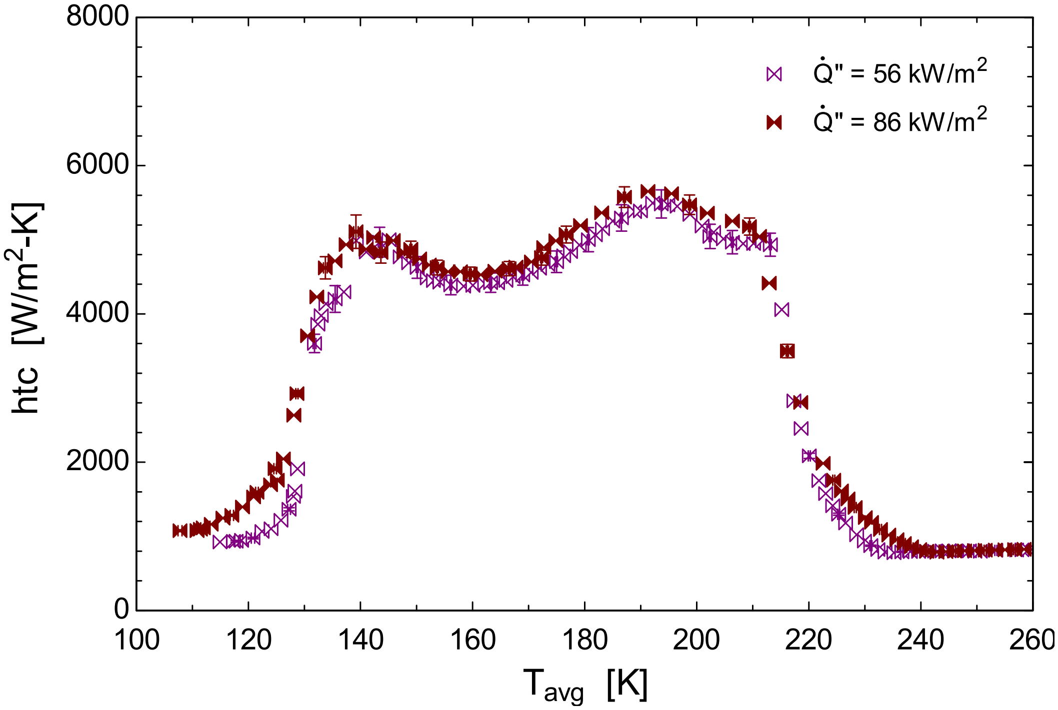

Figure 147. heat transfer coefficient as a function of average temperature, heat flux effect, hydrocarbon mixture (No dilution), *G* = 144 kg/m^2-s, *P* = 270 kPa, *ID* = 1.5 mm, Runs 5 and 6

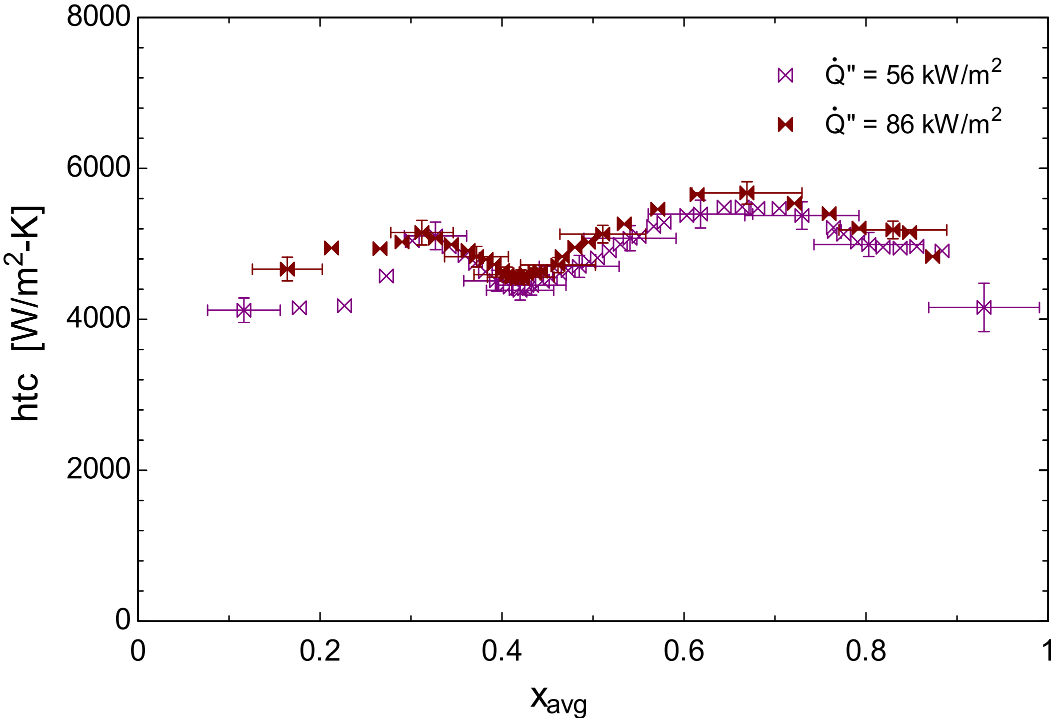

Figure 148. heat transfer coefficient as a function of average quality, heat flux effect, hydrocarbon mixture (No dilution), *G* = 144 kg/m^2-s, *P* = 270 kPa, *ID* = 1.5 mm, Runs 5 and 6

C.6 Heat flux effect (3.0 mm)

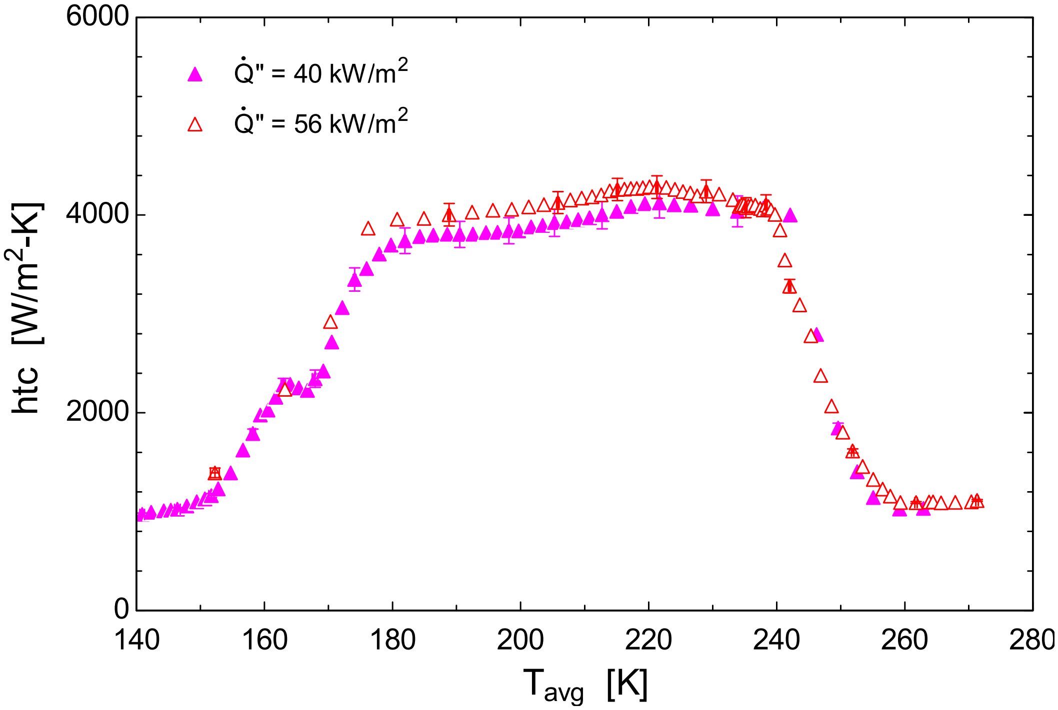

Figure 149. heat transfer coefficient as a function of average temperature, heat flux effect, hydrocarbon mixture (No dilution), G = 144 kg/m^2-s, P = 790 kPa, ID = 3.0 mm, Runs 12 and 13

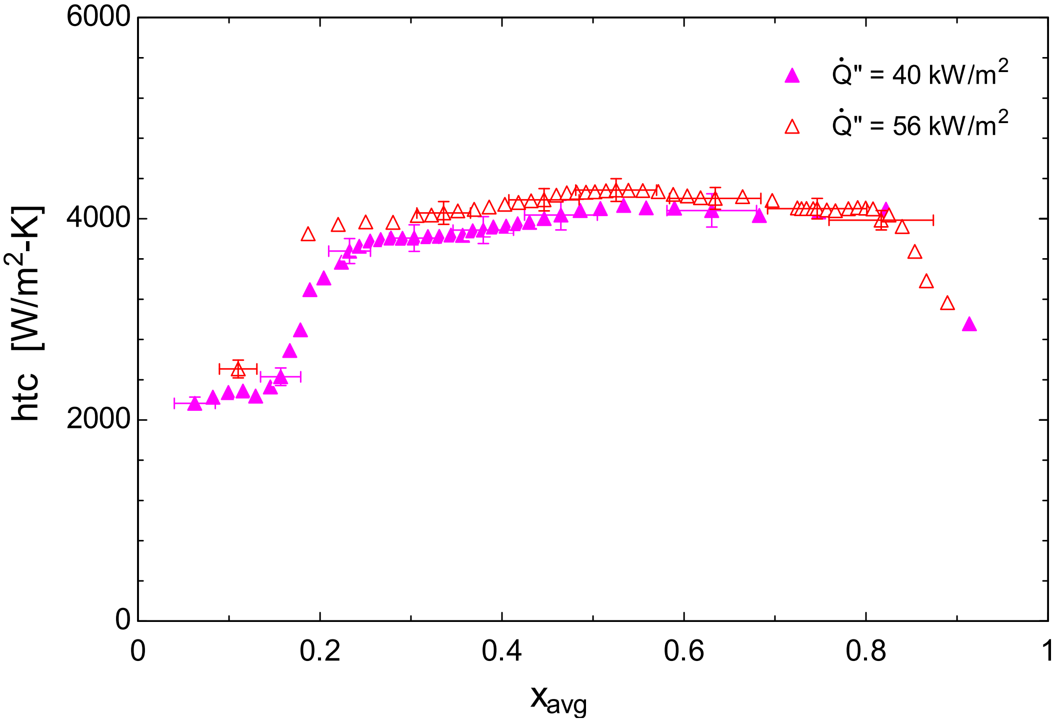

Figure 150. heat transfer coefficient as a function of average quality, heat flux effect, hydrocarbon mixture (No dilution), G = 144 kg/m^2-s, P = 790 kPa, ID = 3.0 mm, Runs 12 and 13

C.7 Pressure effect

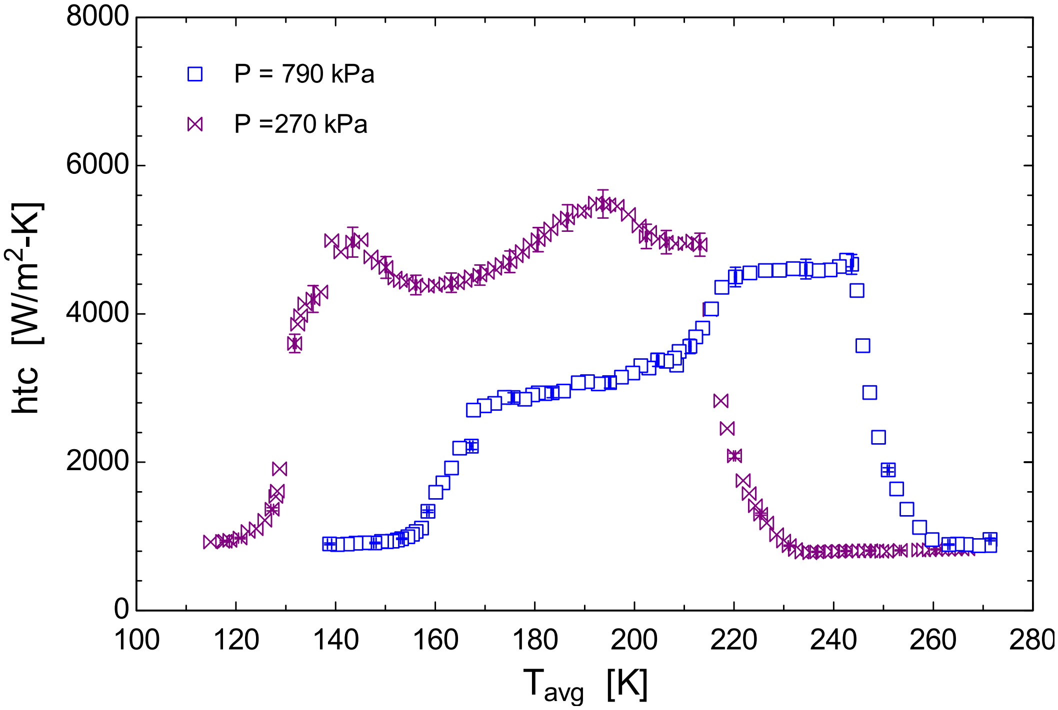

Figure 151. heat transfer coefficient as a function of average temperature, pressure effect, hydrocarbon mixture (no dilution), G = 144 kg/m^2-s, Q'' = 56 kW/m^2, ID = 1.5 mm, Runs 7 and 9

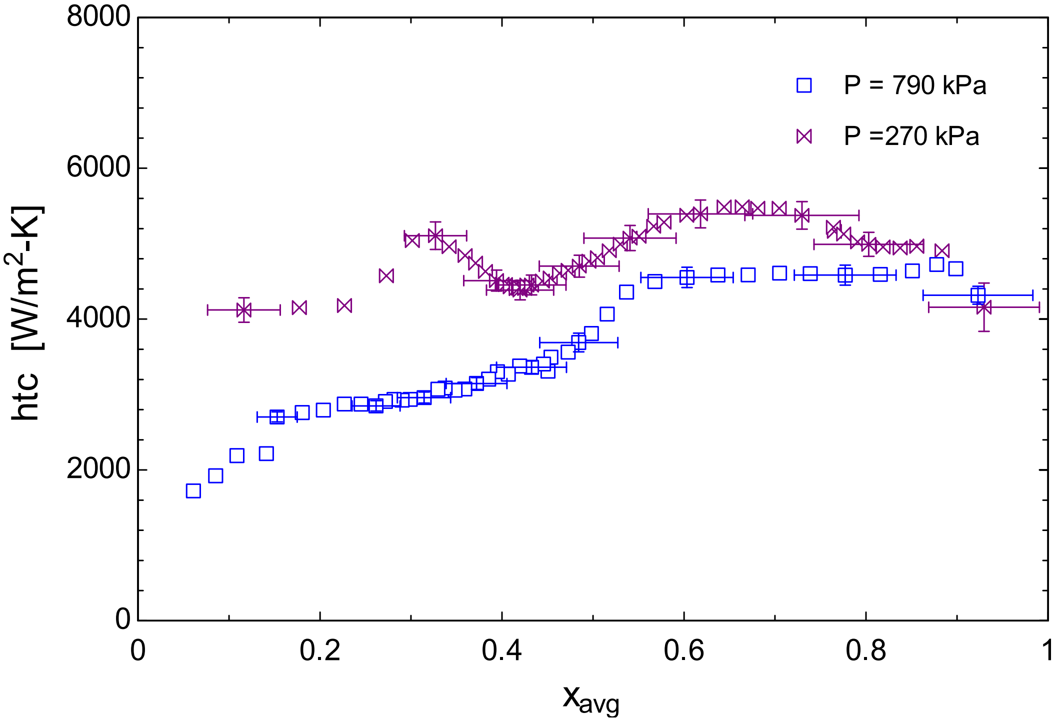

Figure 152. heat transfer coefficient as a function of average quality, pressure effect, hydrocarbon mixture (no dilution), G = 144 kg/m^2-s, Q'' = 56 kW/m^2, ID = 1.5 mm, Runs 7 and 9

C.8 Mass flux effect

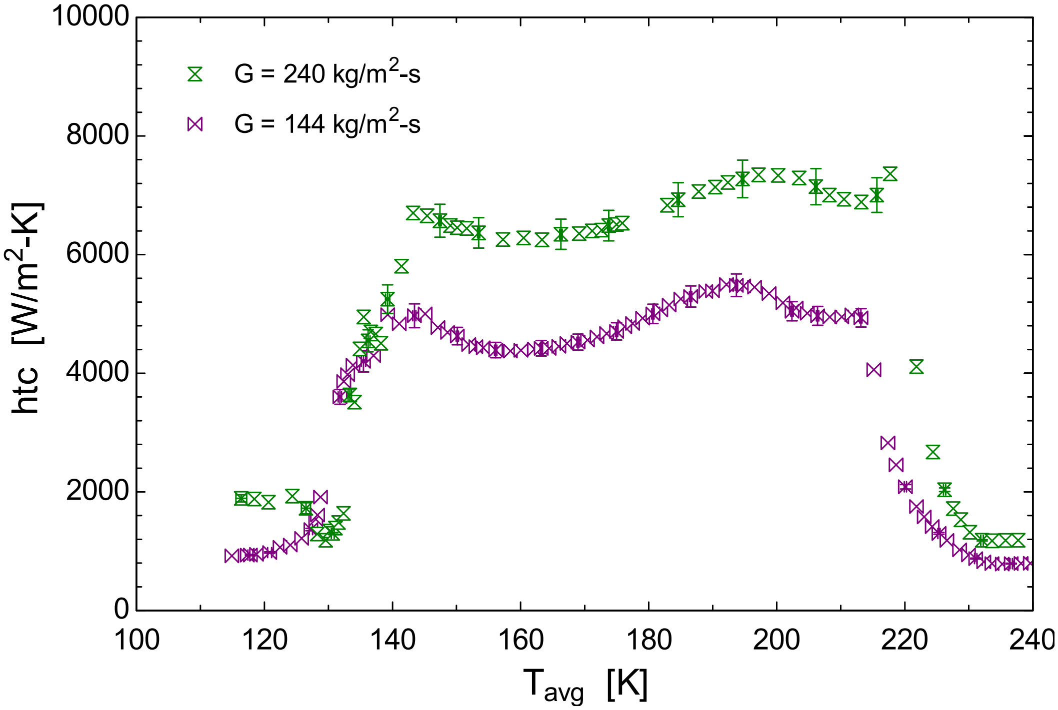

Figure 153. heat transfer coefficient as a function of average temperature, mass flux effect, hydrocarbon mixture (no dilution), P = 270 kPa, Q'' = 56 kW/m^2, ID = 1.5 mm, Runs 7 and 8

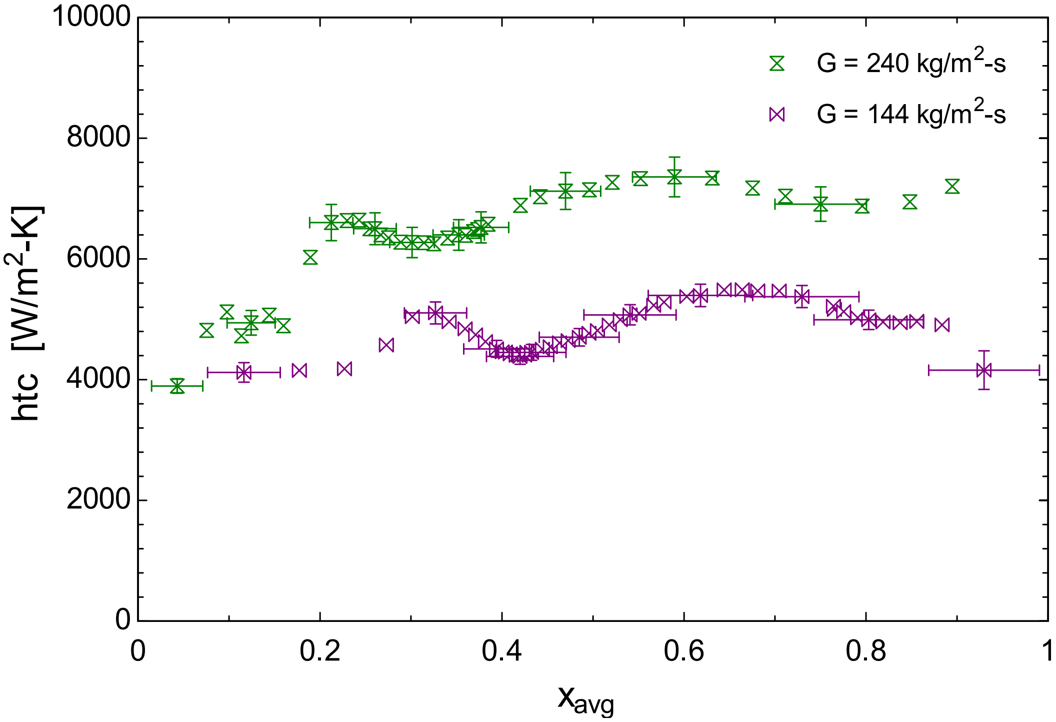

Figure 154. heat transfer coefficient as a function of average quality, mass flux effect, hydrocarbon mixture (no dilution), P = 270 kPa, Q'' = 56 kW/m^2, ID = 1.5 mm, Runs 7 and 8

C.9 Composition effect (0.5 mm)

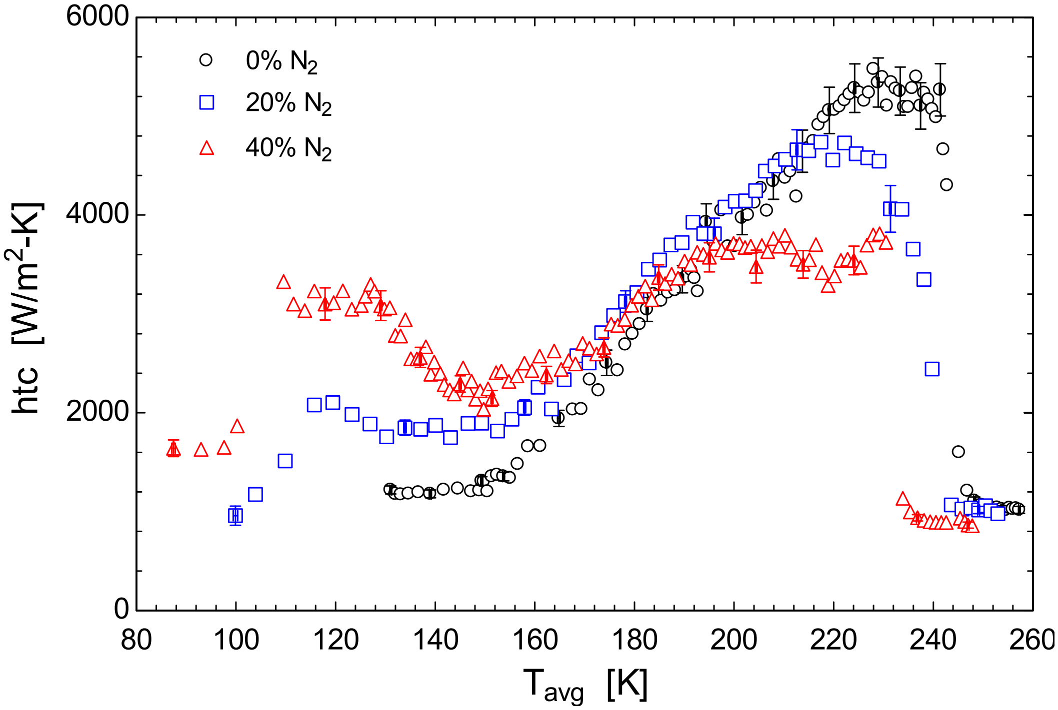

Figure 155. heat transfer coefficient as a function of average temperature, Composition effect, hydrocarbon mixture, G = 144 kg/m^2-s, P = 790 kPa, Q'' = 56 kW/m^2, ID = 0.5 mm, Runs 1, 3 and 4

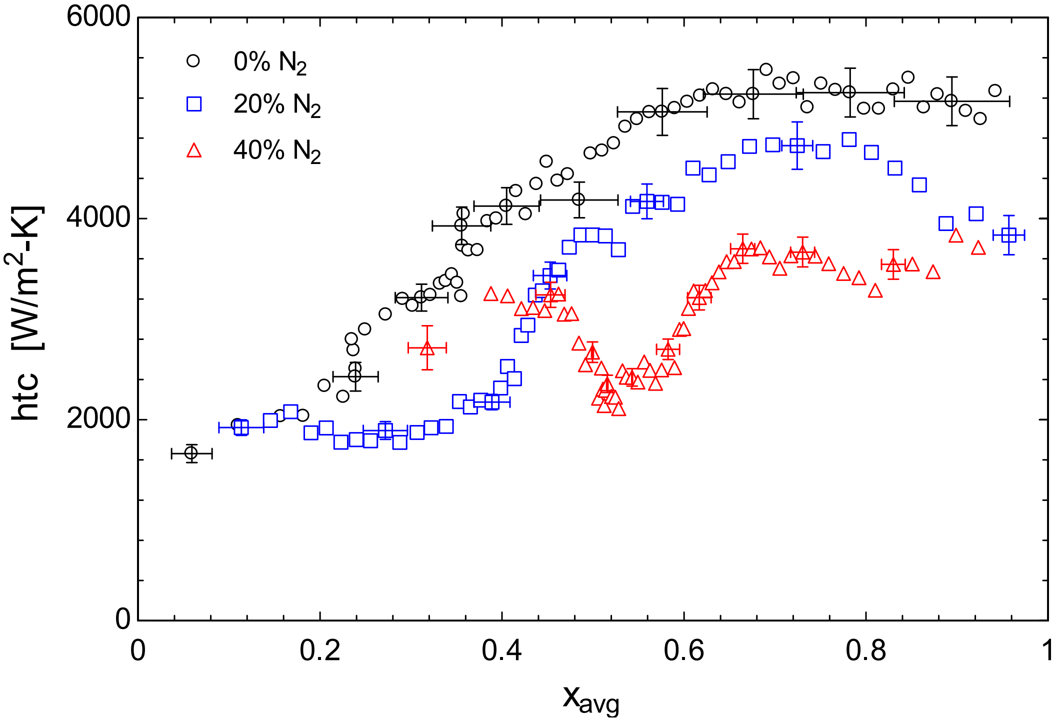

Figure 156. heat transfer coefficient as a function of average quality, Composition effect, hydrocarbon mixture, G = 144 kg/m^2-s, P = 790 kPa, Q'' = 56 kW/m^2, ID = 0.5 mm, Runs 1, 3 and 4

C.10 Composition effect (1.5 mm)

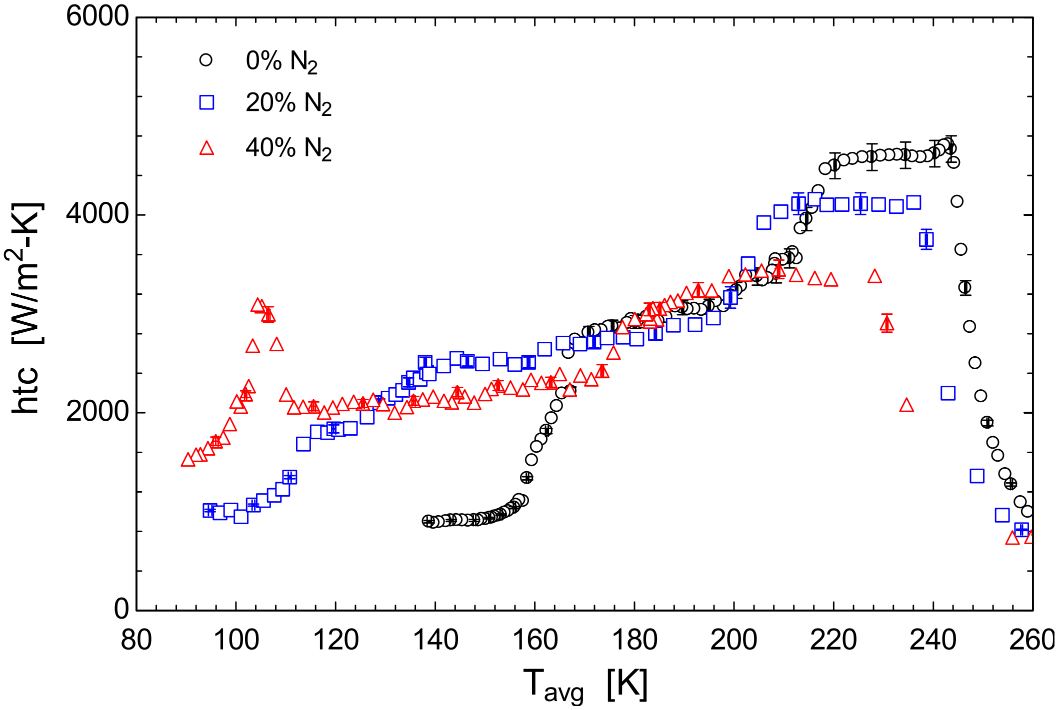

Figure 157. heat transfer coefficient as a function of average temperature, Composition effect, hydrocarbon mixture, G = 144 kg/m^2-s, *P* = 790 kPa, *Q″* = 56 kW/m^2, *ID* = 1.5 mm, Runs 9, 10 and 11

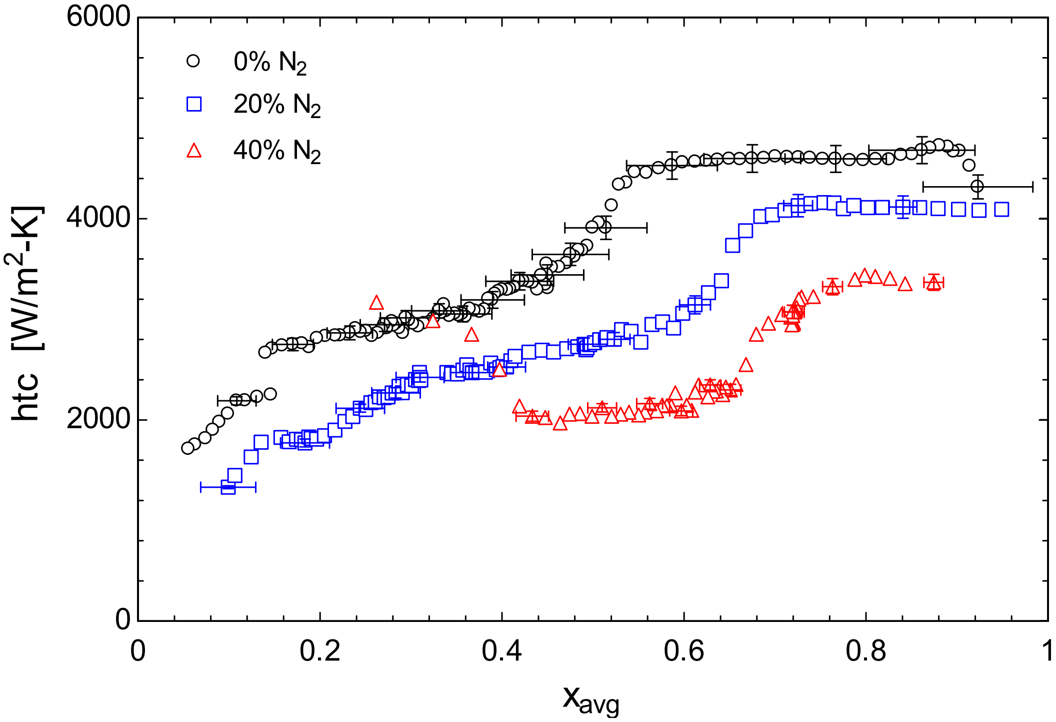

Figure 158. heat transfer coefficient as a function of average quality, Composition effect, hydrocarbon mixture, G = 144 kg/m^2-s, *P* = 790 kPa, *Q″* = 56 kW/m^2, *ID* = 1.5 mm, Runs 9, 10 and 11

C.11 Composition effect (3.0 mm)

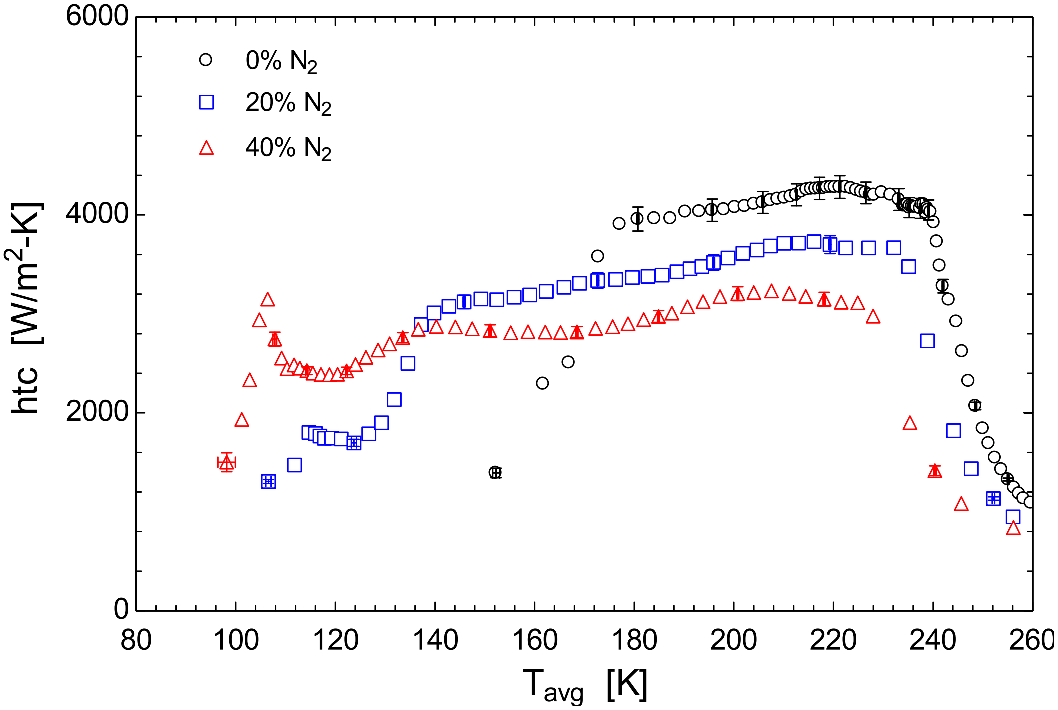

Figure 159. heat transfer coefficient as a function of average temperature, Composition effect, hydrocarbon mixture, G = 144 kg/m^2-s, *P* = 790 kPa, *Q″* = 56 kW/m^2, *ID* = 3.0 mm, Runs 13, 14 and 15

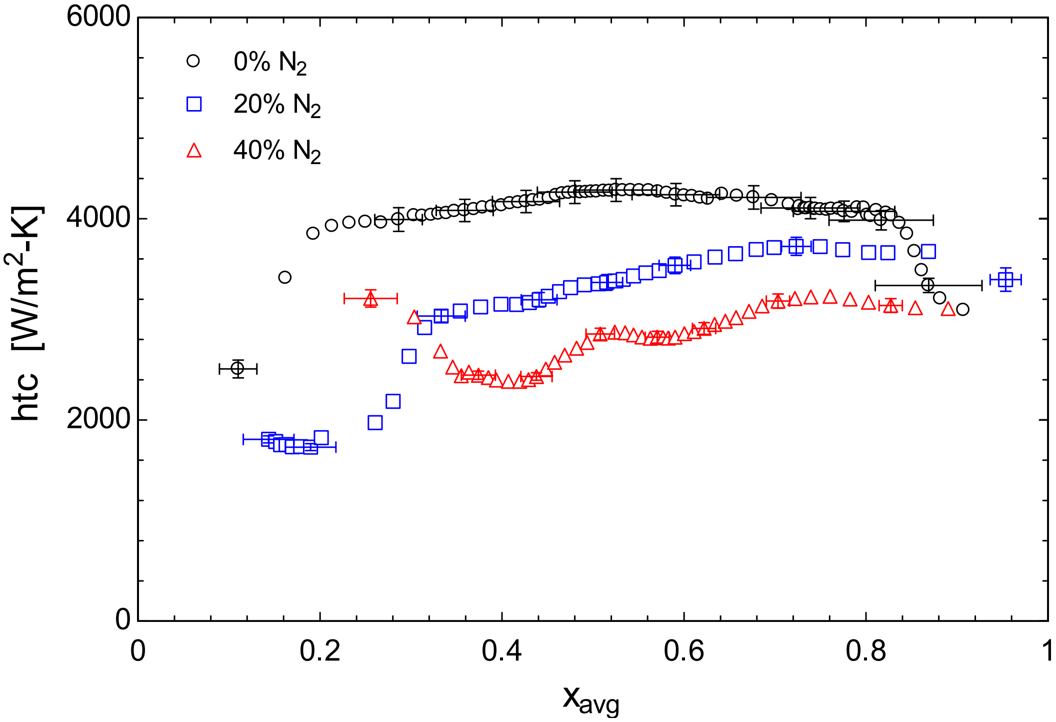

Figure 160. heat transfer coefficient as a function of average quality, Composition effect, hydrocarbon mixture, G = 144 kg/m^2-s, *P* = 790 kPa, *Q″* = 56 kW/m^2, *ID* = 3.0 mm, Runs 13, 14 and 15

C.12 Roughness effect

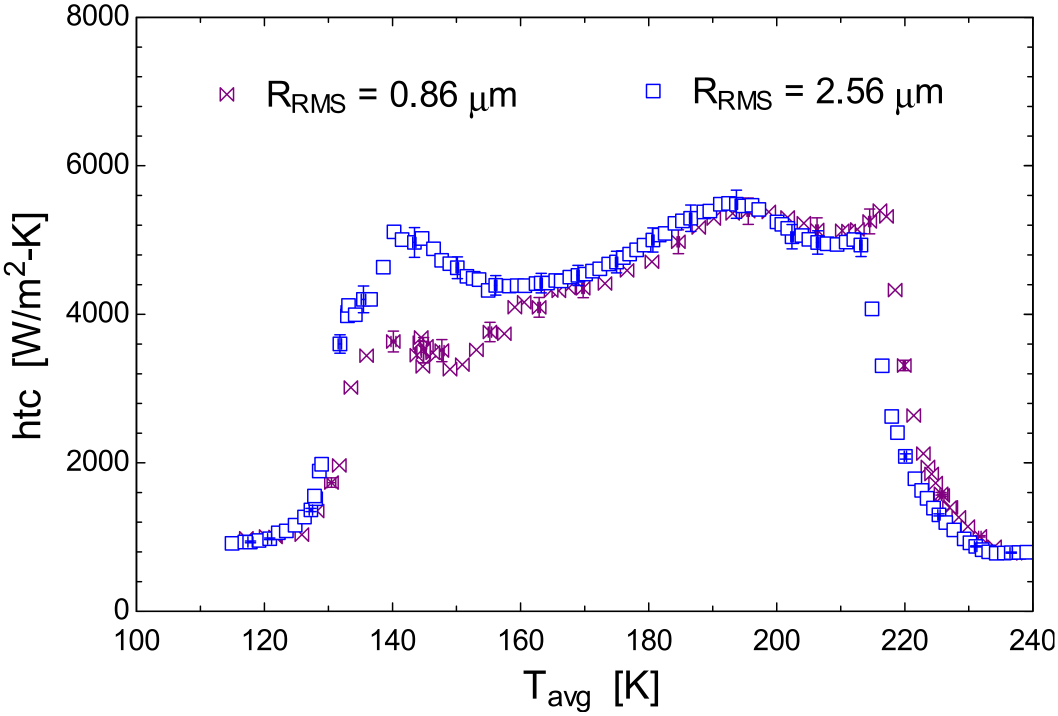

Figure 161. heat transfer coefficient as a function of average temperature, Composition effect, hydrocarbon mixture, G = 144 kg/m^2-s, P = 270 kPa, Q'' = 56 kW/m^2, ID = 1.5 mm, Runs 5 and 7

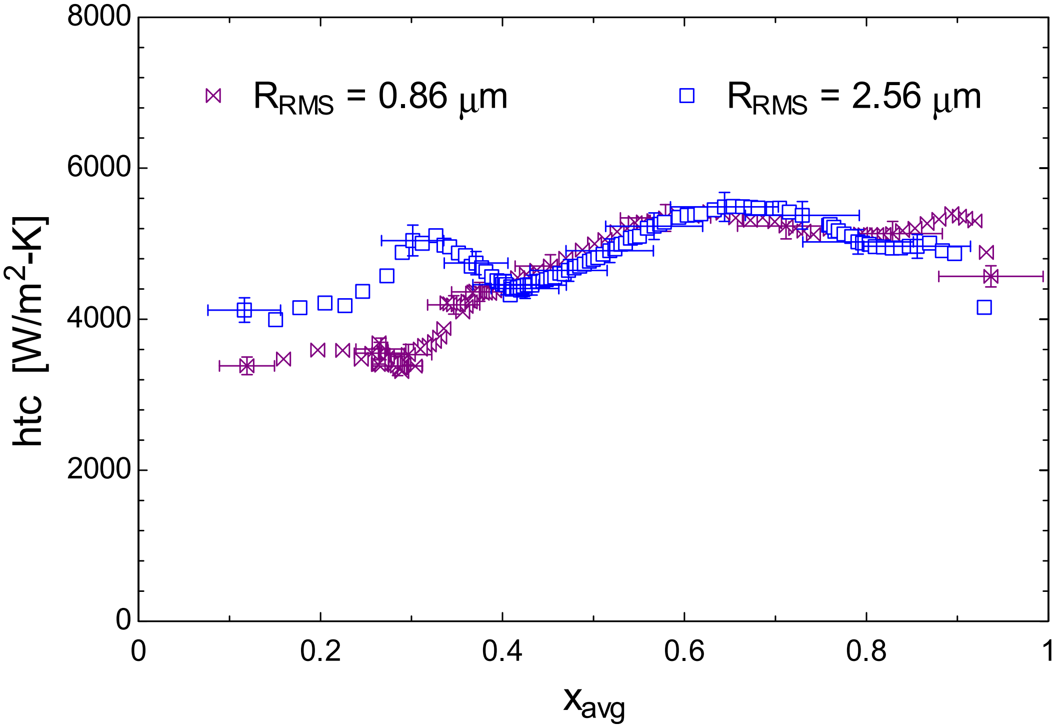

Figure 162. heat transfer coefficient as a function of average quality, Composition effect, hydrocarbon mixture, G = 144 kg/m^2-s, P = 270 kPa, Q'' = 56 kW/m^2, ID = 1.5 mm, Runs 5 and 7

Appendix D: Synthetic refrigerant mixture experimental data

D.1 Diameter effect (0% Argon)

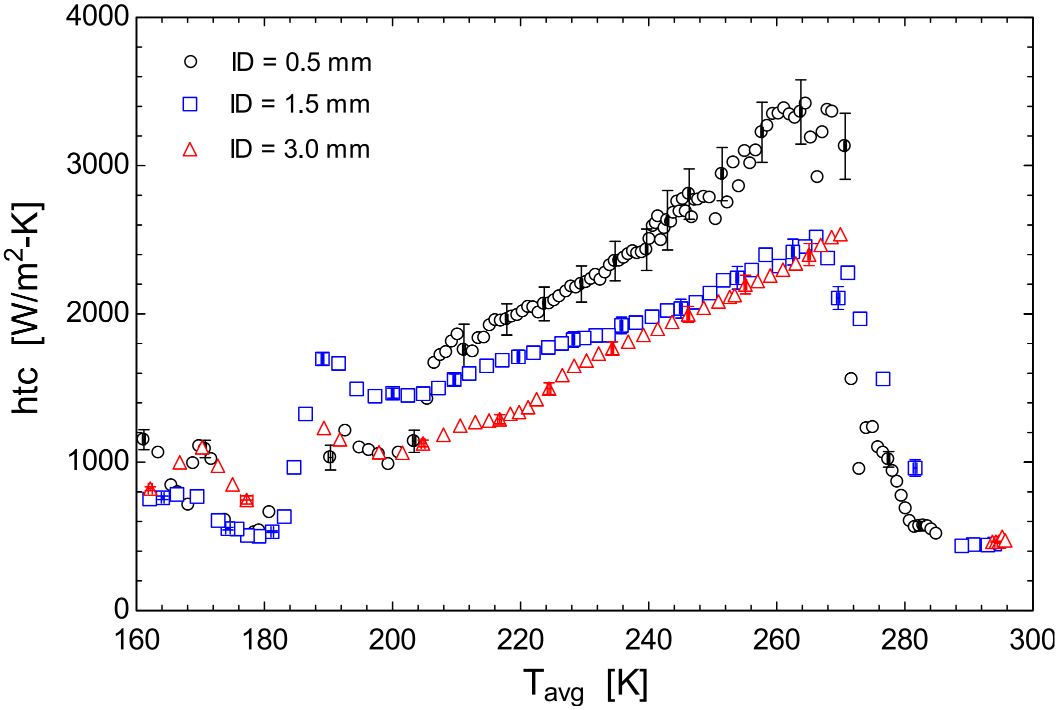

Figure 163. heat transfer coefficient as a function of average temperature, Diameter effect, synthetic refrigerant mixture (no dilution), G = 144 kg/m^2-s, P = 790 kPa, Q'' = 28 kW/m^2, Runs 16, 21 and 27

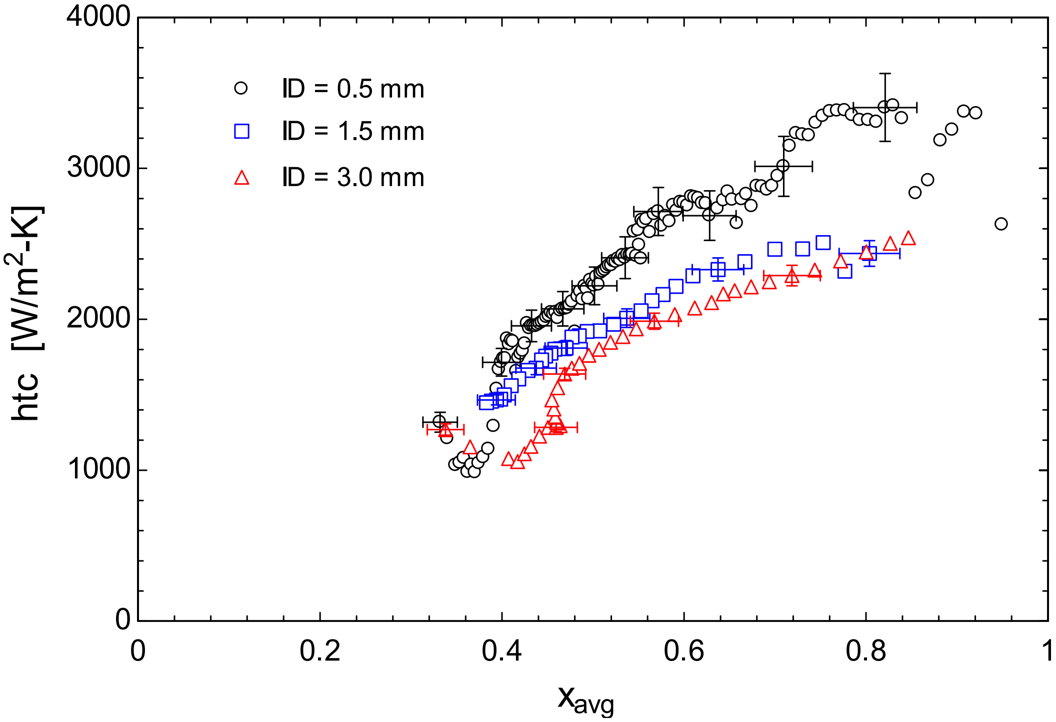

Figure 164. heat transfer coefficient as a function of average quality, Diameter effect, synthetic refrigerant mixture (no dilution), G = 144 kg/m^2-s, P = 790 kPa, Q'' = 28 kW/m^2, Runs 16, 21 and 27

D.2 Diameter effect (20% Argon)

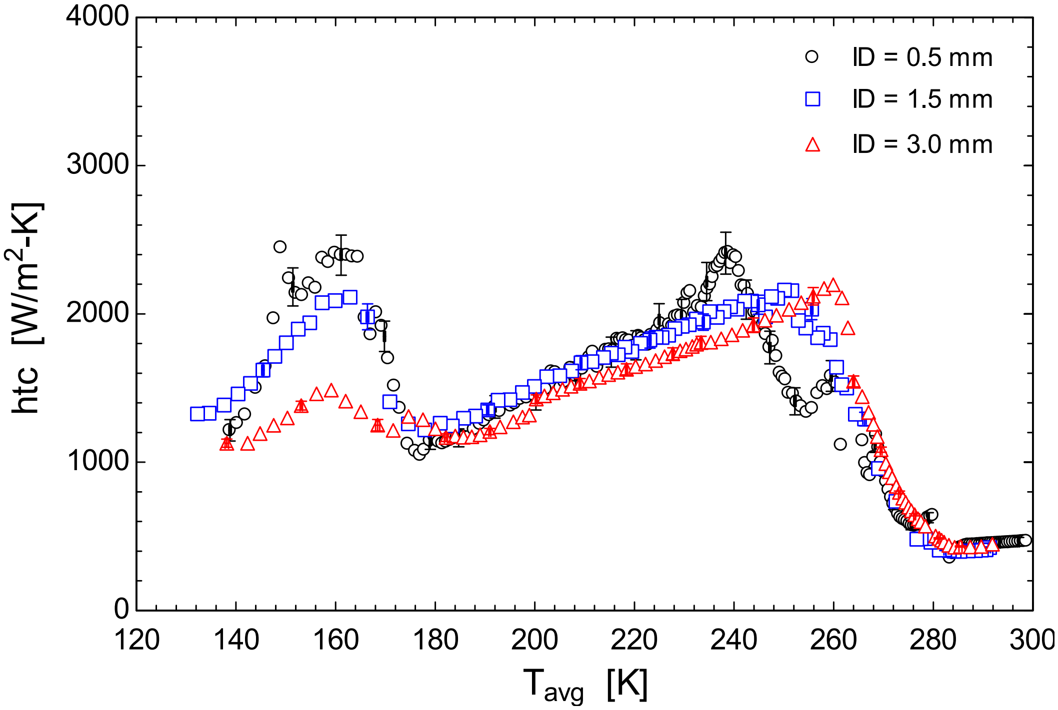

Figure 165. heat transfer coefficient as a function of average temperature, Diameter effect, synthetic refrigerant mixture (20% dilution), G = 144 kg/m^2-s, P = 790 kPa, Q'' = 28 kW/m^2, Runs 18, 24 and 28

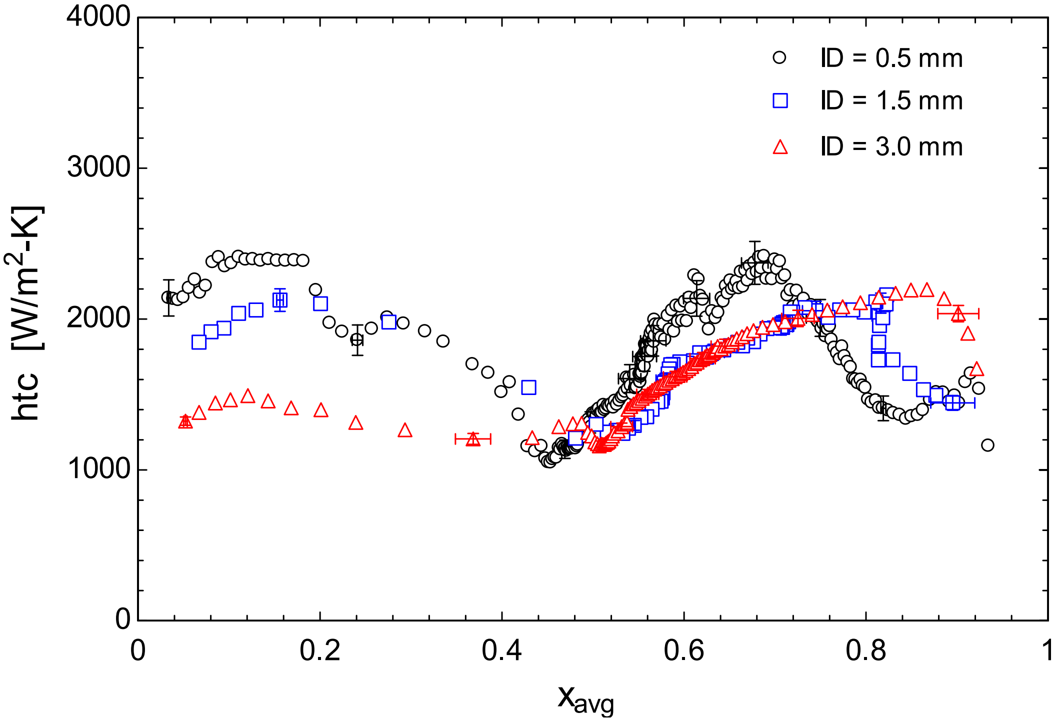

Figure 166. heat transfer coefficient as a function of average quality, Diameter effect, synthetic refrigerant mixture (20% dilution), G = 144 kg/m^2-s, P = 790 kPa, Q'' = 28 kW/m^2, Runs 18, 24 and 28

D.3 Diameter effect (40% Argon)

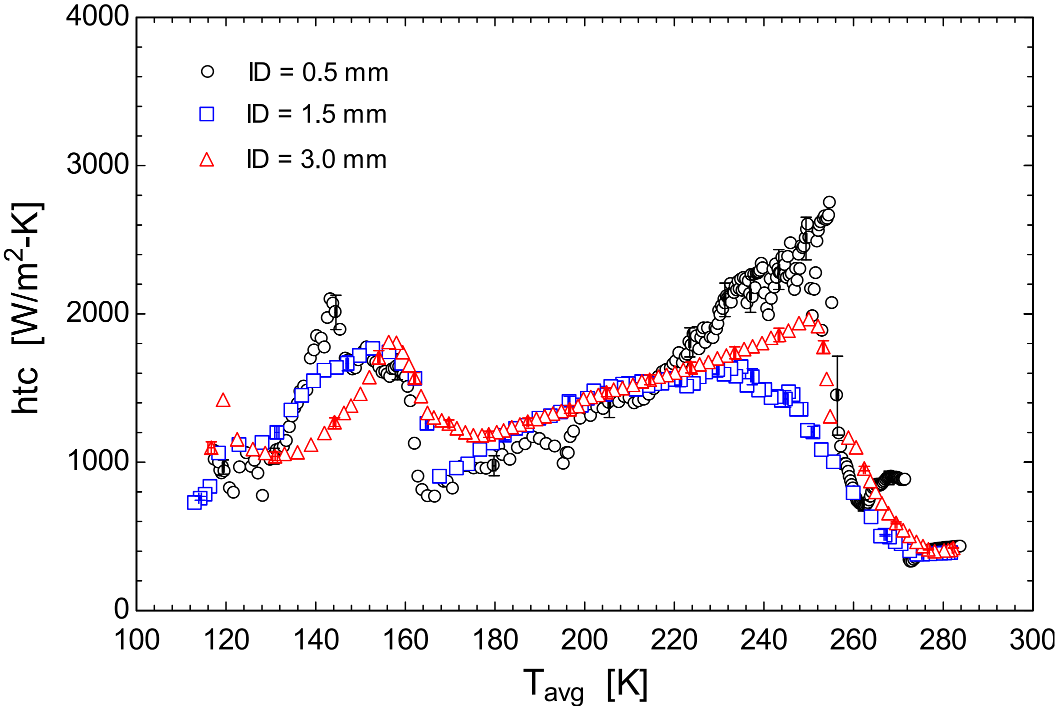

Figure 167. heat transfer coefficient as a function of average temperature, Diameter effect, synthetic refrigerant mixture (40% dilution), G = 144 kg/m^2-s, P = 790 kPa, Q'' = 28 kW/m^2, Runs 19, 25 and 29

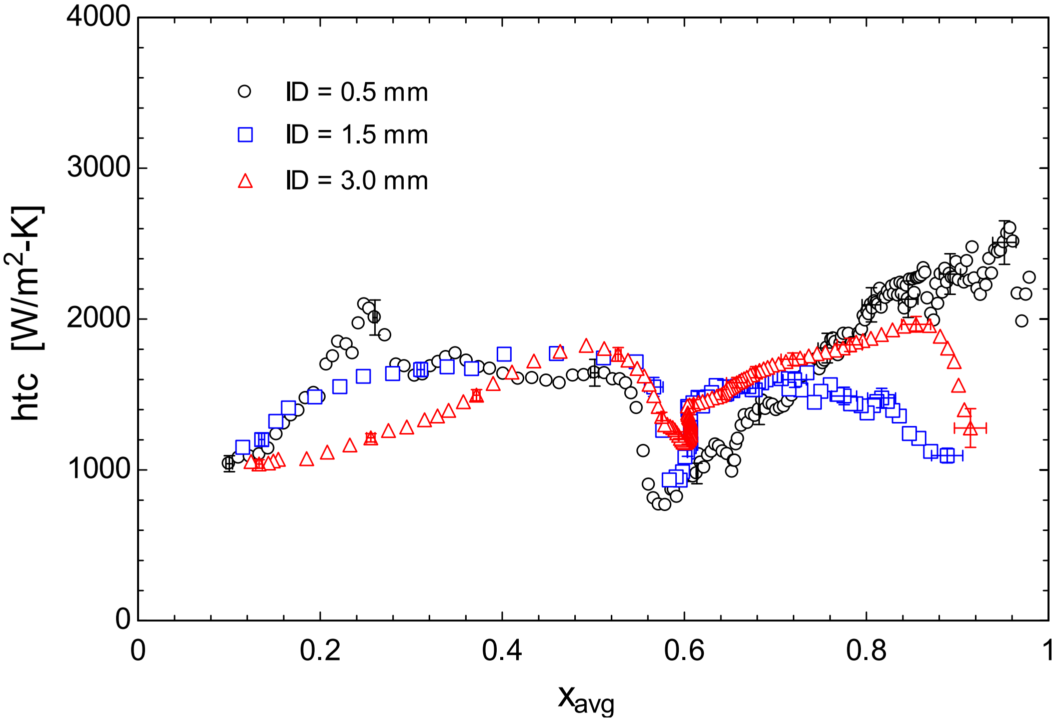

Figure 168. heat transfer coefficient as a function of average quality, Diameter effect, synthetic refrigerant mixture (40% dilution), G = 144 kg/m^2-s, P = 790 kPa, Q'' = 28 kW/m^2, Runs 19, 25 and 29

D.4 Heat flux effect (0.5 mm)

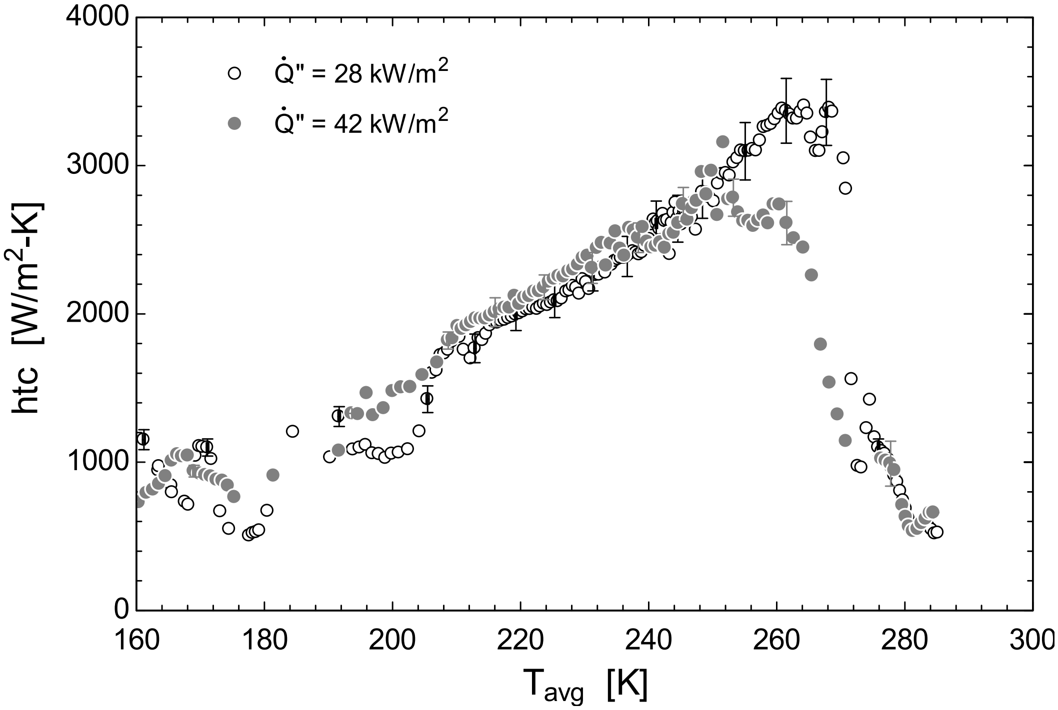

Figure 169. heat transfer coefficient as a function of average temperature, heat flux effect, synthetic refrigerant mixture (No dilution), G = 144 kg/m^2-s, P = 790 kPa, ID = 0.5 mm, Runs 16 and 17

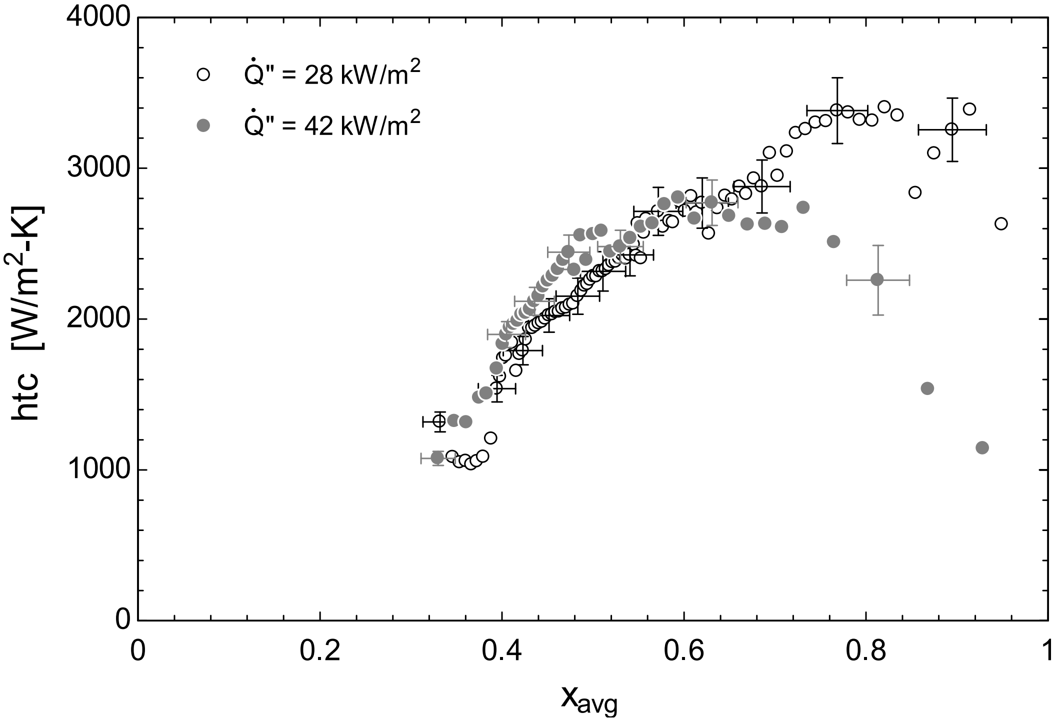

Figure 170. heat transfer coefficient as a function of average quality, heat flux effect, synthetic refrigerant mixture (No dilution), G = 144 kg/m^2-s, P = 790 kPa, ID = 0.5 mm, Runs 16 and 17

D.5 Heat flux effect (1.5 mm)

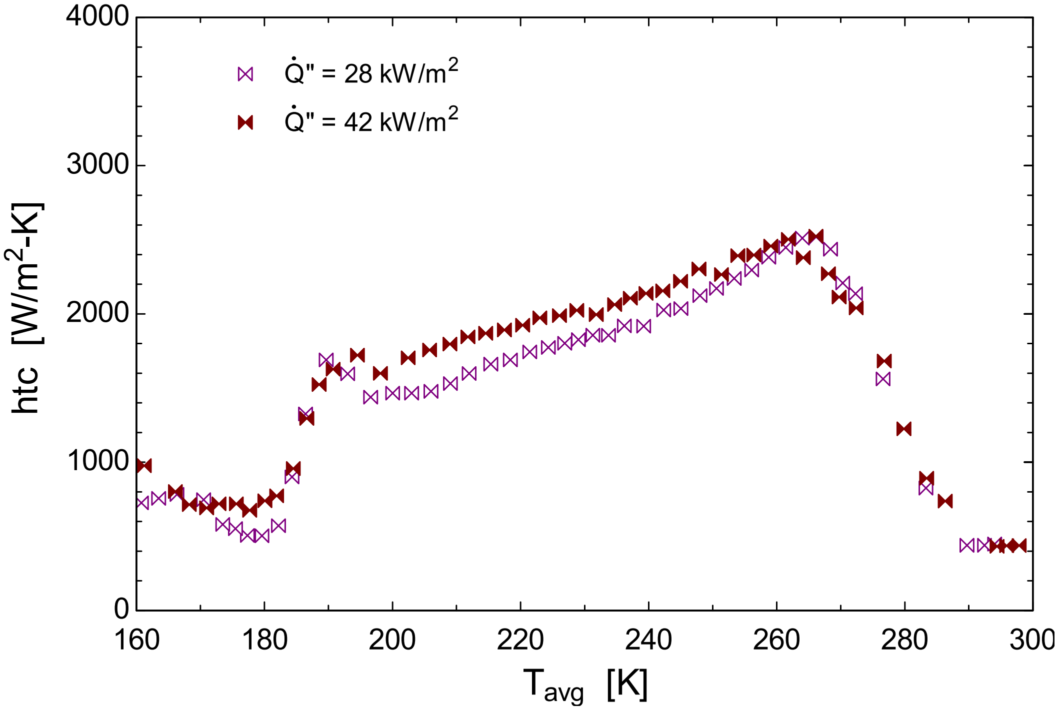

Figure 171. heat transfer coefficient as a function of average temperature, heat flux effect, synthetic refrigerant mixture (No dilution), *G* = 144 kg/m^2-s, *P* = 270 kPa, *ID* = 1.5 mm, Runs 21 and 22

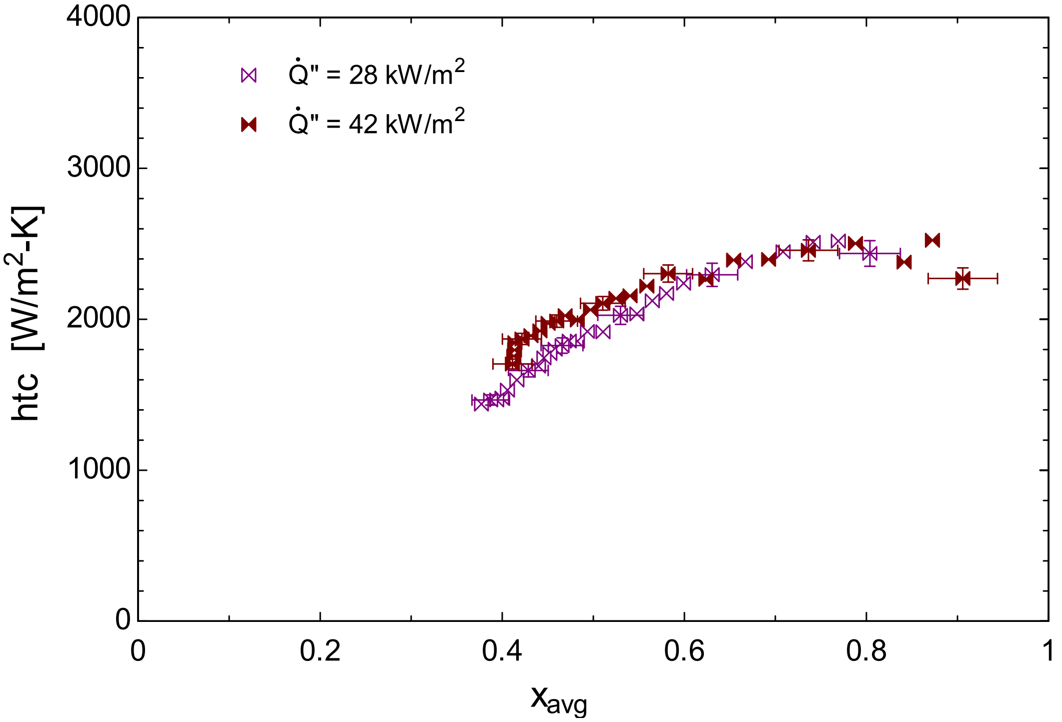

Figure 172. heat transfer coefficient as a function of average quality, heat flux effect, synthetic refrigerant mixture (No dilution), *G* = 144 kg/m^2-s, *P* = 270 kPa, *ID* = 1.5 mm, Runs 21 and 22

D.6 Heat flux effect (3.0 mm)

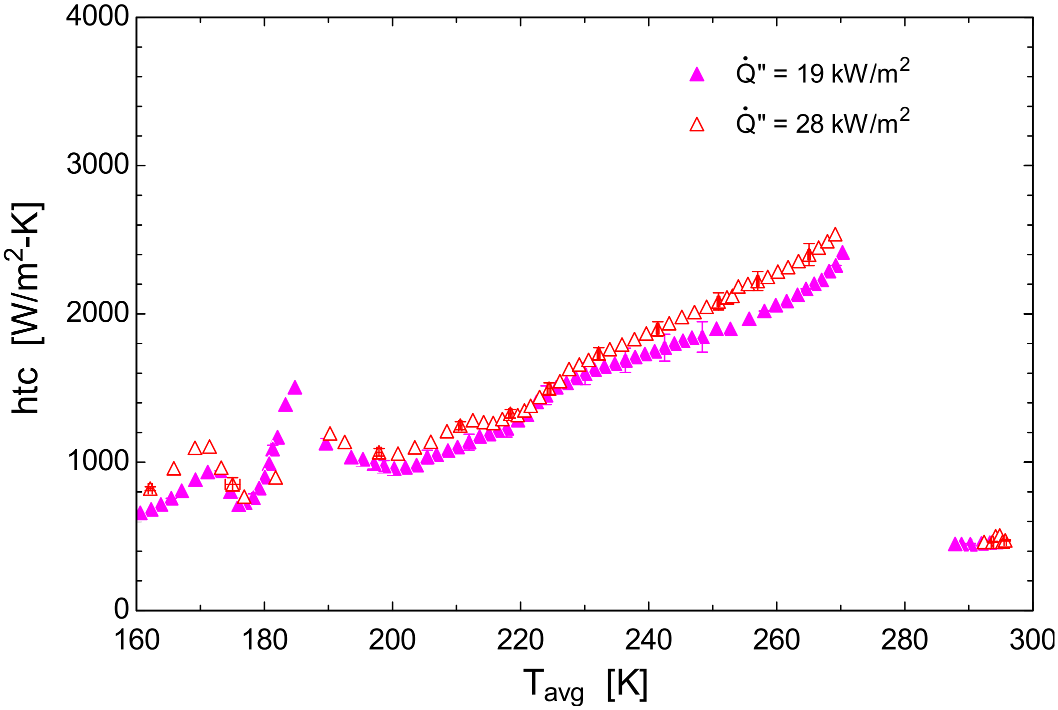

Figure 173. heat transfer coefficient as a function of average temperature, heat flux effect, synthetic refrigerant mixture (No dilution), *G* = 144 kg/m^2-s, *P* = 790 kPa, *ID* = 3.0 mm, Runs 26 and 27

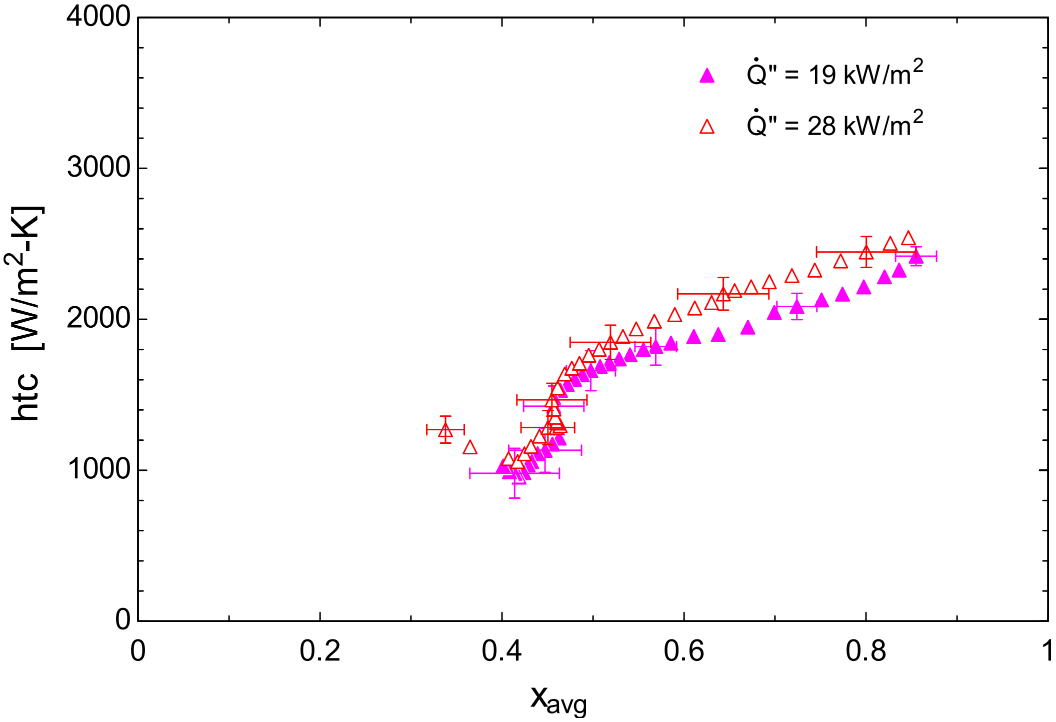

Figure 174. heat transfer coefficient as a function of average quality, heat flux effect, synthetic refrigerant mixture (No dilution), *G* = 144 kg/m^2-s, *P* = 790 kPa, *ID* = 3.0 mm, Runs 26 and 27

D.7 Pressure effect

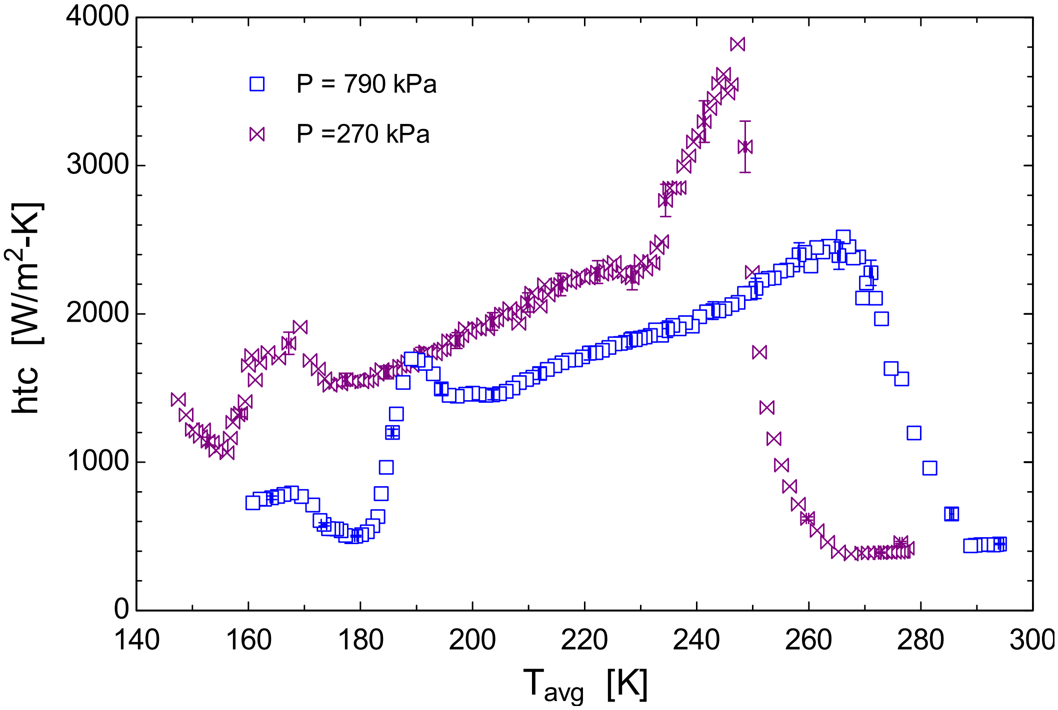

Figure 175. heat transfer coefficient as a function of average temperature, pressure effect, synthetic refrigerant mixture (no dilution), G = 144 kg/m^2-s, Q'' = 28 kW/m^2, ID = 1.5 mm, Runs 20 and 21

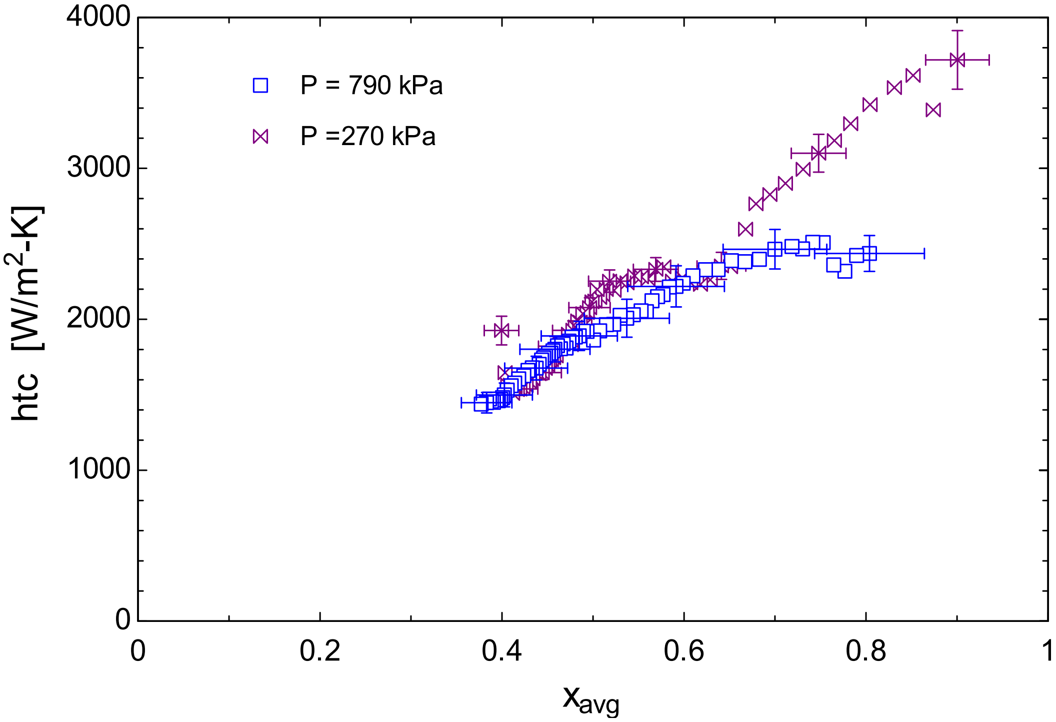

Figure 176. heat transfer coefficient as a function of average quality, pressure effect, synthetic refrigerant mixture (no dilution), G = 144 kg/m^2-s, Q'' = 28 kW/m^2, ID = 1.5 mm, Runs 20 and 21

D.8 Mass flux effect

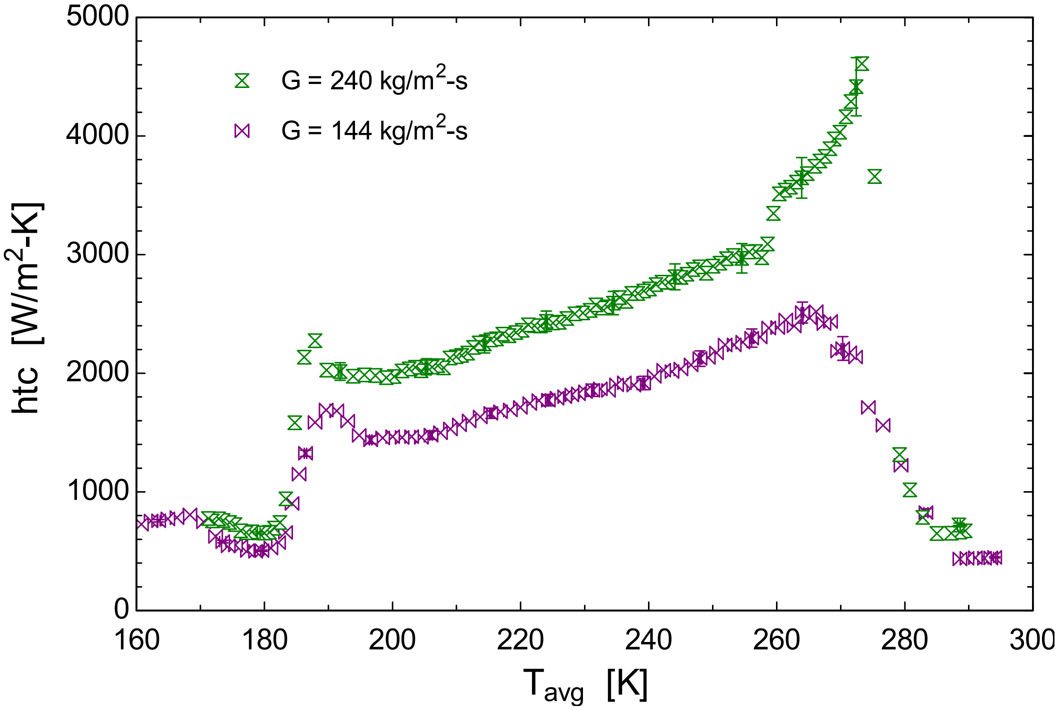

Figure 177. heat transfer coefficient as a function of average temperature, mass flux effect, synthetic refrigerant mixture (no dilution), P = 790 kPa, Q'' = 28 kW/m^2, ID = 1.5 mm, Runs 21 and 23

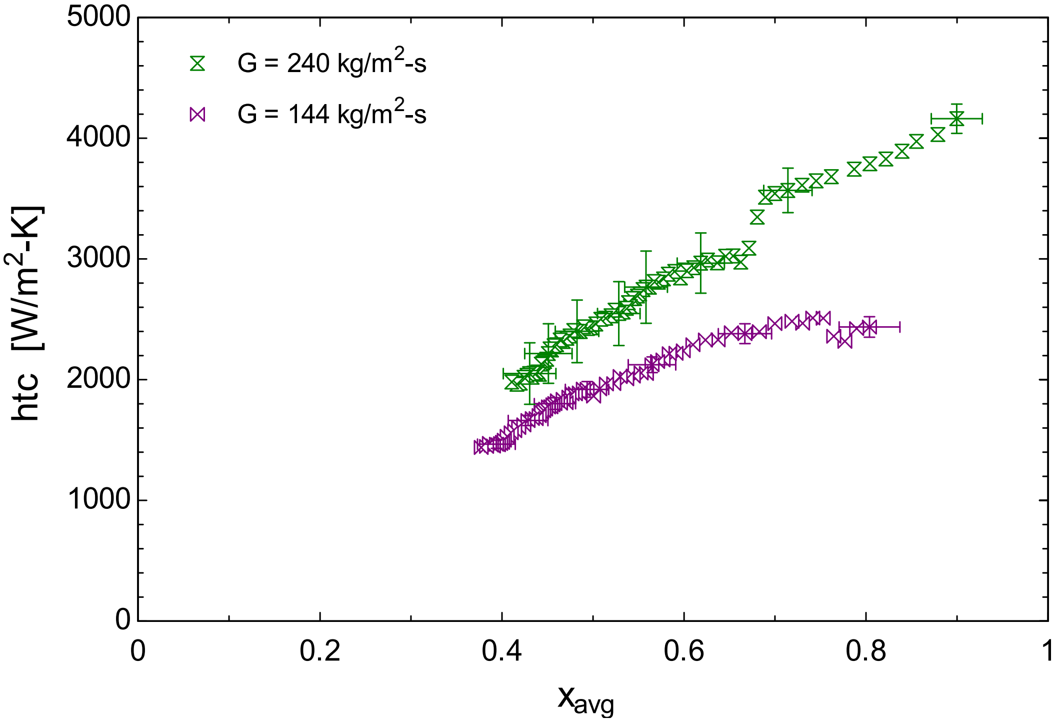

Figure 178. heat transfer coefficient as a function of average quality, mass flux effect, synthetic refrigerant mixture (no dilution), P = 790 kPa, Q'' = 28 kW/m^2, ID = 1.5 mm, Runs 21 and 23

D.9 Composition effect (0.5 mm)

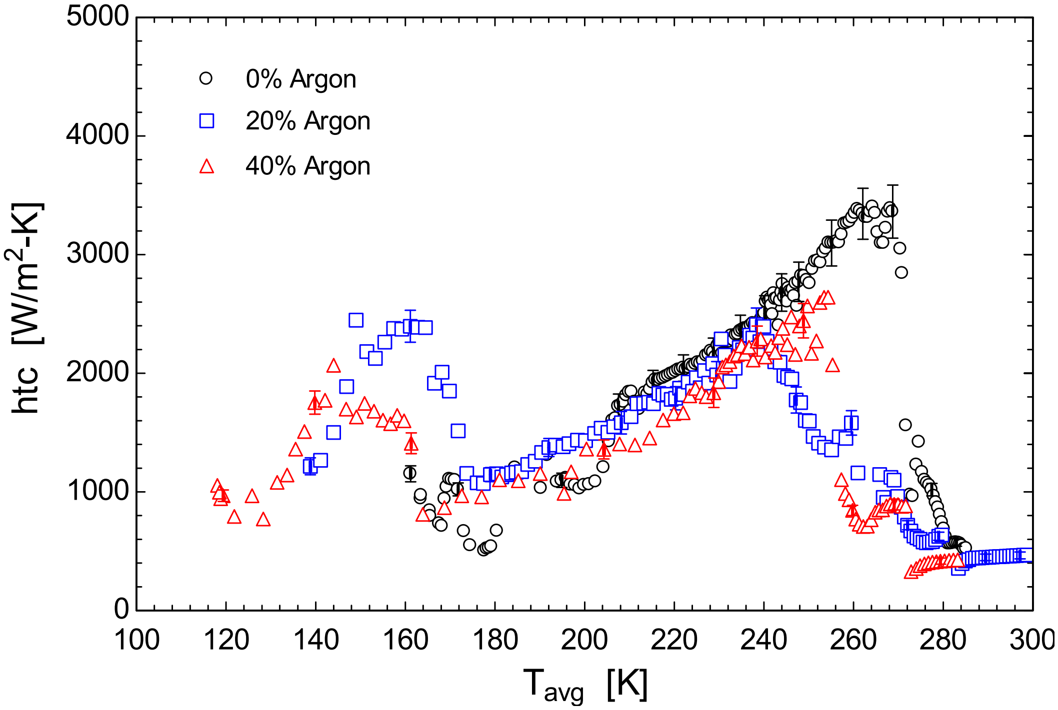

Figure 179. heat transfer coefficient as a function of average temperature, Composition effect, synthetic refrigerant mixture, G = 144 kg/m^2-s, P = 790 kPa, Q'' = 28 kW/m^2, ID = 0.5 mm, Runs 16, 18 and 19

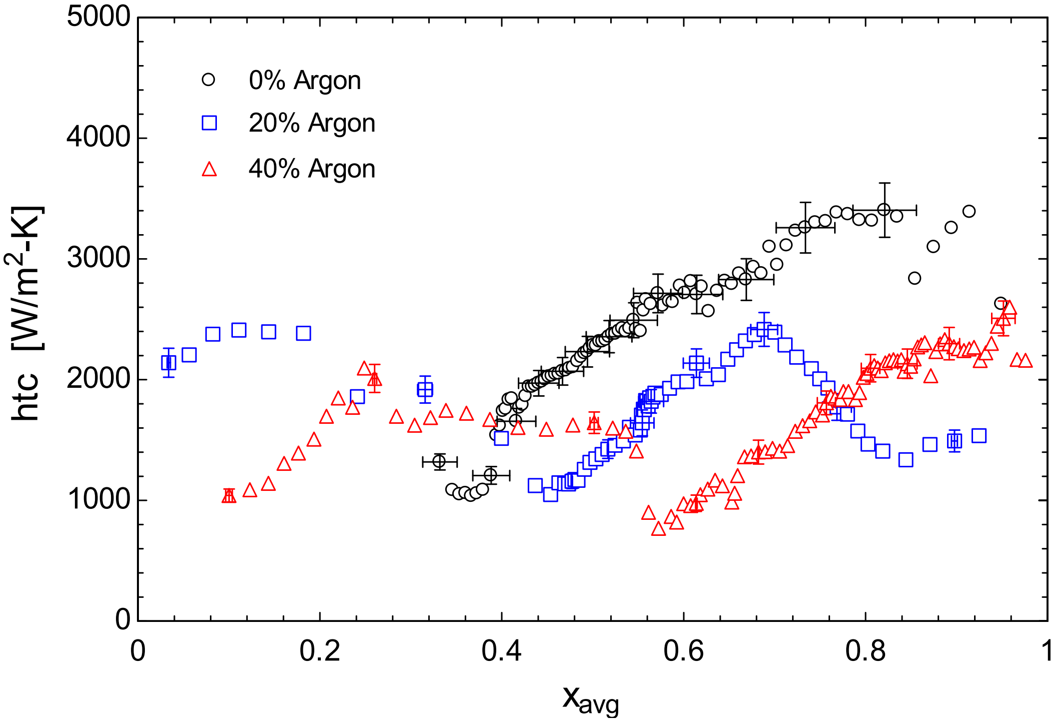

Figure 180. heat transfer coefficient as a function of average quality, Composition effect, synthetic refrigerant mixture, G = 144 kg/m^2-s, P = 790 kPa, Q'' = 28 kW/m^2, ID = 0.5 mm, Runs 16, 18 and 19

D.10 Composition effect (1.5 mm)

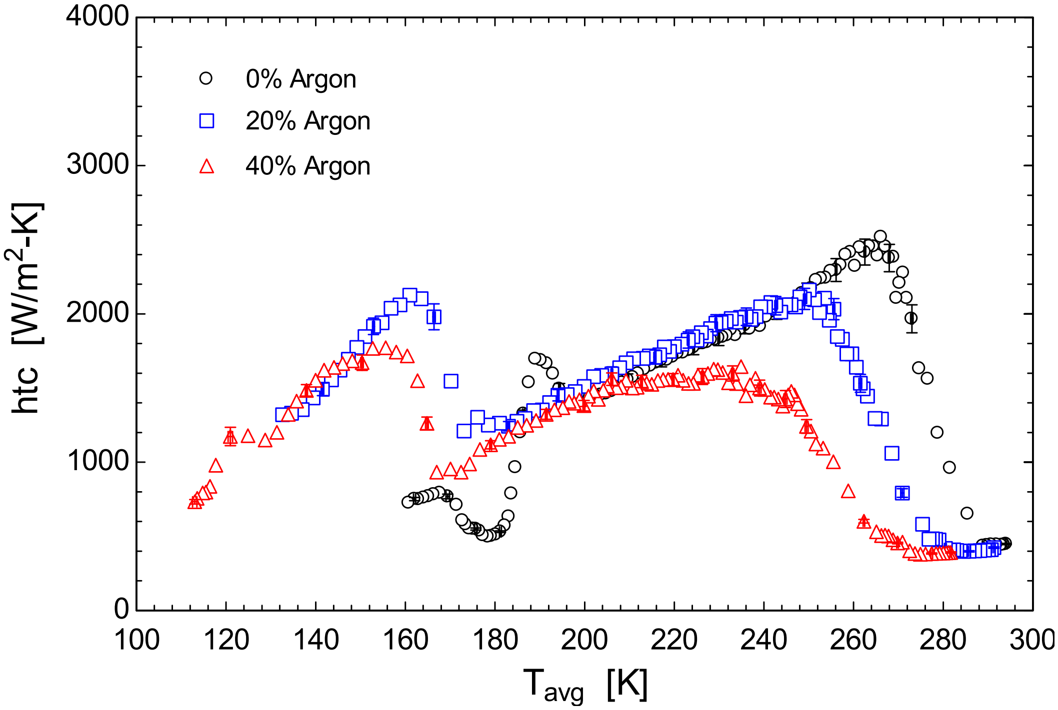

Figure 181. heat transfer coefficient as a function of average temperature, Composition effect, synthetic refrigerant mixture, G = 144 kg/m^2-s, P = 790 kPa, Q'' = 28 kW/m^2, ID = 1.5 mm, Runs 21, 24 and 25

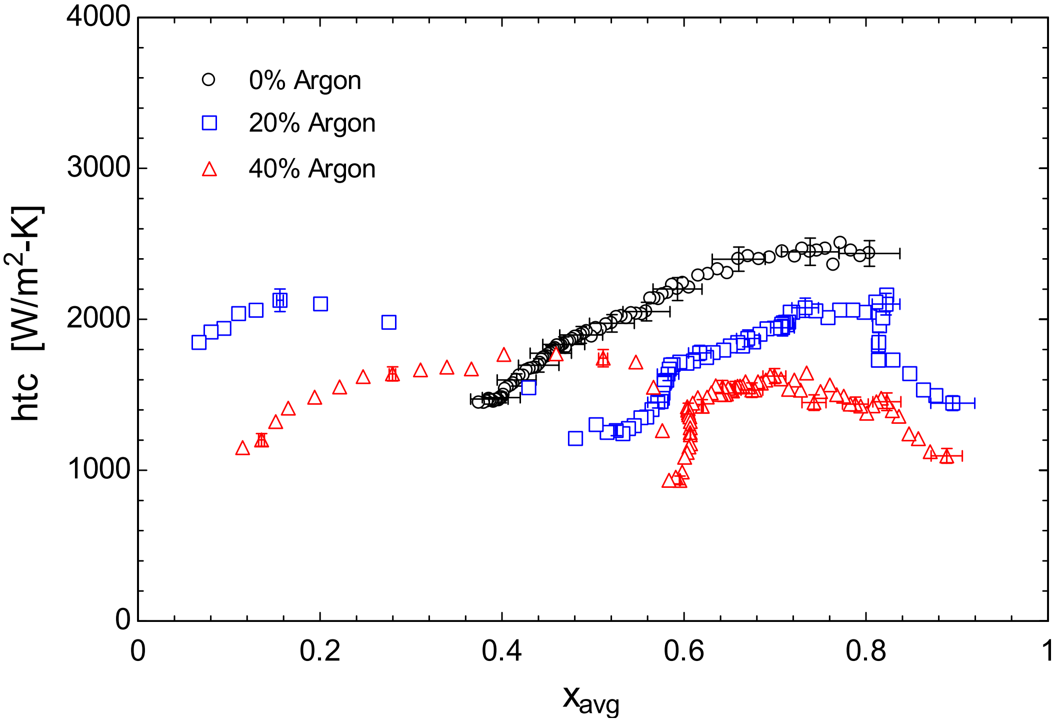

Figure 182. heat transfer coefficient as a function of average quality, Composition effect, synthetic refrigerant mixture, G = 144 kg/m^2-s, P = 790 kPa, Q'' = 28 kW/m^2, ID = 1.5 mm, Runs 21, 24 and 25

D.11 Composition effect (3.0 mm)

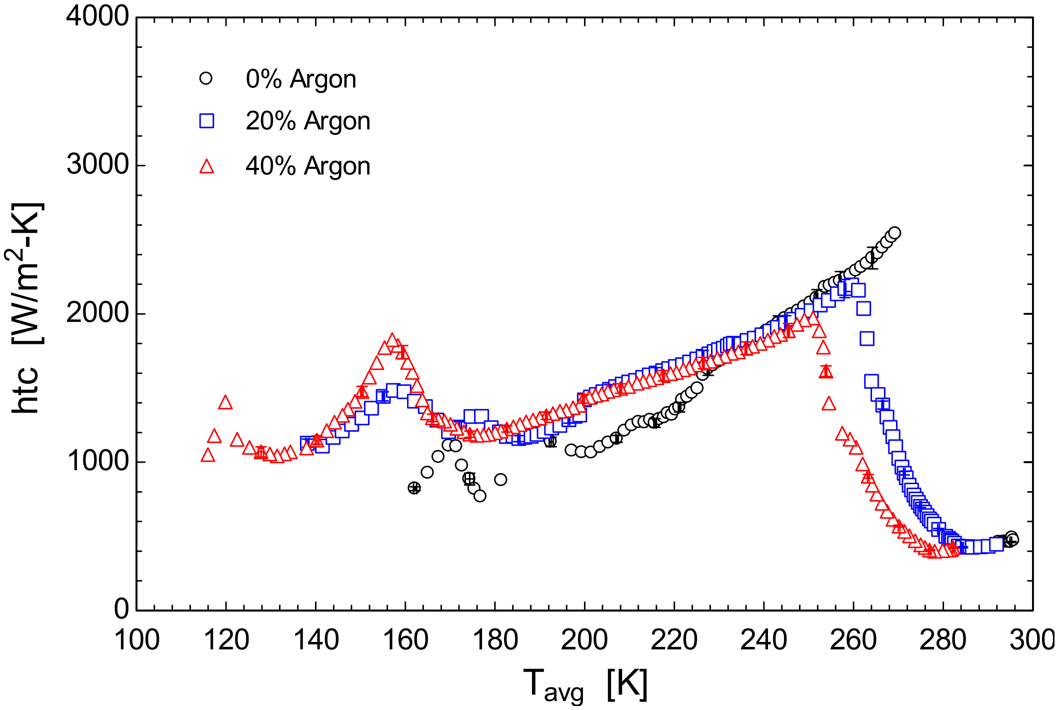

Figure 183. heat transfer coefficient as a function of average temperature, Composition effect, synthetic refrigerant mixture, G = 144 kg/m^2-s, P = 790 kPa, Q'' = 28 kW/m^2, ID = 3.0 mm, Runs 27, 28 and 29

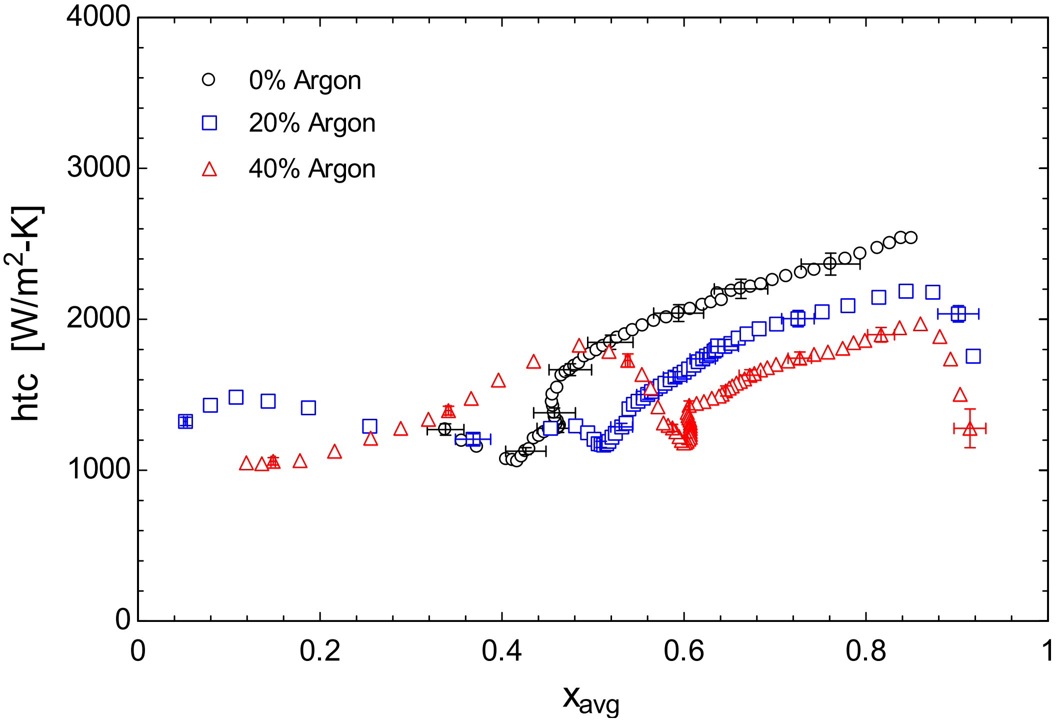

Figure 184. heat transfer coefficient as a function of average quality, Composition effect, synthetic refrigerant mixture, G = 144 kg/m^2-s, P = 790 kPa, Q'' = 28 kW/m^2, ID = 3.0 mm, Runs 27, 28 and 29

Appendix E: Little's model validation

Little proposed a heat transfer coefficient model based on annular flow as shown in Figure 185. Heat is transferred from the wall to the liquid film flowing along the wall. A fraction of this heat vaporizes some liquid at the liquid-vapor interface and the remainder is transferred from the liquid film to the vapor driven by the liquid-vapor temperature difference (ΔT_{lv}).

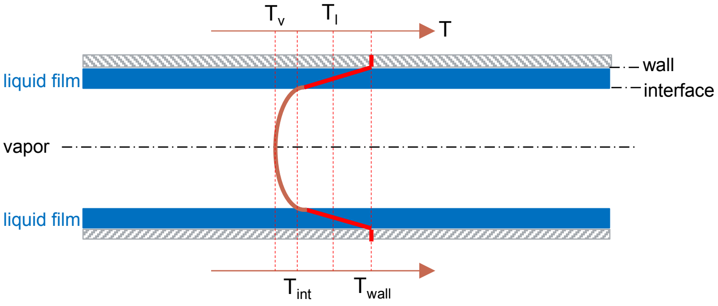

Figure 185. Schematic of zeotropic mixtures during boiling, annular flow, temperature profile

The two-phase heat transfer coefficient may be defined as the ratio of the heat flux applied ($\dot{Q}''$) and the temperature difference between the wall (T_{wall}) and the mixture equilibrium temperature (T_e):

$$\frac{1}{htc} = \frac{T_{wall} - T_e}{\dot{Q}''} \tag{123}$$

The equilibrium temperature, T_e, is experienced at the liquid-vapor interface. The derivation of the Little model defines the equilibrium temperature (T_e) as a weighted average of the liquid and vapor phase temperatures using the corresponding specific heat, Eq. (124):

$$T_e = \frac{(1-x)\,Cp_l\,T_l + x\,Cp_v\,T_v}{(1-x)\,Cp_l + x\,Cp_v} \tag{124}$$

The temperature difference between the liquid and vapor phases, ΔT_{lv}, is given by:

$$T_l - T_v = \Delta T_{lv} \tag{125}$$

Substituting Eq. (124) into Eq. (123) and replacing the vapor temperature, T_v, by the definition shown in Eq. (125), the two phase heat transfer coefficient is given by:

$$\frac{1}{htc} = \frac{1}{\dot{Q}''}\left[T_{wall} - \frac{(1-x)\,Cp_l\,T_l + x\,Cp_v\,(T_l - \Delta T_{lv})}{(1-x)\,Cp_l + x\,Cp_v}\right] = \frac{T_{wall} - T_l}{\dot{Q}''} + \frac{x\,Cp_v\,\Delta T_{lv}}{(1-x)\,Cp_l + x\,Cp_v}\frac{1}{\dot{Q}''} \tag{126}$$

The first term of Eq. (126) is the heat transfer coefficient between the liquid film and the wall tube ($htc_{l,film}$). ΔT_{lv} drives the heat transfer between the liquid film and the vapor core as suggested by Eq. (127):

$$\dot{Q}''_v = htc_{lv}\,\Delta T_{lv} \tag{127}$$

Combining Eqs. (126) and (127), the second term is expressed as a function of the ratio between the heat transfer rate to the vapor phase and the heat transfer rate to the mixture:

$$\frac{1}{htc} = \frac{1}{htc_{l,film}} + \frac{x\,Cp_v}{htc_{lv}\left((1-x)\,Cp_l + x\,Cp_v\right)}\frac{\dot{Q}''_v}{\dot{Q}''} \tag{128}$$

The heat transfer to the vapor core drives a change in temperature of the vapor phase, which is a function of vapor phase specific heat. The heat transfer to the mixture also produces a change in the mixture temperature that is a function of the apparent specific heat of the mixture. It is assumed that the temperature change of the vapor phase has the same magnitude of the temperature change of the mixture ($\Delta T_v = \Delta T$) leading to:

$$\frac{\dot{Q}_v}{\dot{Q}} = \frac{\dot{m}_v \, Cp_v \, \Delta T_v}{\dot{m}\left(\frac{\partial h}{\partial T}\right)_P \Delta T} = \frac{x \, Cp_v}{\left(\frac{\partial h}{\partial T}\right)_P} \tag{129}$$

The Little model is obtained combining Eqs. (128) and (129). Eq. (130) is the final expression for the two-phase heat transfer coefficient and is similar to Eq. (106):

$$\frac{1}{htc} = \frac{1}{htc_{l,film}} + \frac{x^2 \, Cp_v^{\,2}}{\left((1-x)\,Cp_l + x\,Cp_v\right)\left(\frac{\partial h}{\partial T}\right)_P} \frac{1}{htc_{lv}} \tag{130}$$

The Little model defines a turbulent liquid film, similar to what is described by Kattan [98], which uses the hydraulic diameter of the annulus to take into account the velocity of the liquid film in the two phase-region. The hydraulic diameter (D_h) of the annulus is defined as the difference between the inner tube diameter (*ID*) and the diameter of the vapor core (D_v). If the vapor diameter is expressed as a function of the void fraction (α) and the inner diameter of the tube, the hydraulic diameter of the annulus is given by Eq. (131):

$$D_H = ID - D_v = ID\left(1 - \frac{D_v}{ID}\right) = ID\left(1 - \sqrt{\alpha}\right) \tag{131}$$

The Reynolds number of liquid film ($Re_{l,film}$) is obtained starting from the liquid velocity (u_l). The film liquid area (A_l) is included to determine the liquid volume flow rate ($\dot{V}_l$), which allows to determine the liquid mass flow rate ($\dot{m}_l$) when the liquid volume flow rate ($\dot{V}_l$) is combined with the liquid density (ρ_l). The film area (A_l) for the Reynolds number is obtained from the tube area (A) and the void fraction (α). Finally, the Reynolds number of the liquid film is a function of the liquid Reynolds number (Re_l) and the void fraction (α):

$$Re_{l,film} = \frac{D_h \rho_l u_l}{\mu_l} = \frac{ID\left(1-\sqrt{\alpha}\right)\rho_l \dot{V}_l}{\mu_l A_l} = \frac{ID\left(1-\sqrt{\alpha}\right)\dot{m}_l}{\mu_l A_l} = \frac{ID\,\dot{m}(1-x)}{\mu_l A}\frac{\left(1-\sqrt{\alpha}\right)}{(1-\alpha)} = Re_l \frac{1}{\left(1+\sqrt{\alpha}\right)} \qquad (132)$$

Consequently, the heat transfer coefficient of the liquid film using Dittus-Boelter is expressed as a function of the void fraction:

$$htc_{l,film} = 0.023\left(\frac{Re_l}{1+\sqrt{\alpha}}\right)^{0.8} Pr_l^{0.4}\frac{k_l}{ID\left(1-\sqrt{\alpha}\right)} \qquad (133)$$

A similar methodology is used to find the heat transfer coefficient of the core vapor (Eq. (134)
)

$$htc_{lv} = 0.023\left(\frac{Re_v}{\sqrt{\alpha}}\right)^{0.8} Pr_v^{0.4}\frac{k_v}{ID\sqrt{\alpha}} \qquad (134)$$

The void fraction is obtained using the Chisholm model shown in Eq. (135):

$$\alpha_{ch} = \left(1+\frac{(1-x)\rho_v}{x\rho_l}\sqrt{1-x\left(1-\frac{\rho_l}{\rho_v}\right)}\right)^{-1} \qquad (135)$$